

LONG-TIME ATOM INTERFEROMETRY FOR PRECISION  
TESTS OF FUNDAMENTAL PHYSICS

A DISSERTATION  
SUBMITTED TO THE DEPARTMENT OF PHYSICS  
AND THE COMMITTEE ON GRADUATE STUDIES  
OF STANFORD UNIVERSITY  
IN PARTIAL FULFILLMENT OF THE REQUIREMENTS  
FOR THE DEGREE OF  
DOCTOR OF PHILOSOPHY

Susannah Moore Dickerson  
August 2014

# Abstract

Light-pulse atom interferometry is a technique that is exquisitely sensitive to inertial forces. As such, it has exciting applications both in fundamental physics for precision tests of gravity, electrodynamics and quantum mechanics, as well as in practical situations for inertial navigation, geodesy, and timekeeping. In this work, I describe a 10 meter atomic fountain, designed for a precision test of the weak equivalence principle but with additional relevance in bounding proposed modifications of quantum mechanics, directly measuring general relativistic corrections, and detecting gravitational waves. This system is demonstrated to have the largest acceleration sensitivity to date by two orders of magnitude ( $6.7 \times 10^{-12} g$ ). I also present precision measurements of Earth's rotation, the preparation of ultracold clouds to picokelvin effective temperatures, and current work to further improve the acceleration sensitivity through meter-scale separation between two halves of the atomic wavepacket. I close with a discussion of the next step towards an equivalence principle test: the creation of a well-overlapped, dual-species ultracold cloud.

# Acknowledgements

It has been a privilege to work on this project, as much for its science as its people.

Mark Kasevich has been an unfailing source of optimism when times are tough and excitement when the results roll in. From him, I've learned not just the technical aspects of being a good experimentalist (his advice is eerily spot-on), but also how to present the results in a clear and captivating way. His ability to identify and successfully pursue grand scientific visions is a skill I can only hope to emulate in a decade or three.

With me in the lab has been a collection of phenomenal researchers. Jason Hogan is amazingly talented at stripping down data to the essentials, enabling the underlying physics to shine through. Dave Johnson, whose machining intuition is unmatched, taught me about effective apparatus construction, a critical skill for this project. On top of his deep foundation in circuit design and lego construction, Alex Sugarbaker, my yearmate, is incredibly thoughtful about group inclusivity, which was highlighted in the passing of the baton to the new generation of graduate students. Tim Kovachy is the go-to guy for all things high power and large momentum, and his comments are always well-seated in the fundamental theory. Sheng-wey Chiow was the MacGuyver of the lab, performing magic with microwave circuits. Jan Rudolph and Jakob Hammer, two extended visitors to the lab, added a much-appreciated European flair along with their hard work.

Christine Donnelly and Chris Overstreet will be supervising the next stage of the experiment, and I wish them the best of luck. Good things are on their way.

I couldn't have asked for a better set of colleagues than those that are already in the Kasevich Group. Whether it's kickball or spectrum analyzers, Friday beer or the

Schrödinger equation, you all are ready and willing to share, debate, and have fun.

Ping Feng, Sha Zhang, and Beth Noronha, the group staff over the years, have kept the labs running smoothly. In addition, all the members of the Physics Department Main Office have ensured that we are well cared for as graduate students. We are so lucky and grateful that you are on our side.

I'd also like to thank the machinists, Karlheinz, John, Matt, Mehmet, and Scott for their cheerful waves each morning as I pass through their domain on my way to the lab.

I am very grateful to all my friends, both from before and after the start of grad school, for encouragement, collaboration, commiseration, excitement, and celebration. The teas, barbecues, and hiking excursions have all been the highlights punctuating the Ph.D. acquisition experience. So thank you to Alex, Andrew, Beth, Caitlin, Camille, Cat, Chihway, Dave, Dima, Ellen, Eugenie, Jamie, Jared, Jeff, Jon, Kassa, Katie, Keith, Kimmi, Limor, Matt, Michael, Mina, Nicole, Patty, Paul, Rebecca, Sarah, Sharon, Tom, and Tomas.

Finally, my family. When we started dating, little did Karl know that he would earn the titles of therapist, life coach, and personal chef in addition to boyfriend. Thank you for making the bad times manageable and the good times great. Mom (TGMITW), Dad (TGDIRW), Sis (TGSITW): this wouldn't have been possible without you and your bottomless wells of encouragement, patience, and hugs, telephonic or otherwise. Endurance from the Sphinx trail, curiosity from scuba diving, imagination from the little man in the pointy hat, and fearlessness from the Via della Bouchette have all culminated in this work.

Enjoy!

# Contents

<b>Abstract</b>	<b>iv</b>
<b>Acknowledgements</b>	<b>v</b>
<b>1 Introduction</b>	<b>1</b>
<b>2 The equivalence principle and beyond</b>	<b>5</b>
2.1 From Aristotle to Einstein . . . . .	5
2.2 The modern equivalence principle . . . . .	13
2.3 Atom interferometry and precision measurement . . . . .	16
2.3.1 Application to the equivalence principle . . . . .	18
2.3.2 Beyond the equivalence principle . . . . .	19
<b>3 Atom interferometry</b>	<b>23</b>
3.1 Atom optics: beamsplitters and mirrors . . . . .	25
3.1.1 Interferometry with a two-level atom . . . . .	25
3.1.2 From two levels to three and back again . . . . .	27
3.2 Interferometer phase shift formalism . . . . .	30
3.3 Mach-Zehnder interferometry . . . . .	32
3.3.1 Sensitivity to $g$ . . . . .	35
3.3.2 Application to an equivalence principle test . . . . .	36
3.3.3 Systematic effects . . . . .	36
3.3.4 Beam tilt phase shear . . . . .	40
3.3.5 Interferometer contrast . . . . .	40

3.4	Prospects for other interferometer topologies . . . . .	41
<b>4</b>	<b>Apparatus</b>	<b>42</b>
4.1	Ultracold cloud preparation . . . . .	47
4.1.1	Magneto-optical traps . . . . .	48
4.1.2	Evaporation . . . . .	53
4.1.3	Magnetic lensing . . . . .	65
4.1.4	State preparation . . . . .	65
4.1.5	Launching . . . . .	66
4.2	Atom optics . . . . .	69
4.2.1	Frequency . . . . .	70
4.2.2	Polarization . . . . .	71
4.2.3	Wavefront and intensity homogeneity . . . . .	71
4.2.4	AC Stark shifts . . . . .	73
4.2.5	Spontaneous emission . . . . .	75
4.2.6	Implementation . . . . .	75
4.2.7	Atom optics optimization . . . . .	81
4.3	Fluorescence detection . . . . .	82
4.4	Absorption imaging . . . . .	87
4.4.1	Absorption image analysis . . . . .	90
4.5	Rotation compensation system for suppression of the Coriolis force . .	93
4.5.1	Components . . . . .	95
4.5.2	Simulation and design . . . . .	97
4.5.3	Performance . . . . .	101
<b>5</b>	<b>Multi-axis inertial sensing with long-time point source atom interferometry</b>	<b>105</b>
5.1	Introduction . . . . .	105
5.2	Methods . . . . .	107
5.3	High-contrast atom interferometry in the presence of rotations . . .	111
5.4	Dual-axis gyroscope: a precision measurement of Earth's rotation rate	113
5.5	Record acceleration sensitivity . . . . .	114

5.6	Further applications . . . . .	115
5.7	Principal component analysis . . . . .	116
<b>6</b>	<b>Enhanced atom interferometry readout through the application of phase shear</b>	<b>120</b>
6.1	Introduction . . . . .	120
6.2	Methods . . . . .	123
6.3	Generation of a controlled phase shear . . . . .	124
6.4	Deterministic readout of phase via phase shear . . . . .	126
6.5	Gyrocompass: a precision measurement of the direction of true North	126
6.6	Arbitrary control of the applied phase shear . . . . .	129
6.7	Further applications . . . . .	131
<b>7</b>	<b>Delta-kick cooling with magnetic fields and light</b>	<b>132</b>
7.1	Matter wave lensing . . . . .	132
7.1.1	Introduction . . . . .	132
7.1.2	Methods . . . . .	135
7.1.3	Optical dipole lensing to picokelvin temperatures . . . . .	136
7.1.4	Magnetic lensing to nanokelvin temperatures . . . . .	140
7.1.5	Further applications . . . . .	142
7.1.6	Lattice-aided magnetic lens cooling . . . . .	143
7.2	TOP trap theory . . . . .	143
<b>8</b>	<b>A high-performance magnetic shield with large length-to-diameter ratio</b>	<b>153</b>
8.1	Introduction . . . . .	154
8.2	Shielding metrics . . . . .	155
8.3	Segmented v. welded shields . . . . .	157
8.3.1	Shield design . . . . .	158
8.3.2	Measurement apparatus . . . . .	159
8.3.3	Shield performance . . . . .	159
8.4	Finite element analysis . . . . .	163

8.4.1	Two segment shield . . . . .	164
8.4.2	Full 14-segment shield . . . . .	166
8.4.3	Field homogeneity . . . . .	167
8.5	Experimental implementations of shield joining methods . . . . .	170
8.5.1	Fastener torque . . . . .	173
8.5.2	Thermal interference fit . . . . .	173
8.5.3	Metglas wraps . . . . .	173
8.5.4	Welding . . . . .	174
8.6	Discussion . . . . .	177
8.7	Supplemental material: analytical models for magnetic shield design .	179
8.7.1	Transverse shielding ratio . . . . .	179
8.7.2	Axial shielding ratio . . . . .	180
<b>9</b>	<b>Current work – Large momentum transfer atom optics</b>	<b>182</b>
9.1	Preliminary large momentum transfer interferometry results . . . . .	182
9.2	AC Stark compensation . . . . .	187
9.3	Spontaneous emission . . . . .	190
<b>10</b>	<b>Future work – Dual species evaporation for atom interferometry</b>	<b>195</b>
10.1	Dual species cMOT . . . . .	196
10.2	Optical pumping . . . . .	198
10.3	Evaporation considerations . . . . .	199
10.4	Magnetic lensing . . . . .	202
<b>11</b>	<b>Conclusion</b>	<b>212</b>
<b>A</b>	<b>Historical equivalence principle experiments</b>	<b>214</b>
<b>B</b>	<b>Frequency doubling in nonlinear media</b>	<b>216</b>
<b>C</b>	<b>Preliminary absolute gravity and gravity gradient measurements</b>	<b>221</b>
<b>D</b>	<b>Recipe – La Bête Noire</b>	<b>223</b>
D.1	Ingredients . . . . .	223

D.2 Preparation . . . . .	225
<b>E Recipe – Lemon Curd Cheesecake</b>	<b>227</b>
E.1 Ingredients . . . . .	227
E.2 Preparation . . . . .	229
<b>Bibliography</b>	<b>234</b>

# List of Tables

3.1	List of selected phase shifts for Raman interferometry . . . . .	34
4.1	Cloud properties in a quadrupole trap and scalings with gradient . . .	92
4.2	Cloud properties in a TOP trap and scalings with trap frequency . .	94
5.1	Velocity-dependent phase shifts and their sizes . . . . .	107
8.1	Theoretical shield properties of each layer of the constructed shield and all three combined . . . . .	158
10.1	Summary of dual species magnetic lens Monte Carlo simulations . . .	211
A.1	Historical equivalence principle experiments . . . . .	214
B.1	Sellmeier coefficients for the extra-ordinary index of refraction of 5% doped MgO:PPLN crystal . . . . .	219

# List of Figures

2.1	Equivalence principle experiments through the years . . . . .	6
3.1	Example of a $\pi/2-\pi-\pi/2$ Mach-Zehnder atom interferometer sequence	24
3.2	Structure of a three level atom and variable definitions . . . . .	28
4.1	Image of the apparatus . . . . .	43
4.2	Schematics of the apparatus . . . . .	44
4.3	Pseudo-cMOT Experimental Sequence . . . . .	52
4.4	Quadrupole coil snap on/off circuit . . . . .	54
4.5	Microwave knife circuit . . . . .	56
4.6	Schematic of optical plug, quadrupole coils, and bias coils . . . . .	58
4.7	Optical plug power and radial waist requirements . . . . .	58
4.8	Timing of evaporation in the plugged quadrupole trap . . . . .	59
4.9	Characteristics of evaporation in a plugged quadrupole trap . . . . .	60
4.10	Timing of evaporation in the TOP trap . . . . .	62
4.11	Characteristics of evaporation in the TOP trap . . . . .	63
4.12	Alignment of the lattice launch beams . . . . .	67
4.13	Timing of the lattice launch . . . . .	69
4.14	Schematic of the high power, frequency-doubled atom optics system .	78
4.15	Effect of the imaging pulse on the atom distribution . . . . .	85
4.16	Atom distribution characteristics as a function of imaging duration .	86
4.17	Absorption imaging Rb spectroscopy lock . . . . .	88
4.18	Examples of fits to absorption images of atom ensembles in a quadrupole and a TOP trap . . . . .	92

4.19	Schematics and image of the rotation compensation system . . . . .	96
4.20	Simulated angular errors of the retroreflection mirror due to mechanical oscillations excited by acceleration. . . . .	99
4.21	Thermal behavior of the Rotation Compensation System. . . . .	100
4.22	Noise spectral density of the Rotation Compensation System . . . . .	103
5.1	Point source interferometry: schematic diagram of the apparatus and an example image of the interferometer output ports . . . . .	108
5.2	Spatial fringes on the atom population . . . . .	109
5.3	Fringe spatial frequency and contrast versus applied rotation . . . . .	109
5.4	Long-time atom interferometer contrast . . . . .	112
5.5	Dual-axis gyroscope measurements . . . . .	113
5.6	Normalized principal components . . . . .	117
6.1	Phase shear: schematic diagram of the apparatus and an example image of phase shear from a beam tilt . . . . .	122
6.2	Horizontal fringes resulting from beam-tilt phase shear . . . . .	125
6.3	Single-shot phase readout with a $2T = 50$ ms interferometer . . . . .	127
6.4	Gyrocompass using phase shear readout . . . . .	129
6.5	Arbitrary control of spatial fringe direction . . . . .	130
7.1	Schematic of the delta-kick cooling apparatus . . . . .	135
7.2	Comparison of the dipole lensing beam before and after a long propagation distance . . . . .	136
7.3	Matter wave refocusing with an optical dipole lens . . . . .	137
7.4	Effect of beam profile aberration on refocus cloud size and lensing duration	139
7.5	Magnetic lensing in a TOP trap . . . . .	141
7.6	Magnetic lensing in a TOP trap, aided by an optical lattice . . . . .	144
7.7	Simulated particle velocities after release into a TOP trap . . . . .	149
7.8	Position and velocity distributions after magnetic lensing in the TOP trap . . . . .	150
8.1	Measured axial magnetic field along the vacuum tube axis . . . . .	155

8.2	Pictures and schematics of the magnetic shield . . . . .	156
8.3	Measured magnetic field along the axis of a welded 14-segment, three-layer shield . . . . .	161
8.4	Axial dynamic shielding ratio of the welded 14-segment, three-layer shield	162
8.5	Finite element simulation of an imperfect joint in a segmented shield	164
8.6	Finite element simulation of magnetic field lines in the presence of the inner layer of the shield . . . . .	165
8.7	Comparison of measurement and simulation of the segmented shields	167
8.8	Dependence of the axial shielding ratio on the wavelength of the field applied to an infinitely long shield . . . . .	169
8.9	Dependence of the axial shielding ratio on the wavelength of the field applied to a finite shield . . . . .	171
8.10	Residual axial magnetic field for multiple methods of joining the inner layers of a two-segment subset of the full shield . . . . .	172
8.11	Magnetic field on the axis of a two-segment, three-layer shield with all joints welded, before and after degaussing. . . . .	174
8.12	Dynamic axial shielding ratio of two-segment, three-layer shields . . .	176
9.1	Comparison of $2\hbar k$ and $6\hbar k$ Raman interferometers . . . . .	184
9.2	LMT interferometry at 3 GHz detuning . . . . .	185
9.3	Modulation depth for AC Stark shift compensation . . . . .	190
9.4	Fraction of ensemble participating in the interferometer as a function of the phase modulation frequency and the large momentum transfer order.	192
9.5	Duration of a $\pi$ pulse as a function of the phase modulation frequency and the beam intensity . . . . .	193
10.1	Microwave electronics for $^{85}\text{Rb}$ cooling and depump frequencies . . . . .	197
10.2	Impact of optical pumping on the number of $ F = 2, m_F = -2\rangle$ $^{87}\text{Rb}$ atoms transferred into the quadrupole trap . . . . .	200
10.3	Comparison of $ F = 3, m_F = 3\rangle_{85}$ and $ F = 2, m_F = 2\rangle_{87}$ magnetic lensing in a TOP trap . . . . .	204

10.4	Comparison of lattice-aided $ F = 3, m_F = 3\rangle_{85}$ and $ F = 2, m_F = 2\rangle_{87}$ magnetic lensing in TOP trap . . . . .	207
10.5	Comparison of $ F = 2, m_F = -2\rangle_{85}$ and $ F = 1, m_F = -1\rangle_{87}$ magnetic lensing in a TOP trap . . . . .	208
10.6	Comparison of lattice-aided $ F = 2, m_F = -2\rangle_{85}$ and $ F = 1, m_F = -1\rangle_{87}$ magnetic lensing in a TOP trap . . . . .	210
C.1	Preliminary gravity measurements at five launch heights . . . . .	222
D.1	La Bête Noire cross-section . . . . .	224
D.2	La Bête Noire baking sequence . . . . .	226
E.1	Lemon curd cheesecake cross-section . . . . .	228
E.2	Lemon curd cheesecake baking sequence . . . . .	230
E.3	Lemon curd consistency versus cooking time . . . . .	231
E.4	Marbling procedure . . . . .	232

# Chapter 1

## Introduction

A hammer and a feather dropped in vacuum fall under gravity at the same rate despite their difference in mass and composition. This is the equivalence principle in its simplest form. It is the reason why Galileo is associated with the Leaning Tower of Pisa, and it underpins Einstein's theory of general relativity.

Yet at first glance, the equivalence principle arises almost by happenstance. According to Newton's second law, the force  $F_{\text{inertial}}$  applied to an object is directly proportional to its acceleration  $a$ . That constant of proportionality, defined as the inertial mass of the object,  $m_{\text{inertial}}$ , is a property inherent to the object in question. Independently, Newton described the force of gravity acting between two entities as depending on a different, equally inherent property, the gravitational mass. At the surface of the Earth, the gravitational force of the planet on an object with gravitational mass  $m_{\text{gravity}}$  is  $F_{\text{gravity}} = m_{\text{gravity}}g$ , with  $g = 9.8 \text{ m/s}^2$  identified as the acceleration due to gravity.

Since the gravitational force must obey Newton's second law, then

$$F_{\text{inertial}} = F_{\text{gravity}} \implies m_{\text{inertial}}a = m_{\text{gravity}}g .$$

If the gravitational mass and inertial mass are always equal,  $a = g$  and any two objects released simultaneously from rest under gravity will hit the ground at the same time. But if, in violation of the equivalence principle, the gravitational mass differs by some

fraction due to the objects' sizes or compositions, then their inertial accelerations will differ by the same fraction and one object will hit the ground first.

According to the experimental limits to date, the gravitational acceleration is *equivalent* to the acceleration of motion (or  $m_{\text{gravity}}/m_{\text{inertial}} = 1$ ) to a part in  $10^{13}$ . Nevertheless, the possibility still exists that the principle may be violated at a smaller level. As a violation of the equivalence principle would call into question the validity of general relativity, the theory on which we base our current understanding of gravity, there is considerable interest in experiments with even greater precision.

We aim to extend the current limits by two orders of magnitude with atom interferometry in a 10 meter tower. Atom interferometry is an exquisitely sensitive metrological method that, in a simplified sense, treats a laser as a fine-grained ruler against which the position of the atom is quantum-mechanically compared. Small, compact apparatuses are valuable for commercial applications in inertial navigation and geodesy, but much like its optical analogue, the sensitivity of the atom interferometer scales with the enclosed area. Since the atoms are in free-fall during the experiment, this favors a tall apparatus for the longest flight times and the highest sensitivity.

With  $10^{-15}g$  acceleration sensitivity or better, and with individual atoms rather than macroscopic objects as proof masses, a number of fascinating avenues of research beyond the equivalence principle open up. These include measurements of general relativistic corrections to the Newtonian motion of atoms, the charge neutrality of atoms, the fine structure constant, Aharonov-Bohm-like topological phases, modifications of quantum mechanics, and gravitational waves.

To meet the promise of these precision tests of fundamental physics, we have worked both to improve the sensitivity of and to reduce systematic error in acceleration measurements with atom interferometry. We have constructed a long-time atom interferometer with acceleration sensitivities of  $6.7 \times 10^{-12} g$  in a single experimental cycle, two orders of magnitude better than previous limits. We have applied it to precision measurements of Earth's rotation rate and rotation axis, of interest both for the novel implementation of a precision atom gyroscope and for the importance of Earth's rotation as a source of systematic error in an equivalence principle test. We have developed an imaging technique with wide applicability: it aids in the

detection of small signals much like a heterodyne scheme, and it directly reports both interferometer phase and contrast in a single experimental shot, reducing systematic error from experimental drifts. Finally, we have explored lens analogues for atom clouds. We show that such lenses have the ability to produce extremely cold ( $< 50 \text{ pK}$ ), high flux sources of atoms, or to produce small, refocused clouds. Both mitigate systemic errors due to inhomogeneities associated with the cloud's spatial or momentum extent. In addition, the low temperatures achieved set limits on spontaneous heating of the atoms that would herald a modification of quantum mechanics over large distances or long time scales.

I begin this work with a summary of the evolution of our understanding of gravity and the equivalence principle, from Aristotle to Einstein (Ch. 2). This chapter also introduces atom interferometry as a tool for precision measurement and discusses its past and planned use for tests of the equivalence principle and other fundamental properties of the universe. Next, I elaborate on the physics underlying atom interferometry, addressing in particular the theoretical motivations driving certain specifications for the apparatus in this work (Ch. 3). In Ch. 4 I provide a detailed description of the apparatus, including the production of the ultracold atom source and the interferometry lasers.

I then present a series of experimental results. First are measurements showing acceleration sensitivities of  $6.7 \times 10^{-12} g$  in a single experimental cycle, as well as measurements of Earth's rotation rate (Ch. 5). Second is a demonstration of a novel detection technique that extracts information from the spatial population distribution of atoms within a cloud, which we use to determine the direction of Earth's rotation axis (Ch. 6). Third, I describe the cooling of an atom source both by the dipole force of light and by the magnetic force (Ch. 7), with implications for atom interferometry and proposed modifications to quantum mechanics. Fourth is a detailed analysis of the magnetic shield, both in experiment and in simulation (Ch. 8). The shield is a component of the apparatus that proved to be challenging to scale from smaller atom interferometers. Last is the current exploration of large momentum transfer atom optics, which could improve the acceleration sensitivity of a single experimental cycle by orders of magnitude (Ch. 9).

I close with a description of the immediate next step towards an equivalence principle test, the creation of a dual species  $^{87}\text{Rb}$ - $^{85}\text{Rb}$  ultracold cloud (Ch. 10), touching on both experimental and theoretical aspects of the task.

Many of the experimental results described have been published or are to be published in peer-reviewed journals. I contributed significantly to the apparatus construction, data collection, data analysis, and writing for the publications, but much was done in collaboration with others. Chapter 5 was published in [1], and collaborators were Jason M. Hogan, Alex Sugarbaker, David M. S. Johnson, and Mark A. Kasevich. Chapter 6 was published in [2], and collaborators were Alex Sugarbaker, Jason M. Hogan, David M. S. Johnson, and Mark A. Kasevich. Section 7.1 has been submitted for publication [3], and collaborators were Tim Kovachy, Jason M. Hogan, Alex Sugarbaker, Christine Donnelly, Chris Overstreet, and Mark A. Kasevich. Chapter 8 was published in [4], and collaborators were Jason M. Hogan, David M. S. Johnson, Tim Kovachy, Alex Sugarbaker, and Mark A. Kasevich.

# Chapter 2

## The equivalence principle and beyond

### 2.1 From Aristotle to Einstein

The study of gravity is ancient, dating at least as early as the 4th century BC. In the intervening millennia, the understanding of how it rules the trajectories of falling objects has evolved significantly. Concurrently, the methods for supporting and expanding this understanding have changed drastically, with the scientific method supplanting the Socratic method. As a result, the study of the evolution of our understanding of gravity is as much a study of the scientific method as it is a study of gravitational motion.

From Aristotle to Einstein, the approach chosen to investigate the equivalence principle depended in part on the particular researcher's attitude towards the bane of any precision measurement: systematic error. This attitude also appears to be correlated with the researcher's opinion of the role of mathematics in the description of motion.

To the modern experimentalist, systematic errors represent the deviations from an abstract, ideal test, often resulting from environmental effects like changes in temperature. Indeed, we expend a great deal of effort in identifying, characterizing and suppressing such errors. The ultimate goal is an experiment that is as faithful

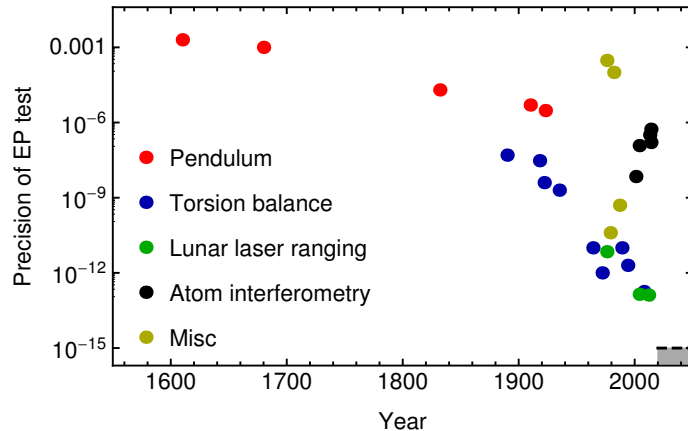


Figure 2.1: Equivalence principle experiments through the years. Galileo Galilei and Newton measured the first two results respectively. Baron Eötvös made the first two torsion balance results. The black dashed line the lower right corner marks  $10^{-15}$ , the level of precision we are pursuing with this work. References can be found in Appendix A.

an approximation as possible of the ideal test, which can be described by a simple mathematical model. This mathematical model has enormous power in predicting the results of future experiments.

But the revelation that systematic error *can* be peeled away from a more fundamental core concept was slow to develop. To Aristotle, systematic error was insurmountable, further evidence of the divide between the perfect heavens and the imperfect Earth. Performing experiments was a fruitless exercise. It was two thousand years before Galileo was able to contradict him with the first widely disseminated precision measurements of gravitational motion. With his clean results, he was able to reveal the mathematical description of the trajectory of an object falling under gravity on Earth – an early success in the rise of precision experiments (Fig. 2.1).

Less than a century later, Newton expanded this narrowly focused model and, in direct conflict with Aristotle, linked the motion on Earth with the motion of the planets as two limits of one theory. He heralded the modern desire to seek ever more general models to unify not only gravity, but also electromagnetism, the weak and strong forces and, potentially, quantum mechanics.

To describe this remarkable evolution, we look to the beginning of the conversation

about gravity. The earliest known writings with the farthest-reaching impact are those of Aristotle (384 - 322 BC). In his worldview, motion was divided into two regimes: celestial and terrestrial. In the heavens, bodies moved eternally in perfect circles, the motion begun by the divine Prime Mover. Terrestrial bodies, on the other hand, moved according to their composition of the four elements. Objects made of earth fell in a straight line to the center of the universe (taken to be the center of the Earth), while those made of fire rose straight in the opposite direction. Water and air were in between, with water heavier than air but lighter than earth. Moreover, the natural state of an object was to be at rest; a terrestrial object set in motion would soon come to rest again if no further force were applied.

In this philosophy, objects of different composition fall at different rates, in violation of the equivalence principle. A hollow bronze sphere, for example, should fall through air more quickly when filled with water than with air since water is the “heavier” substance. In addition, a greater quantity of the same material should fall more quickly: “the greater the mass of fire or earth the quicker always is its movement towards its own place” [5].

Aristotle presented such statements as common-sense facts, and he makes little effort to support them through physical experiments. On occasion, he offers an example: a clod of earth falling through water supports the concept that earth is heavier than water. But these are rare and anecdotal, a far cry from the detailed experiments that typify research today.

As a modern scientist, part of what makes Aristotle’s arguments so curious is his sparing use of mathematics. His reasons for this are likely twofold. First, the math available to Aristotle was limited. Geometry had been reasonably well-studied by Pythagoras and his students, but many years were to pass before the invention of modern algebra (in the 9<sup>th</sup> century by al-Khwarizmi) and calculus (in the 17<sup>th</sup> century by Newton and Leibniz). It is therefore not surprising that Aristotle relied primarily on the simple  $>$ ,  $<$ , and  $=$  operators.

Second, he argued that what geometrical concepts had been developed were disconnected from physical objects. Geometry allows for objects impossible to find in the physical world, like indivisible points and infinite lines. As no massive, infinitely

divisible object could be created from a combination of massless, indivisible points, Aristotle found it inconceivable that mathematics could properly describe a physical object. But for the motion of an object he drew a fine distinction: because motion is not tangible, mathematics is able describe it [6].

The lack of mathematical knowledge cannot excuse, however, Aristotle's description of projectile motion. An object made of earth does not fall radially towards the center of the earth if it is given an initial horizontal velocity. Nor does it excuse his assertion that a sphere twice as heavy as another would fall at a faster rate.

Even prior to Galileo, these assertions were questioned. One of the earliest critics was the Alexandrian philosopher John Philoponus (490 - 570 AD). He proposed an experiment, which he called a “demonstrative argument,” to contradict Aristotle: drop two objects of different weight from the same height and compare the time it takes for them to fall [7]. Philoponus concluded that a factor of two in weight would lead to an “imperceptible” difference, if any at all. It is truly a simple experiment, but one that Aristotle would have deemed contaminated by the systematic error of terrestrial imperfection.

Despite this demonstrative argument, Aristotle still remained vastly influential for the next two millennia, through the astronomical and mathematical advances of the Islamic empire and through the rise of Europe from the Dark Ages. It was in the 16<sup>th</sup> century, just prior to Galileo, when challenges to Aristotle's authority increased. For example, Giovanni Benedetti (1530 - 1590 AD) made a logical argument in favor of the equivalence principle. He considered two equal spheres joined by a string. Per Aristotle, the combined system should have fallen twice as fast as each individual sphere [8]. Benedetti concluded that they did not.<sup>1</sup> In response to a plagiarized version of Benedetti's work, in 1586 AD the Dutch Simon Stevin (1548 - 1620 AD) performed an experimental test comparing the fall of two lead spheres whose weight differed by an order of magnitude. They appeared to hit the ground at the same time. Both Benedetti and Stevin, however, were overshadowed by the fame – or notoriety – of Galileo Galilei (1546 - 1642 AD).

---

<sup>1</sup>Conflicting reports state that he performed an experiment (Ref. [8]) or he made a logical argument (Ref. [6]).

Part of Galileo’s comparative success undoubtedly arose from social factors: his prior fame from his discoveries with the telescope, his role as a favorite of the Grand Duke of Tuscany, his participation in one of the first scientific societies, and the romanticism of his personal sacrifice in the name of science when he risked excommunication for defending the heliocentric model. Confounding his legacy is the glamorization of his experiments by Vincenzo Viviani. A student of Galileo, Viviani appears to have fabricated the exceedingly popular but apocryphal story of Galileo dropping objects from the leaning tower of Pisa.

But Galileo also contributed at least two seminal philosophical changes to the way in which science is pursued. In sharp contrast to Aristotle, he placed a strong emphasis on the ability of experiments to provide useful information for understanding the behavior of nature. He also merged mathematics with these experiments to develop general rules with great predictive power.

While Aristotle believed experiments to be too contaminated by the mundane to provide useful information, Galileo realized that systematic errors were obscuring a more fundamental behavior, and that they could be independently understood and mitigated. “We must find and demonstrate conclusions,” he wrote, “abstracted from the impediments, in order to make use of them in practice under those limitations that experience will teach us” [9].

In his development of phenomenological models, he was now free to make approximations. Following an argument of Archimedes, he ignored the slight differences in the direction of  $g$  due to the spherical Earth since the distance between two of his experiments was much smaller than the distance to the center of the Earth [9]. In his experiments, he corrected for systematic error both before and after the fact. For example, he adjusted the times reported by his water clock,<sup>2</sup> which measured time by the volume of water that dripped from a reservoir, to account for the unmeasured water that adhered to the sides of the collection vessel. He also expended considerable effort to limit the friction of a rolling ball by lining the channel with polished vellum [10].

---

<sup>2</sup>In this water clock, the amount of water that drained from an upper reservoir into a lower reservoir was proportional to the amount of time that had passed. By measuring the volume or weight of water that drained, he could rapidly get a precise measurement of time, down to a little more than a millisecond (calculated from Ref. [6]).

A demonstration of the effectiveness of his novel attitude is in his determination of the time-squared dependence of the distance traversed during free fall. The experiment relied on timing the period of oscillation for pendula of various lengths. He found that quadrupling the pendulum length doubled the period. He then compared the time of a quarter period to the time of free fall from rest through a distance equal to the pendulum length. Their ratio was constant, implying that doubling the duration of free fall quadrupled the distance traversed [6].

In modern equations, we see that he is comparing the pendulum law,  $\tau = 2\pi\sqrt{l/g}$ , to the law of free fall  $x(t) \equiv l = gt^2/2$ . As Galileo discovered, the ratio  $t/\tau = \sqrt{2}/2\pi$  is a constant. And so the measured doubling in  $\tau$  with quadrupled pendulum length also implied a doubling of  $t$  with quadrupled free-fall distance. He later extended this time-squared law of free fall to motion on an inclined plane, highlighting the predictive power of mathematics.

Although the time-squared law is certainly related to the equivalence principle insofar as it relates to the motion of matter under gravity, it does not strictly compare objects of different mass or composition. Instead, Galileo describes two alternate approaches to test the equivalence principle [9]. One is the straightforward experiment of dropping different objects, typically by rolling balls down smooth inclined planes. In another, he compared two 10-meter pendula, one with a bob of lead and one with a bob of cork. Galileo claimed that even after a thousand oscillations, the two pendula were still synchronized to within a period, establishing a precision of  $\sim 10^{-3}$ . Thus, Galileo gave the world an early taste of precision measurement through the mitigation of systematic error and promoted the usefulness of mathematics in physics to describe the behavior of an idealized experiment.

Contemporary Aristotelians would have been uncomfortable with Galileo's direct contradiction of their favored philosopher. To forestall complaints, Galileo wrote in his treatise on this research [9]:

Aristotle says, ‘A hundred-pound iron ball falling from the height of a hundred braccia hits the ground before one of just one pound has descended a single braccio.’ I say they arrive at the same time. You find, on making the experiment, that the larger anticipates the smaller by two inches.

... And now you want to hide, behind those two inches, the ninety-nine braccia of Aristotle, and speaking only of my tiny error, remain silent about his enormous one.

How much of a measurement can systematic error invalidate? According to Galileo, the Aristotelians would discount everything for want of two inches. But for him, a small systematic error could be largely ignored in favor of the greater trend.

Although his achievements were formidable, he was not infallible. He still believed in the Platonic ideal that inertial motion was circular in nature, albeit with a large enough radius to look linear over human-scale distances [9]. As a consequence, he rejected the proposal of his German contemporary, Johannes Kepler (1571 - 1630 AD), that the planets moved in elliptical and not circular orbits. Their motion, he argued, may initially have followed the same laws as on Earth, but ultimately God turned their motion into circles of unvarying speed, “the only kind [of motion] that is suitable to be conserved equably” [9]. It fell to Isaac Newton (1643 - 1717 AD) to unify celestial and terrestrial motion under a single mathematical framework.

Like Galileo, Newton strongly believed in experiments [8]. Our senses could be deceived, but a well-designed experiment could not. Yet even more than Galileo, he placed significant emphasis on a law of physics being able to describe all relevant experimental data, without exception. To be sure, the law of physics would describe an ideal experiment, free from friction, drag, or other confounding factors. But a single systematic-error-free experimental violation of the purported law would revoke it. Furthermore, that law of physics should be as generally applicable as its underlying assumptions allow. If a law describes motion on Earth, it should also extrapolate to motion in the heavens, a significant break from prior claims. These three features – experimental support, abstraction to an ideal, and generality – are still the critical characteristics of a modern law.

Newton’s classical law of gravitation satisfied these requirements. It was extremely powerful in that it could both explain the parabolic trajectory of projectile motion on Earth, and it could produce the elliptical orbits of the planets proposed by Kepler. And yet, Newton could not explain how gravity arose, or why the inertial mass and gravitational mass appeared to be one and the same. “I design here to give a

mathematical notion of those forces,” he wrote, “without considering their physical causes and seats” [8].

In a continuing effort to overthrow Aristotle and to understand the coincidence of inertial and gravitational mass, tests of the equivalence principle in the 18<sup>th</sup> and 19<sup>th</sup> centuries were performed with ever-increasing precision (see Fig. 2.1). Newton himself developed a differential measurement comparing two pendula of equal length, released simultaneously. The hollow bob of one of the two was filled with various materials (e.g., gold, silver, salt, etc.). No matter the contents of the bob, the two pendula remained isosynchronous to  $\sim 10^{-3}$  [8]. Ultimately, such pendulum experiments became limited by systematic errors due to thermal fluctuations of the pendulum length and by excess noise from spurious accelerations due to air fluctuations [11].

To overcome some of these limitations, the Hungarian Lorand Etvos (1848 - 1919 AD) developed the torsion balance in the late 19th century, which provided an immediate and dramatic improvement in experimental precision. Consider a pendulum at an intermediate latitude. The force of gravity balances the centrifugal force of Earth’s rotation or revolution, such that the pendulum comes to rest at an angle to the direction of the gravitational pull. If gravity pulls on different materials or quantities with different strength, pendula with different bobs will come to rest at different angles. In a torsion balance, objects of different mass or composition are placed on either end of a rigid rod, which is suspended to allow free motion. The competing effects of gravity and the centrifugal motion impart a torque to the rod if the equivalence principle is violated. The resulting twist can be sensitively measured. In the past decade, a refined apparatus, designed by the Eot-Wash group at the University of Washington, provided one of the most precise tests of the equivalence principle to date [12–14].

Three centuries and six orders of magnitude improvement in measurement precision after Newton, Albert Einstein (1879 - 1955 AD) determined that the equivalence principle was not just a coincidence, but was an essential part of an even farther-reaching theory, general relativity. Yet although general relativity was revolutionary in the way it describes the force of gravity emerging from a geometrical effect, the methodology behind its design and confirmation follows the pattern established by

Newton and Galileo. The theory, a testable model of a natural phenomenon, was created such that results of all contemporary experiments, after accounting for non-ideal systematic errors, were well-explained. That it could correctly anticipate other, previously undiscovered effects, such as the degree by which light is bent around the sun, is a testament to the predictive power of mathematical models in describing natural effects and to the experimenters' ability to detect ever-smaller signals through the fog of systematic error.

## 2.2 The modern equivalence principle

Einstein's metric theory of gravity contains three grades of the equivalence principle, each growing from the other [15]. These are the weak, Einstein, and strong equivalence principles.

The least restrictive is the weak equivalence principle (WEP), also known as the universality of free fall (UFF). It states that all objects fall under gravity at the same acceleration, regardless of size or composition.

The second definition adds to the WEP the demand that non-gravitational laws of physics are the same in any inertial frame of reference, regardless of that frame's velocity (local Lorentz invariance, LLI) or position in space and time (local position invariance, LPI). This is the Einstein equivalence principle (EEP). It is a particularly powerful combination, as it restricts possible theories of gravity to metric theories, where gravity is a geometrical phenomenon resulting from the curvature of space-time. From the EEP arises much of the common phenomenology of general relativity, including the gravitational redshift.

Finally, the strong equivalence principle (SEP) demands that the EEP holds for all gravitational and non-gravitational forces, even for objects that are massive and dense enough to affect significantly the local gravitational potential (dimensionless gravitational self-energy  $\epsilon \sim GM/(Rc^2) \sim 1$ ). In metric theories of gravity beyond general relativity, additional scalar and/or vector fields may well violate LPI or LLI for gravitational physics.

Because our current understanding of gravity depends on these principles, there is

considerable interest in testing them experimentally. All the experiments previously mentioned – Stevin’s, Galileo’s, Eötvös’ – test the least-restrictive WEP. Since the formulation of the EEP and the SEP, numerous tests have probed the extent to which they hold (see Ref. [15] for an excellent review). Yet tests of the WEP continue to be particularly influential through the tight relationship amongst all three principles and the extreme precision with which it can be verified.

In the definitions above, each statement builds upon the assertions of the previous one. The WEP is the lynchpin of all three: should it fail, all three fail. Further strengthening the connection, in 1960 Schiff conjectured that in order for a theory of gravity to be self-consistent, a test of the WEP is sufficient to test the EEP [16]. As explained by Clifford Will [15],

[T]he same mathematical formalism that produces equations describing the free fall of a hydrogen atom must also produce equations that determine the energy levels of hydrogen in a gravitational field, and thereby the ticking rate of a hydrogen maser clock. Hence a violation of EEP in the fundamental machinery of a theory that manifests itself as a violation of WEP might also be expected to show up as a violation of local position invariance.

While still unproven in general, Schiff’s conjecture has been shown to hold in restricted cases and has been more broadly motivated through plausibility arguments [17, 18].

Beyond the theoretical connection, data from Earth-based WEP tests have set limits on violations of the SEP to a part in  $10^{13}$  [19]. That this limit comes from data about the Earth may be surprising: studies of the SEP are most sensitive with massive, dense objects that can be found only through astronomical observations (at least until the LHC spawns a black hole). The Earth, with  $\epsilon \sim 10^{-9}$ , is a poor proof mass for the SEP. But the necessary astronomical objects are rare and difficult to find,<sup>3</sup> and the Earth-based tests are incredibly precise.

---

<sup>3</sup>Recently, a three-body system comprising a millisecond pulsar and two white dwarfs was observed [20]. The pulsar in this system has  $\epsilon \sim 0.1$  and its nearer, less massive white dwarf has  $\epsilon \sim 10^{-6}$ . As such, this triplet forms an excellent apparatus for a future precision test of the SEP.

The test of the SEP in question revolves around a violation of the WEP for massive objects, called the “Nordtvet effect,” that would result in a differential acceleration of the Earth and the Moon towards the Sun. Via the Nordtvet effect, the same precise lunar laser ranging data that currently sets the limit on a WEP violation (discussed below) also sets a limit on a SEP violation. The result is made more powerful when combined with a complementary WEP measurement of truly negligible self-energy performed with a torsion balance [21, 22]. This second test ensures that an independent WEP violation associated with the different composition of the Earth and Moon does not compensate for the Nordtvet effect.

Finally, the methods and results of WEP tests also stretch to more exotic investigations. For example, searches for deviations from the  $1/r^2$  dependence of gravity at short distances can use similar precision measurement techniques. Such deviations, which could arise if the extra dimensions of string theory have macroscopic spatial extent, have yet to be found. In addition, there is strong and growing interest in understanding the WEP for matter-antimatter and antimatter-antimatter combinations. The ALPHA, GBAR, and AEGIS collaborations, among others, all aim to study the effect of gravity on antihydrogen directly [23–25], but current *matter* tests of the WEP can place strong, if indirect, constraints on any violation of an *antimatter* WEP [26, 27].

With such strong scientific motivation, tests of the WEP remain important and popular experiments to pursue. Two technologies currently set the limit on a WEP violation, both achieving a precision of  $10^{-13} g$ . One is based on the Eötvös torsion balance previously mentioned. The second, lunar laser ranging, takes advantage of retroreflectors placed on the moon during a number of the Apollo missions [28, 29]. By bouncing light off a retroreflector and measuring the time it takes for a pulse to reach the moon and return to Earth, scientists can measure the distance between the Earth and the moon to centimeter-level precision. Both anticipate the gain of another order of magnitude in precision [13], but systematic error may limit further improvement.

In the past two decades, a new technology – atom interferometry – has emerged that can offer exquisite acceleration sensitivity, sufficient to improve WEP tests by two or more orders of magnitude. This extreme sensitivity can be applied to numerous other

applications, including direct measurement of general relativistic corrections, atom-charge neutrality, measurements of the fine-structure constant, and gravitational wave detection. For these reasons, we have constructed a 10-meter scale atom interferometer fountain to achieve  $10^{-15} g$  differential acceleration sensitivity.

## 2.3 Atom interferometry and precision measurement

Like an optical interferometer, a light-pulse atom interferometer comprises a sequence of beamsplitters and mirrors. Where an optical interferometer uses dielectric and metal surfaces to split photons, an atom interferometer uses pulses of light<sup>4</sup> as beamsplitters and mirrors to manipulate the state of each atom. The “paths” or “arms” of the interferometer are distinguished by the atom’s quantum state. Depending on the type of pulse, the two interferometer paths can differ in momentum state (Bragg interferometry), internal atomic state (Doppler-free Raman or microwave interferometry), or both (Doppler-sensitive Raman interferometry).

Also like its optical analogue, the sensitivity of an atom interferometer depends on the enclosed area. That enclosed area may extend in space, as in a vertical fountain with horizontal interferometer beams that separate the arms horizontally. It may extend in space-time, as in a vertical fountain with vertical interferometer beams that separate the arms vertically. Or it may extend in energy-time, as in a clock where just the internal state of the atom changes. In all three of these cases, the area will increase with the interferometer interrogation time. For atoms on Earth under the influence of gravity, extending the interrogation time requires either a trap or a very tall apparatus. The former can be compact but could introduce systematic errors through the interaction of the trap with the atoms. The latter, which we have chosen, can be challenging in its scale but disconnects the atoms from the environment by allowing them to be freely-falling for much of the interferometer duration.

---

<sup>4</sup>There do exist atom interferometers that use matter gratings to create the interference. As this thesis relates exclusively to light-pulse atom interferometry, I will use “atom interferometry” as a short-hand for “light-pulse atom interferometry” unless explicitly noted.

In the case of space or space-time extent, there exists another way to enlarge the interferometer area: large momentum transfer atom optics. These alternatives to the traditional beamsplitter and mirror pulses dramatically increase the momentum separation between the interferometer arms, thereby increasing the area enclosed.

One of the great benefits of light-pulse atom interferometry is the flexibility inherent in the sequence of pulses used. While the first and last pulses will be beamsplitters to prepare and interfere the two arms respectively, the central set of pulses can vary in number and effect (beamsplitter v. mirror) based on the result desired. Thus, a symmetric three-pulse sequence can measure accelerations in one shot, and then a symmetric four-pulse can measure gradients in the next. Or instead, an asymmetric four-pulse sequence can measure acceleration while explicitly canceling gradients, suppressing potential systematic errors [30]. None of these options demand changes to the apparatus beyond altering the timing of certain shutters and laser currents.

With their flexibility and sensitivity, atom interferometers are excellent for precision measurement in both academic and commercial applications. Light-pulse atom interferometers have already been used for measurements of the gravitational [31, 32] and fine-structure [33, 34] constants, gravitational acceleration [35], gravity gradients [36], and Earth's rotation vector [1, 2, 37, 38]. Proposed uses include gravitational wave detection [39, 40], tests of general relativistic corrections to motion under Newtonian gravity [41, 42], and tests of the antimatter equivalence principle [27, 43].

Commercial applications, like inertial navigation and geodesy, also demand a compact and robust apparatus. Up to six axes of inertial measurement have been demonstrated with three interferometer pulse sequences in a single apparatus [44], beneficial for creating a compact system.<sup>5</sup> Precision rotation measurement in a sensor head volume  $< 1/8 \text{ m}^3$  has been published in the literature [38], although commercial sensors (from AOSENSE or MUQUANS) are available in yet smaller sizes.

Atom interferometer setups have also been shown to survive significant physical shocks, and research is ongoing to further improve this robustness. An atom interferometer in a capsule has been dropped many times in a 100-meter tall tower and

---

<sup>5</sup>In Ch. 5 we discuss a measurement that can achieve two rotation components and one acceleration component.

has weathered the 10's of  $g$  deceleration [45]. And despite a noisy environmental background, an interferometer has measured gravity during the parabolic flight of an airplane [46]. Continued interest in putting an atom interferometer on a sounding rocket [47, 48] or on a satellite [40, 49, 50] to extend the free-fall time to a few minutes is encouraging further research on the ability of the technology to withstand vibrations.

### 2.3.1 Application to the equivalence principle

A number of groups around the world are interested in applying atom interferometry to the question of the equivalence principle. Indeed, it is one of the primary scientific motivations behind these large towers, parabolic flights, and sounding rockets, all of which improve sensitivity through extending the free fall time. Perhaps the earliest atom-based WEP test compared an absolute measurement of  $g$  for falling cesium with an FG5 falling corner cube gravimeter, and found agreement to better than a part in  $10^8$  [35]. A later experiment solved the fact that the gravimeters were not spatially-overlapped by sequentially testing  $^{87}\text{Rb}$  and  $^{85}\text{Rb}$  with absorptive light-pulse gratings [51]. They found  $\Delta g/g \sim 10^{-7}$ , limited by contrast loss from vibration at longer interrogation times. Such a sequential procedure is also subject to potential systematic error from drifts between experiments.

Most recent planned and performed experiments take advantage of differential suppression by performing the experiment on the two chosen isotopes simultaneously, which can suppress both common-mode vibration and apparatus drifts. Three recent tests use simultaneous, overlapped ensembles, one comparing  $^{87}\text{Rb}$ - $^{85}\text{Rb}$  in a light-pulse atom interferometer [52], another comparing  $^{39}\text{K}$ - $^{87}\text{Rb}$  also in a light-pulse atom interferometer [53], and a third comparing the Bloch frequencies of fermionic  $^{87}\text{Sr}$  and bosonic  $^{88}\text{Sr}$  confined in a lattice [54]. All three restrict violations to  $\Delta g/g \lesssim 10^{-7}$ . The first is limited by short interrogation times and AC Stark shifts, the second by laser wavefront, magnetic sensitivity and technical noise, and the last by forces from intensity gradients and insufficient integration time.

The choice of isotopes for atom-based WEP tests is varied. In addition to those

already mentioned, other isotope pairs under consideration include  ${}^6\text{Li}-{}^7\text{Li}$  [55],  ${}^{40}\text{K}-{}^{87}\text{Rb}$  [56–58], and  ${}^{41}\text{K}-{}^{87}\text{Rb}$  [58]. In general, there is a greater sensitivity to WEP violations for isotope pairs with a large mass ratio, making lithium-cesium a potentially interesting choice. But other factors can sway the selection. Comparing bosons to fermions or comparing isotopes with highly different proton-to-neutron ratios are both cited as scientific motivation for certain pairs. Recently, a detailed analysis comparing a variety of isotopes (extending beyond the alkali and alkali-earth metals typically used for cold atom experiments) has been performed using the standard model extension, a framework for describing violations of the WEP that encompasses, among other effects, the proton-to-neutron ratio [27, 59]. While lithium-cesium is certainly one of the most sensitive probes by this metric, other perhaps unexpected pairs, like  ${}^6\text{Li}-{}^7\text{Li}$ , are nearly as good.

But technical considerations also contribute to the decision, as they can significantly affect the achievable sensitivity of a device. Here, there is a particularly strong case for a  ${}^{87}\text{Rb}-{}^{85}\text{Rb}$  comparison. With  ${}^{87}\text{Rb}$  and  ${}^{85}\text{Rb}$ , both species can be addressed with the same laser system without the need for a phase lock that can work across nanometers (typically implemented by a frequency comb). Moreover,  ${}^{87}\text{Rb}$  was among the first elements to be cooled to degeneracy [60], and there has been significant work on creating dual species ensembles of  ${}^{85}\text{Rb}$  and  ${}^{87}\text{Rb}$  [61–63]. And based on the standard model extension framework, to connect to the comparisons above, the sensitivity to potential equivalence principle violations is not insignificant.

### 2.3.2 Beyond the equivalence principle

An apparatus with the sensitivity to set new limits on violations of the equivalence principle also has the sensitivity to probe other aspects of fundamental physics. With respect to the apparatus of this work, we have discussed applying it to measurements of general relativistic corrections to Newtonian mechanics [41, 42], tests of atom charge neutrality [64], tests of modifications to quantum mechanics [3], and gravitational wave detection [39, 49].

The adaptation of the apparatus to most of the applications above has been well-described in the referenced literature. Nevertheless, two in particular have recently impacted this work and deserve elaboration. These are tests of quantum mechanics and the exploration of gravitational wave detection techniques.

### Tests of modifications to quantum mechanics

Under the rules of quantum mechanics, there is no limit to the distance by which two halves of a wavepacket may be separated without losing coherence. Similarly, there is no limit to the time for which the two halves may be separated. And while it may be difficult or improbable to place massive, macroscopic objects in a superposition state, it is not impossible.

There are a number of proposed modifications to quantum mechanics, however, that would result in even greater suppression of extended states of macroscopic objects. Reference [65] contains an excellent review of such proposals, and Ref. [66] describes a method to quantify the “macroscopicity” of an experiment, or the degree to which a quantum superposition is extended. Experiments that show quantum effects (e.g., interference fringes) despite large macroscopicity (e.g., massive particles separated far in space and time) carve deep into the arena of proposed modifications.

A general category of modifications is that of spontaneous collapse models [65]. In this framework, particles are probed or measured at random, collapsing their wavefunction to a particular location. For light particles with small spatial extent, these spontaneous collapses are rare, and the Schrödinger equation is valid. But as the wavefunction extends further for longer, or as more particles join together into a single body, the probability of experiencing a collapse increases.

Atoms, while not as massive as the molecules that have been interfered [67], can be separated for large distances and for long times during interferometry (see Ch. 9). As such, a high-contrast, large momentum transfer atom interferometer would exclude a wide region of the parameter space for modifications to quantum mechanics. Should the interferometer exhibit low contrast instead, the temptation would exist to interpret it as a positive sign for modifications. Exceedingly great care would be needed to ensure that the loss of contrast was not a result of a mundane effect.

Another effect of spontaneous collapse models is often an increase in temperature, or a thermalization with some minimum temperature. Coarsely speaking, the collapse of the wavefunction is in effect a measurement of position, and the resulting narrow position distribution corresponds to a heated velocity distribution. Since atom clouds are the coldest entities yet produced, classical temperature measurements can set very good limits on modifications. In Ch. 7 we describe a measurement that limits the heating rate to  $< 100 \text{ pK/s}$ , a rate that excludes much of the parameter space accessed by the interference of much more massive ( $10^7 \text{ amu}$ ) objects in proposed experiments [66].

### Gravitational wave detection

For the past several millennia, astronomy has been defined by the electromagnetic spectrum. Observations of photons ranging from radiofrequencies to gamma rays have revealed a wealth of information about the contents and genesis of the universe. But there exist objects and times that are difficult or impossible to detect optically. Some objects, like black holes, emit little, if any light. And events at times earlier than the surface of last scattering, when neutral particles began to form, are obscured by the short mean free path of photons in that era.

Gravitational waves offer an alternative signal. These waves, anticipated by general relativity, are perturbations in space-time that can propagate through the surface of last scattering and through the intergalactic and interstellar dust that can absorb photons. While gravitational waves have been indirectly detected through, for example, the decay of binary pulsars [68] or the imprint of primordial gravitational waves on the polarization of the microwave background [69], there is strong interest in directly detecting the minute acceleration of a passing wave.

The LIGO, VIRGO, and GEO-600 collaborations have achieved remarkable sensitivities in terrestrial observatories, but have yet to detect a gravitational wave. Their technology is based on optical Michelson interferometers that measure the distance between pairs of proof masses (mirrors) to incredible precision. The proposed space-based counterpart, the LISA collaboration, has also pursued optical interferometry with macroscopic proof masses as their measurement technique.

Atom interferometry has great potential as a sensor of gravitational waves, and proposals exist both for terrestrial [39, 70] and space-based [40, 71] observatories. Neutral atoms are interesting proof masses in part because 1) all atoms of a single isotope are identical, and 2) they can be in free fall, partially isolated from environmental noise. On Earth, the latter is to be compared to the mirror proof masses of an optical interferometer that must be very carefully suspended from thin wires to isolate them from ground vibrations. In space, the atoms can be shuttled away from the noisy satellite hub, unlike the macroscopic mirrors, which would be encased within.

The acceleration sensitivities achievable can be extremely good, comparable to optical interferometry, with a shorter distance between proof masses [40, 71, 72]. Much of the interferometer technology required has already been demonstrated, and much of what remains can be developed and tested in the apparatus of this work. The laser wavefront sensor that emerged from the techniques of Ch. 5, for instance, could be used to make an *in situ* measurement of the interferometer beam phase error. The picokelvin atom source temperatures described in Ch. 7 satisfy the kinematic requirements of a gravitational wave detector. And the large momentum transfer atom optics of Ch. 9 are necessary to meet the sensitivity desired. Others areas of exploration include single-photon interferometry with strontium and laser phase noise stabilization via an atomic clock reference.

# Chapter 3

## Atom interferometry

In a time-domain light-pulse atom interferometer [73], sequential pulses of light coherently, split, reflect, and recombine atomic wavepackets (Fig. 3.1). Forces on an atom affect its trajectory through the interferometer, leading to changes in the phase accumulated by the two arms. Just like in an optical interferometer, this phase difference is converted to an intensity ratio at the two output ports, where here the intensity is the detected atom number. Thus, measuring the population ratio of the output ports provides information about the forces experienced by the atom during the interferometer.

There are multiple approaches for calculating light-pulse atom interferometer phase shifts. These include a perturbative treatment [74], an ABCD matrix formulation [75, 76], and a method of separated phases [71, 77]. The results of all three ultimately arise from solving the Schrödinger equation for the phase evolution of the atomic states. The formalism I summarize in Sec. 3.2 is the separated phase approach, as detailed in Ref. [71], and is excellent for determining the total interferometer phase shift in a general and analytic form. The perturbative treatment, on the other hand, is particularly useful for calculating the impact of experimental perturbations, such as measured magnetic field or gravity gradient variations.

For clarity and concreteness, the theory described in this chapter is couched in terms of acceleration-sensitive interferometry. Similar techniques can also be applied to Doppler-free interferometers, such as clocks, that do not result in a spatial separation

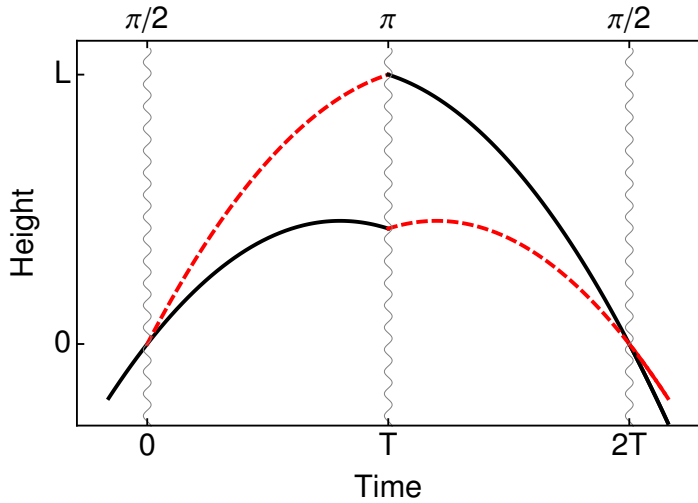


Figure 3.1: Example of a  $\pi/2$ - $\pi$ - $\pi/2$  Mach-Zehnder atom interferometer sequence. The red dashed versus solid black trajectories identify the state of the wavepacket on that path. The two final states after the final beamsplitter pulse are the two interferometer output ports (experimental images of the interferometer output ports can be found in Fig. 5.4.). For a Raman interferometer, the paths differ both in internal state and in momentum state; for a Bragg interferometer, they differ only in momentum. The atom optics pulses are separated in time by the interrogation time  $T$ , and the interferometer reaches a peak height of  $L$  above the initial interaction point. Note that the atoms extend in only one spatial dimension; the area enclosed is a space-time area.

between the arms and are not sensitive to inertial forces like gravity. Likewise, while both Bragg and Raman interferometry can be analyzed with the same formalism, the discussion will center on Raman interferometry, which is used exclusively in this work. As Bragg interferometry is a likely choice for the equivalence principle test, references to the literature are provided when appropriate.

This chapter begins with the theory of the atom optics (Sec. 3.1). The following description of the phase shift formalism and example calculation (Sec. 3.2) leads into a review (Sec. 3.3) of specific contributions to the total phase shift, including the Coriolis and magnetic forces, that are relevant for later portions of this work.

## 3.1 Atom optics: beamsplitters and mirrors

### 3.1.1 Interferometry with a two-level atom

Just as an optical beamsplitter transforms a single beam of light into a superposition of two paths, the atom beamsplitter transforms an atom from a single state into a superposition of two states that follow independent trajectories. An atom mirror transfers the atom completely from one state to the other.

With a two-level atom, atom optics can be implemented through the electric dipole interaction  $H' = -\mathbf{d} \cdot \mathbf{E}$ , where  $\mathbf{d}$  is the atom's electric dipole moment and  $\mathbf{E}$  is an electric field [78]. For an atom in a sinusoidally varying electric field, as is the case in a laser beam, the result is well known: the atom will oscillate (Rabi flop) between the ground and excited states. In general, the atom will be in a superposition of the two states. But if the driving field is resonant with the transition, then there is a time at which the atom will have completely transferred into the excited state (a mirror). At half that time, the atom will be in an equal superposition (a beamsplitter). The frequency of this on-resonance oscillation, the Rabi frequency  $\Omega$ , is determined by the strength of the lasers and the oscillator strength of the transition.

After solving the Schrödinger equation with the interaction Hamiltonian  $H'$  above, we find the amplitude in the ground  $c_g(t)$  and excited  $c_e(t)$  states at a time  $t$  after the

light is first applied through the matrix

$$M_{\Omega t} = \begin{bmatrix} \left( \cos \frac{\Omega' t}{2} - i \frac{\delta}{\Omega'} \sin \frac{\Omega' t}{2} \right) e^{\frac{i\delta t}{2}} & -i \frac{\Omega}{\Omega'} e^{-i\phi} e^{\frac{i\delta t}{2}} \sin \frac{\Omega' t}{2} \\ -i \frac{\Omega}{\Omega'} e^{i\phi} e^{-\frac{i\delta t}{2}} \sin \frac{\Omega' t}{2} & \left( \cos \frac{\Omega' t}{2} + i \frac{\delta}{\Omega'} \sin \frac{\Omega' t}{2} \right) e^{-\frac{i\delta t}{2}} \end{bmatrix} \quad (3.1)$$

where  $\Omega' = \sqrt{\Omega^2 + \delta^2}$ ,  $\Omega$  is the on-resonance Rabi frequency,  $\delta$  is the detuning from the transition ( $\delta > 0$  for blue detuning), and  $\phi$  is the phase of the laser at the atom at  $t = 0$ . The matrix describes the transformation of the initial state to the final state at time  $t$ :

$$\begin{bmatrix} c_g(t) \\ c_e(t) \end{bmatrix} = M_{\Omega t} \begin{bmatrix} c_g(0) \\ c_e(0) \end{bmatrix} \quad (3.2)$$

For interferometry, we are particularly interested in the on-resonance condition ( $\delta = 0$ ) at the times appropriate for a beamsplitter ( $\Omega t = \pi/2$ ) or mirror ( $\Omega t = \pi$ ). In these special cases,

$$M_{\pi/2} = \frac{1}{\sqrt{2}} \begin{bmatrix} 1 & -ie^{-i\phi} \\ -ie^{i\phi} & 1 \end{bmatrix}, \quad \text{and} \quad M_\pi = \begin{bmatrix} 0 & -ie^{-i\phi} \\ -ie^{i\phi} & 0 \end{bmatrix}. \quad (3.3)$$

Consider the action of these matrices on an atom in the ground state,  $[c_g(0), c_e(0)] = [1, 0]$ . The beamsplitter matrix will put the atom in an equal superposition of ground and excited states, as desired. The mirror matrix, on the other hand, transfers the atom entirely to the excited state. But in both cases, the phase of the excited state is shifted relative to the ground state by the laser phase  $\phi$ .<sup>1</sup> Conversely, when transferring an atom from the excited state to the ground state, the ground state is phase shifted by  $-\phi$  relative to the excited state.

From this description, we see not only that it is possible to create beamsplitters and mirrors for atomic wavepackets, but that the application of those atom optics leaves a trace in the form of the laser phase. Since the phase imprinted depends on

---

<sup>1</sup>The  $\pi$  additional phase ultimately cancels in the interferometer pulse sequence.

the position of the atom relative to the laser, the interaction in effect records the position of the atom in its phase. This suggests how an interferometer can be sensitive to inertial motion: if each pulse is akin to a position measurement, two pulses at a known time interval lead to a velocity measurement, and three pulses, as shown in Fig. 3.1, lead to an acceleration measurement.

As a final note, implicit in the definition of the two atomic levels is the conservation of momentum. When the atom absorbs a photon to transfer from the ground to the excited state, it also absorbs that photon's momentum,  $\hbar k$ , where  $k$  is the photon's wavevector. This directly leads to the physical separation of the two arms of the interferometer, as shown in Fig. 3.1.

### 3.1.2 From two levels to three and back again

For the alkali metals, the excited states of the available two-level transitions decay too quickly ( $< 1 \mu\text{s}$ ) for sensitive interferometry.<sup>2</sup> A three-level system, in which a pair of lasers couple two long-lived metastable ground states through an intermediate excited state, is a practical alternative (Fig. 3.2). Moreover, it reduces to an effective two-level system [79].<sup>3</sup>

The transformations to convert the matrix  $M_{\Omega t}$  from the two-level system to the effective two-level system of the three-level atom are

$$\delta \rightarrow \delta_\Lambda = \delta_{2\gamma} + \frac{|\Omega_\alpha|^2}{4\Delta} - \frac{|\Omega_\beta|^2}{4\Delta} \quad (3.4)$$

$$\Omega \rightarrow \Omega_\Lambda = \frac{|\Omega_\alpha| |\Omega_\beta|}{2\Delta} \quad (3.5)$$

$$\phi \rightarrow \phi_\Lambda = \phi_\alpha - \phi_\beta \quad (3.6)$$

where the two-photon detuning  $\delta_{2\gamma}$  and the overall detuning from the excited state  $\Delta$ , defined below, incorporate the effect of the momentum difference between the two

---

<sup>2</sup>Alkaline-earth elements, like strontium, possess narrower lines with longer lifetimes, allowing for single-photon interferometry with applications in gravitational wave detection [40].

<sup>3</sup>A Bragg transition, which couples momentum states separated by  $2n$  photon recoils,  $n \in \mathbb{N}$ , can also be reduced to a two-level system [80].

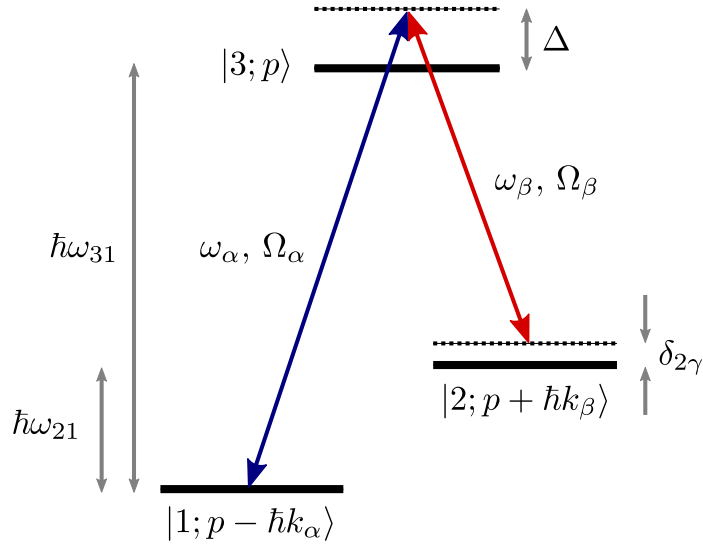


Figure 3.2: Structure of a three level atom and variable definitions. The energy differences between the states  $\hbar\omega_{31}$  and  $\hbar\omega_{21}$  are defined to be positive. A Doppler-sensitive Raman transition transfers atoms between the two ground states,  $|1; p - \hbar k_\alpha\rangle$  and  $|2; p + \hbar k_\beta\rangle$ , with negligible population building in the excited state  $|3; p\rangle$ . In a Doppler-free interferometer,  $k_\beta \rightarrow -k_\beta$ . Although in general the atom momentum and laser wavenumbers are vectors, for simplicity we assume the lasers and atom trajectories are parallel or anti-parallel. The laser frequencies are  $\omega_\alpha$  and  $\omega_\beta$ , and the intensities are encoded in the on-resonance ( $\Delta = \delta_{2\gamma} = 0$ ) single-photon Rabi frequencies,  $\Omega_\alpha$  and  $\Omega_\beta$ . The overall detuning of both lasers from the excited state,  $\Delta$ , is positive for blue detunings. For both  $\Delta$  and the two-photon detuning  $\delta_{2\gamma}$ , the quantity accounts for the energy shift from the change in momentum, but not from the AC Stark shift.

ground states.<sup>4</sup> The terms of the form  $|\Omega_i|^2/(4\Delta)$  represent AC Stark shifts of the levels. The phases of the two lasers at the atom are given by  $\phi_\alpha$  and  $\phi_\beta$ .

In addition to the transformations above, there is an overall  $|\Omega_\alpha|^2 t/(4\Delta)$  phase shift of the final effective two-level ground state (top two elements of  $M_{\Omega t}$ ) and  $|\Omega_\beta|^2 t/(4\Delta)$  phase shift of the final effective two-level excited state (bottom two elements of  $M_{\Omega t}$ ). These account for the modification of each state's time evolution by the AC Stark shift.<sup>5</sup>

The single-photon detuning  $\Delta$  from the excited state is

$$\Delta = \omega_\alpha - \omega_{31} - \frac{pk_\alpha}{m} + \frac{\hbar k_\alpha^2}{2m} \quad (3.9)$$

and includes the effect of the Doppler shift (third term) and recoil energy (last term) on the ground state energy.

The two-photon detuning  $\delta_{2\gamma}$  describes the offset of the laser pair frequency difference from the ground states' frequency difference. When the beams are counterpropagating, the atom's Doppler shift can change the relative laser frequency as measured in the atom's rest frame, making the laser pair resonant with a particular velocity class of atoms. The momentum recoil kick the atoms acquire after interacting with the photons also shifts the energy. The expression for the two photon detuning

<sup>4</sup>In the case where the intermediate excited state is actually a manifold of states, as in the case of the rubidium  $D_2$  line, the AC stark shift and the effective two-photon Rabi frequency incorporate the coupling of the ground state to each of the excited states:

$$\frac{|\Omega_i|^2}{\Delta} \rightarrow \sum_{i=0}^{F'} \frac{|\Omega_i|^2}{4\Delta_i} \quad (3.7)$$

$$\Omega_\Lambda \rightarrow \sum_{i=0}^{F'} \frac{|\Omega_{i1}| |\Omega_{i2}|}{2\Delta_i} \quad (3.8)$$

where  $\Delta_i$  is the single-photon detuning from the hyperfine level  $i = F'$ .

<sup>5</sup>While laser  $\alpha$  ( $\beta$ ) can affect the upper (lower) ground state as well, the larger detuning,  $\Delta + \omega_{21}$ , leads to a smaller effect. Here I assume  $\omega_{21} \gg \Delta$ , so this AC Stark shift is negligible. For the laser parameters in this work, this assumption does not always hold. In fact, we deliberately apply spectator beams that do not drive transitions in order to control the AC Stark shifts of each level (see Sec. 4.2.4 and Sec. 9.3). Nevertheless, this analysis is still illustrative.

is therefore<sup>6</sup>

$$\delta_{2\gamma} = -\frac{p(k_\alpha + k_\beta)}{m} + \left( \frac{\hbar k_\alpha^2}{2m} - \frac{\hbar k_\beta^2}{2m} \right) - \omega_{21} - (\omega_\beta - \omega_\alpha) . \quad (3.11)$$

The first term is the Doppler shift; the second accounts for the recoil energies. Note that if the beams were copropagating instead of counterpropagating 1) the Doppler shift due to the atom's velocity would be common to both beams, and 2) there would be no momentum difference between the ground states. In that case, the two-photon detuning would simply compare the laser frequency difference to the atomic energy level difference, the final two terms of Eq. 3.11.

For the Doppler-sensitive case, the velocity acceptance of the pulse is  $\Delta v \sim \Omega_\Lambda/(k_\alpha + k_\beta)$ . At this excess velocity, the extra Doppler shift detunes the atom such that its probability of transfer to the excited state during a  $\pi$  pulse reduces from 100% to approximately 50%. For pulses with longer  $\pi$  time and therefore lower Rabi frequency  $\Omega_\Lambda$ , the velocity acceptance narrows. Since an experimental ensemble of atoms has a non-zero temperature, long pulses selectively transfer a specific velocity class from the atom distribution into the excited state. Such velocity selection can be both a benefit, reducing velocity inhomogeneity, or a disadvantage, reducing the atom number participating in interferometry.

## 3.2 Interferometer phase shift formalism

In describing the interaction between lasers and atoms for atom optics, we noted that the laser effectively couples the atom's position to its phase. As the atomic wavepacket physically separates during interferometry, a differential phase will be imprinted on

---

<sup>6</sup>The exact form of  $\delta_{2\gamma}$  (and also  $\Delta$ ) depends on the particular momentum associated with the ground states. The formula provided here is correct for the definition in Fig. 3.2, where  $|1\rangle$  is associated with  $p - \hbar k_\alpha$  and  $|2\rangle$  is associated with  $p + \hbar k_\beta$ . If the ground states are instead defined as  $|1; p\rangle$  and  $|2; p + \hbar k_\alpha + \hbar k_\beta\rangle$ , a common alternative, the two-photon detuning is

$$\delta_{2\gamma} = -\frac{p(k_\alpha + k_\beta)}{m} - \frac{\hbar(k_\alpha + k_\beta)^2}{2m} - \omega_{21} - (\omega_\beta - \omega_\alpha) . \quad (3.10)$$

the two arms. This differential laser phase,  $\Delta\phi_{\text{laser}}$ , is one of the three sources of total phase shift that arise in an interferometer. Another source is the differential free evolution as the two halves follow their independent trajectories under the influence of a variety of forces, giving rise to the propagation phase,  $\Delta\phi_{\text{prop}}$ . The third source is also related to the trajectories: imperfect overlap of the trajectories of the two arms at the final beamsplitter pulse leads to a separation phase,  $\Delta\phi_{\text{sep}}$ .

The total interferometer phase is the sum of all three:

$$\Delta\phi = \Delta\phi_{\text{laser}} + \Delta\phi_{\text{prop}} + \Delta\phi_{\text{sep}} . \quad (3.12)$$

Each component involves a phase difference between the upper and lower paths [71]. For the laser phase, it is the sum of the imprinted laser phases  $\pm\phi(t, \mathbf{x})$  at each time and position where the atom's state changes:

$$\Delta\phi_{\text{laser}} = \sum_{\text{upper}} \pm\phi(t, \mathbf{x}) - \sum_{\text{lower}} \pm\phi(t, \mathbf{x}) . \quad (3.13)$$

The sign of the phase at each pulse depends on whether the excited state is transferred to the ground state or vice versa, as according to Eq. 3.3. In the Mach-Zehnder configuration of Fig. 3.1, the result is the familiar combination  $\Delta\phi_{\text{laser}} = \phi_1 - 2\phi_2 + \phi_3$ , where the  $\phi_i$  are the phases of the laser at the first (beamsplitter), second (mirror), or third (beamsplitter) pulses respectively.

The propagation phase is given by the classical action along the trajectory, with the inclusion of the phase evolution due to the internal state energy,  $E$ :

$$\Delta\phi_{\text{prop}} = \frac{1}{\hbar} \sum_{\text{upper}} \int_{t_i}^{t_f} (\mathcal{L} - E) dt - \frac{1}{\hbar} \sum_{\text{lower}} \int_{t_i}^{t_f} (\mathcal{L} - E) dt . \quad (3.14)$$

$\mathcal{L}$  is the classical Lagrangian.

Finally, the atom trajectories in a single output port from the two interferometer arms may not be perfectly matched in position and velocity due to timing asymmetries, gravity gradients, rotations, or other factors. The separation phase accounts for any such mismatch. This phase depends on the position difference between the two arms

at the final beamsplitter pulse,  $\Delta\mathbf{x} = \mathbf{x}_{\text{upper}} - \mathbf{x}_{\text{lower}}$ , and the (canonical) momentum in one of the two output ports of the final interferometer, averaged between the two arms,  $\bar{\mathbf{p}} = ([\nabla_{\dot{\mathbf{x}}} \mathcal{L}]_{\text{upper}} + [\nabla_{\dot{\mathbf{x}}} \mathcal{L}]_{\text{lower}})/2$ . The separation phase is then

$$\Delta\phi_{\text{sep}} = -\frac{1}{\hbar} \bar{\mathbf{p}} \cdot \Delta\mathbf{x} . \quad (3.15)$$

For a combined differential phase of  $\Delta\phi$ , the probability of finding the atom in the ground state at the end of the interferometer is

$$|c_g|^2 = \left| \frac{1}{2} (1 + e^{-i\Delta\phi}) \right|^2 = \frac{1}{2} (1 + \cos \Delta\phi) . \quad (3.16)$$

The probability in the excited state is complementary. Summed over an ensemble of many atoms, the effect is a sinusoidal dependence of the population ratio between the excited and ground states that reflects the differential phase accumulated during interferometer.

### 3.3 Mach-Zehnder interferometry

We are now prepared to calculate the expected interferometer phase shifts for an atom in the presence of a variety of inertial forces. As an example, I will inspect selected phase shifts for a Doppler-sensitive Mach-Zehnder Raman interferometer, the type used most commonly in this work. The counterpropagating interferometer beams are chosen to be parallel and anti-parallel to the direction of the gravitational vector, which also defines the direction of the  $\hat{z}$  axis. The Lagrangian incorporates

- the rotation of the Earth at the latitude  $\theta_{\text{lat}}$ :

$$\boldsymbol{\Omega}_E = (0, \Omega_y, \Omega_z) = (0, |\boldsymbol{\Omega}_E| \sin \theta_{\text{lat}}, |\boldsymbol{\Omega}_E| \cos \theta_{\text{lat}}) \quad (3.17)$$

- gravity,  $\mathbf{g} = -\nabla\Phi(\mathbf{R}_E)$ , and gravity gradients,  $T_{ij} = \partial_i g_j$ , from expanding the gravitational potential  $\Phi$  about the radius of the Earth,  $\mathbf{R}_E$ . Neglecting the

small off-diagonal gravity gradients, the approximate gravitational potential is

$$\Phi(\mathbf{r} + \mathbf{R}_E) = gz + \frac{1}{2} (T_{xx}x^2 + T_{yy}y^2 + T_{zz}z^2) \quad (3.18)$$

The gravitational acceleration is  $\mathbf{g} = -\hat{z} \times 9.8 \text{ m/s}^2$ .

- magnetic fields and a  $z$ -component of the magnetic field gradients:

$$\mathbf{B} = (B_0 + \partial_z B) \hat{z} \quad (3.19)$$

Because we generally prepare the atom in a magnetically-insensitive Zeeman sublevel, the energy shift of the state depends on the state's second-order sensitivity,  $[\alpha] = \text{rad/s/G}^2$ . The total shift between the two states is given by  $\hbar\alpha|\mathbf{B}|^2$ . For the ground state pairs of  $^{87}\text{Rb}$  and  $^{85}\text{Rb}$ , the magnitude of the shift of either state is half the total. Due to their different susceptibilities ( $\alpha_{85} \neq \alpha_{87}$ ), however, the magnetic response will be different for each isotope.

The total Lagrangian is

$$\mathcal{L} = \frac{1}{2} \left[ \frac{\mathbf{p}}{m} + \boldsymbol{\Omega} \times (\mathbf{r} + \mathbf{R}_E) \right]^2 - m\Phi(\mathbf{r} + \mathbf{R}_E) \pm \frac{1}{2}\hbar\alpha|\mathbf{B}|^2 \quad (3.20)$$

where the sign of the magnetic field dependence changes with the state of the atom.<sup>7</sup> When performing the calculation, we also parameterize physical effects like tilts of the beam (by angle  $\theta_i$ ), position scatter of the atoms ( $\delta x, \delta y, \delta z$ ), or a velocity spread ( $\delta v_x, \delta v_y, \delta v_z$ ). The phase shift from Eq. 3.12 is expanded into a set of unique terms that are ordered according to size based on physically relevant parameters. A sampling of the full phase shift list is provided in Tab. 3.1.

The terms of the phase shift list often have an illuminating physical interpretation. Term 1, for example, results from the acceleration of the atom under gravity. Term 2, results from a Coriolis force that couples the rotation of the Earth with the atom's transverse velocity. But such interpretations are not always useful with higher-order

---

<sup>7</sup>For Bragg interferometry, the magnetic field dependence does not change sign since the atoms do not change internal state.

Term	Expression	Fractional size	Laser	Path	Sep
1	$-k_{\text{eff}}gT^2$	1	-1	0	0
2	$2k_{\text{eff}}\delta v_x \Omega_y T^2$	$1.2 \times 10^{-8}$	2	-2	2
3	$-4k_{\text{eff}}\theta_3 v_L \Omega_y T^2$	$9.4 \times 10^{-9}$	-4	0	0
4	$2k_{\text{eff}}\theta_3 \delta v_x T$	$5.3 \times 10^{-9}$	2	0	0
5	$0 \times k_{\text{eff}}R_E T_{xx} \Omega_y^2 T^4$	0	0	$\frac{7}{6}$	$-\frac{7}{6}$
6	$k_{\text{eff}}\theta_3 \delta x$	$2.3 \times 10^{-9}$	1	0	0
7	$-\frac{\hbar k_{\text{eff}}^2 T_{zz} T^3}{2m}$	$2.1 \times 10^{-9}$	0	$-\frac{1}{2}$	0
8	$-2v_L \alpha B_0 \partial_z B T^2$	$6. \times 10^{-10}$	0	0	-2
9	$2g\alpha B_0 \partial_z B T^3$	$5.2 \times 10^{-10}$	0	-2	4
10	$-k_{\text{eff}}T_{zz} \delta v_z T^3$	$3.6 \times 10^{-10}$	-1	-1	1
11	$-k_{\text{eff}}T_{zz} \delta z T^2$	$3.1 \times 10^{-10}$	-1	0	0
12	$-\frac{\hbar k_{\text{eff}}\alpha B_0 \partial_z B T^2}{m}$	$2.7 \times 10^{-13}$	-1	0	0

Table 3.1: List of selected phase shifts for Raman interferometry, their fractional sizes, and their source within the separated-phase framework. A full list for Bragg interferometry and the differential equivalence principle measurement can be found in Ref. [71], although certain parameter sizes are different. All phase shifts are referenced relative to term 1, which has a magnitude of  $2.1 \times 10^8$  rad. While term 5 technically vanishes, it has been placed according to the magnitude of the path and separation contributions. Parameters:  $k_{\text{eff}} = 4\pi/(780 \text{ nm})$ ,  $g = 9.81 \text{ m/s}^2$ ,  $T = 1.15 \text{ s}$ ,  $\delta v_x = \delta v_y = \delta v_z = 1 \text{ mm/s}$ ,  $\Omega_y = 58.2 \mu\text{rad/s}$ ,  $\theta_3 = 60 \mu\text{rad}$ ,  $v_L = 13.2 \text{ m/s}$ ,  $R_E = 6.38 \times 10^6 \text{ m}$ ,  $T_{xx} = T_{yy} = -T_{zz}/2 = g/R_E$ ,  $\alpha = 2\pi \times 575 \text{ Hz/G}^2$ ,  $B_0 = 100 \text{ mG}$ ,  $\partial_z B = 10 \mu\text{G/m}$ ,  $\delta x = \delta y = \delta z = 1 \text{ mm}$ .

terms, where cross-couplings between forces can lead to arcane combinations. For example, the term  $k_{\text{eff}}v_L\theta_3\Omega_yT_{zz}T^4$  (not included in Tab. 3.1) suggests a coupling between four effects: the vertical launch velocity  $v_L$ , a beam tilt at the third pulse of angle  $\theta_3$ , the rotation of the Earth, and a gravity gradient.

In many of the terms, the propagation phase and the separation phase cancel exactly. Usually, a contribution from the laser phase makes the term non-zero, but this is not always the case, as in term 5. The frequent cancellation is a reflection of the connection between the propagation and separation phases: the separation phase depends on the positions of the atom at the final beamsplitter, and the propagation phase is a record of how they arrived at those positions.

### 3.3.1 Sensitivity to $g$

The Mach-Zehnder configuration is an excellent accelerometer, and on Earth the dominant source of acceleration is gravitational. The sensitivity of the interferometer to acceleration depends on two factors: the total phase shift accumulated, and the degree to which the interferometer phase can be resolved. For the parameters of Tab. 3.1, the total phase shift accumulated is  $k_{\text{eff}}gT^2 = 2.1 \times 10^8$  rad. The atom shot-noise limited phase sensitivity, meanwhile, scales with the atom number  $N$  as  $\delta\phi \sim 1/\sqrt{N}$ . Assuming  $N = 10^7$  atoms, the precision with which we can measure gravity in a single experimental cycle is then

$$\Delta g/g = \delta\phi/\Delta\phi \sim 1/\sqrt{N} \times 1/(k_{\text{eff}}gT^2) = 10^{-12} . \quad (3.21)$$

The fact that this sensitivity scales as  $T^2$  is the driving factor behind the increasing height of Earth-based atom interferometry apparatuses, since on a planet  $\Delta\phi$  scales linearly with the apparatus height. The  $T^2$  scaling similarly drives the pursuit of sounding rockets, parabolic flight and space missions, all of which enable longer free-fall times and improved sensitivity.

The total phase shift, however, also depends on the effective wavevector of the light  $k_{\text{eff}}$ , which affects the momentum separation between the arms. Scaling the momentum separation from  $k_{\text{eff}}$  to  $nk_{\text{eff}}$  also scales the largest phase term from  $k_{\text{eff}}gT^2$  to  $nk_{\text{eff}}gT^2$ .

The list of Tab. 3.1 assumes basic two-photon atom optics, but interferometry with  $102 \hbar k$  beamsplitters, for a 50-fold increase in sensitivity, has been demonstrated in a smaller apparatus [81]. Chapter 9 summarizes our recent progress in implementing large momentum transfer (LMT) atom optics in the 10 meter tower.

### 3.3.2 Application to an equivalence principle test

In a test of the equivalence principle, two overlapped ensembles of different species are launched simultaneously. This treatment allows the cancellation of many possible systematic phase shifts that are common to both species. The degree of cancellation depends on the degree of overlap in the ensembles' center-of-mass position and velocity, as well as on the mass difference or magnetic response difference of the isotopes. In general, a systematic phase shift associated with a kinematic error, like  $\delta z$  or  $\delta v_x$ , will be smaller in a differential measurement than shown in Tab. 3.1 because it is typically possible to control the center-of-mass difference between two ensembles better than each ensemble individually. Specific sources of systematic error will be addressed below.

### 3.3.3 Systematic effects

A system that has excellent sensitivity for one type of acceleration is likely to be sensitive to other accelerations as well. Accelerations due to rotations, magnetic fields, and gravity gradients are all sources of systematic error for an equivalence principle measurement. We can implement multiple strategies to mitigate these errors. In addition to thoughtful apparatus design and minimization of kinematic errors, we can alternatively modify the interferometer to amplify the spurious acceleration for precision characterization. Amplification can also lead to a measurement the acceleration that is interesting in its own right, as happened in the case of rotations.

#### Rotations

Term 2 demonstrates an important way in which rotations are imprinted on the atom: through the Coriolis force. Here, the rotation of the Earth couples to the transverse

velocity error to produce a significant phase shift. Within a single cloud of finite velocity width, a different phase will be imprinted on atoms of different velocity. For an equivalence principle test that compares the average phase across entire ensembles, a difference in the transverse velocity of the centroids will lead to a systematic phase error.

The Coriolis force on the atoms arises from the rotation of the apparatus – and the interferometer lasers in particular – during the interferometer sequence. The atoms are in free fall, and do not rotate with the Earth. The interferometer lasers, on the other hand, are attached to the Earth and rotate with it. As a result, the interferometer beams rotate relative to the atoms. Because the interferometer beams define the measurement axis of the interferometer, the frame in which the atoms are measured is rotating, leading to the Coriolis effect.

This description also suggests a way to eliminate the phase shift. By counter-rotating the interferometer beams in a way that exactly cancels Earth's rotation, the atoms are measured in an inertial frame and the Coriolis force vanishes. Mathematically, if the angle of the beam at the three pulses is set to be  $\theta_1 = 0$ ,  $\theta_2 = -\Omega_y T$ , and  $\theta_3 = -\Omega_y(2T)$ , and if an atom begins at position  $\delta x$  with velocity  $\delta v_x$ , then the laser phase associated with these angles is

$$\Delta\phi'_{\text{laser}} = (\delta\mathbf{k}_{\text{eff}} \cdot \mathbf{x})_1 - 2(\delta\mathbf{k}_{\text{eff}} \cdot \mathbf{x})_2 + (\delta\mathbf{k}_{\text{eff}} \cdot \mathbf{x})_3 \quad (3.22)$$

$$= k_{\text{eff}}\theta_1\delta x - 2k_{\text{eff}}\theta_2(\delta x + \delta v_x T) + k_{\text{eff}}\theta_3(\delta x + 2\delta v_x T) \quad (3.23)$$

$$= -2k_{\text{eff}}\delta v_x\Omega_y T^2 \quad (3.24)$$

which exactly cancels term 2.

The prospect of such a cancellation is the motivation behind the construction of the precision tip-tilt mirror of the rotation compensation system described in Sec. 4.5. With precise control over the direction of the interferometer beams, we can also choose to apply our own rotations or beam tilts, as we do in Ch. 5 and Ch. 6 to perform precision measurements of Earth's rotation.

## Magnetic fields

Despite preparing the atoms in a magnetically insensitive Zeeman sublevel, the states still have a second-order dependence on magnetic fields. This dependence is different for  $^{87}\text{Rb}$  and  $^{85}\text{Rb}$ , which have second-order Zeeman coefficients of  $\alpha_{87} = 2\pi \times 575 \text{ Hz/G}^2$  and  $\alpha_{85} = 2\pi \times 1294 \text{ Hz/G}^2$  [82, 83]. Raman interferometry, where the sign of the second-order shift changes with state, is more sensitive to magnetic fields than Bragg interferometry. In Bragg interferometry, only term 12 remains of those that are magnetically sensitive. This term results from the change in the magnetic field over the vertical spatial separation of the two arms,  $\hbar k_{\text{eff}} T/m$ . In the case of a WEP test, the term contributes a relative phase shift error between the species both because of the different magnetic response and because of the slightly different recoil velocities of the two elements. After absorbing a photon of the same wavevector, the  $^{85}\text{Rb}$  atoms travel slightly further than the  $^{87}\text{Rb}$  atoms, and in a magnetic gradient the two experience a slightly different magnetic force that is amplified by their different Zeeman coefficients.

To minimize the impact of the magnetic fields, we constructed a three-layer, 9 m magnetic shield to surround the interferometer region (Ch. 8). The shield reduces the environmental field from several hundred milligauss to less than 1 mG. The residual field exhibits some variation that could lead to a phase shift, but based on the high frequency of that variation, the source of the field is likely within the shields. As such, it may be stable over long time periods. Indeed, measurements made with a fluxgate magnetometer indicate stability of the high-frequency variations over at least two weeks, limited simply by the time span in which such data was taken. With long-term drifts in Earth’s magnetic field suppressed by the magnetic shield, we can mitigate a stable field by precisely measuring it with a magnetically sensitive atomic sublevel and removing its effect in analysis.

## Gravity gradients

The dominant systematic in a WEP test comes from term 7, which is the first to depend on mass. The term also depends on the size of the vertical gravity gradient, as

well as on the square of the laser wavevector. Analogous to term 12 discussed above, this term results from the change in the gravitational field over the vertical spatial separation of the two arms. In a WEP test, the difference in the recoil velocities combined with a gravity gradient leads to the two elements experiencing different gravitational potentials and therefore accumulating different phases.

The term's dependence on the local gravity gradient offers solutions for controlling its size: removing sensitivity to gravity gradients or removing the gravity gradients themselves. Removing sensitivity can be accomplished through an asymmetric four-pulse sequence or through propagation reversal. The asymmetric four-pulse sequence preserves sensitivity to accelerations while removing sensitivity to terms of order  $T^3$  [30]. In propagation reversal, the propagation direction of the lasers is reversed such that the excited state at the first beamsplitter in Fig. 3.1 is kicked down rather than up. Every place  $k_{\text{eff}}$  appears in Tab. 3.1 transforms to  $-k_{\text{eff}}$ . But because term 7 depends on  $k_{\text{eff}}^2$ , its sign does not change. Subtracting the phases of two interferometers with opposite propagation cancels this gravity gradient term while doubling the acceleration phase.

Removing the gradients themselves would involve placing masses in strategic locations to adjust the local gravitational field. Ideally, a sphere of mass surrounding the interferometer can cancel the local vertical gravity gradient [42], but experimentally it may be more feasible to position masses discretely.

Gravity gradients enter in another pair of terms, 10 and 11, which depend on errors in the atom's vertical position  $\delta z + \delta v_z T$ . In a differential test between two species, the corresponding systematic phase shift depends on the error in the vertical position of the ensembles' centroids. Trimming gravity gradients can reduce these errors as well. In addition, an asymmetric three-pulse sequence, where one pulse is delayed relative to the other two, incurs a phase shift that scales with the velocity  $\delta v_z$ , as described in Ch. 6. The amount of asymmetry can consequently be chosen to cancel the  $\delta v_z$ -dependent phase shift from gravity gradients [84].

Beyond the equivalence principle, term 7 is interesting in its own right as it emerges purely from the propagation phase, with no contribution from the laser or separation components. As such, it is a topological phase, analogous to the Aharonov-Bohm

effect of electromagnetism. Perhaps as a reflection of the interest in this phase, it has many names. It is alternately called the topological term, tidal term, quantum term, gravity gradient term or recoil term.

### 3.3.4 Beam tilt phase shear

The notion of deliberately applying a phase to the interferometer has already been raised as a way of canceling the effects of the Coriolis force and gravity gradients. A position-dependent phase shear can also be useful for creating a population fringe within an interferometer output port. In Ch. 6, we discuss in detail how such a population fringe can be used to read out the phase and contrast of an interferometer in a single experimental cycle, or to measure small phase gradients such as the rotations that result in term 2.

Terms 3, 4 and 6 all result from one method of applying a phase shear, namely, a tilt of the beam. In this phase shift list, a beam tilt of angle  $\theta_3$  is applied to the third pulse. Term 3 is a Coriolis phase shift that is constant across the cloud, but terms 4 and 6 combine to describe a linear phase shear where the imprinted phase depends on the position of the atom within the cloud at the time of the third pulse,  $\delta x + 2\delta v_x T$ . Upon imaging, the position-dependent phase results in a spatial modulation of the population fringe, shown below in Fig. 6.2.

### 3.3.5 Interferometer contrast

The interferometer described by Eq. 3.16 has perfect contrast. As the interferometer phase scans from 0 to  $\pi$ , the population in the ground state output port scans exactly from 1 to 0. But experimentally, many factors can spoil perfect contrast. Sources of contrast loss can be roughly divided into two categories: inefficient or inhomogenous atom optics, and inhomogenous interferometer phase shifts.

Pulse durations that differ from  $\pi/\Omega$  or off-resonant lasers both result in poor transfer efficiency of a single interferometer pulse for all atoms in the ensemble. An error in each pulse duration of  $\delta t$  ( $\delta t/2$  for the beamsplitter pulse), for example, reduces the final interferometer contrast from 1 to  $1 - (5/4)(\delta t/\Omega)^2$ . But the transfer efficiency

can also vary within an ensemble: atoms at different locations may experience different laser intensity and therefore different Rabi frequency, or an atom's particular velocity may detune it from the transition through the Doppler shift. A particularly pernicious effect is the intensity-dependent AC Stark shift, which, as shown in Eq. 3.4, impacts the resonance condition. Experimental corrections for inefficient or inhomogenous atom optics will be addressed in more detail below (Sec. 4.2 and Ch. 9), but strategies include choosing large beams, compensating for AC Stark shifts with spectator beams that don't drive interactions, and velocity-selective preparation pulses.

On top of pulse inefficiencies, if the phase shift depends on an atom's individual kinematics within the ensemble, as in terms 2, 4, 6, 10, and 11, a direct average of the phase error over the ensemble position and momentum distribution can lead to a loss of interferometer contrast. For a linear dependence on the position or velocity, e.g. a phase  $\kappa_x \delta x$  or  $\kappa_v \delta v_x$ , the contrast decays as  $e^{-\kappa_i^2 \sigma^2 / 2}$ , where  $\sigma$  is the standard deviation of the ensemble's position or velocity distribution (assumed to be Gaussian). Beyond directly minimizing the phase errors, position and/or velocity-resolved imaging, as demonstrated in Ch. 5 and Ch. 6, allow high-contrast interferometry even in the presence of such inhomogeneities.

### 3.4 Prospects for other interferometer topologies

The Mach-Zehnder interferometer topology is of great interest for its sensitivity to accelerations, but the exact pulse sequence or laser propagation direction of an interferometer can be modified for the application at hand. Sensitive gyroscopes often use horizontal rather than vertically-oriented interferometer beams [37, 44]. Gravity gradiometers can be constructed with a four-pulse sequence, or with simultaneous pairs of three-pulse gravimeter measurements [36, 85]. For gravitational wave detection, four or five-pulse sequences cancel significant systematic phase shifts and improve overall contrast [49]. In all such cases, with an extension for general relativity as needed [42], the formalism described above can be used to understand the interferometer sensitivity and its systematics.

# Chapter 4

## Apparatus

After a brief overview of the main structure of the apparatus and the experimental control system, I will delve into the creation of the launched, ultracold source (Sec. 4.1), the generation of the beams that implement the atom beamsplitters and mirrors (Sec. 4.2), and the detection of the interferometer output ports through fluorescence imaging (Sec. 4.3). I then discuss two other aspects of the system: absorption imaging for detection and diagnosis of the ultracold source prior to launch (Sec. 4.4), and the rotation compensation system used to cancel the Coriolis phase shift associated with Earth’s rotation (Sec. 4.5).

Unless noted specifically, the discussion will focus on the production, interference, and detection of  $^{87}\text{Rb}$  only. The production of  $^{85}\text{Rb}$  will be examined in Ch. 10.

The main apparatus extends over 10 meters from the bottom to the top (Fig. 4.1).<sup>1</sup> To accommodate this large size, it is located at the bottom of a 25 ft deep, 8 ft diameter pit and stretches to the ceiling. At the bottom of the apparatus is the in-vacuum precision tip-tilt rotation stage and retroreflection mirror for Coriolis compensation, as well as a  $\lambda/4$  waveplate (Fig. 4.2). An all-metal gate valve separates this chamber from the 300 L/s ion pump that sits below the 3D magneto-optical trap (MOT) chamber. To the side of the 3D MOT chamber is the 2D MOT chamber, in which a vapor of

---

<sup>1</sup>Certain aspects of the apparatus construction, such as the vacuum chamber, the 9 m solenoid, and the timing system, can be found in greater detail in prior theses, namely Ref. [86] and [87]. More recent additions, such as the titanium sublimation pumps, the lattice launch, and the fluorescence imaging system, can be found in greater detail in Ref. [88].



Figure 4.1: Image of the apparatus, which is located in a 25 ft deep pit and is supported by a structure of 80/20 beams.

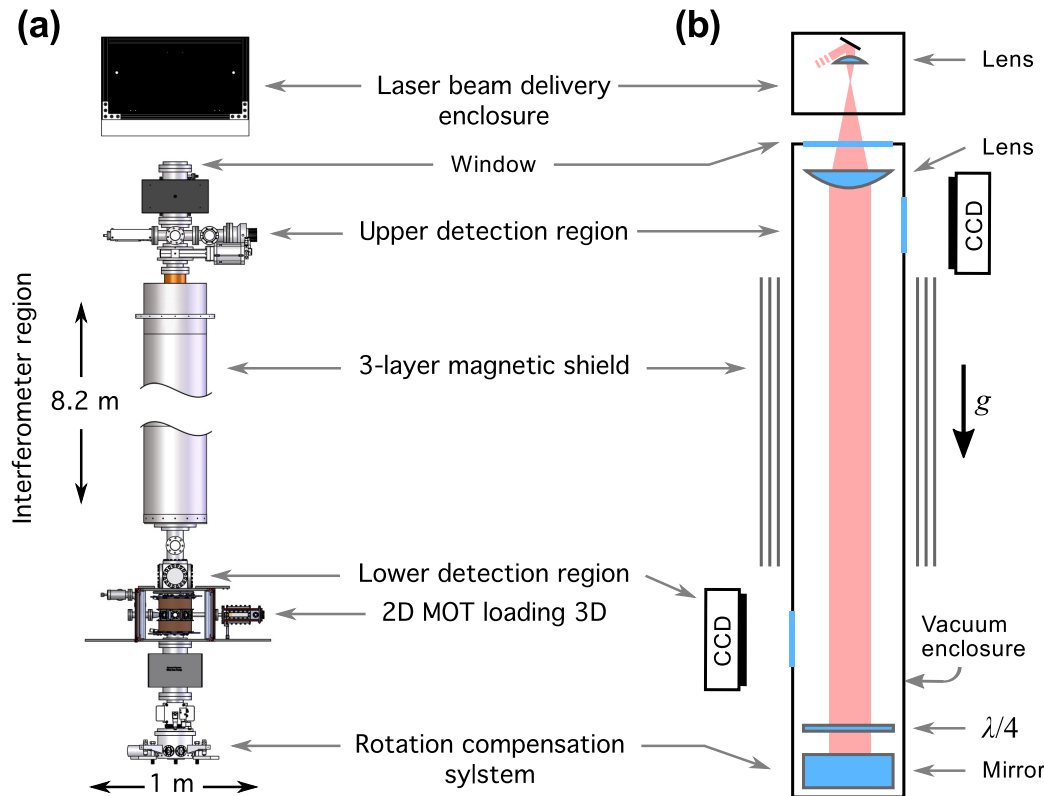


Figure 4.2: Schematics of the apparatus. (a) CAD model of the apparatus, with various regions of interest labeled. The middle of the interferometer region has been cut for ease of viewing. Obscured by the magnetic shield is the 10 cm diameter aluminum vacuum tube, wrapped along its length by a solenoid. (b) Drawing showing the location of selected optics, including the retroreflection mirror, quarter waveplate and lens in vacuum. In red is the path of the interferometer beams and the MOT vertical beam. The lattice beams (not shown) enter the system near the focus between the two lenses. Two of the three CCD cameras are shown. The third camera is located in the lower detection region, with a line of sight parallel to the page normal. Liberty has been taken with the exact azimuthal position of the cameras about the tower.

atoms is cooled into a high-flux beam that enters the 3D MOT chamber through a narrow aperture. The aperture acts as a differential pump to maintain good vacuum in the 3D MOT region. Above the 3D MOT chamber is the detection region, where the large windows allow for good optical access for the two orthogonal cameras. Next, a cross houses an ion gauge in one arm (typically turned off to avoid emitting light that could affect the atoms) and a set of retractable titanium filaments used for the titanium sublimation pump in the other. Both are recessed to maintain a clear optical path for the interferometer beams, as well as a clear flight path for the atoms, which are launched up through this chamber into the magnetically shielded interferometer region above.

The interferometer region consists of a 10 cm diameter aluminum vacuum tube, nearly 9 m in length. Wrapped around the vacuum tube is a solenoid, typically set to provide  $\sim 130$  mG of field (35 mA) to establish the quantization axis. Earth's field is attenuated along the interferometer axis by a 3-layer, welded  $\mu$ -metal magnetic shield (Ch. 8). The on-axis residual field variations are  $< 1$  mG root mean square (RMS) deviation in all three dimensions.

Above the interferometer region is a second all-metal gate valve. Attached above is a cross that contains a second set of retractable titanium filaments, an ion gauge, and a window for a third camera. Next is a second 300 L/s ion pump. Inside this ion pump is a 786 mm focal length lens, the second lens in a telescope that expands the interferometer and MOT beams to their nominal size of 2 cm  $1/e^2$  radial waist. The first lens ( $f = 50$  mm) is located in the laser beam delivery enclosure, outside of the vacuum chamber. A 4 in aperture window at the top of the ion pump provides the necessary optical access.

The vacuum inside the main interferometer chamber is at the few  $\times 10^{-11}$  Torr level, as measured by the ion gauges and the ion pumps at either end. Every six months to a year as necessary, the titanium filaments are pushed by a linear actuator into the line-of-sight of the interferometer region. They are resistively heated with high current to evaporate titanium onto the walls of the long chamber, with the goal of depositing a monolayer of titanium at the center of the tube. This procedure generally reduces the vacuum measured at either end by a factor of 2 to 3.

A compact 3 ft  $\times$  3 ft breadboard, enclosed to reduce environmental drifts, contains the delivery optics for the vertical MOT axis, the atom optics, and the lattice beams. To conserve the limited space at the top of the apparatus, the majority of the frequency generation and amplification occurs in a nearby 19 in rack (for the doubled 1560 nm interferometer beams) or on a separate optical table in an adjacent room (for the MOT and lattice beams). The light is transferred by optical fiber to the delivery enclosure, where only the final stages of amplification, shuttering, or optical switching are performed.

Two fibers also deliver light to the 2D and 3D MOT regions at the bottom of the apparatus from the separate optical table containing the necessary MOT frequencies. In the 2D MOT region, the light is amplified prior to being split into two pairs of counterpropagating beams. The power delivered to the 3D MOT is sufficient without amplification, and so the light is directly split into two pairs of horizontal, counterpropagating beams, with the third axis provided from the upper enclosure.

Whenever possible, radiofrequencies, which are generally responsible for shifting laser frequencies to the appropriate values for cooling and (more critically) interferometry, are externally referenced to a stable, low phase noise source (Oscilloquartz OCXO 8607-BGE).

The timing of all events in an experimental cycle is controlled by a central server. This server parses the user-generated sequence of events and distributes them to the subprograms that control individual elements of hardware (e.g., a frequency source, power supply, or camera). Events that require precise, submicrosecond timing, such as the optical pulses for interferometry, are implemented using an FPGA-based system that can provide a number of digital lines, analog input and output lines ( $-10$  to  $+10$  V), and direct digital synthesis (DDS) frequencies. All these lines are able to change state with less than 10 ns timing jitter [86]. Events that can withstand the millisecond delays of a typical CPU are implemented directly by the subprograms on a nearby computer.

At the end of the cycle, the server compiles the events played, the state of all the hardware elements, and any measurements (e.g., photodetector voltage measurements) into a single XML document stored on a remote file server. While the path and

filename of any images taken by the cameras are recorded in the XML document, the images themselves, typically a little more than a megabyte each, are saved separately. We also save the file parsed by the server to generate the events, allowing us to return to a particular experimental trial at a later date and to reproduce it exactly, provided there have been no changes to the system hardware.

We can then import the XML document and the image into a *Mathematica*-based analysis program, where we have developed a set of custom tools to infer from the images information about a cloud's atom number, spatial size, temperature, etc., or, as in the case of interferometry, the population ratio.

## 4.1 Ultracold cloud preparation

The ensemble that is launched has a strict temperature requirement. At the most basic level, the atoms cannot expand more than the size of the vacuum chamber over the nearly 2.6 s of free-fall time. More stringent is the demand set by interferometry. For good contrast, all atoms in the ensemble must experience a uniform laser intensity during the pulse, which corresponds to a uniform Rabi frequency and a uniform transfer ratio between the interferometer arms. With the interferometer beam at a  $1/e^2$  radial waist of 2 cm, limiting the intensity non-uniformity to below 10% requires a source that is 40 nK or colder.

In addition, because the sensitivity of the interferometer scales as  $\sqrt{N}$ , where  $N$  is the atom number, we want to operate with as many atoms as possible. We also want to operate with a dilute cloud of atoms so that the chemical potential and resulting collisional phase shifts are low.

These requirements are satisfied by the multi-stage cooling procedure we follow. A typical 2D MOT /3D MOT combination serves to collect  $4 \times 10^9$  atoms in less than 4 s and cools them from above room temperature to 100  $\mu\text{K}$  (Sec. 4.1.1). The subsequent evaporation stage cools the atoms further while increasing their phase space density (PSD), resulting in  $\sim 10^6$  atoms at 1  $\mu\text{K}$  (Sec. 4.1.2). Although the cloud at the end of evaporation is too hot and too dense for interferometry, its small size is an excellent seed for the magnetic lens (Sec. 4.1.3, elaborated in Ch. 7). This final stage exchanges

spatial breadth for velocity narrowness, producing an ultracold cloud (2 - 50 nK). This cold cloud is also comparatively dilute, at a few tens to hundreds of microns in scale. The long drift time after launch further dilutes the cloud as it grows in size.

Just prior to launch, the atoms are prepared in a magnetically insensitive Zeeman sublevel to reduce the phase shift associated with stray magnetic fields (Sec. 4.1.4). The cold, dilute atoms are then accelerated with an optical lattice to several meters per second and travel into the interferometer region (Sec. 4.1.5).

### 4.1.1 Magneto-optical traps

The production of a 3D MOT requires a vapor source of rubidium, good vacuum, appropriate magnetic field gradients, and lasers with the necessary power, beam size, frequencies, and polarization. To aid in the efficient collection of atoms, we have implemented a 2D MOT that creates a high-flux pencil-like beam of atoms to load the 3D MOT. The two MOT chambers are separated by a differential pumping stage that allows the vacuum in the 3D MOT chamber to be orders of magnitude lower than that of the 2D MOT, extending the atom lifetime through the later stages of the cooling process. The construction and alignment of the laser system, the 2D MOT and the 3D MOT are described in detail in Ref. [86] and [87], but are summarized here.

#### Laser frequency generation

For each isotope, we generate two frequencies: cooling and repump. The cooling light couples the uppermost hyperfine states of the ground state and excited state manifolds ( $|F = 2\rangle \rightarrow |F' = 3\rangle$  for  $^{87}\text{Rb}$  and  $|F = 3\rangle \rightarrow |F' = 4\rangle$  for  $^{85}\text{Rb}$ ). Despite several linewidths' detuning from other possible transitions, there is a small but significant probability that the atom can couple to a different excited hyperfine state and spontaneously decay from there into a lower ground state. With only the cooling frequency present, all atoms would eventually be pumped into this lower state, and cooling would cease. Repump light couples this lower ground state to the excited state such that the atoms can decay back into the upper ground state, allowing cooling to continue ( $|F = 1\rangle \rightarrow |F' = 2\rangle$  for  $^{87}\text{Rb}$  and  $|F = 2\rangle \rightarrow |F' = 3\rangle$  for  $^{85}\text{Rb}$ ).

The frequency generation and power amplification is performed predominately on a separate optical table and the light is delivered to the 2D MOT and 3D MOT regions by single-mode optical fiber (for the optics layout, see Ch. 2 of Ref. [88]). Only the final stages of amplification and of frequency tuning are performed after delivery, leading to a compact setup where space is most constrained.

All light for the MOT begins with an external cavity diode laser (New Focus Vortex 6013) with linewidth < 1 MHz. This master light is locked 480 MHz blue of the  $|F = 3\rangle \rightarrow |F' = 2\rangle - |F = 3\rangle \rightarrow |F' = 4\rangle$   $^{85}\text{Rb}$  crossover resonance through saturation absorption spectroscopy. The offset frequency is chosen such that the first- and second-order sidebands of a single phase modulator driven at 2.527 GHz provide the repump light for  $^{85}\text{Rb}$  and  $^{87}\text{Rb}$  respectively. Two phase modulators separately produce the cooling frequencies for the two isotopes.

The cooling light for the 2D MOT and 3D MOT is split from a single beam, but a pair of AOMs in a push-pull configuration allows the 2D MOT detuning to be changed by several megahertz relative to the 3D MOT detuning. The 2D MOT is 6 MHz red-detuned, while the 3D MOT is 10 MHz detuned.

The beams from the three phase modulators ( $^{87}\text{Rb}$  cooling,  $^{85}\text{Rb}$  cooling, and repump) are combined prior to amplification, with separate paths for light destined for the 2D MOT, the 3D MOT X and Y axes, and the 3D MOT Z axis.<sup>2</sup> The optical power is increased by a series of booster optical amplifiers and tapered amplifiers. Each path is then coupled into a long optical fiber for delivery.

## 2D MOT

The source of all rubidium for the experiment is a few grams of the natural-abundance alkali deposited onto the coldest point of the 2D MOT chamber. This source can be either heated or cooled to regulate the vapor pressure in the 2D MOT region, although it is typically cooled to 19°C. All other parts of the 2D MOT chamber – in particular the windows – are maintained at a higher temperature (40 - 60°C) than the rubidium source to prevent unwanted migration of atoms onto these surfaces. The chamber is

---

<sup>2</sup>More accurately, a small portion of the amplified light destined for the 3D MOT X and Y axes is itself amplified, and becomes the seed for the 3D MOT Z axis.

pumped through the differential pumping stage by a 300 L/s ion pump attached to the 3D MOT chamber.<sup>3</sup>

Seed light containing the cooling and repump frequencies arrives via single-mode optical fiber. This light is amplified by a tapered amplifier to 300 mW and is then split into six beams. Four beams evenly split the bulk of the power and become the two counterpropagating pairs of the 2D MOT. These beams are cylindrically expanded in a 1 : 8 ratio to take advantage of the long, narrow 2D MOT chamber.

The last pair of low-power beams are the pusher and retarder of a 2D+ MOT. These counterpropagate along the axis of the 2D MOT and serve to improve capture in the 3D MOT by moderately cooling the atoms along this direction. The 2D+ MOT has a factor of up to 10 improvement on the loading rate compared to the 2D MOT alone, increasing the rate from a few  $\times 10^8$  to  $> 10^9$  atoms/s.

Two pairs of rectangular coils create the magnetic gradients required for the 2D MOT. The gradient and bias fields applied by these coils were experimentally chosen to optimize loading rate into the 3D MOT through the 3 mm diameter, 5 cm long bore of the differential pumping stage that separates the 2D MOT and the 3D MOT chambers.

### 3D MOT

Due to the differential pump, the background pressure drops from  $10^{-8} - 10^{-9}$  Torr to a little more than  $10^{-11}$  Torr, allowing for the long lifetimes ( $> 10$  s) needed for the 3D MOT and the long evaporation sequence that follows.

An optical fiber delivers  $\sim 100$  mW of combined cooling and repump light, which is then expanded to a  $\sim 15$  mm radial waist and split four ways to form the two horizontal axes of the 3D MOT. The vertical axis follows the same beam path as the atom optics (Sec. 4.2): it is a retroreflected beam with a radial waist of 2 cm. During the loading stage of the 3D MOT, power in this beam is 90 mW for a peak intensity of 15 mW/cm<sup>2</sup>.

A pair of water-cooled anti-Helmholtz coils generate the necessary magnetic field

---

<sup>3</sup>Ion pumps directly attached to the 2D MOT chamber tend to fail after six months to a year due to rubidium contamination.

gradients. A conversion ratio of  $0.87 \text{ G/cm/A}$  relating the applied current and magnetic gradient for these coils was determined by measuring the current at which the magnetic trap failed to hold atoms against gravity. While the gradient requirements for the 3D MOT are low ( $\sim 6 \text{ G/cm}$ ), the coils can be driven up to  $218 \text{ G/cm}$  for the subsequent evaporation stage.

Three pairs of coils form a cube about the 3D MOT chamber to trim stray magnetic fields. The bias and gradient were optimized for transfer from the cold, dense cloud at the end of the 3D MOT stage into the tight magnetic trap that begins the evaporation sequence.

### Pseudo-compressed MOT

For the fastest and most effective evaporation, it is important to begin with a cold cloud and to minimize the excess energy imparted to the atoms during the transfer from the MOT to the magnetic trap. Towards that end, after the 3D MOT has saturated with atoms, we reduce the average photon scattering rate by ramping up the detuning of the cooling transition from  $10 \text{ MHz}$  to  $44 \text{ MHz}$  and by turning off the repump intensity (Fig. 4.3). Weakening the repump light lowers the scattering rate both by allowing atoms to trickle down into the  $|F = 1\rangle$  level, which is far detuned from the incident light, and by reducing the amount of light on resonance with the  $|F = 2\rangle$  level. With this reduced scattering, the cloud gets colder and denser.

In other work [89], the magnetic gradient is maintained or increased at this time to improve the matching of the cloud size in the MOT to its size in the stiff magnetic trap that follows. The combination of increased detuning from the cooling transition, reduced repump intensity, and increased field gradient defines a “compressed” MOT (cMOT). In our apparatus, however, the best transfer was obtained when the field was ramped to zero over the  $20 \text{ ms}$  of the pseudo-cMOT. It must be noted, however, that due to eddy currents in the steel vacuum chamber, the field at the MOT location is unlikely to fall to zero during this interval. The impact of the eddy currents will be further discussed below (Sec. 4.1.4).

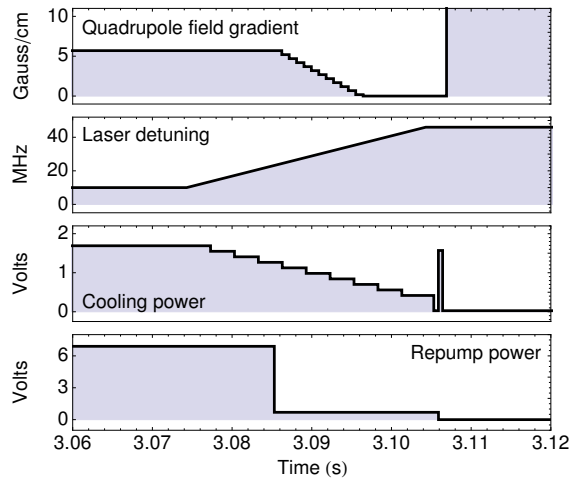


Figure 4.3: Pseudo-cMOT experimental sequence. From top to bottom are the radial quadrupole gradient, the detuning from resonance (positive is red-detuned), the voltage setpoint proportional to the total power incident on the atoms, and the voltage setpoint controlling the repump power (the actuator is nonlinear; anything below  $\sim 1$  volt corresponds to no repump power). During the pseudo-cMOT phase, the quadrupole gradient is lowered while the detuning of the cooling light is increased and the power reduced. The power of the repump light is also reduced midway through the sequence. At the end of the pseudo-cMOT, the laser light is turned off. Soon after, a short pulse of light transfers the remaining  $|F = 2\rangle$  atoms to  $|F = 1\rangle$  and the field is snapped up to 50 G/cm. Note that the applied quadrupole gradient is approximated below a few G/cm due to calibration uncertainty.

### 4.1.2 Evaporation

In evaporative cooling, the hottest (fastest, most energetic) atoms of an ensemble are selectively ejected, lowering the average energy per atom in the remaining ensemble. The remaining atoms are permitted to rethermalize through collisions to a new, colder temperature. The efficiency of evaporation and the final number of atoms at condensation depend nonlinearly on the temperature and atom number of the initial cloud in the magnetic trap. Both a high temperature and a low atom number lower the initial collision rate, resulting in slower rethermalization rates and slower overall evaporation. A high temperature also requires the ejection of more atoms to reach the same final temperature, resulting in a lower atom number. Thus the colder and denser the initial cloud, the faster and more efficient the evaporation.

At the end of the cMOT stage, the atoms are in a mixture of  $|F = 1\rangle$  and  $|F = 2\rangle$ . We choose to evaporate in  $|F = 1\rangle$ . Of its three Zeeman sublevels, only one is trappable ( $m_F = -1$ ), leading to nominally 1/3 of the cMOT atoms successfully captured by the magnetic trap, and all in a single state. In contrast, two of the five Zeeman sublevels of  $|F = 2\rangle$  can be trapped ( $m_F = 1$  and  $m_F = 2$ ). A mixture of states during the evaporation sequence is, however, undesirable. For example, in our implementation of evaporation the  $m_F = 2$  states would be preferentially ejected from the trap. Without the ability to evaporate  $m_F = 1$  atoms simultaneously, the overall evaporation rate slows as atoms in one sublevel act as a refrigerant for atoms in the other. Interactions between the two states can further degrade the evaporation efficiency, and the simplest solution is to eject all atoms in one of the two states [90]. Evaporating in  $|F = 1\rangle$  leads to more atoms in a single Zeeman sublevel for a straightforward evaporation.

To minimize the excess energy given to the atoms during the transfer from the MOT to the magnetic trap, the cloud's size and position at the end of the MOT must be matched to the cloud's size and position once it settles in the magnetic trap. The best transfers give the highest phase space densities in the magnetic trap, characterized by high density and low temperature (see Tab. 4.1).

The transfer into the magnetic trap involves shuttering the MOT light, depumping

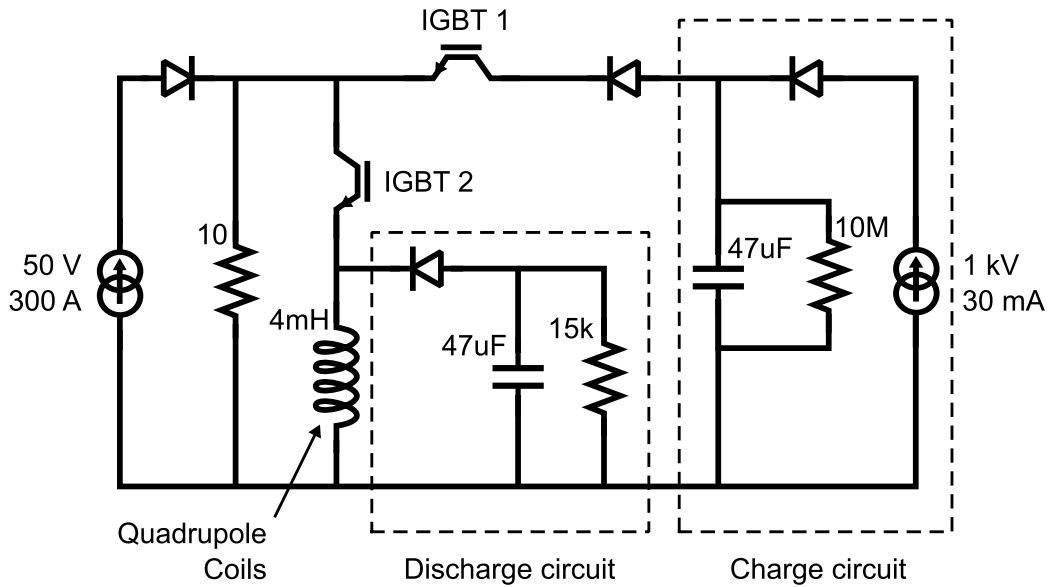


Figure 4.4: Quadrupole coil snap on/off circuit. A pair of insulated gate bipolar transistors (IGBT) serve as high-current switches. At the beginning of an experimental run, IGBT 1 is open and 2 is closed, and the primary 50 V - 300 A power supply controls the voltage across the coil. To rapidly snap to a larger value, we take advantage of an LCR circuit: IGBT 1 closes, converting the stored charge on the charge capacitor into a large current through the quadrupole coils ( $> 55$  A in  $700\ \mu\text{s}$ ). The diode on the output of the charge circuit prevents the current from ringing back into the capacitor. Meanwhile, the setpoint of the primary power supply is changed to match the peak value. To rapidly turn off the quadrupole coils, we perform a similar sequence, where IGBT 2 opens, and the current is converted into a charge stored on the discharge capacitor. This charge decays through the neighboring resistor over several seconds. The charge capacitor is charged to 650 V by an independent high-voltage, moderate-current supply.

the atoms into the  $|F = 1\rangle$  state,<sup>4</sup> and snapping up the magnetic field gradient from the 6 G/cm used for the MOT to 50 G/cm. With an inductor-capacitor resonance circuit (Fig. 4.4), the current through the quadrupole coils reaches the snap setpoint in 700  $\mu$ s. The value of the snap current is chosen experimentally for best transfer. The field is allowed to stabilize for 300 ms before being ramped up to 218 G/cm at a rate of 1 G/cm/ms. The delay allows eddy currents from the snap up to decay. The strong field gradient increases the atoms' collision rate at the expense of temperature (again, see Tab. 4.1). At this initial point, however, the high collision rate is preferred in order to speed up the thermalization and the evaporation.

We can perform two variations of the evaporation procedure: evaporation in an optically-plugged quadrupole trap (Sec. 4.1.2) or evaporation in a time-orbiting potential trap (Sec. 4.1.2). Both, however, start in the same way with an unmodified, high-gradient quadrupole trap. Once the trap reaches its maximum gradient, evaporation begins with the application of the microwave knife.

For atoms in the  $|F = 1, m_F = -1\rangle$  state, microwaves detuned red from the zero-field resonance at 6.834 GHz can remove atoms by exciting them to an untrapped state,  $|F = 2, m_F = -2\rangle$ . In a quadrupole magnetic field, these microwaves define an oblate ellipsoid in space beyond which atoms are no longer trapped. As a hot atom climbs the trap potential, the increasing magnetic field tunes it into resonance with the microwaves and it is ejected.

The microwave knife is a standing wave formed by two microwave antennas on opposite sides of the 3D MOT chamber (Fig. 4.5). The relative phase of the microwaves emanating from the two antennas is tuned to position an antinode at the location of the atoms. The optimal phase provides the maximum Rabi frequency for the microwave transfer between hyperfine levels.

During evaporation, the frequency of the microwaves is swept from 150 MHz red of the zero-field resonance to a few megahertz or less, depending on the protocol. The ending frequency is directly related to the temperature of the final cloud. The frequency sweep is generally broken into a number (3 to 5) of discrete linear ramps,

---

<sup>4</sup>The depump frequency, tuned to the  $|F = 2\rangle \rightarrow |F' = 1\rangle$  transition, is generated using the same phase modulators that are also used to generate the cooling frequencies.

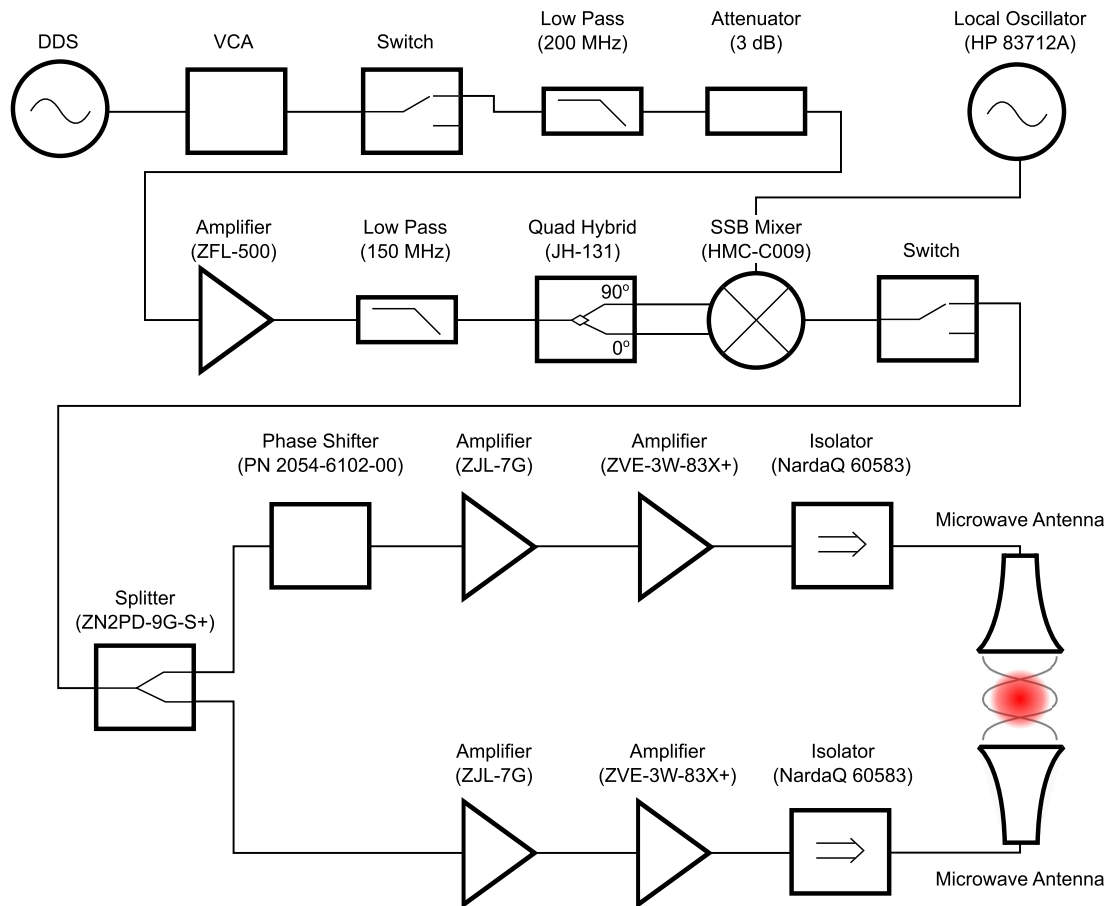


Figure 4.5: Microwave knife circuit. A variable-frequency signal (0 - 120 MHz) from the DDS is amplified and split into two quadratures before being mixed with the local oscillator (6.844 GHz). At the output of the single-sideband mixer, most of the RF power is in the red sideband (> 40 dB above the next-largest spur). This signal is then split in two. One path passes through a tunable phase shifter, and both are emitted from microwave antennas on opposite sides of the 3D MOT chamber. The phase shifter is tuned to maximize the Rabi frequency at the location of the atoms.

where the slopes can be independently adjusted to optimize the final cloud parameters.

When evaluating the evaporation sequence, we typically analyze a cloud imaged immediately after snapping off the trap from a moderate value, 20 to 50 G/cm. We repump the atoms to the  $|F = 2\rangle$  level and produce an absorption image of the cloud with a weak probe beam detuned up to 3 atomic linewidths (18 MHz) from resonance with the cooling transition. Further details of the imaging system and the image analysis are described below (Sec. 4.4).

As the atoms are cooled, their collision rate, density, and phase space density increase, while their temperature and size decrease. Although the tight, 218 G/cm trap is excellent for increasing the initial collision rate, the density and collision rate soon become so large that three-body collisions become a significant atom loss mechanism [91]. When we approach kilohertz collision rates and densities of  $10^{14}$  atoms/cm<sup>2</sup>, we ramp down the trapping gradient to an intermediate value, 131 G/cm or 109 G/cm depending on the trap type. This reduces the peak density by 40% and the collision rate by 50%, and we can continue efficient evaporation.

In an unmodified quadrupole trap, the coldest atoms will collect in the region of zero or near-zero field at the bottom of the trap. At such low fields, the Zeeman levels become degenerate and the atoms can change spin (Majorana flip) from the trapped state to one of the untrapped states [92, 93]. This loss mechanism becomes more important as the cloud gets colder and denser, and it is necessary to block the atoms from reaching this region of low field. We have implemented two methods for doing so: a far-detuned optical plug and a time-orbiting potential trap. While the plugged quadrupole offers higher collision rates and more rapid evaporation, we ultimately use the latter because it produces lower temperatures after the magnetic lens.<sup>5</sup>

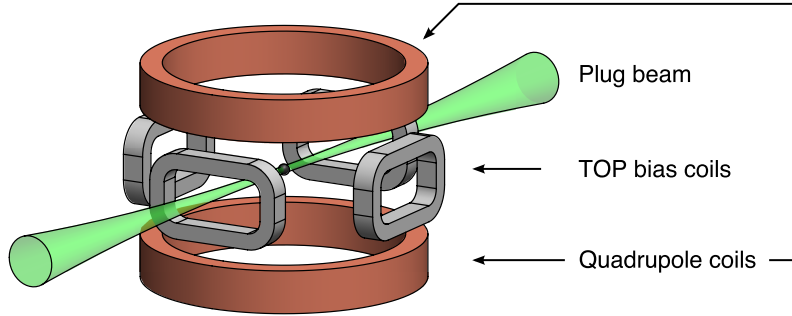


Figure 4.6: Schematic showing the arrangement of the optical plug (green), quadrupole coils (copper), and bias coils (grey). The plug is aligned to intersect with the point at which the quadrupole field is zero.

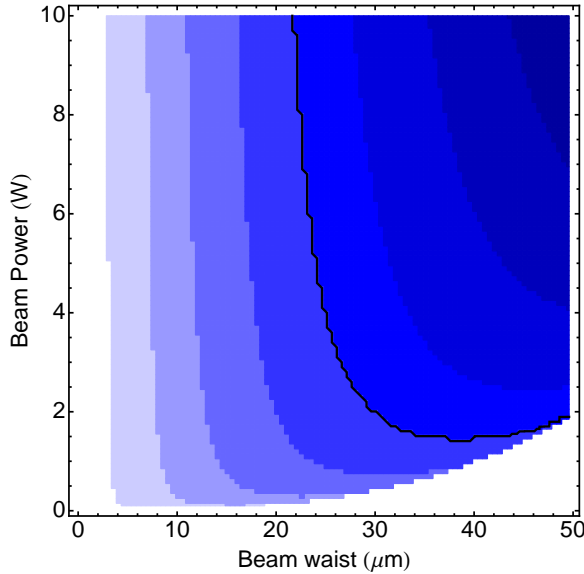


Figure 4.7: Optical plug power and radial waist requirements. To inhibit Majorana loss, the plug should prevent the atoms from entering a region of field less than several hundred milligauss. The field at the plugged quadrupole trap minimum is coded in the color displayed: white corresponds to  $< 0.1$  G, and a color change corresponds to an increase of 0.1 G. The black contour marks the 0.5 G boundary. Note that due to the spatial extent of the cloud, certain parts may experience lower field. For example, the lowest field experienced by an atom with a velocity corresponding to  $10 \mu\text{K}$  is 350 mG, to be compared to 450 mG at the trap minimum.

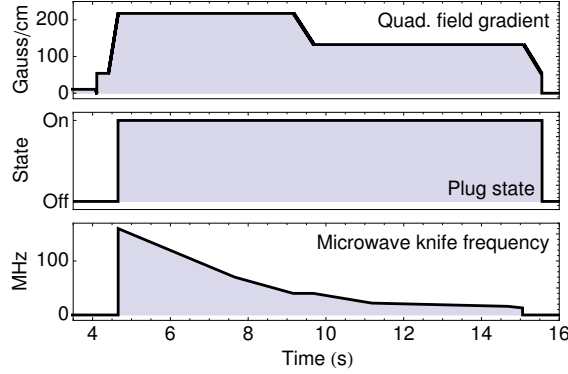


Figure 4.8: Timing of evaporation in the plugged quadrupole. From top to bottom, the plots show the (radial) quadrupole field, the state of the plug (on or off), and the microwave knife frequency (10 MHz is atom resonance at zero field).

### Evaporation in a plugged quadrupole trap

In a plugged quadrupole trap, a blue-detuned beam is aligned to the quadrupole field zero (Fig. 4.6), repelling the atoms via the AC stark shift. The waist, power and detuning of the beam must be sufficient to keep the atoms in a field strength of approximately 0.5 G to prevent Majorana spin flips (Fig. 4.7). We aligned a 532 nm plug beam (Sprout, Lighthouse Photonics) to the minimum of the quadrupole trap along one of the radial axes. The alignment is fine-tuned by optimizing the number of atoms after the final evaporation cut. The 6 W beam is focused to a  $1/e^2$  radial waist of  $20\ \mu\text{m}$ . The new minima of the plugged quadrupole trap occur at  $34\ \mu\text{m}$ , which corresponds to a field of 450 mG. The presence of the plug begins to be necessary for maintaining our atom number by the third segment of our microwave cut, when the atoms have reached  $50\ \mu\text{K}$ , although we typically turn on the plug at the beginning of the evaporation (Fig. 4.8).

We analyze the evaporation efficiency by fitting absorption images of the cloud

---

<sup>5</sup>As a confounding factor, the plug laser broke and took a year to replace as we were developing the magnetic lens procedure (Ch. 7). It is possible that evaporation in a plugged quadrupole trap could also produce the  $< 2\ \text{nK}$  clouds demonstrated with the time-orbiting potential trap. But preliminary data suggested that the temperature after the magnetic lens with a plugged-quadrupole source was limited to 50 nK even as the evaporation cuts deepened to reduce the initial temperature and size before the lens.

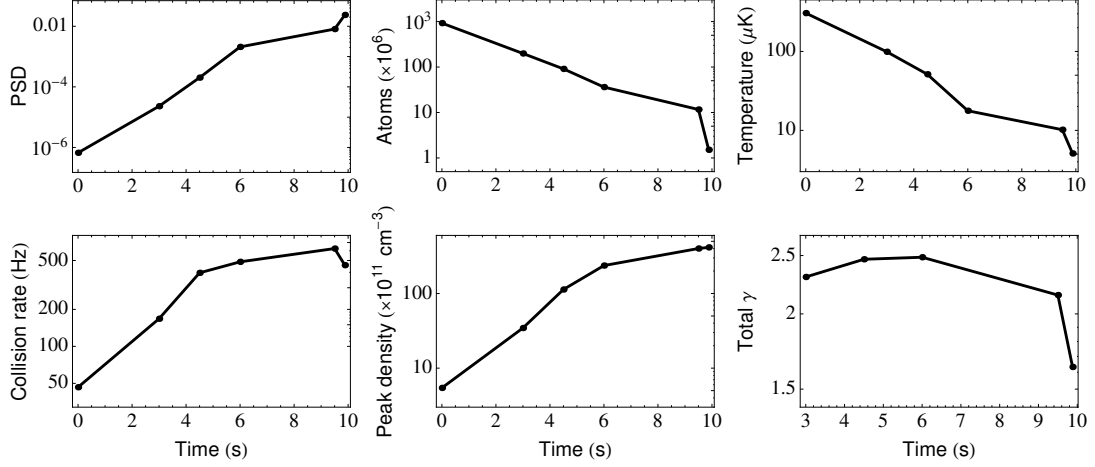


Figure 4.9: Characteristics of evaporation in a plugged quadrupole trap. The time is defined from the start of the evaporation, after the quadrupole has been ramped up to full current. All parameters are based on images taken after snapping the quadrupole field down from 50 G/cm, but are scaled back to the field gradient applied during the evaporation. The field is 218 G/cm until 4.5 s, and 131 G/cm thereafter.

after adiabatically ramping down to a modest quadrupole field (50 G/cm) and then abruptly snapping to zero field via the discharge circuit of Fig. 4.4. Fits of this cloud to the shape expected in a quadrupole magnetic trap yield information about the cloud’s characteristics, including its temperature, atom number, collision rate, and PSD (Fig. 4.9; see Sec. 4.4.1 for more detail on the fitting process). The trends indicate efficient evaporation up to the fifth and final ramp, quantified by the efficiency factor

$$\gamma = \frac{\log (\text{PSD}_f/\text{PSD}_o)}{\log (N_o/N_f)}. \quad (4.1)$$

The quantities  $N_o$  ( $N_f$ ) and  $\text{PSD}_o$  ( $\text{PSD}_f$ ) are the initial (final) atom number and PSD respectively. That is, a factor of 1000 growth in the PSD for a factor of 10 loss in atoms, an efficient evaporation trend, yields  $\gamma = 3$ . Despite precipitous drop in atom number during the last ramp, the rise of the PSD and the fall of the temperature are still significant.

The model behind the fits that provide this information is truly applicable without

the plug beam, when the trap is a pure quadrupole. The plug beam modifies the trapping potential and changes the cloud shape. In fact, for extremely cold, small clouds the modified trap can be approximated as harmonic, very different from the linear quadrupole trap. But although the model of the cloud shape is no longer the most appropriate in this regime, it nevertheless provides a rapid method to evaluate the evaporation efficiency. As further validation, independent time-of-flight measurements after the full evaporation sequences report a release temperature of  $1.4 \mu\text{K}$ , on the same order as the temperature extracted from the fit ( $5 \mu\text{K}$ ).

The modification of the quadrupole trap by the plug can produce additional subtleties in the evaporation process at the coldest temperatures. If the plug is perfectly aligned with the quadrupole field zero, then in our orientation there are two trap minima, one on either side of the beam in the horizontal plane. Thus evaporation can end in the production of two distinct clouds rather than the single cloud desired. A deliberate but slight misalignment of the plug can remove the degeneracy and bias the cloud into one of the two wells, but then the protection against Majorana spin flips is compromised.

### Evaporation in a TOP trap

In an alternative method to mitigate Majorana loss, we implemented a time-orbiting potential (TOP) trap. A TOP trap consists of a quadrupole field combined with a rotating bias field. As long as the bias field is rotating faster than the atom can follow, the atoms see an effective, time-averaged potential that is locally harmonic in all dimensions (see Sec. 7.2 for the theory behind a TOP trap). At the new trap minimum, the atoms now experience a field with the magnitude of the bias field itself. The location of zero field orbits this region at a radius  $r_0 = B_0/A$ , charmingly named the “circle of death,” where  $B_0$  is the strength of the bias field and  $A$  is the radial quadrupole field gradient. Any atom that passes near this location can undergo a spin flip and will be ejected from the trap. Pure TOP evaporation takes advantage of this feature: the hot atoms are removed by a controlled reduction in the strength of the bias field, drawing in the circle of death. We implement a hybrid scheme that also makes use of a microwave knife.

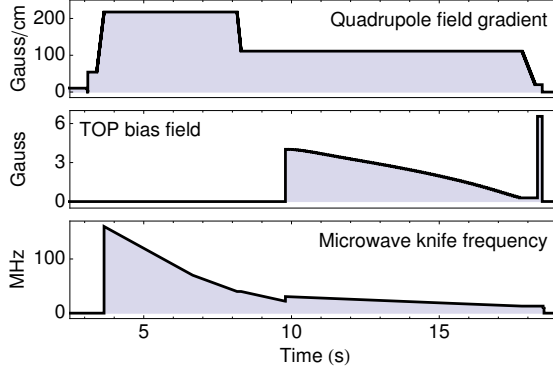


Figure 4.10: Timing of evaporation in the TOP trap. From top to bottom are the magnitude of the (radial) quadrupole field gradient, the TOP bias field, and the detuning of the microwave knife from atomic resonance (10 MHz is atom resonance at zero field). When the TOP bias field turns on mid-sequence, the microwave knife frequency also has a discontinuity to account for the change in the resonance frequency of atoms at the bottom of the TOP trap compared to the pure quadrupole trap.

The rotating bias field is generated by two perpendicular pairs of rectangular coils, sandwiched between the large quadrupole coils (Fig. 4.6; see also Ch. 2 of Ref. [88]). The amplitude of the current in each pair oscillates at 2.6 kHz,<sup>6</sup> with the pairs out of phase by 90°. The field magnitude is set by a voltage-controlled attenuator and can reach up to 7 G.

In general, the collision rate of the harmonic trap will be lower than that of a quadrupole or a plugged quadrupole because the lower curvature does not confine the atoms as tightly. As a consequence, we begin the evaporation sequence in the pure quadrupole in part for a larger collision rate and in part because the initial ensemble is larger than the largest circle of death achievable at the high initial quadrupole gradients (410  $\mu$ m initial cloud radius compared to  $r_0 = 320 \mu$ m).

We diabatically turn on the rotating bias field after the first three microwave ramps (the first 6 s of evaporation) and after the decompression of the quadrupole gradient to 109 G/cm (at 4.25 s; see Fig. 4.10 for timing). At the same time, we increase the detuning of the microwaves to accommodate the new, higher-field trap bottom. The

---

<sup>6</sup>The largest atom trapping frequency during evaporation is < 400 Hz, which satisfies the TOP requirement that the atom trapping frequency be much less than the bias field rotation frequency.

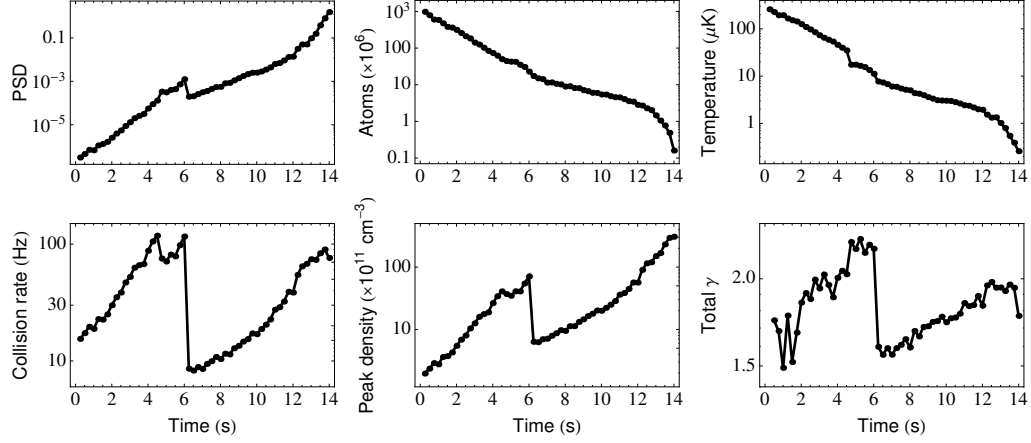


Figure 4.11: Characteristics of evaporation in the TOP trap. The time is defined from the start of the evaporation, after the quadrupole has been ramped up to full current. All parameters are based on images taken after snapping the quadrupole field down from 20.9 G/cm, but are scaled back to the quadrupole field present during evaporation. The gradient is 218 G/cm through 4.25 s and 109 G/cm thereafter. The discontinuity at 6 s arises from the abrupt turn-on of the TOP trap.

turn-on of the bias field must be sudden to minimize the impact of dragging the circle of death through the atom cloud. With an initial bias field of nearly 6 G, the circle of death is at a radius of 550  $\mu\text{m}$ , well outside the cloud size at that time (35  $\mu\text{m}$  before the bias field turn-on; 120  $\mu\text{m}$  after). As a result of the lower curvature of the TOP trap, the collision rate and peak density suffer, leading to an instantaneous drop in the PSD and in the evaporation efficiency  $\gamma$  (Fig. 4.11).

Over the remainder of the evaporation, the rotating bias field is ramped down in a monotonic sweep.<sup>7</sup> Simultaneously, we ramp down the microwave detuning. We adjust the sweeps such that ideally the microwaves, which tend to be more efficient than the circle of death, are responsible for the ejection of hot atoms. In reality, nonlinearities in the response of the voltage-controlled attenuator to the bias field setpoint may result in a trade-off between the dominance of the circle of death and the microwaves. In either case, ramping down the bias field increases the trap frequencies

<sup>7</sup>The bias field setpoint voltage is swept linearly, but nonlinearities in the voltage-controlled attenuator produce the nonlinear sweep seen in Fig. 4.10.

from  $(\omega_\rho, \omega_z) = 2\pi \times (27 \text{ Hz}, 74 \text{ Hz})$  to  $2\pi \times (130 \text{ Hz}, 360 \text{ Hz})$ , thereby improving the collision rate and peak density (Tab. 4.2) and speeding evaporation.

Fits to the final cloud report an atom number of  $2 \times 10^5$  atoms with a PSD of 3, a temperature of 30 nK, and a size of  $(18 \mu\text{m}, 15 \mu\text{m})$  in the radial and vertical dimension respectively. These fits, however, are based on a thermal distribution of atoms that is not strictly appropriate for clouds of such high PSD. They nevertheless can give a good sense for the trends of evaporation, as shown in Fig. 4.11.

An important factor that is overlooked by the thermal model, for example, is the interaction between the atoms in the dense ensemble, characterized by the interaction energy  $E_{\text{int}}$  [94]. For dense clouds, the interaction energy can be larger than the kinetic energy  $E_{\text{kin}}$ , given by the curvature of the wavefunction in the trap. The parameters of the final cloud of Fig. 4.11 yield an order-of-magnitude estimate that favors the interaction energy:  $E_{\text{int}}/E_{\text{kin}} \approx N a/a_{\text{ho}} = 350$ , where  $N$  is the atom number,  $a = 5.77 \text{ nm}$  is the  $^{87}\text{Rb}$  scattering length [94–96],  $a_{\text{ho}} = \sqrt{\hbar/m\omega_{\text{ho}}}$  is a characteristic trap length scale, and  $\omega_{\text{ho}} = (\omega_\rho^2 \omega_z)^{1/3}$  is the geometric mean of the trap frequencies.

In this (Thomas-Fermi) limit, the interaction energy is related to the chemical potential  $\mu$  by  $E_{\text{int}}/N = (2/7)\mu$ . The chemical potential of the ground state is given by

$$\mu = \frac{\hbar\omega_{\text{ho}}}{2} \left( \frac{15Na}{a_{\text{ho}}} \right)^{2/5} \quad (4.2)$$

For the final cloud, the interaction energy evaluates to a temperature of  $(2/7)\mu/k_B = 70 \text{ nK}$  at the evaporation gradient 109 G/cm and a temperature of 8 nK at the imaging gradient 20.9 G/cm, both of which are significant portions of the temperature reported by the thermal fit (300 and 50 nK respectively; the former is scaled from the latter).

The interaction energy in this limit also plays a commanding role in the free expansion of the cloud, as it is rapidly converted into kinetic energy upon release from the trap. For long-drift time interferometry, the release energy is exactly the interesting quantity. It can be directly measured through a time-of-flight experiment where the atoms are permitted to expand ballistically after the magnetic trap is rapidly shut off. Measuring the size of the cloud as a function of the drift time after release from the trap immediately gives the release temperature. After abruptly snapping the

quadrupole strength from the imaging gradient to zero, the time-of-flight temperature is measured to be 19 nK for our deepest evaporation cuts. Thus the 8 nK estimated interaction energy is not so much smaller that it can be easily ignored. Interactions will return as an important concept for matter wave lensing in Ch. 7.

### 4.1.3 Magnetic lensing

The modified delta-kick procedure that comprises the magnetic lens is described in detail in Ch. 7. Briefly, after the final stage of evaporation, the magnetic trap is abruptly transformed into a shallow harmonic trap. Expanding from a near-point source in this new potential, the atom ensemble exchanges velocity width for position width. Once the ensemble reaches its maximum spatial extent – and consequently its minimum momentum extent – the magnetic trap is diabatically turned off ( $< 1\text{ ms}$ ) and the atoms are allowed to freely fall. Depending on the depth of the final evaporation cut, this produces clouds with temperatures ranging from 3 to 50 nK.

### 4.1.4 State preparation

We prepare the atoms in a magnetically insensitive Zeeman sublevel to reduce the sensitivity of the interferometer to background magnetic fields. A pulse of microwaves from the same microwave apparatus used for evaporation transfers the atoms from  $|F = 1; m_F = -1\rangle$  to  $|F = 2; m_F = 0\rangle$ . For this pulse to be efficient across the entire cloud we must have a well-defined bias field and a low gradient. The former lifts any degeneracy between the Zeeman sublevels; the latter ensures that the cloud experiences the same detuning across its entire spatial extent.

The  $110\ \mu\text{s}$   $\pi$  time of the microwaves corresponds to a bandwidth of approximately 10 kHz, demanding a bias field much greater than 15 mG. Given the cloud size of  $\sim 100\ \mu\text{m}$ , the gradient must be much less than 1 G/cm. In addition, changes in the field value during the pulse duration must be small ( $\ll 1\text{ G}$ ) to prevent detuning from the microwave resonance. Yet the snap off of the quadrupole field at the end of the magnetic lensing stage induces strong eddy currents in the steel vacuum chamber. These eddies persist for  $\sim 50\text{ ms}$  and can generate decaying gradients of 10 G/cm,

requiring that we wait to achieve the necessary quiet field environment.

After 60 ms (during which the atoms have fallen  $< 2 \text{ cm}$ ), the field is sufficiently constant to allow reasonably efficient state preparation. The applied bias field combined with the residual field amounts to 700 mG, sufficient to distinguish the magnetic sublevels. To accommodate the inhomogeneities in the field that remain, we have found experimentally that a small, 10 kHz sweep of the microwaves across the resonance and an increase in the pulse time to 155  $\mu\text{s}$  improves the fraction of atoms transferred.

As the atoms have fallen out of the line of sight of the absorption imaging system, we launch the atoms into the fluorescence detection region – discussed further in Sec. 4.3 – to detect the transfer efficiency into the desired state. We can apply a blow-away pulse, a 70  $\mu\text{s}$  pulse resonant with the  $|F = 1\rangle \rightarrow |F' = 0\rangle$  transition, to selectively scatter atoms remaining in the  $|F = 1\rangle$  state. When applied, the  $|F = 1\rangle$  atoms are effectively eliminated from the final image. By comparing images of clouds with and without this pulse, we determine that we can prepare 75% of the initial cloud in the targeted magnetically state.<sup>8</sup> Prior to an interferometer sequence, we typically apply this blow-away pulse in order to purify the state of imaged cloud.

#### 4.1.5 Launching

We launch the atoms from the 3D MOT chamber into the interferometer region using an optical lattice (Fig. 4.12).<sup>9</sup> The pair of beams that form the lattice enter the chamber parallel to each other, but separated by 2.5 beam waists. These are retroreflected by the mirror at the bottom of the apparatus. As the beams are aligned at a 2 mrad angle from the vertical axis, one beam intersects the atoms on the way towards the retroreflection mirror, whereas the other does so after reflection.

If the beams instead were perfectly collimated and retroreflecting, they would form two lattices that travel in opposite directions. When the atom and lattice velocities are near zero, the two lattices compete and the atoms can be split between the two

---

<sup>8</sup>This efficiency holds for the colder, 3 nK source. The 50 nK source tends to be less efficient, possibly due to its larger initial spatial extent and therefore its greater magnetic inhomogeneity.

<sup>9</sup>See Ref. [88] for a detailed analysis of the lattice performance and a discussion of the benefits of blue detuning.

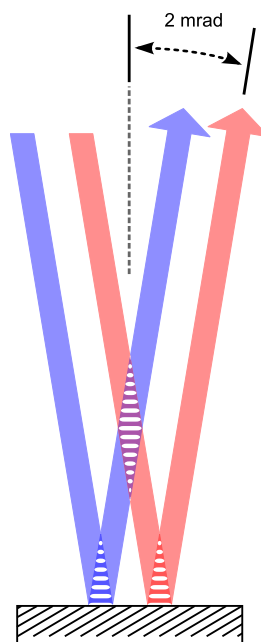


Figure 4.12: Alignment of the lattice launch beams. Both beams enter at a slight angle to the interferometer beam axis, as shown. The region of overlap, which extends vertically approximately 75 cm, is aligned to coincide with the location of the atoms at the end of the cooling stages. To launch the atoms the full height of the tower at 59 g requires 24 cm of travel in the lattice, well within the available overlap.

directions. At non-zero velocities, one of the two lattices is detuned, but it continues to contribute to the spontaneous emission rate. In the W configuration we adopted, the effect of the parasitic lattice is highly suppressed. It will neither compete for atoms nor contribute to spontaneous emission.

Eliminating the parasitic lattice also opens the possibility of a significant suppression of scattering rate through the use of blue-detuned beams. In the blue lattice, the atoms are confined to the low-intensity nodes of the electromagnetic potential and experience a comparatively lower scattering rate than in a red lattice of similar detuning. We typically operate with a lattice detuning of 90 GHz blue of the  $|F = 2, m_F = 2\rangle \rightarrow |F' = 3, m_F = 3\rangle$  cooling transition.

Each of the two laser beams required by the lattice are generated by an intensity-locked tapered amplifier (TA) seeded with light from a double-passed AOM, which permits the beam's frequency to be independently tuned over  $> 60$  MHz. The beams, which have perpendicular linear polarization, are combined into a single fiber, ensuring that the pair are copropagating with the same mode size prior to entering the final delivery optics.<sup>10</sup> These final optics include pickoffs for independent intensity stabilization, a polarization-dependent calcite walk-off crystal to offset one beam from the other while maintaining a high degree of parallelism, and a heated rubidium vapor cell to suppress atom scattering from on-resonance amplified spontaneous emission of the TAs.

Figure 4.13 shows the event sequence required to launch the atoms. We adiabatically turn up the lattice over 10 ms to a depth of  $40E_{\text{rec}}$ , where  $E_{\text{rec}} = (\hbar k)^2 / 2m$  is the atom's recoil energy. During this interval, we sweep the frequency (via the DDS that controls the AOM frequencies) of one of the lattice beams while the other remains constant, such that the lattice nodes fall with the atoms.

In the next 5 - 30 ms (depending on the launch height), we accelerate the atoms at an average acceleration of  $59 g$  until the desired launch velocity is reached. The total velocity imparted by the lattice is constrained to be in multiples of two photon recoils (11.8 mm/s) in order to prevent projection of the atoms into the  $\pm 2\hbar k$  lattice

---

<sup>10</sup>By coupling both beams through a single fiber rather than two independent fibers, we have gained excellent alignment stability at the expense of beam cross-talk. Due to polarization wander in the shared fiber, intensity cross-talk between the beams is  $\sim 1\%$ .

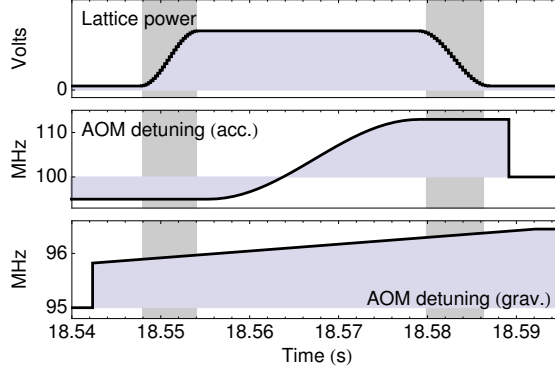


Figure 4.13: Timing of the lattice launch. From top to bottom, the plots show the lattice beam intensity as measured by a photodetector, the detuning of the AOM responsible for acceleration, and the detuning of the AOM responsible for falling with gravity. Note that these AOMs are double-passed, so the actual detuning of the light is twice what is shown here. The grey bars identify the adiabatic ramp up and ramp down of the lattice intensity. Between the grey bars, the atoms are accelerated.

momentum states. In the freely-falling frame, frequency sweeps guide the atoms' velocity in a profile that has smooth acceleration as well as smooth higher derivatives. The mathematical form is the first quarter period of  $[1 - \cos(x)]$ .

Once fully accelerated, we reverse the adiabatic turn-on procedure. The frequency of one lattice beam is kept constant while the other is swept to fall with gravity. At the same time, the intensity of the beams is adiabatically ramped down over 10 ms. With this sequence, we are able to launch a cloud of atoms the full height of the tower with good efficiency ( $> 75\%$ ) in preparation for long-time interferometry.

## 4.2 Atom optics

Driving efficient atom optics transitions places several demands on the lasers used. Not only must the counterpropagating beams have the appropriate frequency and polarization, they must also have low phase and frequency noise, a uniform wavefront and a uniform and stable intensity. In addition, the beams must compensate for the AC Stark shifts imparted by their own intensity, and they cannot induce too much

spontaneous emission, which reduces the number of atoms in the interfering ensemble. Each requirement will be addressed in turn prior to delving into the details of the two implementations. Elaboration specific to large momentum transfer interferometry, in particular with respect to AC Stark shifts and spontaneous emission, will be addressed in Ch. 9.

### 4.2.1 Frequency

Simply to be on resonance with the desired Raman transition, the frequency difference between the two beams must include the 6.834 GHz microwave transition, the recoil shift, the Doppler shift, and any residual AC Stark shift that is not otherwise compensated (Eqs. 3.4 and 3.11). The sign of the Doppler shift contribution to the Raman pair frequency difference plays a large role in whether the launched  $|F = 2, m_F = 0\rangle$  atoms absorb a downwards or an upwards photon first, imparting a net downwards or upward momentum.

The Doppler shift may sometimes be more conveniently addressed when broken into inter-pulse and intra-pulse contributions. With our large launch velocities, the Doppler shift over the course of the interferometer spans  $k_{\text{eff}}\Delta v/2\pi = 67 \text{ MHz}$ . But the interferometer pulses themselves are no more than 0.5 ms, for a frequency shift of  $< 15 \text{ kHz}$ . It is possible, therefore, to use one actuator to enact the large hops between pulses, and a second for a fine frequency ramp during the pulse.

For very short pulses ( $< 50 \mu\text{s}$ ), a fine scan during the pulse is unnecessary: the atoms' velocities do not change by much relative to the pulse bandwidth in the short interval. But as the pulses increase in duration and their linewidth narrows, it becomes important to track the changing Doppler shift through the pulse. In a  $100 \mu\text{s} \pi$  pulse, for example, the Doppler shift will change by 2.5 kHz, a significant amount relative to the 10 kHz FWHM linewidth of the transition. Depending on the capabilities of the available actuators, the sweep in frequency during the pulse may be implemented either with the same device that performs the discrete, inter-pulse hops, or with an independent actuator. We employ both options below.

To mitigate laser phase and frequency noise, we use beams of narrow linewidth. If

the instantaneous linewidth of the laser is broad, then the imprinted phase will vary from atom to atom as the wavefront is blurred by the different frequencies contained. But even if the instantaneous linewidth is extremely narrow, the frequency must be stable over each interferometer pulse, if only to stay on resonance. For example, a square pulse of length  $100\ \mu\text{s}$  has a linewidth of  $10\ \text{kHz}$ . For decent transfer, the frequency jitter should be  $\ll 1\ \text{kHz}$  in magnitude during the pulse, requiring a linewidth of no more than  $100\ \text{kHz}$  over  $1\ \text{s}$ . As an additional constraint, the upwards going beam has been retroreflected, and so travels approximately  $10\ \text{m}$  further than the downwards going beam. For an absolute measurement to be precise to the milliradian level, the coherence length of the beam must therefore be  $< 5\ \text{kHz}$ . Eventually, the wavepacket separation also demands a certain minimum linewidth: with meter-scale wavepacket separations, the light travel time between the two arms demands a coherence length of  $< 50\ \text{kHz}$ . Taken together, these demand a linewidth of no more than a few kilohertz.

### 4.2.2 Polarization

The polarization of the counterpropagating beams can be  $\sigma_+ - \sigma_+$ ,  $\sigma_- - \sigma_-$ , or  $\text{lin} \perp \text{lin}$  to drive velocity-selective Raman transitions. We have chosen the circularly-polarized option both for convenience (the 3D MOT also requires circular polarization) and for future considerations (Bragg transitions can be driven by the same circular polarizations, but would require  $\text{lin} \parallel \text{lin}$ ). Note that due to our retroreflection configuration, the pair of *copropagating* beams that enter the vacuum chamber have opposite circular polarization. The  $\lambda/4$  waveplate above the retroreflection mirror reverses the polarization of the beams, resulting in two pairs of *counterpropagating* beams of the same polarization. One of the two pairs is, in general, detuned from resonance by the Doppler shift, and therefore does not conflict with the transition excited by the other pair.

### 4.2.3 Wavefront and intensity homogeneity

For a homogenous interferometer phase across the ensemble, the wavefront of the interferometer beams must be uniform across the ensemble. Except at zero temperature,

the atoms within the ensemble move across the beam and sample different portions of the beam's wavefront at each of the three pulses in the standard Mach-Zehnder sequence. A nonlinear variation in the wavefront results in atoms of different initial position and transverse velocity imprinting different laser phase and acquiring different total interferometer phase. While we take advantage of this effect to propose a method to measure the beam's wavefront in Ch. 5, in general such wavefront variation leads to interferometer contrast loss when the atom population ratio is averaged across the image of the output ports.

To control our wavefront, we use the largest beams supported by our 10 cm diameter vacuum chamber. A 2 cm  $1/e^2$  radial waist not only has a very long Rayleigh range so that it will not diverge over the 20 m total propagation distance inside the chamber, but it also is small enough that the 10 cm aperture creates less than 1% ripple in the laser wavefront. As a general principle, we also strive to introduce as few optics as possible between the exit of the interferometer beams from their final single-mode optical fibers and their entrance into the vacuum chamber.

The large beam size also presents a uniform intensity to the ensemble. A perfect transfer of an atom from one state to the other calls for a pulse area of precisely  $\Omega t = \pi$ , with the Rabi frequency  $\Omega$  and a pulse time  $t$ . Spatial variations in the intensity result in a perfect  $\pi$  condition for certain atoms, and a less-than-perfect transfer for those where the intensity, and therefore  $\Omega$ , are lower or higher.

In a Gaussian beam, the intensity profile itself presents such a spatial variation, and a beam that is much larger than the size of the ensemble alleviates the inhomogeneity. For our 3 nK clouds, the final  $< 2$  mm  $1/\sqrt{e}$  radius is sufficiently small that the intensity variation is less than 2% for most of the atoms. It is also worth noting that the intensity variation is more important for the  $\pi/2$  pulses, where the effect is linear, than for the  $\pi$  pulses, where the effect is quadratic. Thus, any inhomogeneity is suppressed for the majority of the pulses of a sequential-Raman LMT interferometer, where the acceleration and deceleration are performed by  $\pi$  pulses (Ch. 9).

It is also possible to use adiabatic rapid passage [97–100] or composite pulses [101, 102] to improve the insensitivity to intensity inhomogeneities. The cost is an increase in the number of spontaneous emission events, discussed below, as a result of

the longer pulse areas.

Just as the spatially uniform intensity serves to maintain good transfer from position to position, locking the laser intensity serves to maintain good transfer from pulse to pulse. We lock the intensity to better than 1%.

#### 4.2.4 AC Stark shifts

The intensity of the beams can lead to AC Stark shifts that alter the resonance frequency of the transition. If the beam is far-detuned so that the detuning  $\Delta$  is much larger than any of the hyperfine splittings, the Stark shift of the  $m_F = 0$  Zeeman sublevel of either the  $F = 1$  or  $F = 2$  states is

$$\Delta_{\text{AC}} = \frac{I\Gamma\lambda^3}{8c\pi^2\hbar\Delta} \sim \frac{I}{\Delta}, \quad (4.3)$$

where  $I$  is the beam intensity,  $\Gamma$  is the natural linewidth, and  $\lambda$  the wavelength. For  $m_F \neq 0$ , the prefactor 1/8 changes but the scaling remains the same. A beam that is blue-detuned ( $\Delta > 0$ ) will shift the ground state energy higher, while a red-detuned beam ( $\Delta < 0$ ) does the opposite.

In the case of a two-photon Raman transition, there are two ground states under consideration. A beam containing a single frequency will in general shift both ground states of the atom by different amounts depending on the relative detuning from each state and the oscillator strength of each transition. This results in a net shift in the energy difference between the two ground states, shifting the (microwave) transition resonance frequency. A beam detuned red or blue of both ground states (assuming roughly equal oscillator strength, as is the case for  $^{87}\text{Rb}$ ) will increase the microwave resonance frequency, whereas a beam in between will reduce it. A uniform intensity across the cloud can make this shift the same for all atoms in the ensemble, and a stable intensity can keep the shifted resonance stable, but it is often preferred to suppress the effect by carefully choosing the intensity and/or the frequency content of each of the interferometer beams to cancel the relative AC Stark shift.

Performing this cancellation requires at least one beam between the two ground states and at least one outside. For example, suppose the two-photon transition is

driven by a pair of (counterpropagating) single-frequency beams. One beam is detuned to be midway between the  $F = 1$  and  $F = 2$  states ( $\Delta \sim 2\pi 3.4 \text{ GHz}$ ), and the other is  $2\pi 6.8 \text{ GHz}$  to the red ( $\Delta \sim -2\pi 3.4 \text{ GHz}$ ). The differential AC Stark shift is zero when the latter has three times the intensity of the former.

Maintaining the AC Stark compensation through the intensity balance of independent beams demands stable intensity, stable beam alignment, and an excellent beam mode match. While all are possible, they become increasingly difficult to meet for the large momentum transfer interferometers, which are naturally more sensitive to small degradations in transfer efficiency.

A single multi-frequency beam, however, can cancel its own AC Stark shift. In this scheme, a beam is modulated to produce the necessary spurs of the appropriate relative strengths. Given a maximum available laser power, adding frequency content reduces Rabi frequency since the extra spurs must not drive transitions with the same atoms (which would complicate interferometry). Nevertheless, this method significantly relaxes the demands on the matching of intensity, alignment and mode.

In particular, by applying phase modulation to a beam such that the carrier lies between the two transitions and the sidebands lie outside, the differential AC Stark shift can be canceled with the appropriate choice of modulation strength. Moreover, the proper choice of carrier frequency (approximately midway between the transitions), can lead to a cancellation of the absolute AC Stark shift of each transition independently. Canceling the absolute AC Stark shift is advantageous when the two halves of the atomic wavepacket experience different intensity profiles. This consideration is more critical for LMT interferometry, where the two halves are separated by a large enough distance for beam diffraction effects to become important, and will be discussed further in Ch. 9.

Whether the relative AC Stark shift is compensated through independent-beam intensity balance or single-beam phase modulation,  $\sim 2\pi 3.4 \text{ GHz}$  is the maximum overall interferometer detuning possible when the necessary compensation frequency between  $|F = 1\rangle$  and  $|F = 2\rangle$  participates in the Raman transition. The detuning can be much higher in the single-beam phase modulation scheme if the Raman transition is driven by sidebands. The ability to achieve large detunings is a critical tool when

striving to reduce the impact of spontaneous emission.

#### 4.2.5 Spontaneous emission

Each spontaneous emission event causes the decoherence of an atom in the ensemble. Careful baffling of the apparatus and shuttering of the lasers prevents stray light from exciting the atoms, but scattering from the interferometer beams themselves is impossible to avoid completely. For interferometers where the drift times are short ( $t \ll m\sigma/\hbar k$ , where  $\sigma$  is the cloud size), spontaneous emission results in a loss of contrast: atoms that have scattered a photon are still present within the cloud width and act as an incoherent background. But because of our long drift times, recoil from spontaneous emission early in the interferometer sequence causes decohered atoms to expand out from the rest of the ensemble. They become so dilute as to contribute very few counts to each pixel of the final image, and we detect the spontaneous emission rate as a loss of atom number.

The scattering rate must therefore be made sufficiently low to prevent the complete decoherence (or disappearance) of the ensemble. For a simple two-photon-recoil interferometer, the effect of spontaneous emission is small: above 8 GHz modulation, fewer than 10 % of the atoms scatter a photon (see Fig. 9.4). For large momentum interferometry, however, the number of optical pulses applied to the atoms increases linearly with the momentum separation desired. As a result, the choice of large momentum separation or large atom number must be a compromise, and it will be explored more thoroughly in Ch. 9.

#### 4.2.6 Implementation

We have implemented two schemes for generating the necessary power for the atom optics beams. One is based on TAs locked to a high-finesse cavity, while the other is a higher power scheme, based on 1560 nm light doubled to 780 nm in a nonlinear crystal. The former is used for the work on precision rotation sensing and interferometer readout development, while the latter is used for studying large momentum transfer interferometry because of its lower rate of spontaneous emission.

### Tapered amplifier system

The power for the atom optics comes from the same two 1 W TAs used for the lattice beams. The seed light for the TAs derives from the same optical elements that generate the light for the MOT. During interferometry, however, the repump light is blocked by a shutter and all frequency modulation to generate the cooling sideband is switched off, leaving the beam at a single frequency as it enters the optics box at the top of the tower. Unlike the lattice, however, where this light is shifted by a double-passed AOM for both TAs, the undiffracted beam from the AOM of one TA is picked off and sent through a fiber phase modulator (see Fig. 5.20 of Ref. [86] for a schematic). The phase modulator applies the 6.8 GHz sideband necessary to drive a Raman transition. The modulated light is recombined with the TA’s input path. The seed of the second TA remains the same as for the lattice, shifted by the double-passed AOM. This not only breaks the degeneracy between the blue and red sidebands of the phase modulator, but it also allows for dynamic control of the relative phase and frequency between the two beams, useful for scanning the interferometer phase and compensating for the Doppler shift from gravity.

For interferometry, the output of the TAs follows the same path as the MOT beam. A fiber serves to clean the spatial mode, and an intensity lock on the output of the fiber stabilizes drifts in coupling. The two paths are then combined on a polarizing beam splitter and the copropagating beam passes through the 200 MHz AOM that acts as a rapid switch for the short ( $< 100 \mu\text{s}$ ) pulses. A final  $\lambda/4$  waveplate converts the linearly polarized light into  $\sigma_+$  and  $\sigma_-$  circularly polarized light. They are then expanded to a 2 cm  $1/e^2$  radial waist.

Since the interferometer light is pulled from the MOT beam path, the frequency stability is set by the frequency stability of the master laser. Unlocked, this ECDL has a linewidth of 500 kHz in about 1 s, although the instantaneous linewidth is likely much narrower. To improve the frequency stability, we converted the laser lock from one that locks only to a rubidium vapor cell through saturation-absorption spectroscopy, to one where the laser is locked to a narrow linewidth cavity, which is itself then locked to the rubidium in the vapor cell. This zerodur cavity, described in Ch. 2 of Ref. [103], has a half-width half-maximum linewidth of  $2\pi \times 3.7 \text{ kHz}$ . After folding in

the external cavity lock, the linewidth of the interferometer laser falls to  $< 1 \text{ kHz}$ .

The detuning is also set by the master laser. The unmodulated beam is 1 GHz blue of the  $|F = 2\rangle \rightarrow |F' = 3\rangle$   $^{87}\text{Rb}$  cooling transition. Situated as it is between the  $|F = 1\rangle$  and  $|F = 2\rangle$  manifolds, the AC Stark shift of this frequency tends to slightly reduce the frequency difference needed to make the transition. The beam that passes through the phase modulator, however, has additional frequency content red of  $|F = 2\rangle$  and blue of  $|F = 1\rangle$ . The relative height of the carrier and the sidebands is chosen to slightly increase the same frequency difference. We can then choose the intensity ratio between the modulated and unmodulated beams such that the two effects cancel. We are able to suppress such shifts to  $< 2 \text{ kHz}$  on a pulse of width  $> 10 \text{ kHz}$ .

With only 1 GHz detuning from the  $|F = 2\rangle$  state and with no filter to absorb the TAs' amplified spontaneous emission, the spontaneous emission rate of these interferometer beams is quite high. After just  $17 \pi$  pulses, approximately equivalent to an  $8\hbar k$  interferometer, a third of the atoms remain. Since increasing the detuning demands more laser power than can be supplied by the TAs, we developed the doubled 1560 nm system that can deliver several watts at 780 nm.

### High power, doubled 1560 nm system

The generation of up to 7 W at 780 nm in this scheme begins with a 1560 nm RIO laser (RIO0165-5-01-1-H6) [Fig. 4.14(a)]. This seed light is split into two paths for the two interferometer beams. Independent fiber phase modulators apply sidebands in the 30-40 GHz range.<sup>11</sup> The phase modulators are independently driven by a 0.1-10 GHz stable frequency reference (Phase Matrix FSW-0010, externally referenced to the Oscilloquartz OCXO 8607-BGE low phase noise 10 MHz source) which is quadrupled and amplified. A voltage-controlled attenuator allows for control of the modulation depth.

Each path is amplified by a 30 W fiber amplifier (IPG Photonics EAR-30K-1550LP-SF). The high-power beam is focused through a periodically-poled, lithium niobate

---

<sup>11</sup>A previous iteration allowed sidebands from 0 to 10 GHz. In that version, the Phase Matrix sources were not quadrupled.

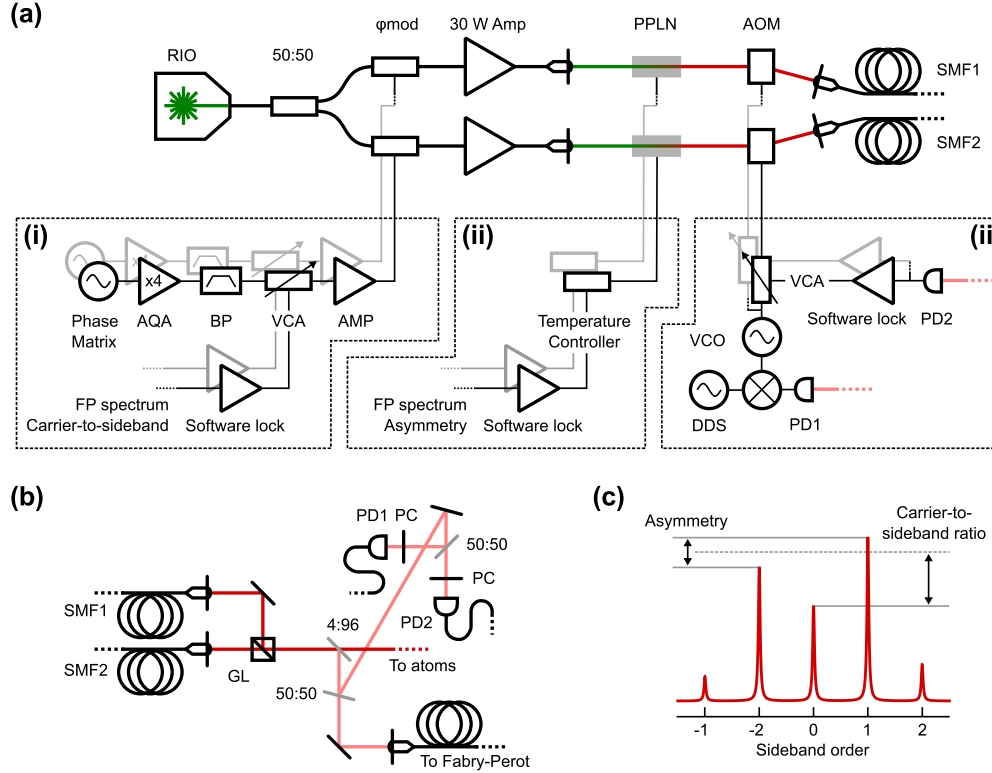


Figure 4.14: Schematic of the high power, frequency-doubled atom optics system. (a) The high-power beam path, from the 1560 nm seed laser (RIO) through the 30 W amplifiers, the doubling stage (PPLN) and the AOM switches. (i) Frequency chain for the phase modulators ( $\phi_{mod}$ ), including the quadrupling stage (AQA: amplifier-quadrupler-amplifier), the actuator for the lock on the modulation depth (VCA: voltage-controlled attenuator), and a final high-power amplifier (AMP: amplifier). The signal for the modulation depth lock comes from the measured Fabry-Pérot (FP) spectrum. (ii) The asymmetry of the sidebands is used to adjust the temperature of the PPLN crystals, moving the doubling efficiency envelope. (iii) Frequency chain to control the AOM switches, including the fast phase lock based on the beatnote measured by a photodetector (PD1) and the slow intensity lock based on the amplitude measured by another photodetector (PD2). (b) Optical path for phase and intensity feedback signals. The 4:96 beam sampler reflects approximately 4% of the incident light. The polarcor (PC) before PD1 is necessary to create the beatnote; the PC before PD2 simply balances the power from each path incident on the photodetector. (c) Simulated trace from a Fabry-Pérot cavity. BP: band pass filter. GL: Glan-laser polarizer. 50:50: non-polarizing beamsplitter, 50% reflection, 50% transmission.

(PPLN) crystal (Covision MSHG1550-1.0-40), which doubles the laser frequency (see Appendix B for details of the doubling process). The efficiency of the doubling grows quadratically with the input power. At full 1560 nm power, the system can produce up to 7 W at 780 nm. In general, we operate below full power to allow headroom for long-term aging. Further losses through the AOMs and fibers that follow reduce the output to 3 W per beam at the atoms.

After the doubling stage, each path passes through an AOM, whose modulation frequency is centered about 80 MHz.<sup>12</sup> One path is blueshifted while the other is redshifted, which breaks the degeneracy of the red and blue first-order sidebands.<sup>13</sup> With 160 MHz separation of the carriers, larger than the maximum 70 MHz relative Doppler shift of the free-falling atoms, only one pair can ever be resonant with the transition. These AOMs also serve as the fast (microsecond level) optical switches that define the pulse duration.

The output of the AOMs are coupled into a pair of fibers, which carry the light into the beam delivery enclosure at the top of the apparatus. In this enclosure, the two paths are collimated by a matched pair of fixed fiber collimators with an output size of 1.15 mm  $1/e^2$  radial waist. They are combined with perpendicular polarizations into a co-propagating beam by a Glan-Laser polarizer (Thorlabs GL15-B), chosen for its excellent polarization properties (extinction of  $10^5:1$ ). This co-propagating beam is launched into the interferometer vacuum tube through a  $\lambda/4$  waveplate (aligned to give < 2% polarization impurity) and a large expansion telescope, which gives the final radial waist of 2 cm.

Compensation for the Doppler shift over the course of the interferometer is performed in two stages. The bulk of the 70 MHz range is accommodated by the Phase Matrix frequency of one of the paths, which can be changed discretely every  $\sim 2$  ms. A fine sweep of the AOMs' frequency accounts for the changing Doppler shift during the short pulses. As this sweep is typically no more than a few kilohertz, it is well

---

<sup>12</sup>The MOT z-axis beam is coupled through the 0<sup>th</sup> order path of one of the two AOMs. An independent shutter blocks this light during interferometry.

<sup>13</sup>If both red and blue pairs were to drive the transition, the two could interfere, causing a position-dependence of the Rabi frequency at a spatial scale of  $c/(2\Delta\nu)$ , where  $\Delta\nu$  is the frequency difference between the mean frequency of each Raman pair.

within the bandwidth of the AOMs and does not strongly affect their coupling into the fibers.

The frequency content, intensity, and differential phase of the interferometer beams are all locked using light from a beam sampler in the path of the co-propagating beams [Fig. 4.14(b)].

A portion of the light is fiber coupled and its frequency content is analyzed after every experimental cycle by a Fabry-Pérot cavity (free spectral range of 3 GHz; Coherent). The spectrum of each path is acquired sequentially by a digital scope (Clever Scope CS328A). We identify the carrier and both first-order sidebands and determine the modulation depth and asymmetry [Fig. 4.14(c)].<sup>14</sup> The modulation depth is characterized by the ratio of the carrier height to the mean of the first-order sideband heights. The asymmetry is characterized by the fractional difference in height of the two first-order sidebands. We use the former to feed back on the control pin of the voltage controlled attenuator in the RF chain of the phase modulators [Fig. 4.14(a)(i)], and we use the latter to adjust the temperatures of the PPLN crystals [Fig. 4.14(a)(ii)]. These slow loops control for the effect of a drifting ambient temperature. The carrier-to-sideband ratio can be controlled to 3%, and the asymmetry to 2%.

The remainder of the light is split into two. One half is used to measure sequentially the intensity of each path at the end of the interferometer sequence, and feed back on the voltage controlled attenuator in the RF chain of the AOMs [Fig. 4.14(a)(iii)]. This slow loop controls thermal drifts in the fiber amplifier output power and beam coupling to 1% or better.

The other half is used for a fast lock to cancel the phase difference accumulated between the two interferometer beams while propagating on their different paths between the RIO and the Glan-Laser combiner. The light is incident on an amplified photodetector to measure the beatnote during each interferometer pulse. This beatnote is mixed with a DDS reference frequency [Fig. 4.14(a)(iii)], and the resulting error signal is used to adjust the frequency and phase of the voltage-controlled oscillator

---

<sup>14</sup>Note that unlike in the figure, the finite free spectral range of the Fabry-Pérot will cause the 30 GHz sidebands to wrap multiple times. As a result the measured spectrum will not show even spacing between the first and second order sidebands.

that powers the AOMs. The phase lock exhibits an excursion of a few radians in the first  $10\ \mu\text{s}$ , but the residual phase noise once locked is  $< 200\ \text{mrad}$ .

#### 4.2.7 Atom optics optimization

For each interferometer pulse, we must find the Raman resonance condition and the Rabi frequency. This is done with a pair of measurements. First, we take a series of experimental shots, each with a different two-photon detuning. The pulse time is constant throughout, and is typically chosen to be less than a  $\pi$  pulse ( $\tau \leq \pi/\Omega$ ). Peak population transfer occurs at the resonance condition.

After finding the resonance frequency, we determine the Rabi frequency. While on resonance, we take a second series of experimental shots where we scan the pulse time. With no decoherence or inhomogenous broadening, this Rabi flop should be sinusoidal. Inhomogenous broadening, which can come from spatially dependent Rabi frequency or detuning, among other sources, causes the flop to decay at the longer pulse times. The duration of the  $\pi$  pulse is chosen to be the time at which the population transfer is at a maximum; the duration of the  $\pi/2$  pulse is the time at which the population transferred is half the maximum. Due to microsecond scale delays in the pulse turn-on time, the duration of the  $\pi/2$  pulse may not be exactly half that of the  $\pi$  pulse.

The Rabi frequency determines the velocity selectivity of the pulses. The HWHM of the transfer efficiency of a square pulse as a function of detuning is approximately  $\Omega$ , corresponding to a velocity of  $\Omega/k_{\text{eff}}$ . A cloud with this RMS velocity spread would experience a maximum transfer of 55%, decreasing as the inverse of the velocity spread. To get a transfer of  $> 99\%$  ( $> 90\%$ ), the velocity spread must be  $< \Omega/k_{\text{eff}}/10$  ( $< \Omega/k_{\text{eff}}/3$ ).

To be more concrete, consider a cloud with a velocity width that is a certain fraction  $f$  of the recoil velocity  $v_{\text{rec}}$ . Since the Doppler shift of this velocity is  $k_{\text{eff}}v_{\text{rec}}f = 2\pi \times 15 \times f\ \text{kHz}$ , a transfer of 99% (90%) would require the  $\pi$  time to be  $< 3.3/f\ \mu\text{s}$  ( $11/f\ \mu\text{s}$ ). For our typical 3 nK clouds ( $f = 1/10$ ), this implies a  $\pi$  time of  $< 33\ \mu\text{s}$  ( $110\ \mu\text{s}$ ).

When the available Rabi frequency is insufficient compared to the cloud velocity

width, we benefit by first performing a low-intensity, velocity selective  $\pi$  pulse followed by a blow away of the non-transferred atoms to clear them from the image.<sup>15</sup> The atoms remaining are now better contained within the velocity acceptance of the higher-intensity interferometer pulses, improving the transfer efficiency of each pulse as well as the interferometer contrast. In addition, this procedure clears any atoms that launched in the higher-order lattice bands, which otherwise might overlap with the interferometer output ports.

To cancel the AC Stark shifts, we take two Raman resonance scans at different interferometer beam powers. If we are compensating with the intensity ratio between the two beams, then we compare a scan where both beams are at full power to one where both beams are at half power. If we are instead performing single-beam compensation with the phase modulation depth, we compare a scan where both beams are at full power to a scan with one (but not both) at half power. In either case, the intensity ratio or modulation depth that balances the AC Stark shifts leaves the resonance insensitive to the applied power change.

With these calibrations in place, creating an atom interferometer is then a matter of applying the necessary sequence of pulses. Examples of two-photon Mach-Zehnder interferometry and a discussion of the image analysis procedure can be found in Ch. 5 and 6 (e.g., Fig. 5.4).

### 4.3 Fluorescence detection

We image the atoms in the detection region located between the 3D MOT chamber and the bottom of the magnetic shield. Four large (4 in diameter aperture) windows provide good optical access. Two CCD cameras (Photometrics Quantix 6303E) pointing in orthogonal directions allow imaging along two axes.

The CCDs are  $3072 \times 2048$  pixels in size, where each pixel is  $9\text{ }\mu\text{m}$  on a side. The compact, three-lens imaging system has a magnification of 2.7, measured by comparing the imaged distance between two ensembles separated by two photon recoils after a

---

<sup>15</sup>As the velocity-selective pulse transfers atoms from  $|F = 2\rangle$  to  $|F = 1\rangle$ , the blow away is performed with a short ( $2\text{ }\mu\text{s}$ ) pulse resonant with the  $|F = 2\rangle \rightarrow |F' = 3\rangle$  cycling transition.

known drift time  $t_D$  to the expected distance  $2v_{\text{rec}}t_D$ .<sup>16</sup> The imaging system includes an interference filter centered around 780 nm with a FWHM transmission bandwidth of 10 nm (Edmund Optics, NT65-239). This filter, along with careful baffling, significantly reduces the background signal from ambient light. The predominant source of background light incident on the CCD is the scattering of the imaging light itself off the vacuum chamber.

The two interferometer output ports can be imaged simultaneously if they are spatially separated by more than the cloud width. Such simultaneous detection allows for the normalization of the population ratio by the total atom number, which reduces systematic error in the extracted population ratio from atom number fluctuations. Interferometers with  $\gtrsim 1$  s drift time after the final beamsplitter pulse naturally create this separation due to the momentum difference between the ports. For those interferometers with insufficient drift time prior to imaging, we apply an optical pulse to push the atoms in the  $|F = 2\rangle$  state with a few tens of photons, separating the ports in  $\lesssim 200$  ms. This pulse is resonant with the atoms in the freely falling frame, and so is usually detuned by  $kv/2\pi = 16$  MHz, where  $v$  is 12 to 13 m/s.

Prior to imaging, we repump the atoms in the  $|F = 1\rangle$  state, as most of the imaging power is resonant with the  $|F = 2\rangle$  atoms. As a result, we simultaneously image both interferometer output ports, which otherwise would contain  $|F = 1\rangle$  atoms in one of the two output ports.

The imaging light derives from the 3D MOT beam path. We pulse the  $z$ -axis MOT beams for 1 - 5 ms, with both repump and cooling frequencies present. The cooling light is close-detuned, only 2 MHz red of the transition. Like in a MOT, the repump returns atoms that fall into the  $|F = 1\rangle$  state back up into the  $|F = 2\rangle$  state, significantly increasing the average number of photons scattered per atom. Also like in a MOT, the imaging beam brings the cloud almost to rest. Without this deceleration, the ensemble would traverse the entire field of view of the imaging system in less than the 5 ms pulse duration, generating a low-intensity streak of counts. Instead, we detect a well-localized cloud with well-preserved spatial information. We take advantage of this spatial resolution to detect a spatial population modulation from a transverse

---

<sup>16</sup>See Ref. [88] for a diagram of the three-lens system.

phase gradient across the cloud (see Sec. 5 and Sec. 6).

The imaging pulse strongly affects the cloud shape (Fig. 4.15). While any particular image shows the atom distribution integrated over the imaging duration, we can infer the distribution at a particular time by subtracting two images with nearly identical imaging durations, normalized by peak height. For example, the distribution after 5 ms of imaging duration is found by subtracting an image taken with a 4.5 ms duration from one taken with a 5 ms duration.

Because the imaging beam consists of retroreflected, red-detuned light, it might be expected that the effect of the imaging beam on the cloud distribution could be described by optical molasses theory [104]. As a function of imaging duration  $t$ , however, the measured ensemble width grows nearly linearly in the transverse dimension (scaling as  $t$ ), and very slowly if at all in the vertical dimension (scaling as 1) [Fig. 4.16(a) and (b)]. This is inconsistent with the predictions in an optical molasses, where the random walk associated with absorption and isotropic spontaneous emission would predict the transverse RMS velocity to scale as  $t^{1/2}$  and the transverse size to scale as  $t^{3/2}$ . The comparable scalings for the vertical RMS velocity and size would be 1 and  $t$  respectively.

Moreover, the measured transverse growth and the vertical size are not so large as to overwhelm the expected effect of the molasses. The effect of an optical molasses should contribute 4 mm in quadrature to both the transverse and vertical radius at 5 ms imaging, with 200 mW in the 2 MHz red-detuned, 2 cm  $1/e^2$  radial waist beam. Such a contribution could be easily detected in Fig. 4.16, further evidence that the mechanism underlying the behavior cannot be simply that of an optical molasses.

The direction of the vertical center-of-mass drift of the ensemble is independent of the direction of the initial atom motion (upwards or downwards). The imaging pulse always pushes the atoms downwards [Fig. 4.16(c)]. The drift may have its source in an intensity imbalance between the downwards-propagating and retroreflected upwards-propagating beams. Small losses on the waveplate and mirror of the retroreflected beam could cause a downwards force on the atoms. That force may be partially counterbalanced by the force that prevents the ensemble from expanding vertically, but the effect could still be significant. With an intensity imbalance of just 1%, the

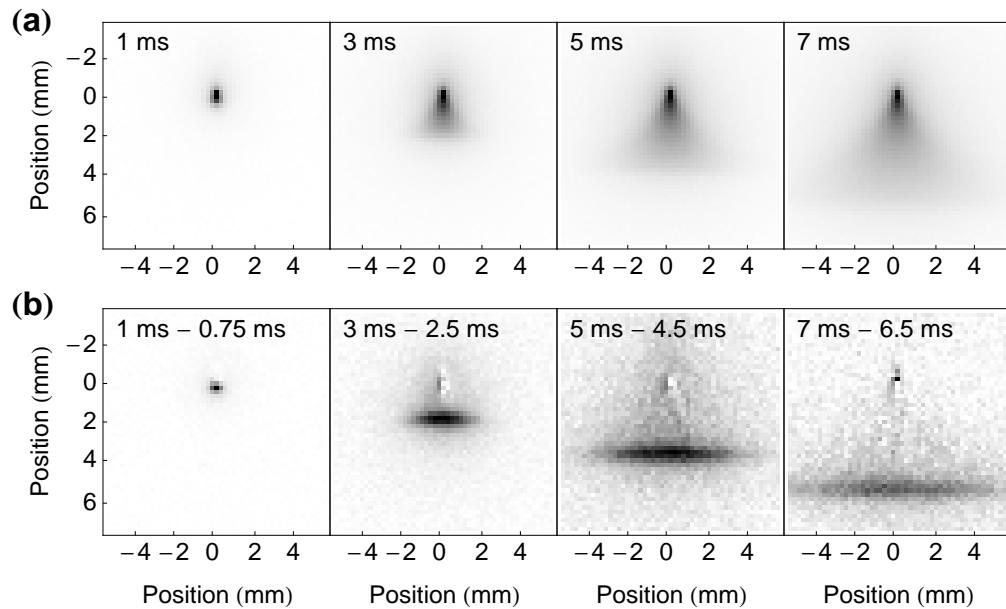


Figure 4.15: Effect of the imaging pulse on the atom cloud distribution. Darker pixels indicate more light emitted at that location. The cloud was launched to a height of 100 cm above the detection region, and imaged as it flew upwards. (a) Background-subtracted images at several imaging pulse durations, as denoted in the upper left corner. (b) Differences between pairs of images. The peak height of each image is normalized prior to subtraction to mitigate atom number fluctuations. The two numbers in the upper left indicate the durations of the imaging pulse for each of the images involved. The residual reveals the location of the atoms during that time interval. The small dark spot that remains at a position of 0 mm as the imaging duration grows may be a result of imperfect subtraction rather than fluorescence of atoms.

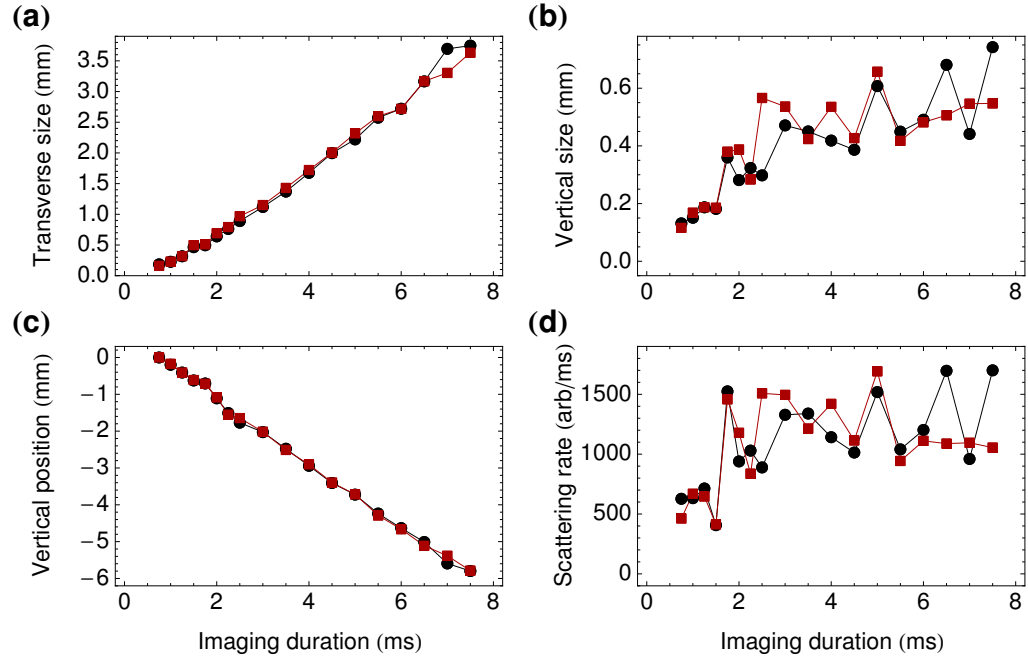


Figure 4.16: Atom distribution characteristics as a function of imaging duration. In black and red are the two orthogonal cameras, North and West respectively. Differences between pairs of images including those shown in Fig. 4.15(b) are fit to Gaussians, and their RMS radial size, position, and volume extracted. (a) The transverse cloud size grows linearly at a rate of 0.55 (0.53) mm/ms on North (West). (b) The vertical radius grows 10 times more slowly, possibly showing a plateau above 3 ms. (c) The cloud is pushed downwards at a constant rate of 0.88 mm/ms on both cameras. (d) The total volume of the fit normalized by the relevant time interval, which represents the scattering rate of photons scattered during that interval, plateaus above 2 ms. Note the strong correlation between the scattering rate and the vertical cloud size.

drift velocity should grow with the imaging duration as  $0.5 \text{ mm/ms} \times t$ . Although this scaling with imaging time is incorrect, the order-of-magnitude scale is close.

For our image analysis, especially as described in Sec. 5 and 6, knowledge of the behavior in Fig. 4.16 without knowledge of the exact mechanism is sufficient to account for systematic errors associated with the deformation of the ensemble during imaging. A full understanding of the mechanism would likely include the magnetic field environment in the detection chamber, which is strongly affected by the magnetic shield. If the magnetic gradient is sufficiently strong, the theory of a MOT rather than an optical molasses would be more appropriate.

## 4.4 Absorption imaging

We use absorption imaging to characterize the atomic cloud at various stages of its cooling prior to the launch. In this method, probe light shines through the cloud and is imaged directly onto a CCD camera. When the light is resonant or near-resonant with an atomic transition, the cloud scatters light from the beam creating a shadow in the image. The more atoms in the cloud at a particular location, the darker the shadow.

Following standard practice (see, e.g, Ref. [89]), we calculate the optical depth (OD) of the cloud along the camera’s line-of-sight using a sequence of three images: a signal image with both the cloud and the probe light, a reference image with the probe light pulsed but after the cloud has fallen out of view, and a background image with neither cloud nor probe light.

From the optical depth at each pixel location  $\text{OD}_{i,j}$ , the detuning  $\Delta$  of the probe light from the imaging transition, and the theoretical on-resonance optical cross-section of that transition  $\sigma_0$  [82], we can determine the number of atoms in the cloud (in the limit of a very low-intensity probe):

$$\frac{1}{\sigma} (1 + 4\Delta^2/\Gamma^2) \sum_{i,j} \text{OD}_{i,j} \delta x^2 \quad (4.4)$$

where  $\delta x$  is the size of each square pixel.

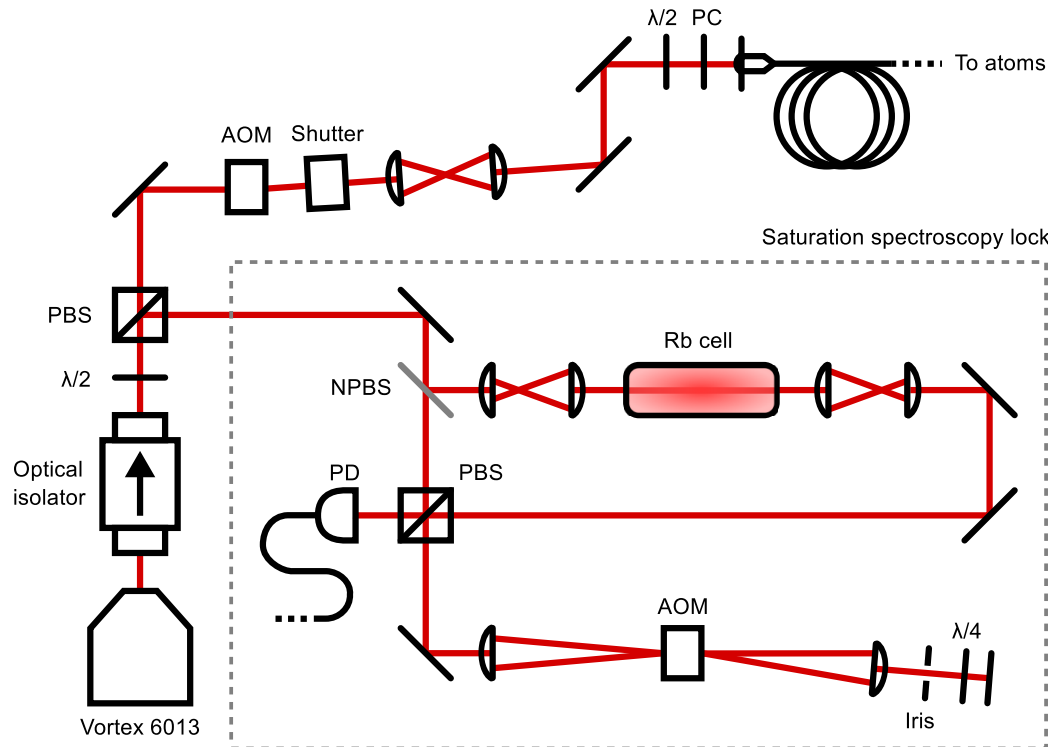


Figure 4.17: Absorption imaging Rb spectroscopy lock. The acousto-optic modulator (AOM) in the saturation spectroscopy lock is chopped between two frequencies to produce the lock error signal. Changing the average frequency of this AOM changes the detuning of the imaging light incident on the atoms. At the rubidium cell, the pump and probe beams each contain  $\sim 150 \mu\text{W}$ . Telescopes expand them to improve absorption through the cell. PBS: Polarizing Beam Splitter. NPBS: Nonpolarizing Beam Splitter, 70% transmission, 30% reflection. PC: Polarcor. PD: Photodetector.  $\lambda/2$ : half waveplate.  $\lambda/4$ : quarter waveplate.

For optimal shadow contrast, the imaging light must be single-frequency and narrower than the natural linewidth of the transition. To create this source, we lock a Vortex laser (linewidth  $\sim 0.5$  MHz) to a transition in a rubidium vapor cell using saturation-absorption spectroscopy. We sample a portion of the Vortex light for the lock (Fig. 4.17).

The imaging lock is similar to the master laser lock for the MOT frequencies. But rather than use a phase modulator to generate the necessary sidebands on the pump light, we use an AOM (Isomet 1205C-603F) and rapidly switch the RF input between two frequencies separated by 2 MHz ( $\nu_{\text{mod}} \pm 1$  MHz). The pump light is double-passed through this AOM, imprinting a frequency upshift of  $2\nu_{\text{mod}} \pm 2$  MHz relative to the counterpropagating probe beam and the Vortex laser.

By alternating frequencies, we effectively compare two parts of the spectrum separated by 4 MHz. Demodulating at the switching frequency (820 kHz), produces an error signal that is a derivative of the Doppler-free saturation-spectroscopy spectrum. The demodulation and the PID lock are implemented through a Cesium Lock board from AOSense. A slow, software-based feedback loop provides extra integral gain to account for large but slow temperature changes. This loop reads the output voltage from the lock circuit and changes the Vortex's piezo setting through the GPIB interface as necessary.

When the system is locked to a particular transition, the frequency of the Vortex is  $\nu_{\text{mod}}$  below that transition due to the mean frequency upshift  $2\nu_{\text{mod}}$  of the pump beam. We therefore upshift the portion of the light that is used for the imaging beam with another AOM (Isomet 1205C-1). This AOM also serves as a fast optical switch, as the imaging pulses are typically short (35  $\mu$ s).

Due to the high densities of the cold clouds, the atoms often absorb all the light from the imaging beam when it is on resonance, and the image appears saturated. It is therefore useful to be able to detune the imaging beam by several linewidths to produce a clear picture of the cloud shape. Because the imaging light diffracted by the (single-pass) AOM is fiber coupled, we must apply a fixed RF frequency 80MHz to maintain optimal coupling. Instead, we change  $\nu_{\text{mod}}$  over a  $\sim 20$  MHz bandwidth to give detunings from  $-20$  to  $+20$  MHz.

Approximately 2 mW of probe light is delivered by optical fiber to the 3D MOT chamber, where it is expanded to a  $\sim 4$  mm radial waist. A polarizer provides a well-defined linear polarization. For most of the images in this work, the polarization was defined exclusively by this element. But in order to optically pump the atoms into an extreme Zeeman sublevel (Sec. 10.2) we later added a quarter waveplate to generate circular polarization, which minimally affected the detected optical depth.

#### 4.4.1 Absorption image analysis

Much of the information we gather about the properties of the clouds (e.g. temperature, collision rate, peak density, etc.) comes from fitting the absorption images. The functional forms that serve as our models are derived from the shape of the thermal atom distribution in the magnetic trap in question.

For a thermal cloud with kinetic energy  $E(\mathbf{v})$  in a trap of potential  $U(\mathbf{x})$ , the probability density distribution is given by the normalized Maxwell-Boltzmann distribution:

$$P(\mathbf{x}, \mathbf{v}) = \frac{e^{-[E(\mathbf{v})+U(\mathbf{x})]/(k_B T)}}{\int e^{-[E(\mathbf{v})+U(\mathbf{x})]/(k_B T)} d^3 v d^3 x} \quad (4.5)$$

Since a camera detects an atom's position but is agnostic to its velocity, we integrate over the velocity portion of the distribution, which removes all  $E(\mathbf{v})$  dependence. We then integrate over one of the three axes, chosen to be  $y$ , representing the camera's line of sight. The remainder is the probability distribution for the column density of the cloud.

$$P(\mathbf{x}) = \frac{\int e^{-U(\mathbf{x})/(k_B T)} dy}{\int e^{-U(\mathbf{x})/(k_B T)} d^3 x} \quad (4.6)$$

We find analytical solutions for both a quadrupole trap, which describes the first few stages of our typical evaporation, and a harmonic trap, which describes the TOP evaporation. From these solutions, we can infer the cloud properties mentioned above not only at the field strength immediately before the traps are snapped off for the image, but also at any other field strength of interest through the derived scalings (Tab. 4.1 and Tab. 4.2). This scaling capability is particularly useful because the quadrupole coils can be safely snapped to zero field only from a certain maximum

current (58 A or 50 G/cm), which is typically well below the fields used for evaporation (218 G/cm, 131 G/cm, and 109 G/cm). Imaging directly in the strong field gradients is undesirable as it results in non-uniform absorption patterns due to the non-uniform spin orientations within the cloud.

### Imaged cloud shape in a magnetic quadrupole

Atoms in a pure quadrupole trap with a radial gradient  $A$  and under the influence of a gravitational acceleration  $g$  feel a potential

$$U(x, y, z) = \mu A \sqrt{x^2 + y^2 + 4z^2} + mgz \quad (4.7)$$

where  $\mu = \mu_B m_F g_F$  represents the magnetic parameters of the atom with the Bohr magneton  $\mu_B$ , the Zeeman level  $m_F$ , and the Landé  $g$ -factor  $g_F$ . For the typical evaporation in this work,  $m_F = -1$  and  $g_F = -1/2$ . Performing the integration of Eq. 4.6 yields an image with a column density distribution

$$P_{\text{quad}}(x, z) = \frac{(\beta^2 - 4)^2}{32\pi\rho^3} \sqrt{x^2 + 4z^2} K_1\left(\frac{1}{\rho}\sqrt{x^2 + 4z^2}\right) e^{-\frac{\beta}{\rho}z}. \quad (4.8)$$

Here,  $K_1$  is the modified Bessel function of the second kind,  $\beta = mg/(\mu A)$  compares the gravitational strength to the magnetic strength, and  $\rho = k_B T/(\mu A)$  defines a length scale. An example of the cloud shape is shown in Fig. 4.18(a).

To fit to an absorption image (in units of OD), we include an overall amplitude scale factor  $N$  as well as a constant background  $c$  and a position offset  $(x_0, z_0)$ , yielding  $NP_{\text{quad}}(x - x_0, z - z_0) + c$ . Knowing the fit parameters, we can find a variety of properties of the cloud (Tab. 4.1). The scalings with quadrupole gradient assume an ideal gas. The temperature and volume before and after an adiabatic compression or decompression are then related by  $T_1 V_1^{2/3} = T_2 V_2^{2/3}$ . At the highest PSD values the assumption of an ideal gas breaks down because the gas is no longer in the classical regime, nor is it non-interacting. Nevertheless, the scalings are suitable for the majority of the evaporation ramp.

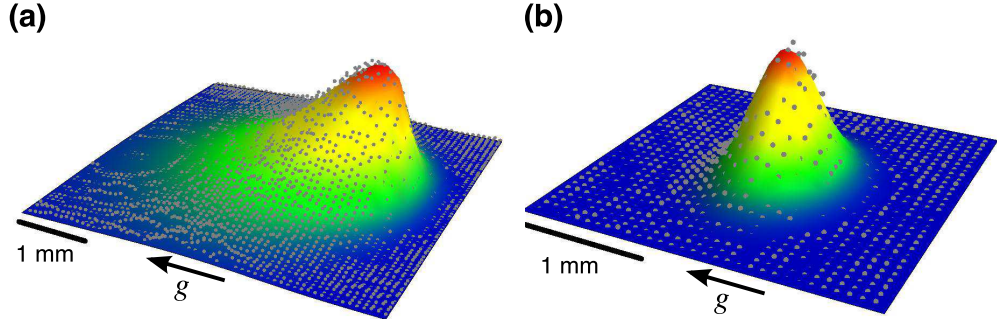


Figure 4.18: Examples of fits to absorption images of atom ensembles in (a) a quadrupole trap and (b) a TOP trap. The data is shown as gray points. The fit is the colored surface. Gravity, which strongly affects the shape in the quadrupole trap in particular, pulls the clouds down (leftwards in the plots, as indicated).

Property	Formula	Scaling
Atoms	$N \frac{\delta x^2}{\sigma_\gamma}$	1
Size	$\sigma = \rho \delta x$	$A^{-1/3}$
Peak Density	$n_{\text{peak}} = \frac{N (\beta^2 - 4)^2}{64\pi\sigma^3}$	$A$
Temperature	$T = \frac{\mu A \sigma}{k_B}$	$A^{2/3}$
Collision Rate	$n_{\text{peak}} \sigma_{\text{Rb}} \sqrt{\frac{k_B T}{m}}$	$A^{4/3}$
Thermal Wavelength	$\lambda_T = \sqrt{\frac{2\pi\hbar^2}{mk_B T}}$	$A^{-1/3}$
PSD	$n_{\text{peak}} \lambda_T^3$	1

Table 4.1: Cloud properties in a quadrupole trap and scalings with gradient. Formulas incorporate the parameters of the fit derived from Eq. 4.8 with the addition of the image pixel size  $\delta x$ , the photon-atom scattering cross-section  $\sigma_\gamma$ , and the atom-atom scattering cross-section  $\sigma_{\text{Rb}}$ .

### Imaged cloud shape in a TOP trap

The exact potential for a TOP trap with gravitational sag is  $U = \mu B_{\text{TOP}} + mgz$ , where  $B_{\text{TOP}}$  is given by Eq. 7.8. While the exact expression for  $B_{\text{TOP}}$  is not simple, during evaporation the atoms will largely remain near the trap minimum. Consequently, we can expand the potential about the minimum  $z_{\text{sag}}$ :

$$U(\rho, z) = \frac{1}{2}m\omega_\rho^2\rho^2 + \frac{1}{2}m\omega_z(z - z_{\text{sag}})^2 \quad (4.9)$$

where here  $\rho = \sqrt{x^2 + y^2}$  and  $\omega_\rho$ ,  $\omega_z$ , and  $z_{\text{sag}}$  are given by Eqs. 7.9, 7.10, and 7.11.

As the potential contains only independent variables that are squared, the resulting probability distribution is Gaussian:

$$P_{\text{TOP}}(x, z) = \frac{1}{2\pi s_x s_z} e^{-\frac{x^2}{2s_x^2} - \frac{(z - z_{\text{sag}})^2}{2s_z^2}}, \quad (4.10)$$

where  $x$  and  $z$  are pixel coordinates in the image, and  $s_x = \omega_\rho^{-1}\sqrt{k_B T/m}$  and  $s_z = \omega_z^{-1}\sqrt{k_B T/m}$  define the cloud width. Just as in the case for the quadrupole trap, the final fitting function for absorption images (in units of OD) also includes an overall scale factor, background, and position offset:  $NP_{\text{TOP}}(x - x_0, z - z_0) + c$ . The cloud properties derived from the fit parameters are given in Tab. 4.2. An example of a fit to the atom distribution is given in Fig. 4.18(b).

## 4.5 Rotation compensation system for suppression of the Coriolis force

The phase shift due to the Coriolis force on the atoms (term 2 of Tab. 3.1) is one of the primary sources of systematic error in the differential acceleration measurement of the equivalence principle test. As described in Sec. 3.3.3, this phase shift can be largely compensated by rotating the retroreflection mirror to cancel Earth's rotation rate. Given the  $\sim 3$  s duration of the interferometer and the  $\Omega_y = 58 \mu\text{rad/s}$  rotation rate of the Earth, the retroreflection mirror must be rotated through a range of  $200 \mu\text{rad}$ .

Property	Formula	Scaling
Atoms	$N \frac{\delta x^2}{\sigma_\gamma}$	1
Size	$(\sigma_\rho, \sigma_z) = (s_x, s_z) \delta x$	$\left( \frac{\omega_z^{1/6}}{\omega_\rho^{2/3}}, \frac{\omega_\rho^{1/3}}{\omega_z^{5/6}} \right)$
Peak Density	$n_{\text{peak}} = \frac{N}{(2\pi)^{3/2} \sigma_\rho^2 \sigma_z}$	$\omega_\rho \omega_z^{1/2}$
Temperature	$T = \frac{m}{k_B} \sigma_\rho \sigma_z \omega_\rho \omega_z$	$\omega_\rho^{2/3} \omega_z^{1/3}$
Collision Rate	$n_{\text{peak}} \sigma_{\text{Rb}} \sqrt{\frac{k_B T}{m}}$	$\omega_\rho^{4/3} \omega_z^{2/3}$
Thermal Wavelength	$\lambda_T = \sqrt{\frac{2\pi\hbar^2}{mk_B T}}$	$\omega_\rho^{-1/3} \omega_z^{-1/6}$
PSD	$n_{\text{peak}} \lambda_T^3$	1
Trap Minimum Position	$z_{\text{sag}} = z_0 px$	$\frac{B_0}{A^2} \omega_z^{-2/3}$

Table 4.2: Cloud properties in a TOP trap and scalings with trap frequency. Formulas include the parameters of the fit derived from Eq. 4.10 with the addition of the image pixel size  $\delta x$ , the photon-atom scattering cross-section  $\sigma_\gamma$ , and the atom-atom scattering cross-section  $\sigma_{\text{Rb}}$ . Note that the expression provided for the temperature is a geometric mean of two dimensions of the cloud. Alternative expressions could highlight just one of the dimensions, or combine all three, but this version serves to set the scale. Expressions for the trapping frequencies in the TOP trap are given in Eq. 7.9 and Eq. 7.10. An expression for the trap minimum position is given in Eq. 7.11.

To suppress Coriolis phase shifts below  $10^{-15} g$  with a  $1 \mu\text{m}/\text{s}$  center-of-mass velocity offset between the ensembles of  $^{85}\text{Rb}$  and  $^{87}\text{Rb}$ , the precision of the rotation must be  $\lesssim 1 \text{nrad}/\text{s}$ . Towards that end, we have built a precision nanopositioner stage, the Rotation Compensation System (RCS).

### 4.5.1 Components

The RCS is composed of a mirror resting on a platform controlled by three nanopositioners (Fig. 4.19). The entire system is contained within a custom vacuum enclosure connected to the 3D MOT chamber through a short, flexible bellows. An all-metal gate valve separates the two, and permits the exchange of optical elements in this lower enclosure – which includes the 4 in diameter quarter-wave waveplate in addition to the retroreflection mirror – without breaking vacuum in the main interferometer region.

The mirror is a custom 4.00 in diameter, 2.00 in thick Ohara CCZ substrate (equivalent to Zerodur), polished on both upper and lower surfaces to a wavefront of  $\lambda/4$  (CVI-Melles Griot). The upper surface is coated for  $> 99\%$  reflectivity at 780 nm while the lower surface is coated for  $< 0.25\%$  reflectivity at the same wavelength.

The three nanopositioners (Nano-OP30; Mad City Labs) contact the mirror platform with even spacing around the circumference of a circle of 15 cm diameter centered on the mirror. They are rigidly attached to the walls of the vacuum enclosure. These nanopositioners have a design range of  $30 \mu\text{m}$  and position noise of  $3 \text{ pm}/\sqrt{\text{Hz}}$ , for a maximum angular range of  $400 \mu\text{rad}$  (assuming the height at the center of the mirror stays at a constant offset of  $10 \mu\text{m}$ ) and an angular noise of  $0.04 \text{nrad}/\sqrt{\text{Hz}}$ . These specifications are more than sufficient to cancel Earth’s rotation rate by the desired five orders of magnitude. A three-axis, 20-bit controller (Nano-Drive3; Mad City Labs) sets the extension of all three nanopositioners. The nanopositioners are mounted in an inverted manner, such that an increase in the extension of a nanopositioner pulls down the mirror platform.

The mirror and nanopositioners are connected through an inch-thick aluminum platform fabricated by Mad City Labs in conjunction with the nanopositioners and

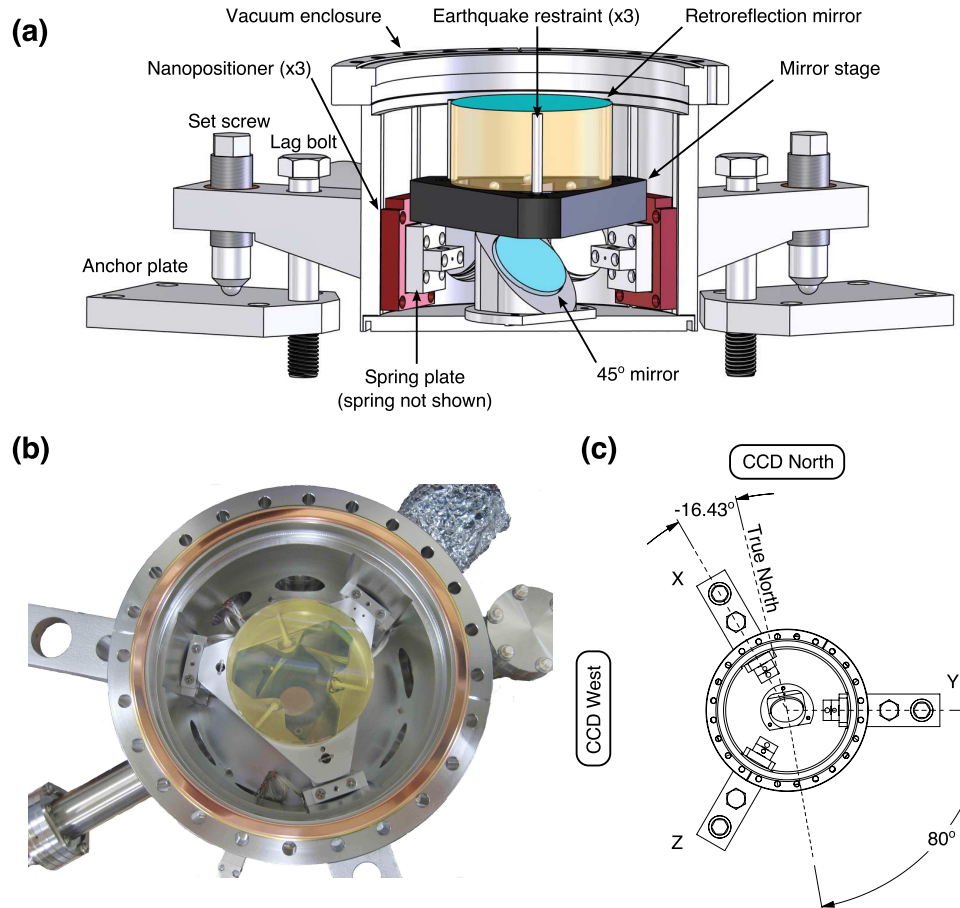


Figure 4.19: Schematics and image of the rotation compensation system. (a) Section view of the model for the system, looking along the Z axis (as labeled in (c)). (b) A top-down view of the 4 in retroreflection mirror, the rotation compensation system, and the vacuum enclosure. Visible through the center of the retroreflection mirror is the 45° mirror mounted on the floor of the enclosure. Also visible are the vents drilled radially into the mirror to the apex of each cone contact. The six ports in the side of the vacuum enclosure are used for vacuum pumping and the nanopositioner electrical feedthroughs. (c) Top-down schematic showing the direction of true North, as measured in Ch. 6, in addition to the orientation of the 45° mirror relative to the three tabs and the location of the two CCD cameras.

controller. The platform has point, line, and plane constraints for both the mirror and the nanopositioners. The plate is tightly connected to the nanopositioners by stiff springs. Three cones drilled into the underside of the mirror fit over glass spheres which rest on the kinematic constraints on the platform. Three rods secured to the platform's surface prevent the mirror from sliding off the platform in the event of an earthquake.

The center of the platform is open to allow for optical access to the underside of mirror. Fixed to the enclosure floor immediately beneath the retroreflection mirror is a 2 in diameter mirror at  $45^\circ$ . This secondary mirror directs the small fraction of light transmitted through the reflective coating of the retroreflection mirror out an anti-reflective window installed in the side of the vacuum enclosure. While the wavefront of the beams is distorted by the 2 in thick mirror substrate, the ability to sample the lattice and MOT beams provides a valuable diagnostic of their shape and size. This optical access to the underside of the retroreflection mirror will also ultimately allow for a beam to be directed into the chamber for an independent optical measurement of the angle of the mirror's reflective surface [105, 106].

Because a 9 m tall interferometer requires nearly  $200 \mu\text{rad}$  of the RCS range, we coarsely tune the angle of the retroreflection mirror using three tabs on the outside of the vacuum chamber. The height of each tab is fixed by a 1/2"-13 bolt with a spherical washer pair and a 1.035"-40 set screw. Anchored to the concrete floor underneath the RCS are three stainless steel plates, with a tapped hole for the bolt and a flat surface for the set screw. The bellows that connect the RCS to the all-metal gate valve provide the necessary angular flexibility.

#### 4.5.2 Simulation and design

The design of the system minimizes wavefront error, mechanical oscillations and thermal angular offsets, all of which could lead to systematic errors in the applied rotation. Finite element simulations, performed using the COMSOL software, are a useful tool for modeling such errors, and as such informed the final design.

To maintain the wavefront quality of the reflected beam, sag of the mirror surface

under gravity is reduced by choosing a thick mirror substrate and by positioning the contact points appropriately. Connecting the mirror and the platform through kinetic constraints minimizes distortion of the mirror surface. Simulations show that the effective wavefront distortion associated with gravitational sag is reduced to  $< \lambda/1000$  for a 2 in thick substrate with three contact points located at 22.5% of the mirror diameter from the mirror edge. The resulting wavefront error of a reflected beam is therefore limited by the current mirror's wavefront specification and can be improved with a more-finely polished mirror.

For mechanical stability, the mirror platform must be thick and the acceleration of the mirror smooth. Mechanical oscillations can be excited when accelerating the platform. While the mirror rotation may be implemented as a continuous linear sweep of the mirror angle such that the nanopositioners are not accelerating during the interferometer itself, sweeping the mirror through the large angular range necessary is technically difficult to perform with the desired precision. A logical solution is to digitally set the platform's coarse angle prior to each of the three interferometer pulses and to apply a precise ramp to each of the nanopositioner analog inputs during the pulse itself, which would require a sweep range of  $< 1 \mu\text{rad}$ . This procedure, however, requires accelerating the platform from rest before each pulse.

Shown in Fig. 4.20 are the results of simulations modeling the acceleration the mirror-platform system with two different platform thicknesses (3/8 in and 1 in) and two different acceleration profiles (parabolic and sinusoidal). From each simulation we record the angle of the plane defining the mirror's surface during and after the mirror's acceleration. The error of this angle was determined by subtracting the analytically predicted angle of the mirror's surface from the simulated angle.

The results indicate that a smooth, no-jerk acceleration coupled with a thick platform can reduce the amplitude of the angular oscillations by more than three orders of magnitude, from over 10 nrad to less than 0.1 nrad. The amplitude of the oscillations were found through a fit of the last 5 ms of each simulation to the sum of a linear and sinusoidal angular error. The linear portion, corresponding to an error in the applied rotation rate of a part in  $10^5$ , may be attributed to rounding differences between the simulation and the analytics. These simulations guided the choice of the

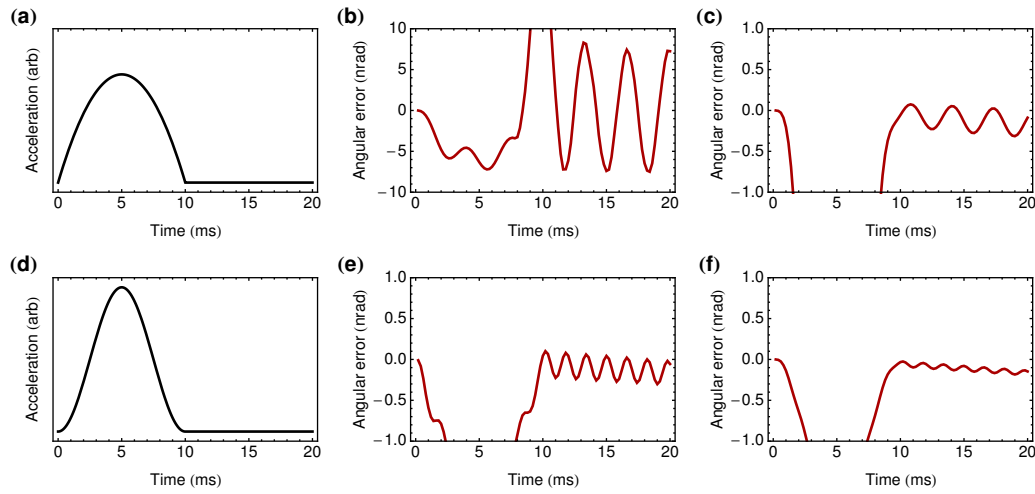


Figure 4.20: Simulated errors in the angle of the retroreflection mirror indicate that a smooth acceleration and thick mirror platform dramatically prevent the excitation of mechanical oscillations. (a) and (d) show the parabolic or sinusoidal acceleration applied to the nanopositioners in their respective rows. In (b) and (e), the mirror platform was thin ( $3/8$  in), whereas in (c) and (f) it was thick (1 in). Note that the scale is an order of magnitude larger for (b) than for (c), (e) or (f). The amplitudes of the oscillations immediately after the acceleration are 7.5, 0.16, 0.15 and 0.03 nrad for (c), (d), (e) and (f) respectively. The frequency of these oscillations is higher for (e) and (f), as expected for a thicker plate.

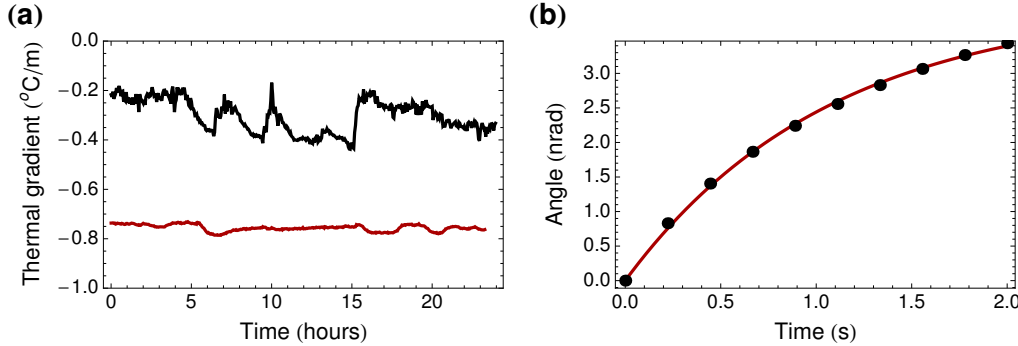


Figure 4.21: Thermal behavior of the Rotation Compensation System. (a) The thermal gradient at the location of the installed RCS at the bottom of the experimental pit, measured over the course of a day. In the lower red trace, a box enclosed the thermocouple and multimeter used in the measurement. In the upper black trace no enclosure was present, leading to a lower average gradient but more fluctuations. (b) Finite element simulation of the response of the retroreflection mirror's angle to a 1 millidegree step change in the applied thermal gradient. The black points are the result of the simulations, and the red line is an exponential fit to these points. The fit indicates a 1.1 s time constant and a total displacement of 4.0 nrad.

1 in platform thickness.

Finally, thermal gradients across the whole system, including the vacuum enclosure, can result in angular errors of the mirror's surface through the differential thermal expansion on opposite sides of the enclosure. To analyze this effect, we measured thermal gradients in the installation location of the RCS and used the results in a finite element model of the RCS and its vacuum enclosure.

It is important to note that only time-changing gradients cause a systematic error in the interferometric measurement. To lowest order, a static gradient will cause a static angular error of the mirror's surface, but will not influence the rate of change of this angle by the nanopositioners. As only the rate of change of the mirror's surface influences the degree to which the Coriolis phase shift is compensated, a static thermal gradient is benign. Even so, the simulation of the static thermal gradient establishes a sense of scale regarding the influence of thermal gradients on the mirror's surface.

The thermal gradient at the RCS location was measured via thermocouple. The thermal gradient and the rate of change of that gradient strongly depended on whether

or not the thermocouple-multimeter system was enclosed [Fig. 4.21(a)]. With an enclosure, air currents are strongly suppressed and the speed with which the thermal gradient changes is reduced by a factor of  $\sim 10$ . But without these air currents, the heat generated by the multimeter is not as easily dissipated, resulting in a ( $\sim 3\times$ ) stronger thermal gradient offset. In the final installation, a multimeter would not be included within any enclosure built, so the thermal load on the RCS is likely best described by the thermal gradient variation with the enclosure ( $6.6 \mu^\circ\text{C}/\text{s}$ ), but by the mean thermal gradient without ( $0.24^\circ\text{C}$  across the RCS).

In the simulations, we applied a step change in the thermal gradient and analyzed the response of the system. A 1 millidegree step across the RCS fit to a 4.0 nrad total angular change with a 1.1 s time constant [Fig. 4.21(b)]. Thus, if thermal drifts change the temperature difference across the RCS by even a few tenths of a degree, the angle of the retroreflection mirror would change by nearly  $1 \mu\text{rad}$ . Fortunately, these thermal drifts happen slowly and are insignificant over the time of the interferometer:  $6.6 \mu^\circ\text{C}/\text{s}$  corresponds to only 52 prad during a 2 s interferometer, well below the  $\sim 1 \text{nrad}$  precision desired.

### 4.5.3 Performance

We carried out three tests of the RCS performance. First, we optimized its response by tuning the bandwidth of the controller's feedback loop. Next, we characterized the relative calibration of the digital setpoints and analog sensor signals. The digital setpoints control the high voltage applied to (and therefore the height of) the nanopositioners, while the analog signals report the length of the attached piezoresistive sensors that independently measure the nanopositioner height. Finally, we analyzed the noise of the piezoresistive sensors to make a statement about the system's precision.

#### System bandwidth

To optimize the system we evaluated the measured step response of the system. We applied a step of  $10 \mu\text{m}$  to each nanopositioner and tuned the bandwidth of each axis to minimize oscillations measured by the piezoresistive sensors. The optimized

bandwidths were  $(X, Y, Z) = (17.3, 15.6, 16.2)$  Hz, for a settling time of  $\sim 100$  ms.

### Relative calibration of digital setpoint and analog sensors

We tested the controller calibration by comparing the digital height setpoint to the analog height reported by the piezoresistive sensor. The digital and analog values differed by at most 10 to 20 nm, depending on the axis, and the trend was softly nonlinear as a function of the commanded height. We found that the nonlinear component is stable to the subnanoradian level over nearly a week. Over that same week timescale, however, the linear error changed by  $\sim 0.5$  nm per micrometer of commanded height, which represents a significant error for Coriolis suppression at the  $10^{-4}\mu\text{rad/s}$  level and below. The approach to alleviating these errors depends, however, on their sources.

Because this test relies on the factory-determined calibration of the digital and analog outputs, it is impossible to determine whether the measured differences arise from errors in the nanopositioner calibration, the piezoresistive sensor calibration, or a combination of the two. Should the piezoresistive sensor calibration be responsible for all the relative errors, it would imply that the nanopositioner calibration is perfectly one-to-one. The errors would not impact the Coriolis suppression performance and no action is required. On the other hand, should the nanopositioners be responsible for the errors, correction would be necessary. Since the nonlinear error is stable, we have demonstrated that it can be removed to  $< 1$  nrad in a feed-forward manner using a look-up table to modify the commanded height for the expected nonlinearity. For the linear error, future experiments could test whether the drift is correlated with thermal drift. If so, better thermal stabilization could mitigate the effect. Alternatively, for a sufficiently slow drift we could periodically perform a diagnostic sequence to adjust the feed-forward calibration as necessary.

Determining which element is responsible demands an independent measurement of the mirror angle. We have built a proof-of-principle prototype of a precision optical angle sensor with the potential to reach sensitivities of 10 nrad and possibly less, sufficient to measure 1 nm nanopositioner errors. The optical lever scheme, building on Ref. [105] and [106], linearly amplifies the angle by bouncing a laser beam off

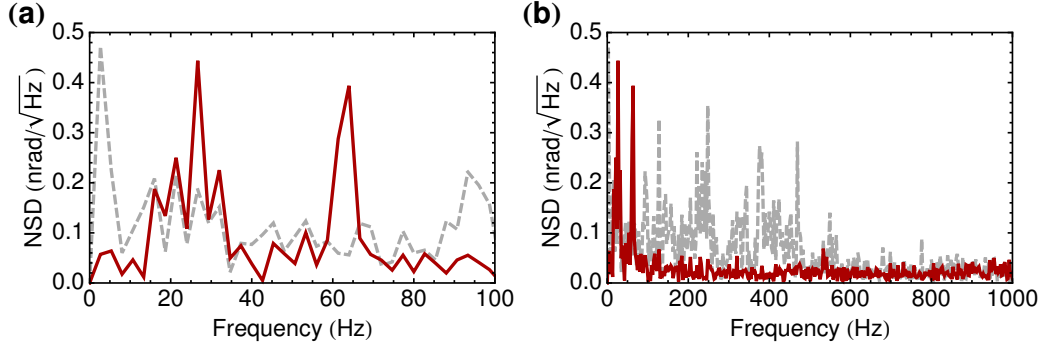


Figure 4.22: Noise spectral density (NSD) of the Rotation Compensation System. In solid red is the NSD when the RCS is on the vibrationally-quiet granite table. In dashed grey is the NSD when the RCS is on a vibrationally-noisy countertop. (a) The NSD up to 100 Hz. Because the bandwidth of the nanopositioners is  $< 20$  Hz, the noise in that band is particularly relevant. (b) The NSD up to 1 kHz, highlighting the apparent reduction of noise when on the quiet granite table.

the surface of interest multiple times before measuring the total displacement with a position-sensitive detector. For the RCS, this beam would be incident on the underside of the retroreflection mirror, accessed through the window in the RCS vacuum enclosure. The prototype was promising, with up to 10 bounces improving the high-frequency sensitivity. But the signal within the nanopositioner bandwidth was dominated by air currents, and future work would repeat the measurement within an enclosure.

### System precision

Even without perfect accuracy in the calibration, the noise of the piezoresistive sensor is related to the precision of the system. The three nanopositioners were set to  $10 \mu\text{m}$  and the voltage across the sensor was recorded simultaneously for each axis over 0.38 s. The position noise was then converted into an angular noise of the mirror. The noise spectral density, shown in Fig. 4.22, translates into 0.6 nrad RMS angular noise up to 20 Hz, the bandwidth of the nanopositioners. In the band up to 1 kHz, the RMS angular noise rises to only 1.5 nrad. Insofar as this DC measurement reflects the rotational precision achievable in the short-pulse limit (pulse durations of  $< 10 \mu\text{s}$ ,

where the rotation of the Earth during the pulse is negligible), this precision meets our requirements for Coriolis suppression.

As a final note, the precision reported by the piezoresistive sensors does depend on the vibrational environment of the RCS. The results above were performed on a granite table set on a concrete pad isolated from the building. Yet even in the noisier environment of a countertop (a factor of  $> 10$  larger vibrational accelerations above 40 Hz), the RMS angular noise increased by only a factor of two in both the 20 Hz and 1 kHz bands, which is still within our requirements for Coriolis suppression. The vibrational environment at the bottom of the pit at the permanent location of the RCS is comparatively quiet, as the RCS is anchored to the solid concrete floor.

# Chapter 5

## Multi-axis inertial sensing with long-time point source atom interferometry

We show that light-pulse atom interferometry with atomic point sources and spatially resolved detection enables multi-axis (two rotation, one acceleration) precision inertial sensing at long interrogation times. Using this method, we demonstrate a light-pulse atom interferometer for  $^{87}\text{Rb}$  with 1.4 cm peak wavepacket separation and a duration of  $2T = 2.3$  s. The inferred acceleration sensitivity of each shot is  $6.7 \times 10^{-12}g$ , which improves on previous limits by more than two orders of magnitude. We also measure the Earth’s rotation rate with a precision of 200 nrad/s.

This chapter also appeared as Ref. [1], and was written with collaborators Jason M. Hogan, Alex Sugarbaker, David M. S. Johnson, and Mark A. Kasevich.

### 5.1 Introduction

Light-pulse atom interferometry enables precision tests of gravity [31, 39, 71] and electrodynamics [107] as well as practical applications in inertial navigation, geodesy, and timekeeping. Phase shifts for light-pulse atom interferometers demonstrate sensitivity to the initial velocity distribution of the atom source, often resulting in

inhomogeneous dephasing that washes out fringe contrast [37]. In this Letter, we show that use of spatially resolved imaging in combination with an initially spatially localized atomic source allows direct characterization of these phase shifts. We refer to this technique as point source interferometry (PSI).

The contrast loss associated with such inhomogeneous dephasing is not fundamental, but is a consequence of atom detection protocols that average over velocity-dependent phase shifts. With PSI we establish a correlation between velocity and position and use spatially-resolved detection to form an image of the ensemble that reveals its velocity-dependent phase structure. A simple way to realize this correlation is through ballistic expansion of the ensemble. In the limit that the ensemble size at detection is much larger than its initial size, each atom's position is approximately proportional to its initial velocity. Consequently, any initial velocity-dependent phase shift results in a spatial variation of the interferometer phase, yielding a position-dependent population difference between the two output ports of the interferometer.

An important example of velocity sensitivity is due to rotation of the interferometer laser beams [35, 71]. Rotation at a rate  $\Omega$  leads to a phase shift (Table 5.1, term 2) that depends on  $(v_x, v_y)$ , the initial transverse velocity of the atom. In a rotating frame, this effect may be interpreted as a Coriolis acceleration. PSI also allows observation of longitudinal velocity-dependent phase shifts in asymmetric atom interferometers [45] (e.g., Table 5.1, term 3; in this work,  $\delta T = 0 \mu\text{s}$ ).

To demonstrate PSI, we induce a velocity-dependent phase shift in a  $^{87}\text{Rb}$  Raman light-pulse atom interferometer. We launch cold atoms from the bottom of a 10-meter tall vacuum enclosure [Fig. 5.1(a)] and apply a three-pulse accelerometer sequence  $(\pi/2 - \pi - \pi/2)$  [108]. The first pulse serves as an atom beamsplitter, coherently driving the atoms into a superposition of states  $|F = 1; p\rangle$  and  $|F = 2; p + \hbar k_{\text{eff}}\rangle$ , where  $p$  is the initial momentum,  $F$  is the hyperfine level, and  $\hbar k_{\text{eff}} = 2\hbar k$  is the momentum difference between the two states. Over the subsequent  $T = 1.15 \text{ s}$  interrogation interval, the two parts of the atom's wave function separate vertically by  $\frac{\hbar k_{\text{eff}}}{m} T = 1.4 \text{ cm}$  [Fig. 5.1(b)], at which time a mirror pulse reverses the relative momenta and internal states. After an identical drift time, a final beamsplitter pulse interferes the atom wave packets. We then image the atom fluorescence using a pair of CCD cameras located below

Term	Phase Shift	Size (rad)
1	$k_{\text{eff}}g T^2$	$2.1 \times 10^8$
2	$2\mathbf{k}_{\text{eff}} \cdot (\boldsymbol{\Omega} \times \mathbf{v}) T^2$	5.1
3	$k_{\text{eff}}v_z\delta T$	3.5
4	$\frac{\hbar k_{\text{eff}}^2}{2m} T_{zz} T^3$	0.44
5	$k_{\text{eff}}T_{zi}(x_i + v_i T) T^2$	0.18
6	$\frac{1}{2}k_{\text{eff}}\alpha(v_x^2 + v_y^2) T^2$	0.04

Table 5.1: Velocity-dependent phase shifts and their sizes assuming the following:  $k_{\text{eff}} = 2k = 2 \cdot 2\pi/780 \text{ nm}$ ,  $T = 1.15 \text{ s}$ , initial velocity spread  $v_i = 2 \text{ mm/s}$  (50 nK), initial positions  $x_i = 200 \mu\text{m}$ ,  $|\boldsymbol{\Omega}| = 60 \mu\text{rad/s}$ , gravity gradient tensor components  $T_{zi} = 3075 \text{ E}$ , interferometer pulse timing asymmetry  $\delta T = 100 \mu\text{s}$ , and wavefront curvature  $\alpha = (\lambda/10)/\text{cm}^2$ . Note that for  $T_{zx}, T_{zy} = 50 \text{ E}$  the size of term 5 is significantly smaller. The acceleration (term 1) and gravity curvature (term 4) phase shifts are shown for reference.

the interferometry region [Fig. 5.1(c)]. By the time of imaging, 2.6 s after launch, the 50 nK atomic source has expanded to 30 times its original size, establishing the position-velocity correlation necessary for PSI.

We imprint a velocity-dependent phase shift by rotating the atom interferometer laser beam axis at a tunable rate  $\delta\boldsymbol{\Omega}$ . Figure 5.2 shows typical detected atom distributions for several different values of  $\delta\Omega_x$ .

The velocity-dependent phase gradient we observe in Fig. 5.2 is proportional to the applied rotation rate (Fig. 5.3). For faster rates, the phase shift is large enough that multiple fringe periods appear across the ensemble. Without spatially resolved detection, averaging over these fringes would yield negligible contrast. With PSI, we realize record duration light-pulse atom interferometry, even in the presence of large rotation rates.

## 5.2 Methods

To create the cold atomic source, we load  $4 \times 10^9$  atoms from a magneto-optical trap into a plugged quadrupole trap, where we evaporate with a microwave knife [109, 110]. A magnetic lensing sequence in a time-orbiting potential (TOP) trap collimates the

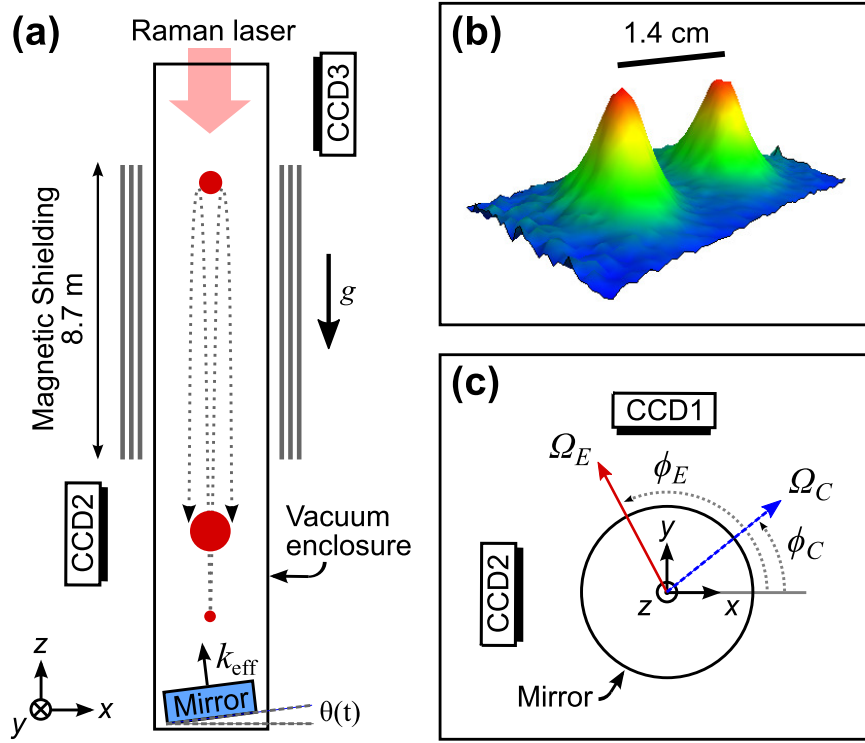


Figure 5.1: (a) Schematic diagram of the apparatus, viewed from the side. The atom cloud (red circle) is cooled and launched from below the magnetically-shielded interferometry region. The two interferometer output ports are imaged by both perpendicular cameras (CCD1 and CCD2). All interferometry pulses are delivered from the top of the tower and are retroreflected off a mirror (at angle  $\theta(t)$ ) resting on a piezo-actuated tip-tilt stage. (b) Image of the ensemble after a beamsplitter pulse showing the separation between two halves of the atomic wavepacket. For this shot we launched the atoms with extra velocity to reach CCD3. (c) Top view of the tip-tilt stage and lower cameras with the direction and magnitude of the Earth rotation  $\Omega_E$  and an (arbitrary) applied counter-rotation  $\Omega_C$ . In our apparatus,  $\phi_E \approx 105^\circ$ .

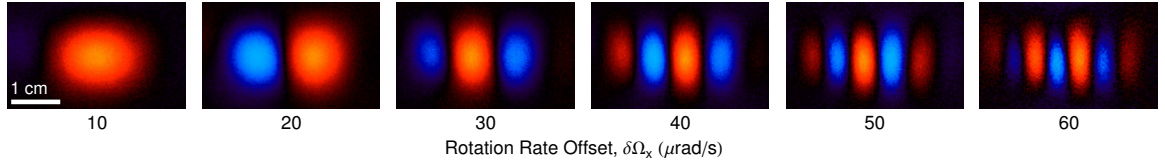


Figure 5.2: Spatial fringes on the atom population observed on CCD2 versus rotation rate offset  $\delta\Omega_x$ . Blue versus red regions show anti-correlation in atom population. The second output port, with fringes  $\pi$  rad out of phase, is not shown. Each image is the second-highest variance principal component arising from a set of 20 measurements (see Sec. 5.7 for a discussion of principal component analysis).

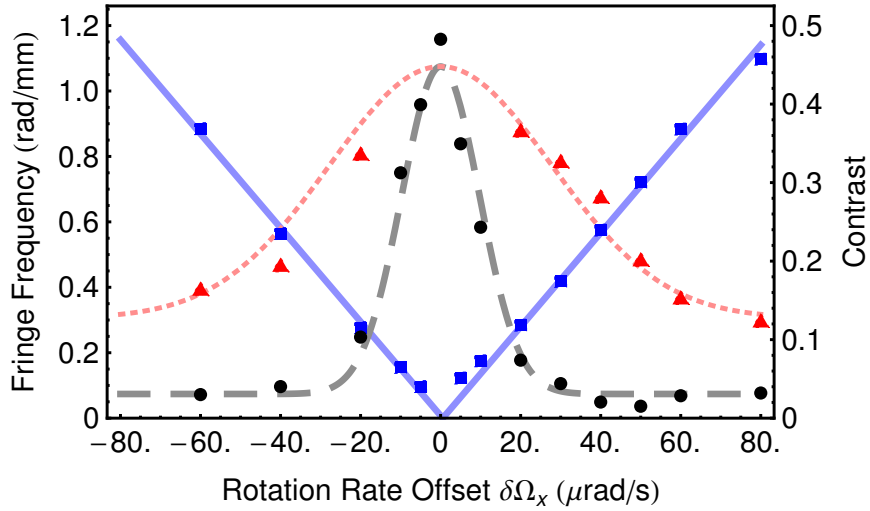


Figure 5.3: Fringe spatial frequency (blue squares, solid line) and contrast versus applied rotation for the data in Fig. 5.2. The fitted slope of the fringe spatial frequency is consistent with term 2 of Table 5.1 to  $< 10\%$ . Fringe contrast is observed over a wide range of rotation rates (red triangles, dotted line), while the contrast from integration detection decays rapidly (black circles, dashed line). Both Gaussian fits are constrained to be centered at the observed point of zero phase gradient ( $\delta\Omega_x \approx 0 \mu\text{rad/s}$ ), and the fringe contrast fit is further constrained to have the same peak value as the integrated contrast fit, since the methods should agree in the large wavelength limit.

atom source in 3D, cooling and expanding the cloud while maintaining high phase space density.<sup>1</sup> The final cloud contains  $4 \times 10^6$  atoms at 50 nK with an initial radius of  $200\text{ }\mu\text{m}$ . Alternatively, we can produce clouds at 3 nK with  $10^5$  atoms and an initial radius of  $30\text{ }\mu\text{m}$  by evaporating in a TOP trap with a microwave knife prior to the magnetic lensing sequence.

A microwave pulse transfers the ultracold atoms into a magnetically-insensitive Zeeman sublevel. They are then coherently launched with an optical lattice [113], which transfers 2386 photon momenta with a peak acceleration of 75 g. They enter the interferometer region, a 10 cm diameter, 8.7 m long aluminum vacuum tube. A solenoid wound around the tube provides a bias magnetic field, and three layers of magnetic shielding suppress the environmental field to  $< 1\text{ mG}$  [4].

A small fraction of the atoms are launched into  $\pm 2\hbar k$  momentum states. We purify the ensemble's vertical momentum with a  $135\text{ }\mu\text{s}$  Raman  $\pi$ -pulse, which transfers a 25 nK ( $0.3\hbar k$ ) subset of the ensemble into  $|F = 1\rangle$ . A short pulse resonant with  $|F = 2\rangle \rightarrow |F' = 3\rangle$  blows away atoms that did not transfer.

A pair of fiber-coupled 1 W tapered amplifiers (TAs) generate the retroreflected interferometer pulses. The seeds for the two TAs are derived from a common source cavity-stabilized to a linewidth of  $< 1\text{ kHz}$  and detuned 1.0 GHz blue from the 780 nm D<sub>2</sub> line ( $|F = 2\rangle \rightarrow |F' = 3\rangle$ ). The seed for one TA passes through a fiber phase modulator that generates the 6.8 GHz sideband necessary for Raman interferometry. An acousto-optic modulator (AOM) chirps the other seed to correct for the atoms' Doppler shift. The output of the TAs are combined on a polarizing beamsplitter cube, and the copropagating beams are diffracted by an AOM that acts as a fast optical switch. The beamsplitter and mirror pulses are  $35\text{ }\mu\text{s}$  and  $70\text{ }\mu\text{s}$  in duration, respectively. The beams have a 2 cm  $1/e^2$  intensity radial waist. The relative power of the two beams is chosen empirically to suppress intensity-dependent detunings by balancing AC Stark shifts (to  $< 2\text{ kHz}$ ).

Prior to detection, we spatially separate the output ports by applying a short

---

<sup>1</sup>The procedure is similar in principle to  $\delta$ -kick cooling [111], but uses the atoms' continuous expansion over  $\sim 100\text{ ms}$  against a shallow ( $\sim 5\text{ Hz}$ ) harmonic trap [112] rather than a short (few ms) impulse [45]. The magnetic fields are rapidly turned off when the atoms have reached their minimum velocity (maximum expansion) in all three dimensions. See Ch. 7.

pulse ( $\sim 50$  photon recoils) resonant with  $|F = 2\rangle \rightarrow |F' = 3\rangle$ . We wait 50 ms before simultaneously halting and imaging the atoms with a 2 MHz red-detuned beam. The atoms are nearly at rest after the first 300  $\mu\text{s}$  of the 5 ms imaging time. The scattered light is collected by two orthogonal CCD cameras, each with a numerical aperture of 0.25 [Fig. 5.1(c)]. The time from initial atom loading to the final image is 20 s.

### 5.3 High-contrast atom interferometry in the presence of rotations

We precisely control the direction of the interferometer beams with an in-vacuum, piezo-actuated tip-tilt stage onto which the retroreflection mirror is kinematically constrained. The stage has 1 nrad measured precision and a range of 400  $\mu\text{rad}$ . The stage platform is secured kinematically to three nanopositioners (Nano-OP30; Mad City Labs) by stiff springs. The nanopositioners are bolted to the vacuum enclosure, which is anchored to the vibrationally-quiet ( $10^{-8} g/\sqrt{\text{Hz}}$ ) concrete floor.

The rotation of the Earth is a significant source of velocity-dependent phase shifts. At our latitude in Stanford, California, the effective rate is  $\Omega_E = 57.9 \mu\text{rad/s}$ , which induces fringes of periodicity similar to the highest rotation rate in Fig. 5.2. With the tip-tilt stage we apply a compensating rotation of equal and opposite magnitude ( $\Omega_C = -\Omega_E$ ) to eliminate these phase shifts [37, 71, 114]. We implement this rotation by incrementing the mirror's angle in discrete steps between each interferometer pulse. In Figs. 5.2 and 5.3 we add a variable rotation rate  $\delta\Omega_x$  to this nominal rotation compensation vector.

Figures 5.4(a) and 5.4(b) show images of both output ports for a rotation-compensated interferometer using two atom source temperatures. The interferometer in Fig. 5.4(a) (3 nK) has an integrated interferometer contrast of 80% while that in Fig. 5.4(b) (50 nK) shows a contrast of 48%.<sup>2</sup> The contrast is reduced for the hotter source because of Rabi pulse area inhomogeneities due to larger horizontal cloud

---

<sup>2</sup>Integrated contrast is calculated by summing image counts inside regions of interest around each output port and then forming the normalized population ratios  $r_i$  for a set. The contrast of the set is  $c = [\text{Max}(r_i) - \text{Min}(r_i)]/[\text{Max}(r_i) + \text{Min}(r_i)]$ .

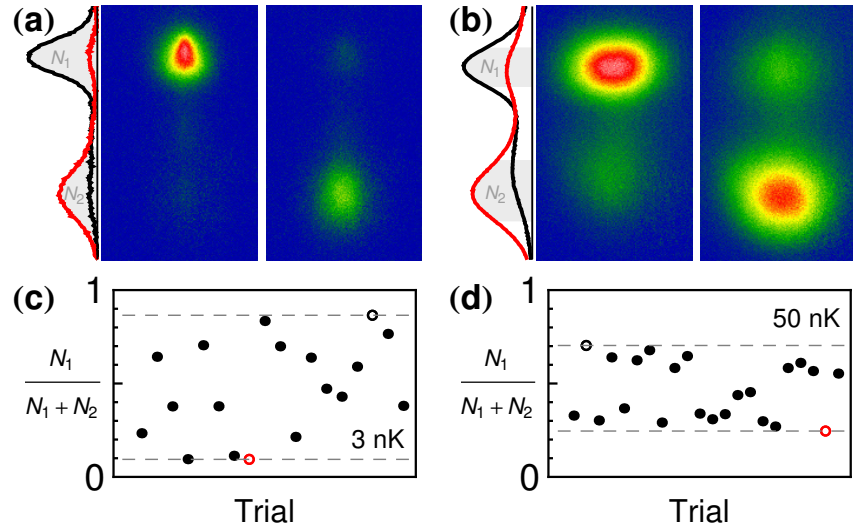


Figure 5.4: Images of the interferometer output ports using (a) 3 nK and (b) 50 nK atom sources with rotation compensation ( $\Omega_C = -\Omega_E$ ). The upper (lower) port consists of  $N_1$  ( $N_2$ ) atoms in state  $|F = 1\rangle$  ( $|F = 2\rangle$ ). Each pair of images represents the two extremes in the observed population ratio,  $N_1/(N_1 + N_2)$  (open circles in (c) and (d)). Population ratio variations between trials reflect interferometer phase variations caused by vibration of the retroreflection mirror. Also shown in (a) and (b) are the atom densities integrated horizontally for the two images (black and red curves), with the shaded regions used to determine the port atom numbers,  $N_i$ . The lower port has been optically pushed, resulting in a hotter cloud with fewer peak counts. Both ports are heated by a 5 ms imaging pulse. This heating is most evident for 3 nK clouds.

diameter (with respect to the spatially nonuniform laser beam intensity) and larger Doppler width.

With PSI, we maintain spatial fringe contrast even in the presence of large net rotation rates (Fig. 5.3). By comparison, the conventional integrated contrast for the same data decays rapidly with increasing rotation rate because a spatial average over the fringe pattern washes out the interference. The reduction in the PSI fringe contrast at higher rotation rates is not fundamental, but results from heating during imaging and imperfect alignment between the applied rotation  $\delta\Omega$  and the camera line-of-sight.<sup>3</sup>

<sup>3</sup>Imaging integrates along the line-of-sight (LOS) of the camera (perpendicular to the CCD chip).

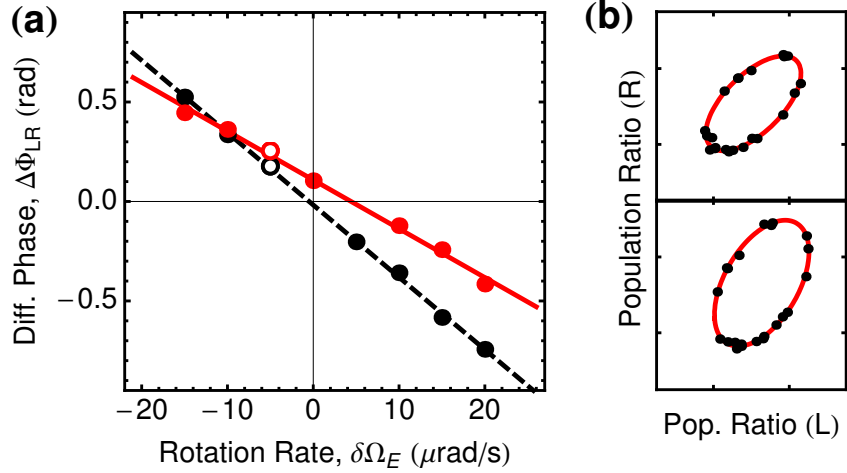


Figure 5.5: (a) PSI dual-axis gyroscope. We extract the differential phase  $\Delta\Phi_{LR}$  between the left and right sides of the ensemble as a function of the rotation rate  $\delta\Omega_E$ , as measured on cameras CCD1 (black, dashed) and CCD2 (red, solid). (b) Sample ellipses emerging from the right-versus-left population ratios of CCD2 (upper) and CCD1 (lower), corresponding to the open circles of part (a).

To compute spatial fringe contrast in Fig. 5.3, we divide the fitted amplitude of the population fringes by the fitted amplitude of the underlying cloud (see Sec. 5.7 for a detailed description of the fitting procedure). While fringes are visible on each raw image, we use Principal Component Analysis (PCA) as a filter to isolate the population fringe from the cloud shape in a model-independent way for more robust fits [115]. The fitted fringe frequency provides the magnitude of the phase gradient.<sup>4</sup>

## 5.4 Dual-axis gyroscope: a precision measurement of Earth's rotation rate

We also measure the rotation rate of the Earth. After coarsely compensating for the Earth's rotation with the tip-tilt stage, we tune the applied rate by adding a small

---

For maximum fringe contrast, the spatial fringe wavevector must be perpendicular to the camera LOS, aligning the planes of the population variation with the LOS.

<sup>4</sup>With an optimized imaging protocol, the minimum detectable PSI fringe period is limited by the initial cloud size ( $300 \mu\text{m}$  in this work). Our imaging process limits the minimum detectable fringe period to  $\sim 1 \text{ mm}$  (e.g., due to heating effects).

rotation  $\delta\Omega_E \equiv \Omega_C - \Omega_E$  along the nominal direction of true North ( $\phi_C \approx \phi_E + \pi$ ). We observe the resulting phase gradient simultaneously on CCD1 and CCD2. The magnitude of the observed phase gradient depends on the projection of the net rotation rate onto each camera [see Fig. 5.1(c)]. To detect small phase gradients that generate less than  $2\pi$  radians of phase across the ensemble, we extract the differential phase  $\Delta\Phi_{LR}$  by splitting each image about a vertical line and analyzing the left and right halves as independent interferometers.

Figure 5.5(a) shows  $\Delta\Phi_{LR}$  as a function of  $\delta\Omega_E$  as observed on CCD1 and CCD2. Each measurement is the result of 20 interferometer cycles. We parametrically plot the population ratio of the left half versus the right [e.g., Fig. 5.5(b)] and extract the differential phase and contrast using an ellipse fitting procedure [116, 117]. The horizontal intercept of a linear fit to this data provides a measurement of Earth's rotation rate with a precision of 200 nrad/s.

The difference in the intercepts observed by the two cameras indicates that the rotation compensation direction  $\phi_C$  is slightly misaligned from true North  $\phi_E$  such that  $\Delta\phi \equiv \phi_C - (\phi_E + \pi) \neq 0$ . This results in a spurious rotation ( $\Delta\phi\Omega_E \sin \phi_E$ )  $\hat{x}$  that imprints a phase gradient visible on CCD2 (see Table 5.1, term 2) independent of  $\delta\Omega_E$ . Likewise, a spurious rotation ( $-\Delta\phi\Omega_E \cos \phi_E$ )  $\hat{y}$  imprints a phase gradient visible on CCD1. The slopes for the two cameras in Fig. 5.5 are different because of unequal projection of  $\boldsymbol{\Omega}_E$  and small differences in the projected widths of the ensemble.

## 5.5 Record acceleration sensitivity

Although the mean interferometer phase is dominated by seismic noise contributions at long  $T$ , we can infer an acceleration sensitivity using the observed differential phase noise between different parts of the imaged cloud. Rather than compare the left half versus the right half as we did in the gyroscope analysis, we instead divide the output ports in two using a checkerboard pattern and study the differential phase between the combined even and combined odd grid squares. Varying the grid size  $s$  in this

analysis reveals correlated phase noise at different spatial scales.<sup>5</sup> Analyzing 280 trials with  $\Omega_C \approx -\Omega_E$ , we find the differential even-odd phase noise is 2.0 mrad per shot for grid sizes from  $s = 3$  mm down to 0.7 mm, the smallest size analyzed. Combined with the acceleration response (Table 5.1, term 1), this implies an acceleration sensitivity of  $6.7 \times 10^{-12}g$  in one shot,<sup>6</sup> an improvement of more than two orders of magnitude over previous limits [118]. By comparison, the atom shot-noise limit for the  $4 \times 10^6$  atoms used in this interferometer at 50% contrast is  $\sim 4 \times 10^{-12}g$  in one shot. Note that this grid analysis rejects low spatial frequency variations of the phase across the cloud that originate, for example, from fluctuations in initial kinematics. The results are applicable to measurements where these effects are expected to be common, such as for overlapped ensembles of two species of atoms in an equivalence principle test.

## 5.6 Further applications

PSI does not require a 10-meter apparatus. A dual-axis gyroscope with shot-noise-limited rotation noise of  $100 \mu\text{deg}/\sqrt{\text{hour}}$  can be realized with  $10^6$  atoms prepared at 3 mK in an interferometer with  $T = 10$  ms and  $4\hbar k$  atom optics cycling at 25 Hz (with atom recapture).

PSI can measure the interferometer beam optical wavefront in situ. This is desirable in precision atom interferometry applications, including gravitational wave detection [49]. Each atom in an expanding ensemble samples the laser phase at three locations, thereby measuring wavefront aberrations. Term 6 of Table 5.1 models the interferometer response to a parabolic wavefront curvature of the form  $k\alpha(x^2 + y^2)/2$ . Our measured phase noise implies a wavefront sensitivity of  $\alpha \sim \frac{\lambda}{500}/\text{cm}^2$  in one shot.

Finally, PSI allows measurement of multiple components of the gravitational gradient tensor (Table 5.1, term 5). The sensitivity we report is also sufficient to observe

<sup>5</sup>To ensure that results are independent of the initial grid registration, we compute two grid alignment quadratures (analogous to sine and cosine) for each dimension by offsetting the grid by  $s/2$  in each direction. We then average over alignment using the root mean square of these four results.

<sup>6</sup>The sensitivity is  $\delta a/g = \delta\phi/k_{\text{eff}}gT^2$ , where  $\delta\phi = (2.0 \text{ mrad})/\sqrt{2}$  is the absolute phase noise combining all the atoms from both the even and odd grid squares.

<sup>7</sup>Since a single trial takes 20 s, this per-shot sensitivity corresponds to  $3.0 \times 10^{-11} g/\sqrt{\text{Hz}}$ .

the gravity curvature induced phase shift (Table 5.1, term 4) [119]. Such sensitivity enables precision tests of the equivalence principle and general relativity [39, 71].

## Acknowledgements

The authors would like to acknowledge the valuable contributions of Tim Kovachy, Sheng-wei Chiow, Jan Rudolph and Philippe Bouyer. AS acknowledges support from the NSF GRFP. SMD acknowledges support from the Gerald J. Lieberman Fellowship. This work was supported in part by NASA GSFC Grant No. NNX11AM31A.

## 5.7 Principal component analysis

Principal Component Analysis (PCA) is a statistical analysis procedure that can identify correlations within a data set in a model-independent way [115]. When applied to a set of images, the result is a basis of orthonormal image vectors that spans the initial image set. These basis image vectors are called the principal components, and they are typically ordered by their variance. The higher the variance, or ‘strength,’ the better the basis image accounts for the variability of the set of images as a whole. By projecting a particular image in the original set onto a subspace of the principal component basis, we can isolate different correlations of interest from other correlations or backgrounds [81, 115].

Since interference is an anti-correlation between atom populations between output ports and (in the case of spatially-dependent phase) between neighboring slices within an output port, we can use PCA to distinguish between the constant overall shape of the ports, the interfering atom populations, and sources of technical noise (e.g. camera electronic noise) and systematic noise (e.g. launch velocity or cloud shape jitter).

In Fig. 5.6 we show the first six of 20 principal components for a set of 20 images. For this set, a rotation of  $40 \mu\text{rad}/\text{s}$  was applied in excess of what was required for rotation compensation. The lower (unpushed) port of the second principal component is also displayed in Fig. 2 of the main text. The first component shows the features most common in all the images of the set: the overall envelope of the two output ports.

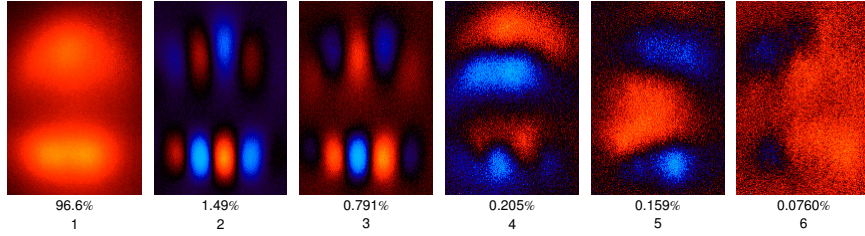


Figure 5.6: Normalized principal components, numbered according to their mean percentage overlap with the original images. These normalized basis images are colored to identify regions of correlation (same color) and anticorrelation (blue versus red). The upper port has been heated by the push used to spatially separate the two ports, resulting in a reduction of the contrast of the fringes in that port.

The next pair of principal components are the two quadratures of the fringe (sine and cosine). Both quadratures emerge as principal components because the input image set consists of images with widely varying overall interferometer phase (the phase is scanned randomly over multiple radians due to the vibrations of the retroreflection mirror). Any possible interferometer phase can be represented by a weighted sum of these two principal components. Note that given an infinite number of images with uniformly distributed phase, the variance of these two components should be identical; this is not the case for the specific finite data set used for Fig. 5.6 because in this set (by chance) there are more “sine-like” images than “cosine-like” images. Alternatively, given a set of images with a fixed interferometer phase (i.e., no vibration noise), the spatial fringes would appear on the first principal component as a common feature of all the images. Notice that a  $\pi$  phase shift between the two output ports of a single principal component is clearly visible in these images, a signature of interference. The depth of the fringes in the upper port is reduced due to heating from the optical push used to spatially separate the output ports.

PCA can be used as a filter by projecting each image into a subspace spanned by the strongest principal components. The projection onto the first three components (cloud shape, sine fringe, and cosine fringe) typically shows greater than 99% overlap with the original image. The higher principal components may nevertheless contain valuable information. The fourth component in Fig. 5.6, for example, shows a common-mode vertical correlation between the two output ports, indicative of a jitter

in the vertical launch velocity of the initial cloud. For higher principal components, however, the spatial frequencies tend to increase until the basis images appear to consist of high-frequency noise (not shown).

We take advantage of the linearity of PCA to robustly estimate the fringe contrast. We project each image in the set both onto (1) the overall cloud envelope (principal component 1) and separately onto (2) the subspace of the cosine and sine quadratures (principal components 2 and 3). We then independently fit these two projections for the un-pushed port, binned vertically to reduce dimensionality. The contrast is then given by the ratio of the amplitudes of those two fits. Fitting the fringe and the envelope separately increases the robustness of the fit by reducing cross-talk between fitting parameters.

We model the general shape of the upper ( $P_U(x, z)$ ) and lower ( $P_L(x, z)$ ) output ports as Gaussians in two dimensions (we have already integrated over the third dimension in the creation of the 2D image). The expected population distribution within each cloud depends on the interferometer phase, which we allow to vary transversely with  $x$ :  $\Delta\phi(x) = k_x x + \phi$ . If the clouds are well-separated, we can integrate (bin) over the vertical dimension, leaving to good approximation

$$P_U(x) = A_U e^{-\frac{x^2}{2\sigma_x^2}} \left( \frac{1}{2} + \frac{c}{2} \sin [k_x x + \phi] \right) \quad (5.1)$$

$$P_L(x) = A_L e^{-\frac{x^2}{2\sigma_x^2}} \left( \frac{1}{2} - \frac{c}{2} \sin [k_x x + \phi] \right) \quad (5.2)$$

The two output ports differ only by a  $\pi$  phase shift. When we use PCA, we fit each of the two terms in an output port separately. Considering just one port, the population in that port is modeled as

$$P_L(x) = P_1(x) + P_{\text{fringe}}(x) \quad (5.3)$$

$$P_1(x) = A_1 e^{-\frac{x^2}{2\sigma_x^2}} \quad (5.4)$$

$$P_{\text{fringe}}(x) = -A_{\text{fringe}} e^{-\frac{x^2}{2\sigma_x^2}} \sin [k_x x + \phi] \quad (5.5)$$

We then independently fit Eqs. 5.4 and 5.5 to the envelope and fringe projections,

respectively. Comparing Eq. 5.3 to Eq. 5.2 we see that the contrast  $c$  can be recovered by  $A_{\text{fringe}}/A_1$ , the ratio of the amplitude of the fringe to the amplitude of the envelope. The fit to the spatial frequency of the fringe,  $k_x$ , is a direct measurement of the phase gradient.

When the wavelength of the fringe is long compared to the cloud size, a fit to the fringe of a single output port cannot accurately determine the spatial frequency and the phase, leading to a mischaracterization of fringe amplitude and the contrast. In this small-gradient regime, ellipse analysis can provide more accurate information about the phase gradient.

# Chapter 6

## Enhanced atom interferometry readout through the application of phase shear

We present a method for determining the phase and contrast of a single shot of an atom interferometer. The application of a phase shear across the atom ensemble yields a spatially varying fringe pattern at each output port, which can be imaged directly. This method is broadly relevant to atom interferometric precision measurement, as we demonstrate in a 10 m  $^{87}\text{Rb}$  atomic fountain by implementing an atom interferometric gyrocompass with 10 millidegree precision.

This chapter also appeared as Ref. [2], and was written with collaborators Alex Sugrbaker, Jason M. Hogan, David M. S. Johnson, and Mark A. Kasevich.

### 6.1 Introduction

Light-pulse atom interferometers use optical pulses to split, redirect, and interfere freely-falling atoms [73]. They have proven widely useful for precision metrology. Atom interferometers have measured the gravitational [31, 32] and fine-structure [107] constants, are used in on-going laboratory tests of the equivalence principle [71] and general relativity [41, 59], and have been proposed for use in gravitational wave detection

[39, 40]. They have also enabled the realization of high performance gyroscopes [37], accelerometers [46], gravimeters [35], and gravity gradiometers [36].

Current-generation light-pulse atom interferometers determine phase shifts by recording atomic transition probabilities [73]. These are inferred from the populations of the two atomic states that comprise the interferometer output ports. Due to experimental imperfections, interference contrast is not perfect – the dark port never exhibits complete extinction. It is therefore necessary to independently characterize contrast prior to inferring phase. Typically, this is done with a sequence of multiple shots with different phases, such that the population ratio is scanned through the contrast envelope [120]. Such a protocol relies on the stability of the contrast envelope. In many cases, the contrast varies from shot to shot, introducing additional noise and bias in the phase extraction process.

We present a broadly applicable technique capable of resolving interference phase on a single experimental shot. This is accomplished by introducing a phase shear across the spatial extent of the atom ensemble. The shear is manifest in a spatial variation of the atomic transition probability, which, under appropriate conditions, can be directly observed in an image of the cloud [Fig. 6.1(b)]. Using this phase shear readout (PSR), it is no longer necessary to vary the phase over many shots to determine the contrast envelope. Instead, the contrast of each shot can be inferred from the depth of modulation of the spatial fringe pattern on the atom ensemble. The interferometer phase is directly determined from the phase of the spatial fringe.

PSR fringes reveal rich details about atom interferometer phase shifts and systematic effects, much as spatially varying optical interference patterns yield information about optical systems and their aberrations. The intentional application of a phase shear is analogous to the use of a wedged optical shear plate, where a large applied shear highlights small phase variations across a laser beam [121].

Previous work has employed spatial modulation of the atom population in a variety of atom interferometry experiments [45, 122–128]. Here we use beam pointing to introduce shear in a way that is broadly applicable to existing light-pulse interferometer configurations. In particular, this method does not require Bose-Einstein condensed or ultra-cold atomic sources. Moreover, manipulating and measuring the spatial

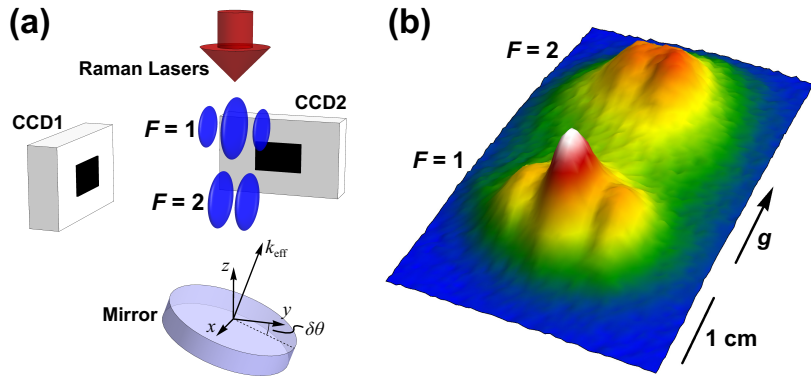


Figure 6.1: (a) Schematic diagram of the apparatus, showing beam-tilt phase shear readout. Atoms are cooled and launched upward into an interferometer region, not shown. Once they fall back to the bottom, the wavepackets are overlapped, yielding an interference pattern (blue fringes) imaged by two perpendicular cameras (CCD1,2). An additional optical pulse separates the output ports ( $F = 1$  and  $F = 2$ ) by pushing the  $F = 2$  atoms downwards. All atom-optics pulses are performed by lasers incident from above and retroreflected off of a piezo-actuated mirror. Tilting this mirror by an angle  $\delta\theta$  for the third atom-optics pulse yields a phase shear. (b) A fluorescence image of the atomic density distribution taken with CCD2 after interference. Spatial fringes result from a third-pulse tilt  $\delta\theta = 60 \mu\text{rad}$  about the  $x$ -axis. The pushed  $F = 2$  atoms are heated, yielding reduced apparent contrast, and we ignore the  $F = 2$  port in subsequent analysis.

population modulation facilitates measurements of small phase gradients, as we demonstrate by implementing a precise atom interferometric gyrocompass. Finally, we demonstrate arbitrary control over the phase shear axis by combining laser beam pointing and atom-optics pulse timing asymmetry.

## 6.2 Methods

The apparatus and methods are similar to our previous work [1]. Using evaporative cooling followed by a magnetic lens, we obtain a cloud of  $4 \times 10^6$   $^{87}\text{Rb}$  atoms with a radius of  $200 \mu\text{m}$  and a temperature of  $50 \text{ nK}$ .<sup>1</sup> These atoms are prepared in the magnetically insensitive  $|F = 2, m_F = 0\rangle$  state and launched vertically into an 8.7 m vacuum tube with a chirped optical lattice. They fall back to the bottom after 2.6 s, and we use a vertical fluorescence beam to image them onto two perpendicular CCD cameras (Fig. 6.1).

While the atoms are in free-fall in a magnetically shielded region [4], we perform light-pulse atom interferometry with a  $\pi/2 - \pi - \pi/2$  acceleration-sensitive configuration with a duration of  $2T = 2.3$  s. The atom-optics pulses are applied along the vertical axis using two-photon Raman transitions between the  $|F = 2, m_F = 0\rangle$  and  $|F = 1, m_F = 0\rangle$  hyperfine ground states (the lasers are detuned 1.0 GHz blue of the  $|F = 2\rangle \rightarrow |F' = 3\rangle$  transition of the D<sub>2</sub> line). The atom-optics light is delivered from above and retroreflected off of an in-vacuum piezo-actuated tip-tilt mirror.

The effective wavevector  $\mathbf{k}_{\text{eff}}$  of the Raman transitions is determined by the pointing direction of the retroreflection mirror [71], which is set for each atom-optics pulse with 1 nrad precision. The mirror has three independent piezo actuators in a tripod configuration that allow arbitrary 2-axis tip-tilt control. We compensate for phase shifts arising from Earth's rotation by applying appropriate tilts for each of the three pulses [1, 71], but additional mirror tilts can be used to induce shear for PSR.

---

<sup>1</sup>At this low density atomic collisions are negligible.

### 6.3 Generation of a controlled phase shear

To generate a controlled phase shear, we tilt the piezo-actuated mirror for the final  $\pi/2$  pulse by an angle  $\delta\theta$  with respect to the initial two pulses (in addition to the tilts needed for rotation compensation). In the semi-classical limit, the phase shift for a three-pulse interferometer is  $\Delta\Phi = \mathbf{k}_1 \cdot \mathbf{x}_1 - 2\mathbf{k}_2 \cdot \mathbf{x}_2 + \mathbf{k}_3 \cdot \mathbf{x}_3$ , where  $\mathbf{k}_i \equiv \mathbf{k}_{\text{eff},i}$  is the effective propagation vector at the time of the  $i$ th pulse and  $\mathbf{x}_i$  is the classical position of the atom [73, 120]. For example, tilting  $\mathbf{k}_3$  by an additional angle  $\delta\theta$  about the  $x$ -axis yields a phase  $\Phi_H = k_{\text{eff}} \delta\theta y_3$  across the cloud, where  $y_3$  is the horizontal position at the third pulse [Fig. 6.1(a)]. This shear is independent of the details of the previous atom-laser interactions and of the implementation of the atomic source (in particular, its spatial extent, temperature, and quantum degeneracy).

Figure 6.1(b) shows an image of the interferometer output with horizontal phase shear. An optical “pushing” pulse,  $5 \mu\text{s}$  long and resonant with the  $|F = 2\rangle \rightarrow |F' = 3\rangle$  transition, spatially separates the interferometer output ports.<sup>2</sup> Complementary fringes appear across each port, corresponding to the spatial variation of the atomic transition probability. For linear shears, we can write the phase as  $\phi(\mathbf{r}) = \boldsymbol{\kappa} \cdot \mathbf{r} + \phi_0$ , where  $\phi_0$  is the overall interferometer phase and  $\boldsymbol{\kappa}$  is the wavevector of the spatially varying component. This implies a spatial modulation of the atomic distribution given by  $P(\mathbf{r}) = \frac{1}{2} + \frac{C}{2} \sin(\boldsymbol{\kappa} \cdot \mathbf{r} + \phi_0)$ , where  $C$  is the contrast.

Since the retroreflection mirror can be tilted about an arbitrary horizontal axis, beam-tilt PSR can yield fringe patterns with  $\hat{\boldsymbol{\kappa}}$  anywhere in the  $xy$  plane, orthogonal to the laser beam axis [see Fig. 6.1(a)]. For instance, it is possible to choose a tilt axis parallel to the line-of-sight of either CCD. We then see a spatial fringe pattern with one camera, but no contrast with the other. Hereafter, we tilt about the  $x$ -axis, yielding fringes on CCD2.

The spatial frequency  $\kappa$  of beam-tilt PSR fringes is set by the tilt angle  $\delta\theta$ . Figure 6.2(b) shows the expected linear dependence. By appropriate choice of  $\delta\theta$ , the fringe period can be tuned to an arbitrary value (in practice, high spatial frequencies are limited by the depth of focus of the imaging system). Because we detect the atoms

---

<sup>2</sup>We spatially separate the output ports because the imaging procedure is not state selective.

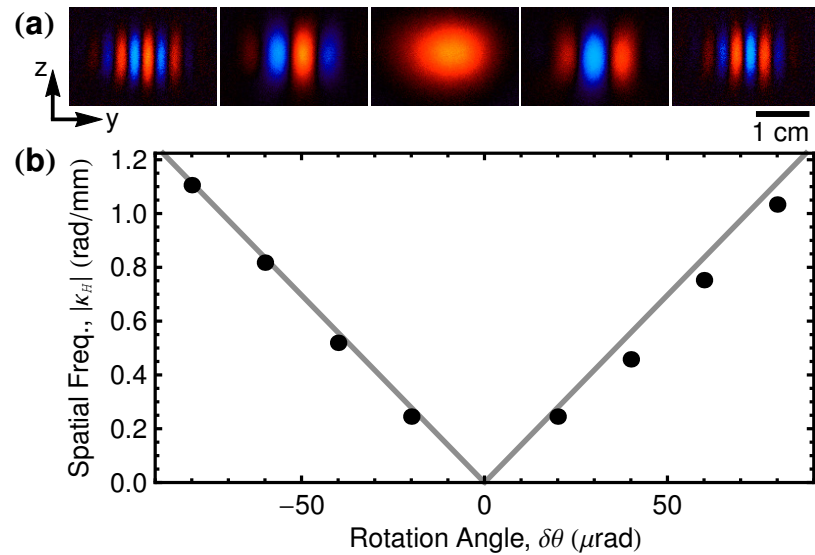


Figure 6.2: Horizontal fringes resulting from beam-tilt PSR in a  $2T = 2.3$  s interferometer. (a) Spatial fringes observed on CCD2 with third-pulse tilt angles  $\delta\theta = -80, -40, 0, +40, +80 \mu\text{rad}$  (left to right). Red versus blue regions show anti-correlation in atom population. Each image is the second-highest variance principal component arising from a set of 20 fluorescence images [1]. (b) Measured fringe spatial frequency  $|\kappa_H|$ , resulting from images filtered using principal component analysis [1,115]. We bin the images vertically and fit a Gaussian modulated by the interference term  $P(\mathbf{r})$ . The curve is a prediction with no free parameters that includes a reduction in the measured wavelength from heating during imaging [129].

at a final drift time  $t_d = 2.7$  s that is later than the third pulse time  $t_3 = 2.5$  s (both measured from the time of trap release), we must correct for the continued motion of the atoms. In the limit where the initial size of the atomic source is much less than the final spatial extent of the cloud (point source limit [1, 130]), the position at  $t_d$  of an atom with velocity  $v_y$  is  $y \approx v_y t_d \approx y_3 t_d / t_3$ . The detected horizontal fringe spatial frequency is then  $\kappa_H \equiv \partial_y \Phi_H = k_{\text{eff}} \delta\theta t_3 / t_d$ .

## 6.4 Deterministic readout of phase via phase shear

We demonstrate single-shot phase readout by implementing a short interferometer sequence ( $2T = 50$  ms) near the end of the 2.7 s drift time. In this case, the atom cloud has a large spatial extent for the entire pulse sequence. For each shot, we set the interferometer phase with an acousto-optic modulator and read it back using beam-tilt PSR with  $\delta\theta = 60 \mu\text{rad}$ . Figure 6.3 shows the expected correspondence between the applied and measured phases. The spread in the measured phase is due to technical noise associated with spurious vibrations of the Raman laser beam delivery optics. This spread exceeds  $2\pi$  at longer interrogation times, but fringe fits still yield a precise phase for each shot.

## 6.5 Gyrocompass: a precision measurement of the direction of true North

To show how PSR can enable precision measurements, we implement an atom interferometric gyrocompass in a long interrogation time ( $2T = 2.3$  s) configuration. In this case, the Raman laser axis is rotated to compensate Earth's rotation, keeping this axis inertially fixed throughout the interrogation sequence. At the latitude of our lab in Stanford, California, this corresponds to an effective rotation rate of  $\Omega_E = 57.9 \mu\text{rad/s}$  about an axis along the local true North vector, which is at an angle  $\phi_E \approx 15^\circ$  with respect to the negative  $x$ -axis (coarsely determined cartographically). However, a small misalignment  $\delta\phi_E \ll 1$  between the rotation axis of the retroreflection mirror

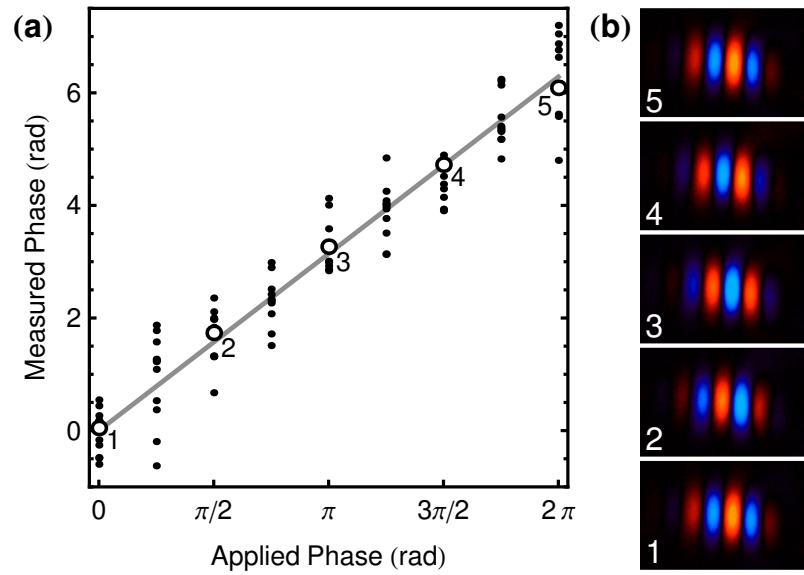


Figure 6.3: Single-shot phase readout with a  $2T = 50$  ms interferometer. (a) Measured phase versus the applied phase of the final atom-optics pulse for 96 shots. A line with unity slope is shown for reference. The measured phase is fit from images like those in (b). The measurement scatter is dominated by vibrations of the Raman laser beam delivery optics. (b) Five sample interferometer shots [open circles in (a)], separated in measured phase by  $\sim \pi/2$  rad. All images are filtered with principal component analysis.

and true North results in a residual rotation  $\delta\Omega \approx \delta\phi_E\Omega_E (\sin\phi_E\hat{x} - \cos\phi_E\hat{y})$  that leads to a Coriolis phase shift  $\Phi_C = 2\mathbf{k}_{\text{eff}} \cdot (\delta\Omega \times \mathbf{v}) T^2$  that varies across the cloud. As before, in the point source limit  $v_y \approx y/t_d$ , so the Coriolis phase gradient is  $\kappa_{C,y} \equiv \partial_y \Phi_C = 2k_{\text{eff}} T^2 \delta\phi_E \Omega_E \sin\phi_E / t_d$ . To realize a gyrocompass, we vary the axis of applied rotation by scanning  $\delta\phi_E$ , and identify true North with the angle at which  $\kappa_{C,y} = 0$ .

It can be challenging to measure small phase gradients with spatial frequencies  $\kappa \ll 1/\sigma$ , where  $\sigma$  is the width of the atom ensemble. In this limit, less than one fringe extends across the cloud, so the fringe fitting method in Fig. 6.2(b) cannot be used. Instead, the gradient can be estimated by measuring phase differences across the ensemble (e.g., with ellipse fits [1, 116]), but this procedure can be sensitive to fluctuations in the atomic density distribution (width, position, and shape).

To circumvent these issues, we take advantage of PSR by applying an additional shear that augments the residual Coriolis shear  $\Phi_C$ . An additional tilt of  $\delta\theta = \pm 60 \mu\text{rad}$  about the  $x$ -axis is added for the final interferometer pulse. This introduces a horizontal shear  $\Phi_H$  with approximately 2.5 fringe periods across the cloud, enough to use fringe fitting to extract the spatial frequency. Subtracting off the known contribution of the additional tilt then yields a measurement of the small residual Coriolis shear. This technique of shifting a small phase gradient to a larger spatial frequency is analogous to a heterodyne measurement in the time domain. In both cases, the heterodyne process circumvents low frequency noise.

Depending on the sign of the tilt angle, the applied shear adds to or subtracts from  $\Phi_C$ . The combined phase gradient is then  $\kappa_{\pm} \equiv k_{\text{eff}} |\delta\theta| t_3 / t_d \pm \kappa_{C,y}$ . By alternating the sign of the additional  $60 \mu\text{rad}$  tilt and subtracting the results, we realize a differential measurement whereby systematic uncertainty in the applied shear is mitigated:  $\Delta\kappa \equiv \kappa_+ - \kappa_- = 2\kappa_{C,y}$ , independent of  $|\delta\theta|$ .

Figure 6.4 shows the expected linear scaling of the differential spatial frequency  $\Delta\kappa$  as a function of the applied rotation angle  $\delta\phi_E$ . A linear fit to the data yields a horizontal intercept that indicates the direction of true North with a precision of 10 millidegrees. An apparatus optimized for gyrocompass performance could achieve similar or better precision in a more compact form factor. Also, this method does

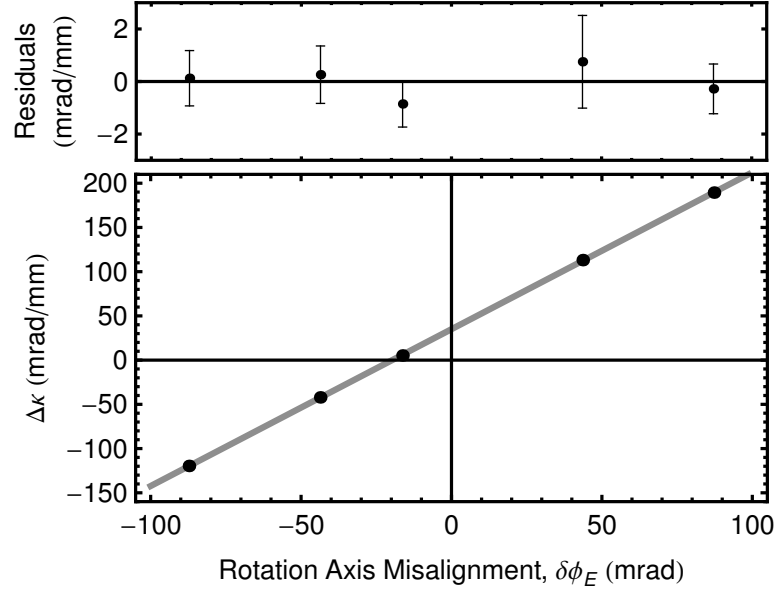


Figure 6.4: Gyrocompass using PSR. Each  $\Delta\kappa$  point is the combination of 40 trials, 20 each at two applied tilt values ( $\delta\theta = \pm 60 \mu\text{rad}$ ). The horizontal intercept of a linear fit gives the direction of true North.

not require a vibrationally stable environment since the measurement uses the fringe period, not the overall phase.

## 6.6 Arbitrary control of the applied phase shear

Finally, we show how combining beam tilts and interferometer timing asymmetries provides arbitrary control over the spatial wavevector  $\kappa$  of the applied phase shear. While a beam tilt applies a shear transverse to the interferometer beam axis, timing asymmetry yields a shear parallel to the beam axis ( $\kappa \parallel \mathbf{k}_{\text{eff}}$ ) in the point source limit [45]. To create an asymmetric interferometer, we offset the central  $\pi$  pulse by  $\delta T/2$  such that the time between the first and second pulses ( $T + \delta T/2$ ) is different from the time between the second and third pulses ( $T - \delta T/2$ ). The resulting phase shift,  $\Phi_V = k_{\text{eff}} v_z \delta T$ , depends on the atoms' Doppler shift along the direction of  $\mathbf{k}_{\text{eff}}$ . The phase shear at detection is then  $\kappa_V = \partial_z \Phi_V = k_{\text{eff}} \delta T / t_d$ . Figure 6.5(a) shows the

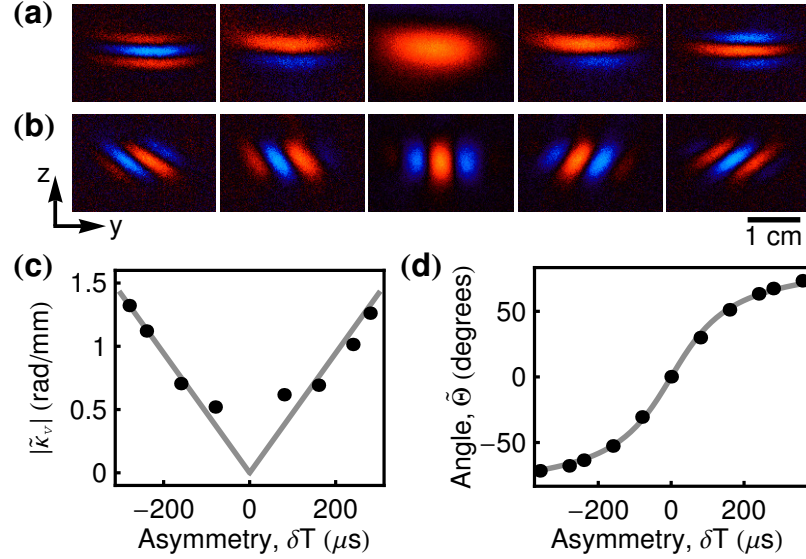


Figure 6.5: Arbitrary control of spatial fringe direction. (a) Second-highest variance principal components from sets of 20 trials with timing asymmetry  $\delta T = -240, -160, 0, +160, +240 \mu\text{s}$  (left to right) (b) Comparable images for trials with both a beam tilt  $\delta\theta = 40 \mu\text{rad}$  and  $\delta T = -160, -80, 0, +80, +160 \mu\text{s}$ . (c) Measured fringe spatial frequency extracted from fits to principal component filtered images with vertical fringes. (d) Measured fringe angle extracted from fits to images with tilted fringes. In both (c) and (d) the curves are predictions with no free parameters.

resulting vertical fringes, which are orthogonal to those from beam tilts [Fig. 6.2(a)] and are simultaneously visible on both CCD cameras. The fitted fringe frequency shown in Fig. 6.5(c) exhibits the expected linear dependence on  $\delta T$ , deviating at low spatial frequency due to the difficulty of fitting a fringe with  $\kappa \sim 1/\sigma$ .

For vertical fringes, the imaging pulse reduces the detected spatial frequency by stretching the cloud vertically. We independently characterize this stretch by measuring the fringe period as a function of imaging duration  $\tau$  and extrapolating to  $\tau = 0$ . The results indicate a fractional stretch rate of  $\alpha = 0.12 \text{ ms}^{-1}$ . The modified prediction for the spatial frequency is  $\tilde{\kappa}_v = \kappa_v / (1 + \alpha\tau)$ . With the  $\tau = 2 \text{ ms}$  imaging time used, this agrees well with the measurements of Fig. 6.5(c) with no free parameters.

By combining beam tilt shear  $\kappa_H$  with timing asymmetry shear  $\kappa_V$ , we can

create spatial fringes at arbitrary angles. The composite shear is at angle  $\Theta = \arctan(\kappa_V/\kappa_H) = \arctan[\delta T / (\delta\theta t_3)]$ . Figures 6.5(b) and (d) show fringe images and extracted angles using a  $\delta\theta = 40\,\mu\text{rad}$  beam tilt combined with a range of timing asymmetries. To find the angles, we apply Fourier and principal component filters and fit with a two-dimensional Gaussian envelope modulated by an interference term  $P(\mathbf{r})$ . We again correct for stretching during detection, which affects the measured angles. The modified prediction,  $\tilde{\Theta} = \arccot[(1 + \alpha\tau)\cot\Theta]$ , shows good agreement with the measured angles of Fig. 6.5(d) with no free parameters.

## 6.7 Further applications

We have demonstrated a precision gyrocompass with PSR, but arbitrary control of the shear angle facilitates measurements of phase shifts and gradients from any origin. For example, a vertical gravity gradient  $T_{zz}$  induces a phase shear  $k_{\text{eff}} T_{zz} v_z T^3$ . This translates the measured angles of Fig. 6.5(d) such that  $\Theta = \arctan[(\delta T - T_{zz} T^3) / (\delta\theta t_3)]$ . For our parameters, this yields an effective asymmetry of 2 ns/E. PSR also enables measurements of nonlinear phase variations, including optical wavefront aberrations [1]. For precision measurements dependent on absolute phase (gravimetry, atomic recoil measurements, etc.), PSR can suppress systematic error by making phase measurements independent of drifts in the contrast envelope. Finally, we expect PSR to be enabling for future inertial sensors operating on dynamic platforms, where single shot estimation of phase and contrast is vital.

## Acknowledgements

The authors would like to thank Philippe Bouyer, Sheng-wei Chiow, Tim Kovachy, and Jan Rudolph for valuable discussions and contributions to the apparatus. AS acknowledges support from the NSF GRFP. SMD acknowledges support from the Gerald J. Lieberman Fellowship. This work was supported in part by NASA GSFC Grant No. NNX11AM31A.

# Chapter 7

## Delta-kick cooling with magnetic fields and light

### 7.1 Matter wave lensing

Using a matter wave lens and a long time-of-flight, we cool an ensemble of  $^{87}\text{Rb}$  atoms in two dimensions to an effective temperature of less than  $50_{-30}^{+50}$  pK. A short pulse of red-detuned light generates an optical dipole force that collimates the ensemble. We also report a three-dimensional magnetic lens that substantially reduces the chemical potential of evaporatively cooled ensembles with high atom number. These cooling techniques yield bright, collimated sources for precision atom interferometry. By observing such low temperatures, we set limits on proposed modifications to quantum mechanics.

This section also appeared as Ref. [3], and was written with collaborators Tim Kovachy, Jason M. Hogan, Alex Sugarbaker, Christine Donnelly, Chris Overstreet, and Mark A. Kasevich.

#### 7.1.1 Introduction

The development of techniques to produce colder atomic ensembles has driven numerous advances in atomic physics, including enhanced capabilities in precision measurement

[1, 131, 132], quantum information [133], and quantum simulation [134]. A longstanding goal has been to demonstrate efficient cooling protocols to reach effective temperatures of tens of pK, enabling ultra-precise atomic sensors with applications including geodesy [49], tests of general relativity [42, 45, 118], gravitational wave detection [40, 49], and tests of quantum mechanics [66].

Evaporative cooling in an adiabatically relaxed trap offers one route to extremely low temperatures [135]. A powerful alternative cooling method,<sup>1</sup> often called delta-kick cooling, is to freely expand an atom cloud and then reduce its velocity spread with a collimating lens [111, 136–142]. Compared to evaporation, lensing typically requires less time and avoids intrinsic atom loss. The lens is implemented by a transient harmonic potential, realized magnetically [112, 137], electrostatically [143], or optically [136]. In previous work, lensing has yielded effective temperatures as low as  $\sim 1$  nK [45, 144].

The potential cooling performance of such a lens depends on the available expansion time. Consider an initial atom ensemble (condensate or thermal state) with RMS size  $\Delta x_o$  and velocity spread  $\Delta v_o$ , allowed to expand for a time  $t_o$  before application of the lens potential. The temperature ratio is  $\eta \equiv (\Delta v_\ell / \Delta v_o)^2$ , where  $\Delta v_\ell$  is the RMS velocity after the lens is applied. For an ideal harmonic potential that has been tuned to minimize  $\Delta v_\ell$  (the collimation condition), the expected temperature ratio is bounded by  $\eta_c = (\Delta x_o / \Delta x_\ell)^2 \equiv \gamma^2$ , where  $\Delta x_\ell$  is the RMS size of the ensemble when the lens is applied and  $\gamma$  is the size ratio [136]. Correlations between position and velocity in the initial ensemble (e.g., arising from mean field interactions during expansion) can lead to temperatures that are lower than this bound [145]. Generally, to achieve low temperatures it is beneficial to have a long expansion time so that  $\Delta x_\ell \approx \Delta v_o t_o \gg \Delta x_o$ .

In this work, we use a long expansion time  $t_o > 1$  s in a 10 m vacuum tube to demonstrate long-time delta-kick cooling, continuously manipulating the RMS velocity of ensembles of <sup>87</sup>Rb atoms through a minimum value of  $< 70$   $\mu\text{m/s}$ . This corresponds to 50 pK effective temperatures at collimation (we define the effective temperature  $T$  by  $\frac{1}{2}k_{\text{B}}T = \frac{1}{2}m\Delta v^2$ , where  $m$  is the atom mass [78]). The dipole lensing potential [78, 136]

---

<sup>1</sup>Here ‘cooling’ is understood to mean effective temperature reduction. The lens does not reduce the ensemble phase space density.

is generated from the transverse intensity profile of a vertically-propagating Gaussian beam, providing cooling in two dimensions. As a pre-cooling stage, we implement three-dimensional lens cooling using a magnetic potential.

An ideal harmonic lens (frequency  $\omega$ ) exerts a force  $F_H = -m\omega^2x$ , where  $x$  is the transverse position. For the dipole potential lens, the lens duration  $\delta t$  is short (thin-lens limit,  $\omega\delta t \ll 1$ ), so we may approximate its effect as an impulse that changes the atom's velocity by  $\delta v(x) = -\omega^2\delta t x$ . The lens focal time is defined as  $1/f \equiv \omega^2\delta t$  so that a point source of atoms expanding for time  $f$  would be perfectly collimated.

At pK temperatures, the time necessary for the ensemble size to noticeably increase can be very long ( $> 10$  s), making time-of-flight expansion an ineffective probe of temperature. To circumvent this, we extend the duration of the dipole-potential lens interaction beyond the collimation condition to refocus the ensemble. As in optics, the minimum achievable image size after refocusing is a measure of the degree of collimation. Thus, we can infer the collimated temperature of the atom ensemble from the refocused cloud size.<sup>2</sup>

To formalize this relationship, we solve the quantum Liouville equation for the evolution of an arbitrary initial state during the lensing sequence. In the delta-kick limit ( $\omega\delta t \ll 1$ ) this reduces to solving the classical Liouville equation [30, 147, 148]. To account for aberration in the lens, we assume a general  $F(x)$  for the lens force. Calculating the expectation values of the velocity width of the distribution after the lens and the position width at detection, we find that the minimum refocused size  $(\Delta x_i)_{\min}$  sets a bound on the minimum velocity spread  $\Delta v_\ell$  achievable at collimation. By this metric, the minimum velocity variance for the lens (including aberrations) can be inferred by:

$$(\Delta v_\ell)^2_{\text{bound}} \equiv \frac{(\Delta x_i)_{\min}^2}{t_i^2} = \Delta v_\ell^2 + \delta A \gtrsim \Delta v_\ell^2 \quad (7.1)$$

where  $t_i$  is the time between the lens and detection ('image time'), and  $\delta A$  arises from lens aberrations present during refocusing. For a wide class of aberrations (including those encountered in this work),  $\delta A$  is positive, so  $(\Delta v_\ell)^2_{\text{bound}}$  provides an upper bound on the collimated temperature.<sup>3</sup>

---

<sup>2</sup>An analogous method has been used to measure the temperature of electron beams [146].

<sup>3</sup>Correlations between lens aberrations and the initial atom distribution can yield  $\delta A < 0$ , but

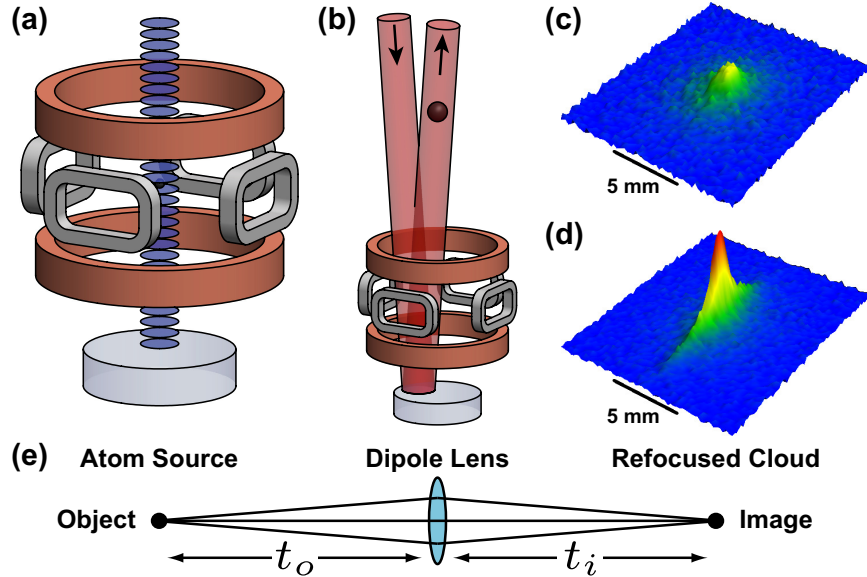


Figure 7.1: (a) Schematic of the apparatus (including vertically-oriented quadrupole trap, horizontal TOP coil pairs, and blue-detuned launching lattice). (b) A 3 W laser, 1.0 THz red-detuned from the  $^{87}\text{Rb}$   $D_2$  line, acts on the atom cloud as a dipole lens (the  $\sim 1$  mrad beam angle is exaggerated for clarity). (c) Fluorescence image of a 1.6 nK cloud after 2.8 s of free-fall. (d) The distribution in (c) refocused using the dipole lens. There is no observed axial heating. (e) Optical analogy showing the object, lens, and image, with object distance  $t_o$  and image distance  $t_i$ .

### 7.1.2 Methods

The cooling performance demonstrated here depends critically on an optics configuration that minimizes aberration by reducing spatial intensity perturbations on the dipole-lensing beam. The beam is spatially filtered by propagation through an optical fiber and collimated to a  $1/e^2$  radial waist of  $\sigma = 3.4$  mm. Intensity perturbations with spatial frequency  $\kappa$  lead to forces  $\propto \kappa$ , so high spatial frequency perturbations ( $\kappa\sigma > 1$ ) are particularly detrimental [147]. For example, a 1% perturbation with  $\kappa \sim (100 \mu\text{m})^{-1}$  can result in a spurious force comparable in magnitude to the lensing force, substantially heating the cloud. To avoid this, the beam propagates for 16 m or more from the collimation lens (retroreflected after 10.6 m) before interacting with

---

even in the worst case the correction to  $(\Delta v_\ell)_{\text{bound}}$  is within our stated uncertainty.

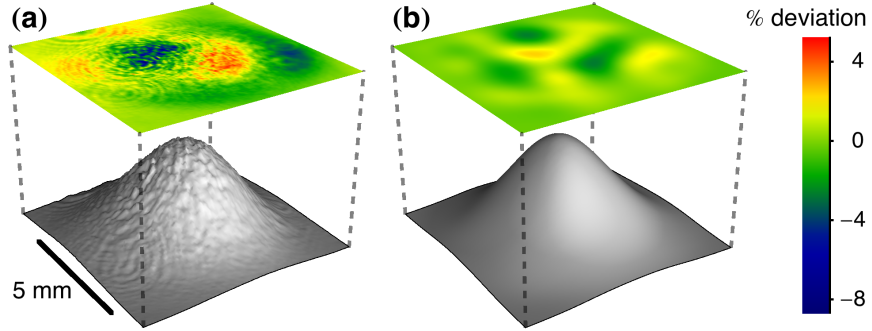


Figure 7.2: Comparison of the dipole lens beam intensity profile after numerical paraxial wave propagation of the measured profile by (a) 0.25 m and (b) 16.25 m. The residuals of fitting a 2D Gaussian are shown above each beam profile.

the atoms [Fig. 7.1(b)], allowing high spatial frequencies to diffract from the beam (Fig. 7.2). With  $\delta t = 30$  ms and  $t_o = 1.1$  s, the lens substantially refocuses the atoms at a time  $t_i = 1.8$  s later [Fig. 7.1(d)].

The atom source is a cloud of  $10^5$   $^{87}\text{Rb}$  atoms with initial RMS size<sup>4</sup>  $\Delta x_o = 56 \mu\text{m}$  and an effective temperature of  $1.6 \pm 0.1$  nK [Fig. 7.1(c)]. To prepare this ultracold source, we evaporate in a time-orbiting potential (TOP) trap [Fig. 7.1(a)]. The atoms are further cooled with a magnetic lens (details follow) and prepared in a magnetically-insensitive state. We then launch them upwards into a 10 m vacuum tube with a chirped optical lattice [1, 149]. After 2.8 s,<sup>5</sup> the atoms fall back down, and we image them with a vertical fluorescence beam onto two CCD cameras (looking from North and West).

### 7.1.3 Optical dipole lensing to picokelvin temperatures

To evaluate the performance of the optical lens, we vary the lens duration and measure the width of the lensed cloud. As the lens acts only transversely, we bin the corresponding images in the vertical dimension and analyze in 1D. Extracting cloud widths requires accounting for the point spread function (PSF) of the imaging system.

<sup>4</sup>Determined by Gaussian fits to absorption images.

<sup>5</sup>The release from the magnetic trap occurs 100 ms before the end of the lattice launch.

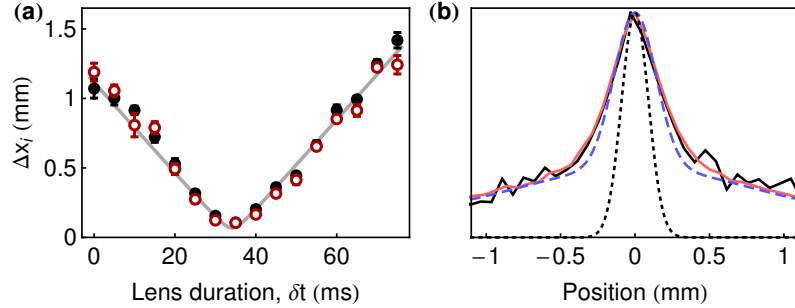


Figure 7.3: (a) Filled black (open red) points denote measured RMS cloud widths on the North (West) camera. Each point is the weighted mean of Gaussian fits to 6 experimental shots. The dashed gray curve is a simultaneous fit to the measurements from both cameras and reports a minimum size of 70  $\mu\text{m}$  at a lens duration of 34 ms. (b) Vertically-binned images comparing the transverse size of a  $90 \pm 10 \mu\text{m}$  cloud used to characterize the PSF (solid red/gray) to a cloud refocused 2.8 s later (solid black). The good overlap indicates high-fidelity refocusing. Dotted black: Gaussian profile extracted from a fit of the refocused cloud. The fit accounts for the broadening and distorting effects of the PSF (dashed blue).

We fit all imaged clouds to a Gaussian profile convolved with a smooth representation of the PSF [147].

To characterize the PSF, we fit a cloud with a known, small size; this fixes the PSF parameters for subsequent analysis. We use a cloud imaged after a short drift time (100 ms; the time needed to reach the fluorescence imaging region) as the small source [Fig. 7.3(b)]. To directly measure this cloud’s size, we image it with a low-aberration imaging system.<sup>6</sup> The measured width of  $90 \pm 10 \mu\text{m}$  is consistent with an extrapolation from the known cloud parameters at the end of the TOP sequence.

Figure 7.3(a) shows the fitted transverse cloud size  $\Delta x_i$  versus lens duration  $\delta t$  for the two camera axes, demonstrating the continuous variation of the atom cloud through collimation and refocus. For this data, the lens is applied  $t_i = 1.8$  s before

<sup>6</sup>This imaging system was not used for primary data collection because of its comparatively poor photon collection efficiency.

detection. We fit the data with the predicted cloud size [147],

$$\Delta x_i^2 = (\Delta x_i)_{\min}^2 + \frac{1}{m^2} \Delta F^2 t_i^2 (\delta t - \delta t_{\min})^2 \quad (7.2)$$

where  $\Delta F^2$  is a fitting parameter characterizing the variance of the lensing force (including any aberrations), and  $\delta t_{\min}$  is the lens duration to refocus the cloud.

The point at  $\delta t = 35$  ms is nearest to the fitted refocusing time and sets the best bound on the achievable collimation temperature  $T$ . From Eq. 7.1, we find that  $(\Delta v_\ell)_{\text{bound}} \equiv (\Delta x_i)_{\min}/t_i = 65 \pm 20$   $\mu\text{m/s}$  for the North axis and  $70 \pm 25$   $\mu\text{m/s}$  for the West axis. These bound the effective temperature at collimation to below  $T_{\text{bound}} \equiv m(\Delta v_\ell)_{\text{bound}}^2/k_B = 40_{-20}^{+40}$  pK and  $50_{-30}^{+50}$  pK for the North and West axes, respectively. This  $T_{\text{bound}}$  estimate includes extra heating  $\delta A$  that arises between collimation time  $\delta t_c$  and refocus  $\delta t_{\min}$ . Since heating from aberrations scales as  $\delta t^2$ , we can estimate  $T$  by multiplying the aberration contribution  $((\Delta v_\ell)_{\text{bound}}^2 - \gamma^2 \Delta v_o^2)$  by  $(\delta t_c/\delta t_{\min})^2 \approx (0.6)^2$ , yielding effective temperatures of  $30_{-10}^{+10}$  pK and  $35_{-10}^{+15}$  pK for the North and West axes, respectively [147]. The temperature uncertainties result primarily from the standard deviation of the measured cloud sizes, likely caused by shot-to-shot fluctuations in the strength of the lens (e.g., due to fluctuations in optical power or alignment). Uncertainties in the measured PSF do not contribute significantly.

Next, we measure the refocused cloud size  $(\Delta x_i)_{\min}$  and corresponding lens duration  $\delta t_{\min}$  for various lens application times  $t_o$ , with the total atom drift time held constant (Fig. 7.4). Each point is the result of a fit of Eq. 7.2 to a scan of the lens duration [like Fig. 7.3(a)] at one of four fractional object times:  $t_o/(t_o + t_i) = 0.32, 0.39, 0.60$ , and  $0.71$ . Also shown is the ideal harmonic lens scaling for  $(\Delta x_i)_{\min}$  and  $\delta t_{\min}$ . Neglecting  $x\text{-}v$  correlations, the focal time  $f_{\min} \equiv (\omega^2 \delta t_{\min})^{-1}$  satisfies the thin lens formula from geometric optics  $\frac{1}{f_{\min}} = \frac{1}{t_i} + \frac{1-\gamma^2}{t_o}$  (the  $\gamma$  correction results from finite velocity spread and vanishes in the point source limit  $\gamma \ll 1$ ). An identical correction arises in optics with a finite source divergence, e.g., a Gaussian laser beam) and the image size  $(\Delta x_i)_{\min} = \Delta x_o \frac{t_i}{t_o} \sqrt{1 - \gamma^2}$  scales as the magnification of the lens  $\frac{t_i}{t_o}$ .

The deviation of the data in Fig. 7.4 from the harmonic lens theory results

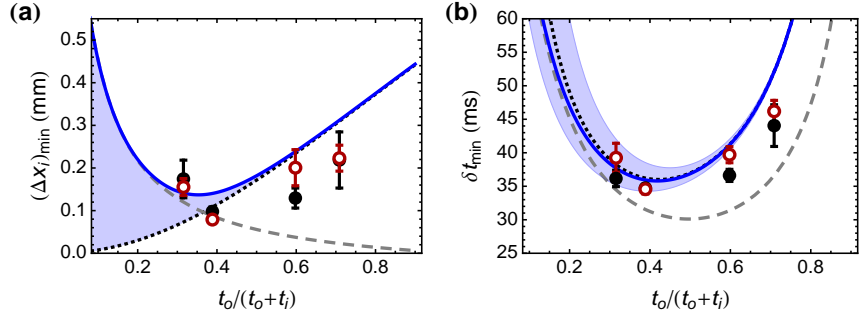


Figure 7.4: (a) Minimum RMS width of the cloud as a function of the fractional object time. (b) The lens duration required to refocus the atom cloud. The filled black (open red) points represent measurements on the North (West) camera. Solid blue: expected behavior for a cloud of finite initial size ( $56 \mu\text{m}$ ) and no initial  $x$ - $v$  correlations in an optical beam with a Gaussian profile. The blue shaded regions represent the corresponding ranges possible with correlations. The curve in (a) has no free parameters. For (b), the optical power is a free parameter that fits to 2.8 W. Dashed gray: expected behavior for an ideal harmonic potential of the same strength as at the center of the beam [147]. Dotted black: expected behavior for a cloud with zero initial size subject to Gaussian aberrations.

primarily from large-scale aberrations due to the Gaussian profile of the optical potential. Modeling the lens potential as a 2D Gaussian, we calculate  $(\Delta x_i)_{\min}$  and  $\delta t_{\min}$  assuming Gaussian initial ensemble velocity and position distributions (Fig. 7.4) [147]. Although the cooling performance of the lens is partially limited by the finite expansion time  $t_o$ , further extending  $t_o$  would not improve cooling performance, since a larger  $\Delta x_e$  would increase the effect of Gaussian aberration.

The ability to transversely cool an atom cloud to very low effective temperatures and to precisely refocus the cloud after long drift times enables many atom optics applications [1, 45]. Refocusing the atoms allows us to extend the effective free-fall time to 5.1 s by relaunching the ensemble. Without refocusing, the cloud is larger than the launch lattice beams, and the relaunch is inefficient. Similarly, a series of relay lenses (or an initial collimation lens) could be integrated with light-pulse atom interferometry to maintain a small transverse cloud size at the beamsplitter pulses, even for very long interrogation times. This would ensure a homogeneous atom optics

beam intensity across the cloud, which is critical for large momentum transfer atom interferometry [81].

### 7.1.4 Magnetic lensing to nanokelvin temperatures

To minimize the impact of anharmonicities of the dipole lensing beam, we pre-cool the atoms with a magnetic lens. This increases the effective  $f/\#$  of the dipole lens by reducing the duration  $\delta t$  required for collimation. It has the added benefit of cooling along the third axis not addressed by the dipole lens.

The magnetic lens is performed by abruptly releasing tightly-confined atoms into a shallow harmonic potential provided by a 2.6 kHz TOP trap with spinning bias field  $B_0$  and radial quadrupole gradient  $\nabla B$  [Fig. 7.1(a)] [150]. Abruptly turning off the shallow trap when the ensemble has reached its maximum size yields a colder cloud [112].

A full expansion of the cloud occurs twice every trap period. Synchronizing the radial ( $\rho$ ) and vertical ( $z$ ) oscillations to optimize 3D cooling requires a trap frequency ratio of  $\omega_z/\omega_\rho = (n_z + 1/2) / (n_\rho + 1/2)$  for integers  $n_z$  and  $n_\rho$ . In the absence of gravity, the irrational ratio  $\omega_z/\omega_\rho = 2\sqrt{2}$  makes perfect synchronization impossible, but with gravity the ratio is tunable by selecting the appropriate gradient  $\nabla B$  [151].

Figure 7.5(a) shows the evolution of the cloud while in the lens. The center of mass oscillates vertically because the atoms start above the minimum of the shallow trap. To better illustrate the effect of the magnetic lens on the cloud shape, we use a hotter evaporated source with a release temperature of  $1.4 \mu\text{K}$  (dominated by chemical potential). We plot the evolution of the cloud widths (from 2D Gaussian fits) in Fig. 7.5(b).<sup>7</sup> The peak of the third vertical expansion ( $n_z = 3$ ) aligns with that of the second radial expansion ( $n_\rho = 2$ ).<sup>8</sup>

To precisely tune the lens duration for minimum temperature, we launch the atoms to the top of the tower for a long-time-of-flight velocity measurement. A 162 ms lens duration gives a minimum effective temperature of  $(T_\rho, T_z) = (50, 40) \text{ nK}$  and reduced

<sup>7</sup>The cloud shape is in general non-Gaussian due to the anharmonicity of the trap.

<sup>8</sup>With  $n_z = n_\rho = 0$ , the shallower trap allows for more expansion but has larger effective anharmonicities.

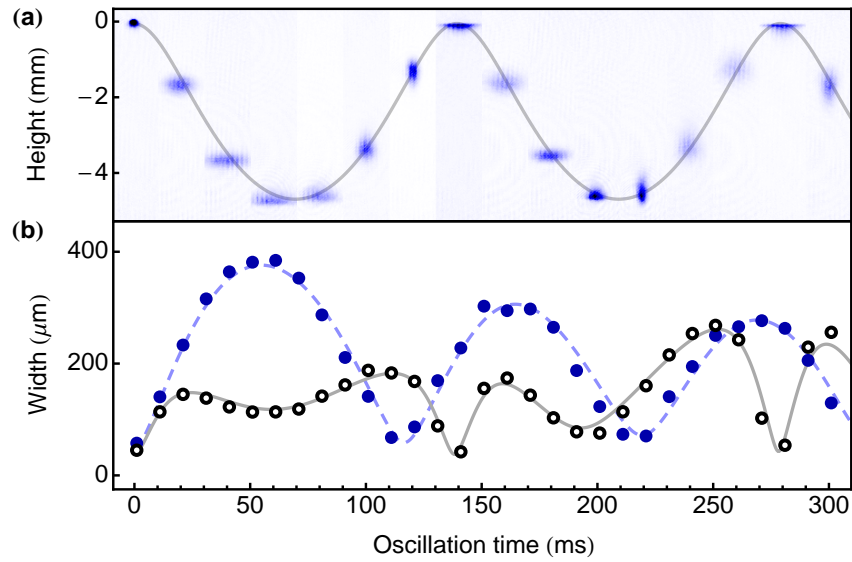


Figure 7.5: Magnetic lensing in the TOP trap. (a) Absorption images of the ensemble oscillating in the trap. (b) Radial (filled blue circles) and vertical (open black circles) RMS cloud widths. The curves, based on numerical solutions for trajectories of non-interacting particles in the exact TOP potential, closely match the cloud behavior. The solid grey curves are simultaneous fits to the center-of-mass trajectory and the vertical width with only seven physically-motivated free parameters. The dashed blue curve results from a 2D Monte Carlo simulation of the atom distribution using the fitted parameters (including  $\nabla B = 20.9 \pm 0.1 \text{ G/cm}$ ,  $B_0 = 6.9 \pm 0.3 \text{ G}$ ) but no free parameters. The initial radial size distribution is scaled from the fitted vertical size by the ratio of the measured initial cloud widths.

chemical potential. With the same magnetic lensing sequence, but with a deeper evaporation cut, we produce the 1.6 nK source to input to the dipole lens.

As an alternative method for 3D lensing in the TOP trap, we have synchronized the turning points by delaying the vertical expansion with an optical lattice (Sec. 7.1.6) Dipole lensing in 3D could be accomplished with crossed optical beams.

### 7.1.5 Further applications

Our dipole lensing results constrain modifications to quantum mechanics at macroscopic scales that predict spontaneous heating of a free gas [65, 66]. The measured cloud size  $(\Delta x_i)_{\min}$  constrains the heating rate for  $^{87}\text{Rb}$  to  $20 \pm 30 \text{ pK/s}$  [147].

This dipole lensing technique has the potential to reach even colder temperatures. Fundamentally, the diffraction-limited collimation temperature for a wavepacket with size  $\Delta x_\ell$  at the lens is determined by the minimum velocity width  $\hbar/(2m\Delta x_\ell)$  allowed by the uncertainty principle ( $\sim 10 \text{ fK}$  for the  $\Delta x_\ell \approx 400 \mu\text{m}$  clouds used in this work). Reaching the diffraction limit requires an uncertainty-principle-limited source. After the magnetic lens and lattice launch, the atom cloud exceeds this limit by a factor of  $m\Delta v_o\Delta x_o/(\hbar/2) \approx 60$  or less [145] (possible heating during the lattice launch may contribute substantially to this excess). A larger lensing beam could reduce Gaussian aberrations, and the beam could be more strongly spatially filtered, perhaps by an optical cavity or a longer propagation distance. The cooling performance could be further enhanced by operating in space, allowing for longer expansion times.

### Acknowledgements

The authors would like to thank Sheng-wey Chiow, Naceur Gaaloul, and Jan Rudolph for valuable discussions and contributions to the apparatus. TK acknowledges support from the Fannie and John Hertz Foundation; TK, AS, and CAD from the NSF GRFP; and TK and CO from the Stanford Graduate Fellowship. This work was supported in part by NASA GSFC Grant No. NNX11AM31A.

### 7.1.6 Lattice-aided magnetic lens cooling

As mentioned above (Sec. 7.1.4), it is not possible to perfectly synchronize the vertical and radial expansions in a gravity-sagged TOP trap for arbitrary quadrupole gradients  $\nabla B$ . For example, when we apply  $\nabla B = 23 \text{ G/cm}$  the first turning points occur at approximately  $(t_\rho, t_z) = (46, 19) \text{ ms}$ . There are no coincident points of maximal radial and vertical expansion for many periods. However, by initially holding the atoms in a vertical optical lattice, the vertical expansion is delayed enough for both to reach their first maximum simultaneously. For this delay, we use the same lattice beam that later launches the atoms [Fig. 7.1(a)].

In the presence of the optical lattice,  $t_\rho$  is approximately 5 ms smaller than without the lattice. This is a consequence of the lattice holding the atoms closer to the location of the quadrupole field zero, where the radial trapping frequency is higher. To fine-tune the lens parameters, we launch the atoms for a long time-of-flight temperature measurement and adjust the lattice hold duration  $\delta t_{\text{lat}}$  and total oscillation time in the magnetic trap  $\delta t_{\text{mag}}$  for optimal temperature. For  $\delta t_{\text{lat}} = 22 \text{ ms}$  and  $\delta t_{\text{mag}} = 41 \text{ ms}$ , the  $1.4 \mu\text{K}$  source is cooled to  $(T_\rho, T_z) = (70, 60) \text{ nK}$ .

The lattice-assisted magnetic lens oscillations can be seen in Fig. 7.6. The slight radial COM oscillation results from imperfect alignment of the optical lattice. Some atoms are not well-trapped by the optical lattice and can be seen oscillating out of phase with the majority of the atoms.

## 7.2 TOP trap theory

The magnetic lens serves as one of the fundamental blocks of our cooling sequence. As such, it is of practical importance to understand sources of aberration in this lens, which potentially limit its performance. The TOP trap, used to generate the lensing potential, is often described in the small oscillation limit near the trap minimum. In this limit, the trapping potential is harmonic, ideal for lensing. But anharmonicities (aberrations) begin to play a significant role at distances larger than  $B_0/A$ , the ratio of the rotating bias field  $B_0$  to the quadrupole gradient  $\nabla B \equiv A$ . Despite the added

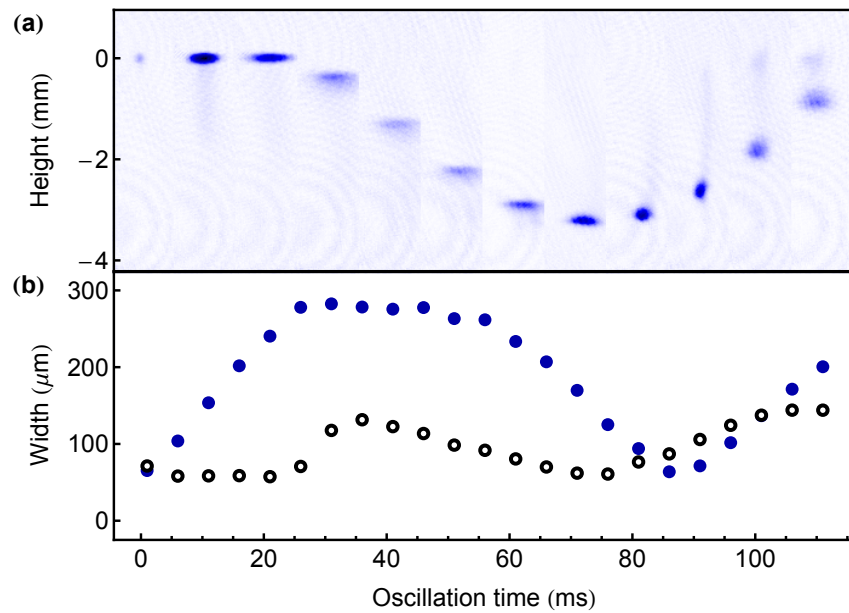


Figure 7.6: Oscillations of the ensemble in the anisotropic TOP trap with an optical lattice. (a) A sequence of absorption images of the cloud after oscillating in the TOP trap. (b) Radial (filled blue circles) and vertical (open black circles) RMS cloud widths as determined by Gaussian fits to the absorption images. The lattice prevents the atoms from falling or expanding vertically for the first 22 ms.

complexity of the anharmonicities, understanding the motion of an ensemble of atoms in the TOP trap is approachable.

Here I analyze the TOP trap in both the harmonic and anharmonic limits. After finding an analytic form of the anharmonic TOP potential, I numerically solve for the trajectories of atoms within that potential in order to understand the role of anharmonicity in a magnetic lens. This procedure contributed to the fit and simulations that generated the curves in Fig. 7.5.

The potential associated with the TOP magnetic field,  $B_{\text{TOP}}$ , is  $U_{\text{TOP}} = \boldsymbol{\mu} \cdot \mathbf{B}_{\text{TOP}}$ , where  $\boldsymbol{\mu} = \mu \hat{r}$  is the magnetic dipole of the atom ( $\mu = \mu_B g_F m_F$ , where  $\mu_B$  is the Bohr magneton,  $g_F$  is the Landé  $g$ -factor and  $m_F$  is the Zeeman sublevel). We assume, however, that any changes in the magnetic field occur at a rate slower than the Larmor precession frequency, such that the atom's magnetic dipole is always aligned with the magnetic field. The potential is then simply scaled from the magnitude of the magnetic field,  $U_{\text{TOP}} = \mu B_{\text{TOP}}$ .

To generate the TOP magnetic field, a bias field  $\mathbf{B}_0$  is added to a quadrupole field  $|\mathbf{B}_q| = A\sqrt{\rho^2 + 4z^2}$ , where  $A$  is the radial field gradient,  $\rho$  is the radial coordinate, and  $z$  is the coordinate on the axis of symmetry. In our apparatus, the latter is aligned with the vertical axis. For a static bias field  $\mathbf{B}_0 = B_0 \hat{x}$ , the zero of the quadrupole field translates by  $B_0/A$ . If  $\mathbf{B}_0$  is applied diabatically, atoms that were once trapped near the quadrupole field minimum now experience a field of magnitude  $B_0$  and a force towards the new location of zero field. By rotating the direction of the bias field at a rate faster than the travel time to the new zero location, atoms can be trapped in a region of non-zero field. The path of the rotating zero-field point, at radius  $r_0 = B_0/A$ , is the “circle of death,” so called because atoms passing through this circle are ejected from the trap by Majorana spin flips [92, 93]. This combination of non-zero-field trap minimum (to prevent Majorana loss of the bulk of the coldest atoms) and a radius of ejection (to selectively evaporate hot atoms) allowed the creation of the first BEC [60].

The time-averaged TOP trap shape is, to lowest order, harmonic but not isotropic.

Well within the circle of death ( $\rho, z \ll r_0$ ), the trap shape is given by

$$B_{\text{TOP}} = \frac{\omega}{2\pi} \int_0^{2\pi/\omega} |\mathbf{B}_q + \mathbf{B}_0| dt \quad (7.3)$$

$$\approx Ar_0 + \frac{A}{4r_0} (\rho^2 + 8z^2) , \quad (7.4)$$

where the field has been Taylor expanded before being time-averaged. The different coefficients of  $\rho$  and  $z$ , a consequence of the asymmetry of the quadrupole potential, reflect the  $2\sqrt{2}$  difference in the trapping frequencies of the radial and vertical dimensions.

This approximation is typically valid when performing most evaporation protocols, as the cloud is small and near the trap minimum. It does not apply to our protocol for magnetic lensing due to the significant gravitational shift in the potential minimum of the TOP trap. The atoms, which had been held near the quadrupole minimum prior to the lensing stage, explore a large vertical region ( $z \sim r_0$ ). Because the circle of death is in the plane perpendicular to  $\hat{z}$ , the atoms are not ejected from the trap, but instead undergo a highly anharmonic center-of-mass oscillation [Fig. 7.5(a)].

This center-of-mass motion is largely governed by the potential along the  $z$  axis, which is conveniently time-independent. The on-axis magnetic field is

$$B_{\text{TOP}}|_{\rho=0} = \sqrt{B_0^2 + 4A^2 z^2} . \quad (7.5)$$

The force associated with the TOP magnetic field is given by the gradient of the potential,  $F_{\text{TOP}} = -\frac{d}{dz}U_{\text{TOP}} = -\mu\frac{d}{dz}B_{\text{TOP}}|_{\rho=0}$ . When combined with the gravitational force, the acceleration experienced by the atom in the combined gravito-TOP potential is

$$a_{\text{TOP}} = \frac{-4\mu A^2 z}{\sqrt{B_0^2 + 4A^2 z^2}} - g . \quad (7.6)$$

From  $a_{\text{TOP}}$ , we can numerically solve the one-dimensional, second-order differential equation to find the trajectory of an atom released into the TOP trap with an initial position  $z_0$  and vertical velocity  $v_0$ , sufficient for finding the center-of-mass oscillations

of Fig. 7.5(a).<sup>9</sup>

Understanding and modeling the effect of anharmonicities on the cloud expansion during the magnetic lens, however, also requires knowing the potential in the radial dimension. To find the anharmonic temperature limit in both the radial and vertical dimensions, we use a fully 3D (2D cylindrically symmetric) analytic expression for the time-averaged TOP field, with no approximations.<sup>10</sup>

With the substitution  $\beta = \frac{2AB_0\rho}{|B_0|^2 + |B_q|^2}$ , the analytic solution for the time-averaged TOP field is

$$B_{\text{TOP}} = \frac{1}{2\pi} \sqrt{|B_0|^2 + |B_q|^2} \int_0^{2\pi} \sqrt{1 + \beta \cos \tau} d\tau \quad (7.7)$$

$$= \frac{1}{\pi} \sqrt{|B_0|^2 + |B_q|^2} \left[ \sqrt{1 - \beta} E\left(\frac{-2\beta}{1 - \beta}\right) + \sqrt{1 + \beta} E\left(\frac{2\beta}{1 + \beta}\right) \right] \quad (7.8)$$

where  $E(x)$  is the complete elliptic integral. By setting  $\rho = 0$  we recover the expected field given in Eq. 7.5.

For a lowest-order understanding of the kinematics in the magnetic lens and for field strength scalings during evaporative cooling (where the atoms sit at the trap minimum; Tab. 4.2), it is instructive to expand the 3D TOP potential about the trap minimum. The trapping frequencies ( $\omega_\rho$  and  $\omega_z$ ) and the gravitational sag of the trap minimum ( $z_{\text{sag}}$ ) are, respectively:

$$\omega_\rho = \frac{(4A^2\mu^2 - m^2g^2)^{1/4} (4A^2\mu^2 + m^2g^2)^{1/2}}{4\mu\sqrt{mAB_0}} \quad (7.9)$$

$$\omega_z = \frac{(4A^2\mu^2 - m^2g^2)^{3/4}}{\mu\sqrt{2mAB_0}} \quad (7.10)$$

$$z_{\text{sag}} = \frac{B_0mg}{2A\sqrt{4A^2\mu^2 - m^2g^2}}. \quad (7.11)$$

---

<sup>9</sup>A correction to the center-of-mass oscillation predicted by this one-dimensional model comes from the different *vertical* force applied to atoms of different *radial* position. For the magnetic fields under consideration, the vertical force changes by less than 3% over 1 mm, yielding a negligible correction to the center-of-mass motion.

<sup>10</sup>While we make no approximations, we do assume that the TOP trap is formed by a perfect quadrupole field and a perfectly uniform bias field. Experimentally, the finite size and separation of the field-generating coils will introduce further complexity that is not currently modeled and that would likely require a fully numerical finite-element simulation to address.

Taking the ratio of  $\omega_z$  and  $\omega_\rho$  yields

$$\frac{\omega_z}{\omega_\rho} = 2\sqrt{2} \sqrt{\frac{1 - \chi^2}{1 + \chi^2}} \quad \text{where} \quad \chi \equiv \frac{mg}{2\mu A}, \quad (7.12)$$

which shows how the ratio of the oscillation frequencies can be tuned by adjusting the magnetic gradient  $A$ . We take advantage of this fact to synchronize the expansions in the vertical and radial dimensions, as shown in Fig. 7.5, and to produce clouds cold in three dimensions.

For a better understanding of the limits that TOP anharmonicities place on the temperature reduction of the magnetic lens, we calculate the trajectories of a number of particles in the 3D potential associated with Eq. 7.8. Specifically, we probe the standard deviation of the particle velocities at the end of a lensing sequence for an ensemble of atoms with a given initial velocity distribution. We assume that the initial cloud size is zero for computational simplicity, but this choice has a useful consequence. In a perfectly harmonic trap, there exists a time at which a cloud of zero initial size has precisely zero temperature. As a result, any residual temperature found in the (slightly anharmonic) TOP trap sets a practical lower bound on the minimum temperature achievable for a cloud of any initial size.

From the general solution for the magnetic field  $B_{\text{TOP}}$ , the radial and vertical acceleration of an atom is described by  $\mathbf{a}_{\text{TOP}} = (\ddot{\rho}, \ddot{z}) = -\nabla(\mu B_{\text{TOP}} + mgz)$ . Given an initial position and velocity, we can numerically solve the coupled set of differential kinematic equations at a particular quadrupole gradient and bias field. As a demonstration, we consider the typical parameters of our magnetic lensing protocol ( $A = 20.9 \text{ G/cm}$  and  $B_0 = 6.9 \text{ G}$ ).

For an array of initial velocities, the simulated trajectories (Fig. 7.7) predict a minimum in the velocity spread near 166 ms in both vertical and radial dimensions, close to the experimental value of 162 ms. From these plots, we can already infer that the minimum velocity spread will be non-zero, a consequence of the trap anharmonicities.

To find the residual temperature, we perform a stochastic simulation in which we assign each trial particle an initial vertical and radial velocity sampled randomly from a thermal (Gaussian) distribution. We find the temperature after a certain oscillation

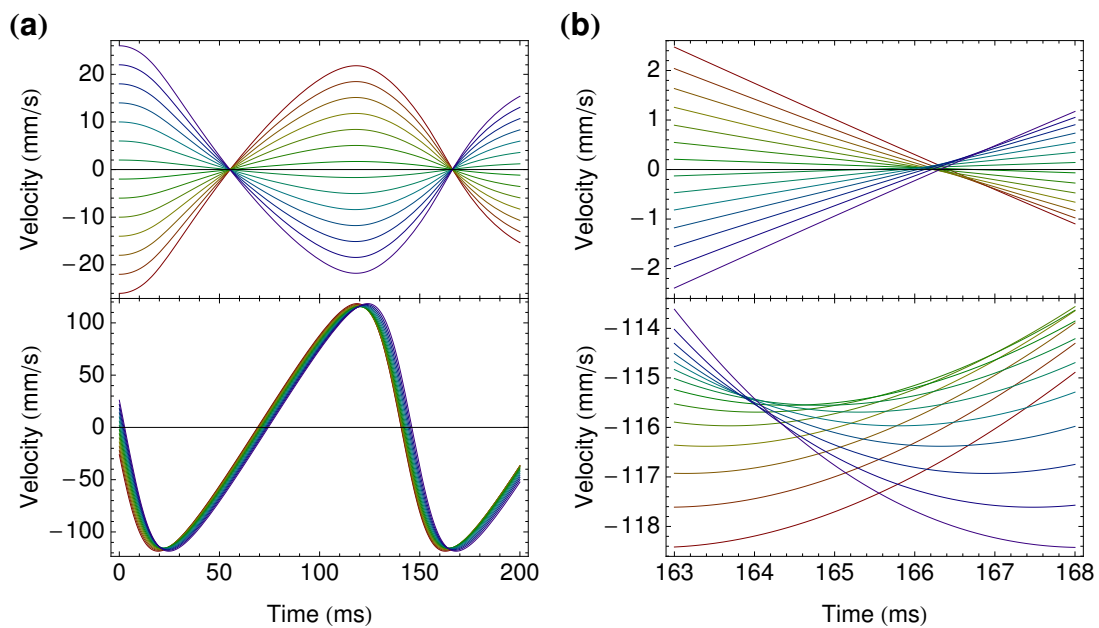


Figure 7.7: Simulated particle velocities after release into a TOP trap. Upper plots show radial velocities, lower plots show vertical velocities. Initial velocities range from -26 mm/s (red) to 26 mm/s (purple) (a) A wide scan of the trap oscillations. (b) A view focused around the minimum velocity spread.

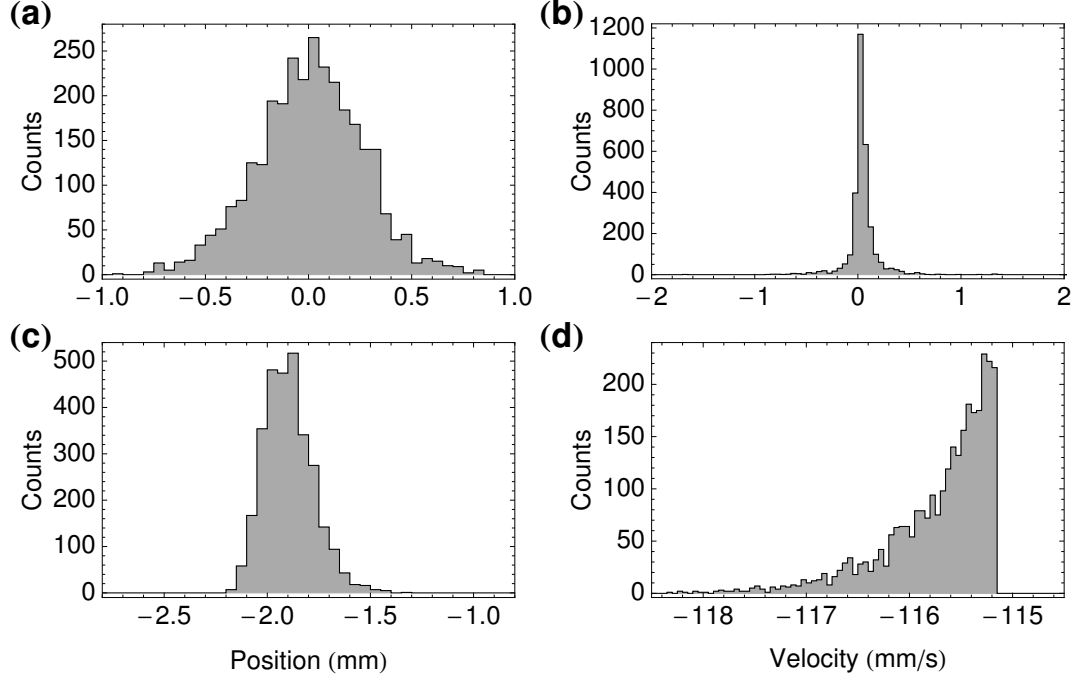


Figure 7.8: Position and velocity distributions after 166 ms in the TOP trap. (a) Radial position distribution. (c) Vertical position distribution. The effective temperature of the radial (b) and vertical (d) velocity distributions are 0.24 nK and 3.3 nK respectively, limited by anharmonicity.

time in the TOP trap by calculating the standard deviation of the velocities of an ensemble of such trials.

Figure 7.8 shows the radial and vertical position and velocity distributions at the nominal simulated collimation time,  $t = 166$  ms. Each distribution is determined from the trajectories of 3000 particles sampled from an initial  $1 \mu\text{K}$  (9.8 mm/s) distribution and released into the TOP trap. Due to the anharmonicity of the trap, neither the radial nor the vertical position distributions are Gaussian at the end of the lens. The latter is asymmetric and the former is better fit by a Lorentzian. The strong asymmetry of the vertical velocity distribution is directly related to the caustic shape displayed by the vertical velocities near the lens time [Fig. 7.7(b)].

The RMS velocity widths of the two dimensions correspond to 0.24 nK radially and 3.3 nK vertically. The difference between the two limits is likely due to the difference

in the degree of anharmonicity experienced by the extended cloud. Over the  $\sim 0.5$  mm spatial diameter of the cloud at  $t = 166$  ms, the  $\sim 5$  Hz radial trapping frequency changes by less than 1 mHz, whereas the  $\sim 8$  Hz vertical trapping frequency changes by more than 1 Hz. While the degree of anharmonicity along the vertical direction ( $\frac{d\omega_z}{dz}$ ) can be lower at heights near to or far from the quadrupole minimum, gravity demands that the atoms oscillate through the region of high anharmonicity in between, thereby limiting the minimum temperature.

Even though this model ignores interactions between particles, it nevertheless serves as a good description of the motion in the TOP trap. Evidence of this is found in the excellent agreement between simulation and experiment in Fig. 7.5. To create those curves, we first perform a simultaneous fit to the vertical center-of-mass motion and the vertical width of the absorption images shown. The model for the vertical center-of-mass motion is determined by numerically integrating Eq. 7.6. The model for the vertical width would ideally be found through the standard deviation of the final velocity. Analytically, this involves integrating the square of the final velocity over the initial position and momentum distributions. But finding the analytical solution for the final velocity is nontrivial, making this method impractical. We have already demonstrated the comparable numerical calculation above, using 3000 particles. But this solution, as described, is quite slow and is therefore undesirable for a fit where the fitting parameters must be iteratively varied to find the optimal combination. Instead, we approximated the integral as a Riemann sum over a 6 by 6 (position by velocity) rectangular grid of possible initial conditions. This significantly improved the speed of the calculation by limiting the number of particles needed for each iteration, and yet agreed well with simulations involving larger ensembles.

This simultaneous fit yields values for the initial vertical size, initial temperature, initial position, initial center-of-mass velocity, quadrupole gradient, and bias field. We then perform a simulation similar to that of Fig. 7.8, but using 500 particles drawn from an initial distribution with a non-zero initial size as well as a non-zero initial velocity width. The initial velocity distribution (in both dimensions) and the initial vertical width are set to the values returned by the vertical fits. The initial

radial width is set to be the fitted vertical width, scaled by the measured radial-to-vertical width ratio. This choice addresses the difference in the vertical and radial trapping frequencies, which result in clouds with different vertical and radial widths, while taking advantage of the information gleaned from the fit. With no further free parameters, the simulation produced the radial breathing mode shown in Fig. 7.5, which agrees well with the data.

The under-prediction of the initial cloud sizes by the fit and simulation may be a consequence of applying a non-interacting model to an interacting cloud. Repulsive interactions, like those observed in ultracold  $^{87}\text{Rb}$  clouds, typically result in larger clouds and are strongest when the cloud is small. As the cloud is small in all three dimensions only at the beginning of the lensing sequence, the measured cloud size should exceed the non-interacting width predominately in those early times, consistent with the behavior we find.

In addition to more accurate modeling of the experimental realities of the magnetic fields, future directions of this simulation may involve incorporating interactions by extension to a Gross-Pitaevskii-based model. With a better understanding of the impact of interactions on the performance of the lens, we might be able to devise optimized lensing sequences that better mitigate the additional interaction energy, leading to yet-colder temperatures.

# Chapter 8

## A high-performance magnetic shield with large length-to-diameter ratio

We have demonstrated a 100-fold improvement in the magnetic field uniformity on the axis of a large aspect ratio, cylindrical, mumetal magnetic shield by reducing discontinuities in the material of the shield through the welding and re-annealing of a segmented shield. The three-layer shield reduces Earth's magnetic field along an 8 m region to  $420 \mu\text{G}$  (rms) in the axial direction, and  $460$  and  $730 \mu\text{G}$  (rms) in the two transverse directions. Each cylindrical shield is a continuous welded tube which has been annealed after manufacture and degaussed in the apparatus. We present both experiments and finite element analysis that show the importance of uniform shield material for large aspect ratio shields, favoring a welded design over a segmented design. In addition we present finite element results demonstrating the smoothing of spatial variations in the applied magnetic field by cylindrical magnetic shields. Such homogenization is a potentially useful feature for precision atom interferometric measurements.

This chapter also appeared as Ref. [4], and was written with collaborators Jason M. Hogan, David M. S. Johnson, Tim Kovachy, Alex Sugarbaker, and Mark A. Kasevich.

## 8.1 Introduction

Large experiments sensitive to magnetic fields often demand equally large enclosures of highly permeable material such as mumetal, an Fe-Ni alloy, to shield the apparatus from uncontrolled magnetic fields. [152–157] Our goal is to test Einstein’s Equivalence Principle via atom interferometry within a 9-meter tall, 10 centimeter diameter vacuum tube. [71, 73] Since this measurement is sensitive to inhomogeneities in the magnetic field, we shield this region with a set of three long cylindrical magnetic shields in order to minimize this systematic error.

Because mumetal must be hydrogen-annealed for the best performance, [158, 159] limited furnace sizes require large shields to be constructed from several smaller segments that are mechanically joined together. The joints, however, break the high permeability path of the shield material and allow field to leak through to the shielded region.

Tightly compressing overlapping shield material between aluminum clamps has been a successful method for joining flat plates to create a contiguous shield. [160] But joining cylindrical segments to form a longer cylindrical shield is more challenging due to the tight tolerances on the circumference required to minimize the gap between segments. As a consequence, researchers have had to resort to active cancellation of the field in cylindrical geometries. [157]

Consistent with this past work, we measured significant spikes in the magnetic fields near the joints of our long, cylindrical, segmented shield (Fig. 8.1). The peaks vanished after each layer of the shield was welded, reannealed and degaussed (Sec. 8.3). In particular, degaussing improved the homogeneity of the field. Using a detailed finite element model that includes the segmented shield’s joints, we find that because the long shield perturbs more of the surrounding field, it channels more magnetic field than shorter shields of the same diameter (Sec. 8.4). This is related to the lower overall shielding performance of long shields in axial fields. When a joint interrupts the path of the field through the material, a peak in magnetic field arises within the shielded region, indicating that material continuity is of utmost importance for the performance of the shield. We find that uniformity is most important for the innermost layer of

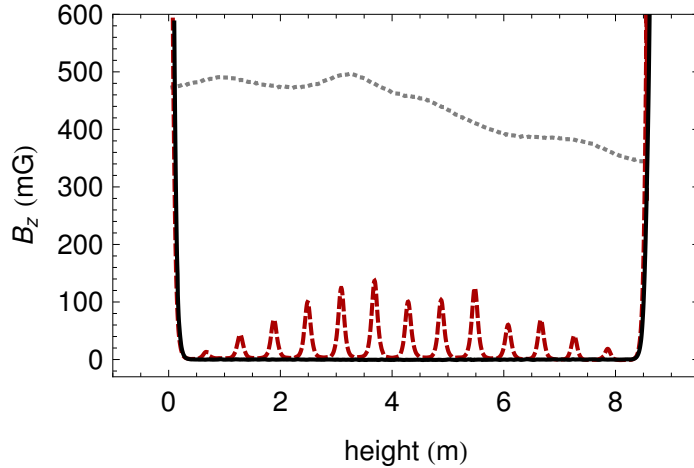


Figure 8.1: Measured axial magnetic field along the vacuum tube axis. The dotted grey curve is the ambient magnetic field measured before the shields were installed. The dashed red curve is the field with the segmented shields. The solid black curve is the field with the welded shields.

the shield, where the peak is transmitted immediately into the nominally shielded region. In addition, the finite element models show that despite the long shield’s weak axial shielding performance, it can highly suppress inhomogeneities in the external field. Finally, we experimentally explore several methods for creating better magnetic continuity in the shield (Sec. 8.5). No method produced a better shielding ratio or field uniformity than welding and subsequently annealing the three shield layers.

## 8.2 Shielding metrics

A shield’s performance is often characterized by its shielding ratio, defined as the ratio of the magnitude of the ambient magnetic field to the field inside the shielded region ( $S = B_{\text{Ext}}/B_{\text{Int}}$ ). [161, 162] In the context of cylindrical shields, this ratio is defined for both fields transverse to the cylinder’s axis (transverse shielding ratio  $S_T$ ) and parallel to that axis (axial shielding ratio  $S_A$ ).

In addition we define a dynamic shielding ratio, which is the ratio of a change in the external field to the corresponding change in the internal field ( $\Sigma = \Delta B_{\text{Ext}}/\Delta B_{\text{Int}}$ ).

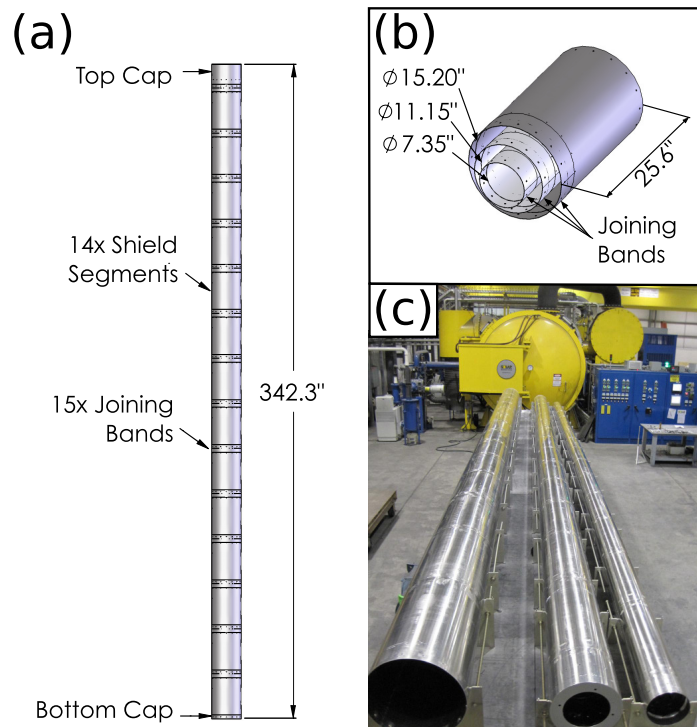


Figure 8.2: The magnetic shield. (a) When fully-assembled, the shield is 342" (8.7 m) in length and consists of three layers. In this segmented version, each layer of the shield consists of 14 segments, plus bottom and top end caps. (b) Each segment has a row of PEM nuts welded to the bottom edge and a joining band welded to the top. The holes in this band allow the top of each segment to be fastened to the nuts at the bottom of the next. The three layers nest within each other. (c) The joining bands were removed and the segments were welded together and re-annealed. The three layers of the welded shield are pictured here in front of the annealing furnace (Solar Atmospheres).

This is useful in evaluating the response of the shield to slow variations in the ambient field. While the two definitions for the shielding ratio would yield identical results in the case of a purely linear material, nickel-iron materials like mumetal are ferromagnetic and have hysteresis, [163] a feature that is most apparent when discussing the impact of degaussing on the uniformity and magnitude of the internal field (Sec. 8.3.3 and 8.5.4). Because the dynamic shielding ratio  $\Sigma$  probes the linear response of the shield when  $\Delta B_{\text{Ext}}$  is small, it corresponds more accurately to the theoretical shielding ratio, which in general is calculated from formulas that do not account for hysteresis and therefore do not distinguish between  $\Sigma$  and  $S$ .

The design of multi-layer cylindrical magnetic shields typically begins with analytical equations for the transverse shielding ratio [164] and the axial shielding ratio. [161, 165, 166] Through the years, the models of magnetic shielding, especially for transverse fields, have been detailed and developed in several reviews [161, 167–169] and are neatly summarized by Ref. [162]. In the supplemental material (Sec. 8.7) we have briefly highlighted the formulas used to calculate  $S_T$  and  $S_A$ , which we apply below to our shield geometry.

In this article we focus on the axial shielding ratio and axial dynamic shielding ratio, as we find that they are more sensitive than the transverse shielding ratios to the quality of the joint between two cylindrical segments of a long shield.

For precision measurements, the magnetic field homogeneity is often just as important as the magnitude of the field in the shielded region. [71] We will characterize the homogeneity by its root-mean-square (rms) deviation in the region of interest.

### 8.3 Segmented v. welded shields

We now summarize the design of the shields and the apparatus used to measure the field in the shielded region before discussing the difference in the performance of the segmented and welded shields.

Shield	OD (in.)	Len. (in.)	$\gamma$	$1/N$	$S_T$	$S_A$
Inner	7.35	334.2	45	687	170	2.0
Middle	11.15	338.3	30	353	112	2.3
Outer	15.25	342.4	22	219	81	2.5
All three	—	—	—	—	$4 \times 10^5$	8.0

Table 8.1: Theoretical shield properties of each layer of the constructed shield and all three combined. The transverse shielding ratio ( $S_T$ ) and axial shielding ratio ( $S_A$ ) are calculated from each layer’s geometry using the formulas presented in the supplemental material (see Sec. 8.7). For each layer, we indicate its outer diameter (OD), length (Len.), length-to-diameter ratio ( $\gamma$ ) and inverse demagnetizing factor ( $1/N$ ). The material thickness is 0.050”, and magnetic permeability is assumed to be  $2.5 \times 10^4$ .

### 8.3.1 Shield design

The shield consists of three concentric cylindrical layers made of 0.050”-thick Amumetal [Amuneal Manufacturing Co.; Fig. 8.2(a)]. Assuming a conservative value of the permeability of Amumetal of  $\mu = 2.5 \times 10^4$  and the design dimensions, the theoretical transverse shielding ratio is  $S_T = 4 \times 10^5$ . The axial shielding ratio is similarly calculated to be  $S_A = 8.0$ , although finite element simulations (Sec. 8.4) predict a value of  $S_A = 5.0$ . (The discrepancy vanishes if multi-layer axial shielding ratios are calculated and simulated for shields with closely-spaced layers.) With a more aggressive permeability  $\mu = 1 \times 10^5$ , which we typically use in simulations, we calculate that  $S_T = 3 \times 10^7$  and  $S_A = 21$  ( $S_A = 78$  simulated).

The axial and transverse shielding ratios for the three full-length shield layers individually and combined are summarized in Table 8.1.

For the segmented shield, each layer is composed of fourteen shield segments and two endcaps. Each segment is 26” in length, including a 4” joining band tack-welded to the top with a 2” overlap [Fig. 8.2(b)]. The segments and endcaps were hydrogen annealed after all forming and welding to achieve the highest permeability. The shield was fastened together by connecting the holes placed every 2.5” around the circumference of the joining band of one segment to the PEM nuts at the bottom of the next.

For the welded shield, the joining bands were removed and each segmented layer

of the shield was welded into a continuous layer (Amuneal Manufacturing Co.). The layers were then re-annealed in a hydrogen atmosphere in a vacuum furnace [Solar Atmospheres; Fig. 8.2(c)].

### 8.3.2 Measurement apparatus

To measure the magnetic fields at the center of the magnetic shields, we built a shuttle to move a fluxgate magnetometer (Applied Physics Systems model 540) along the length of the 10 cm diameter vacuum chamber at the center of the magnetically-shielded region. The magnetometer rode in a custom fabricated aluminum shuttle, centered in the cylinder by six delrin wheels. This shuttle was raised and lowered by a stepper motor via four nylon cables. Only non-magnetic materials were used in the construction of the shuttle system.

At each measurement point, the position of the stepper motor and the three vector components of the magnetic field are recorded with a resolution of 5 to 500  $\mu\text{G}$ , depending on the magnetometer gain setting. Data were taken at 0.15" intervals along the entire 342" length of the shield. The position data were then processed to correct for non-linearities in the position of the shuttle that arise from cable stretching (a  $\sim 2\%$  correction). The height of the magnetometer was defined from the bottom of the outer shield layer.

Because the offset of the magnetometer was typically set to zero at the center of a segment where the field is lowest, the absolute offset of the magnetic field is not known to better than a few mG. While uncertain calibration limits our measurement of the (absolute) shielding ratio, the dynamic shielding ratio and the homogeneity characterization are unaffected. In the future we plan to measure the absolute magnetic field within the chamber using cold clouds of rubidium atoms as magnetometers. [35, 170]

### 8.3.3 Shield performance

We followed a standard degaussing procedure to demagnetize the shields and improve their performance. [157, 171] Degaussing reorders the domains and removes residual

magnetization by cycling through the material's hysteretic response. [172]

Figure 8.1 shows the magnetic field measured inside the vacuum tube without shields, with the degaussed segmented shields, and with the degaussed welded shields. While the segmented shield greatly reduces the magnetic field in certain regions, the shielding is ineffective in locations that coincide with the joints between segments. This leads to a magnetic field profile with regularly-spaced peaks that are a large fraction of the ambient field.

By welding, annealing, and degaussing the three layers, we were able to reduce the maximum axial field peak height on the shield's axis from over 100 mG to below a few mG, with a residual rms deviation of 420  $\mu$ G (rms) in the axial direction between the heights of 0.5 m and 8.1 m [Fig. 8.1, 8.3(a)]. Degaussing greatly improved the shield's axial uniformity, reducing the broad 5 mG feature to less than 1 mG and eliminating variations correlated with the joint positions [Fig. 8.3(a), inset]. The two transverse directions displayed rms values of 460 and 730  $\mu$ G (rms) along the shield's axis over the same height range, in large part due to rapid variations in the lower half of the shield [Fig. 8.3(b)]. These remaining variations in the field are repeatable. They are hypothesized to be from residual magnetism of material used to construct the vacuum chamber located inside the magnetic shield, but their source is currently unknown (see Sec. 8.6 for more discussion).

The dynamic shielding ratio of the welded shield was inferred by measuring the field along the axis of the shield while applying different external fields in sequential measurements. The applied field was generated by a 10" long solenoid wrapped around the outer layer of the shield at a height of 4.8 m, and the peak field was changed from 200 mG parallel to 200 mG antiparallel to the axis in five measurements. The shield was degaussed prior to the first measurement, with no applied external field. We did not degauss between measurements in order to avoid confounding the dynamic shielding ratio with the homogenizing effect of degaussing.

At each position along the shield's axis, we fit a line to the data of measured internal field versus calculated applied field. The inverse of the slope of this fit yielded the dynamic axial shielding ratio at that position. To correct for the difference between a small solenoid and a uniformly applied field, we compared finite element models

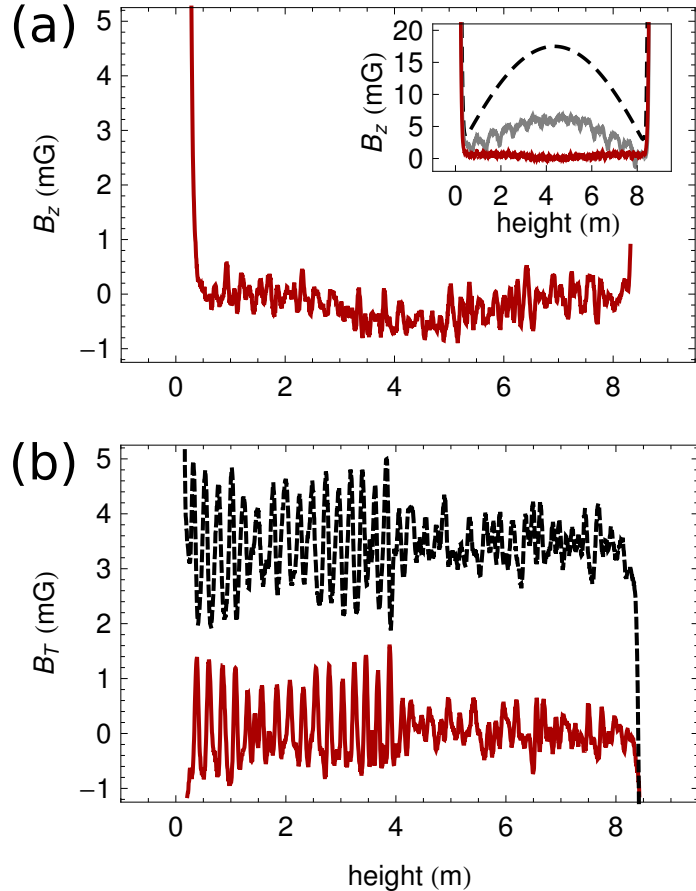


Figure 8.3: Measured magnetic field along the axis of a welded 14-segment, three-layer shield after degaussing for the (a) axial and (b) transverse magnetic fields. The inset of (a) shows the field improvement in uniformity after degaussing. In solid light grey is the measured field before degaussing. The solid red curve is the measured field after degaussing. The dashed black curve shows the simulated background expected from a perfectly uniform, finite length shield. In (b), the dashed black and solid red curves show the measured field components in the two transverse directions. The dashed black curve has been offset by 3.5 mG for clarity.

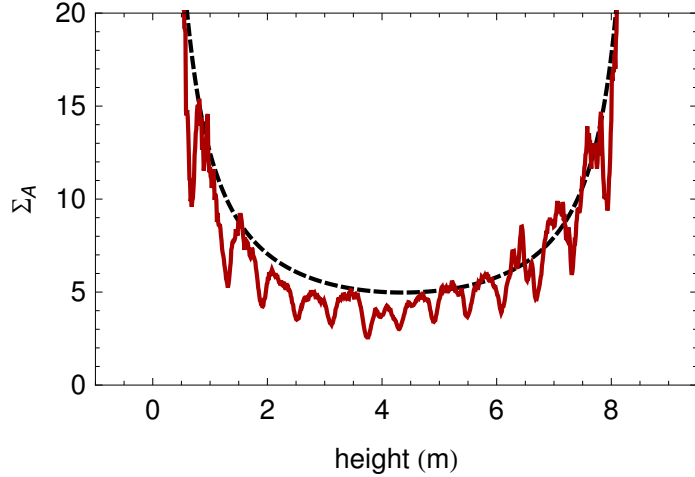


Figure 8.4: Axial dynamic shielding ratio of the welded 14-segment, three-layer shield. In solid red is the dynamic shielding ratio inferred from measurement. In dashed black is a finite element model for a three-layer continuous shield with  $\mu = 2.5 \times 10^4$  and radii, lengths, and thicknesses the same as the constructed shield. The dips in the dynamic shielding ratio correspond with welds between segments.

(described in Sec. 8.4) simulating the response of the magnetic shield to this small solenoid versus the response to a uniform applied field. The ratio of these two responses simulated with the same peak applied field is a height-dependent correction factor that transforms the shielding ratio measured with the small solenoid to the shielding ratio that would be measured with a uniform applied field. With this method we produced Fig. 8.4.

From Fig. 8.4, we note that the dynamic shielding ratio ( $\sim 4$ ) is much smaller than the shielding ratio we might expect from Fig. 8.1, but it is consistent with theoretical calculations (Table 8.1) as well as finite element simulations when the permeability of the material is  $\mu = 2.5 \times 10^4$ , a reasonable value for annealed mumetal. We also note that the dynamic shielding ratio is worst at the location of the welds. From the dynamic shielding ratio alone, we would expect the residual field to show a broad background peak with sharper peaks at the weld locations, similar to (albeit larger than) the field within the shield prior to degaussing (see the inset of Fig. 8.3). That no such features are observed seems to imply that the degaussing procedure

leaves the magnetization of the shield in such a state as to cancel the residual field to the milligauss level. Yet while the shield currently produces a uniform field, its performance will be more sensitive to time-dependent variations in the ambient field than the simple (degaussed) shielding ratio would suggest.

To better understand the difference in the behavior of the segmented and welded shields, we performed finite-element simulations to analyze the impact of joints on field uniformity at the shield’s axis. The results of this analysis indicate that the uniformity of the permeability of the shields – and especially of the innermost layer – is critical for the ultimate performance of a long shield.

## 8.4 Finite element analysis

To simulate the performance of the segmented shield, we built a dimensionally accurate, axially-symmetric model in a commercially-available finite element software package. [173] This cylindrically-symmetric model included end caps, the three shield layers, and the joining bands. Based on inspection of the assembled segmented shield, we included a 0.006” radial gap between each shield segment and joining band, and a 0.010” axial gap between each shield segment, which are typical tolerances for welded sheet-metal structures. In reality, the gap size varies not only from segment to segment but also around the circumference of a single joining band. Our simplified model, however, captures the essential physical effect.

Finally, we applied a  $B_{z,0} = 500 \text{ mG}$  constant background magnetic field along the axial direction of the shield to approximate the Earth’s magnetic field. The permeability was defined to be a constant value, typically  $\mu = 10^5$ . Saturation of the shield material, in which high magnetic flux within the material can reduce its permeability, was not modeled.

For simplicity, we will present the results of the joint between just two adjacent segments of the inner layer before discussing the effect of all fourteen segments of all three layers.

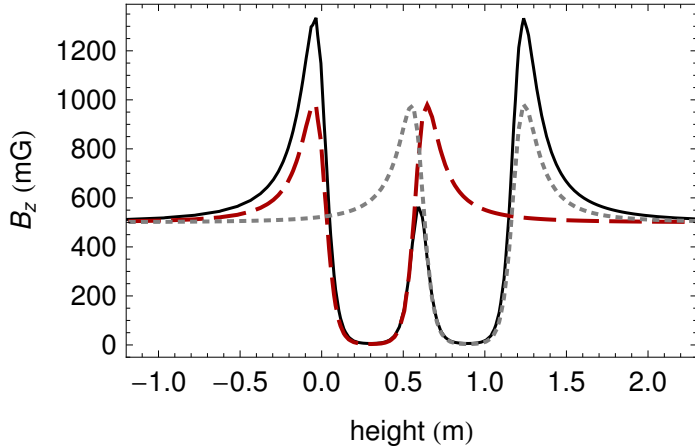


Figure 8.5: Finite element simulation of an imperfect joint in a segmented shield with an applied field of  $B_{z,0} = 500$  mG. The axial magnetic field on-axis is shown in solid black. The peak occurs at the air gap ( $\mu = 1$ ,  $0.010''$  in height) between the two segments. The magnetic fields for each segment alone are shown as dashed red and dotted grey curves. The peak is caused by the imperfect magnetic circuit between the segments allowing the field to escape the shield and into the shielded region.

#### 8.4.1 Two segment shield

Figure 8.5 shows the axial magnetic field ( $B_z$ ) along the axis of the simulated two-segment shield. The dashed curves represent the axial magnetic fields when each segment is simulated alone. The field is significantly amplified at each end of the segment before it diminishes exponentially within. If the two segments are simulated together, the field amplification at the ends is even greater. The amplification is a consequence of the longer shield perturbing more of the Earth's field, leading to a focusing effect at the ends of the shield (Fig. 8.6). This extended reach of longer shields is tightly related to the higher concentration of field found within long shields, discussed further below.

Where the segments of the two-segment shield are imperfectly joined, there is a peak in the magnetic field. As the figure demonstrates, the shape of the peak is related to the focusing of the field at the entrance and exit of each segment.

One method of reducing the height of the peak is to add shielding. Adding two external layers of shielding to the model ( $t = 0.05''$ ,  $D = 11.2''$  and  $15.3''$ ) redirects

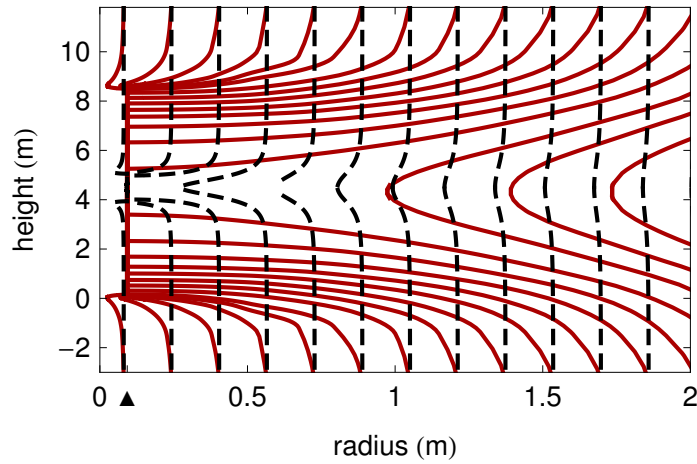


Figure 8.6: Finite element simulation of magnetic field lines in the presence of the inner layer of an 8.5 m shield (solid red) and a 1.2 m shield (black dashed). The former has the same length as the full, 14-segment shield, while the latter has the same length as a two-segment subset. The system is cylindrically symmetric about the left vertical axis. The triangle on the horizontal axis marks the radius of both shields (0.0927 m). Note that the longer shield strongly affects the ambient field at much further distances than the shorter shield.

field from the innermost shield to the outer layers, resulting in a factor of  $\sim 10$  suppression of both the field channeled by the inner shield and the residual peak due to the joint. Such a solution, however, does not address the source of the problem, which is the break in the permeability of the shield at the joint.

In a multi-layer shield, the uniformity of the permeability of the innermost layer is critical to ensure the uniformity of the field at the center of the final shield. To show this we modeled two complementary cases: a perfectly uniform inner layer and segmented outer layers with gaps compared to a segmented inner layer with gaps and perfectly uniform outer layers. We then extracted the height of the residual peak, as measured from the minimum field to the peak maximum along the shield axis. For the uniform inner layer, the peak height was  $1.6 \times 10^{-6}$  of the applied field. For the segmented inner layer, the peak was more than three orders of magnitude larger. Clearly, the inner layer must be uniform for the best performance; the field from any gaps in the outer layers will then be largely shielded by the uniform inner layer.

Apart from constructing a monolithic inner layer, the addition of a joining band that spans the gap between two segments can reduce the peak by diverting field around the axial gap. But although simulations show that a joining band does improve the homogeneity of field on the shield's axis, the extent of the benefit depends on the mechanical tolerance of the fit between the inner diameter of the joining band and the outer diameter of the segments. While flat plates can be effectively clamped, [160] clamping cylindrical segments proved experimentally more challenging (Sec. 8.5).

### 8.4.2 Full 14-segment shield

The results of the simulation of the full, three-layer, fourteen segment shield compared to the measured field are shown in Fig. 8.7. The finite element model qualitatively captures the shield's measured performance: the axial field peaks are on the order of 100 mG at the shield joints and are largest at the center of the shield.

The larger relative height of the central peak is a consequence of the change in the concentration of magnetic field channeled within the shield material along the axial direction. Near the ends, the shield redirects the nearest field lines through its

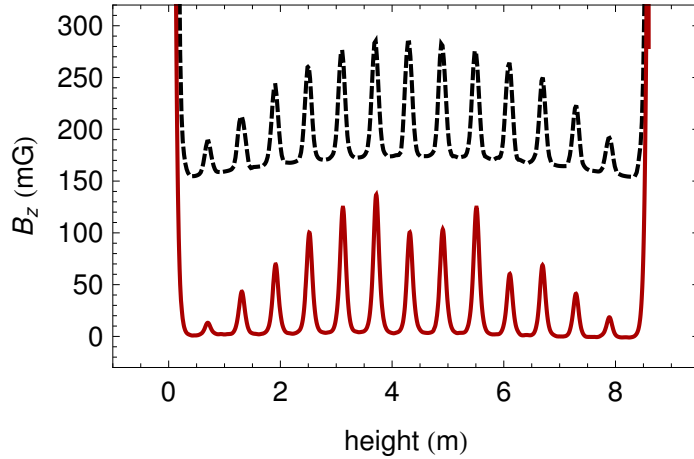


Figure 8.7: Measurement of the segmented shields compared to simulation. The dashed black curve is simulation; it has been offset by 150 mG for clarity. The solid red curve is a measurement of the initial segmented shield. The peaks in the simulated curve, which arise due to the modeled gaps between segments, align well with the measured peaks.

material; at the middle of the shield, the shield draws in additional field lines from further away (Fig. 8.6). By symmetry, the peak field is at the center of the shield, and so any disruptions to the permeability of the material at the shield’s center are more dramatic.

The peak height of the field in the shield increases monotonically with the length of the shield since longer shields perturb a larger volume of the ambient field (see Sec. 8.7). Even a small defect in the permeability can therefore result in a sizable and undesirable residual field peak. For example, we simulated filling the modeled axial gaps with material of permeability one tenth that of the shield. This resulted in peaks with amplitude up to  $10^{-3}$  of the applied field, an indication of the care needed when designing long segmented shields.

### 8.4.3 Field homogeneity

In atom interferometry, systematic errors associated with magnetic fields depend both on the magnitude of the field and its gradient, making a smooth, homogeneous field

advantageous. [71] Fortunately, cylindrical magnetic shields preferentially suppress axial magnetic fields that vary on short length scales even when the axial shielding ratio is small. [157] Discussion of this effect in the literature is limited, and can be simply summarized: because the transverse shielding ratio suppresses the transverse gradients, enforcing  $\nabla \cdot B = 0$  suppresses the gradient  $\partial B_z / \partial z$ , producing a more uniform axial field along the cylinder axis. Finite element analysis permits a quantitative study of this homogenization because it allows for the modeling of the necessary non-uniform ambient fields.

We begin by describing the field homogenization due to a cylindrical, infinitely long shield; later we will discuss shields of finite length. In general this shield is modeled after our inner layer, with a thickness of  $t = 0.050"$  and outer diameter of  $2r = 7.35"$ . The permeability of the material was chosen to be  $\mu = 2.5 \times 10^4$  to match the value inferred from the dynamic shielding ratio of the full, welded shield (Fig. 8.4). However all three parameters are varied in order to characterize their effect on homogenization.

We apply a spatially-varying field that is both experimentally realizable and simple to model in our cylindrical coordinate system. The field is generated by a solenoid with radius  $R$  whose current varies sinusoidally along its length with a wavelength  $\lambda$ . At the axis of this solenoid the field vector is purely axial ( $B_0 \sin(2\pi z/\lambda + \phi) \hat{z}$ ), although it has a non-zero radial component at non-zero radius.

The shielding ratio is determined through the on-axis fractional change of the amplitude of the applied sinusoidal field when the shield is added to the simulation. The amplitude is found by fitting a single period centered in the simulation's space to a sinusoid with fixed phase and wavelength, leaving only the amplitude and constant offset as free parameters. The resulting ratio is independent of the exact phase  $\phi$  of the field chosen, indicating that the infinite shield is a linear system.

The wavelength-dependent axial shielding ratio takes on a characteristic long-pass shape, modified at very short wavelengths to account for a slowing in the rate of rise of the shielding ratio (Fig. 8.8). The simulations can be fit well by a three-parameter formula composed of a long-pass factor and a short-wavelength roll-off factor:

$$S_A(\lambda) = \frac{1 + (\lambda/\alpha)^2}{(\lambda/\alpha)^2} \frac{(\lambda/\beta)^n}{1 + (\lambda/\beta)^n} \quad (8.1)$$

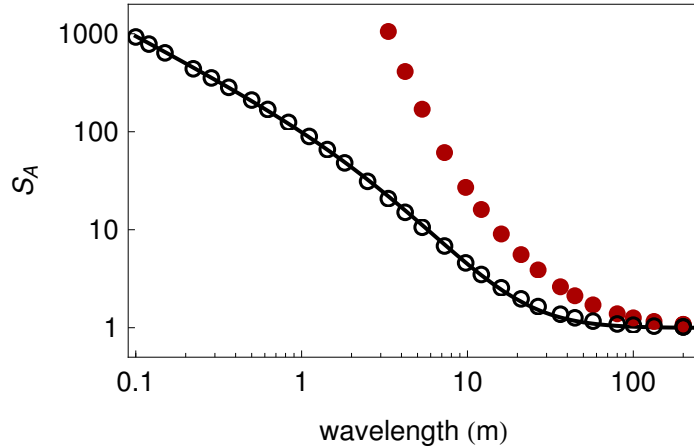


Figure 8.8: Dependence of the axial shielding ratio  $S_A$  on the wavelength of the field applied to an infinitely long shield. The open black circles show  $S_A$  for a single shield with the same diameter and thickness as the inner layer of the constructed shield. The filled red circles show  $S_A$  for the same system, but include two outer layers with the same diameters and thickness as the outer layers of the constructed shield. The solid curve is a fit to Eq. (8.1).

The long-pass corner wavelength is given by  $\alpha$ , and the deviation from this long-pass factor at short wavelengths begins at  $\beta$ . For very long wavelengths ( $\lambda \gg \alpha$ ), the shielding ratio approaches the expected limit for infinite shields,  $S_A = 1$ . As the wavelength decreases ( $\beta < \lambda < \alpha$ ), the shielding ratio increases dramatically, slowing to a new slope at very short wavelengths ( $\lambda \ll \beta$ ). For the single-layer shield of Fig. 8.8,  $\alpha = 22$  m,  $\beta = 3.4$  m, and  $n = 1.1$ .

The simulations indicate that  $\alpha$  scales with  $\sqrt{\mu tr}$ , and that  $n$  is independent of the radius of the shield. Further analytic analysis is necessary to fully understand the physics governing the relationship between the shield's geometry and its homogenizing capability.

In the case of the finite shield, the linearity of the system begins to fail at wavelengths near the length of the shield (Fig. 8.9), at which point the phase  $\phi$  becomes important. At wavelengths shorter than the shield, applying a field with either phase results in shielding ratios that follow the infinite shield's long-pass response. At wavelengths longer than the shield, however, applying a field with an antinode

centered on the shield (Fig. 8.9, open circles) results in a broad feature of wavelength twice the shield’s length. This feature is similar to that seen in the data and simulation of Fig. 8.3(a) (inset). Meanwhile, applying a field with a node centered on the shield (Fig. 8.9, filled circles) results in a feature of the same wavelength as the shield’s length with a node at the shield’s center. Note that at infinitely long wavelengths we expect  $S_A$  for the antinode applied field to approach the value for a uniform applied field, but the nonlinearity of the system at these wavelengths causes our particular method of calculating  $S_A$  to deviate from this limit.

The homogenization analysis thus far involves a single-layer shield and does not account for further improvements in wavelength-dependent shielding due to the outer two layers of the complete shield (Fig. 8.8). Yet for our shield length, the inner layer already strongly suppresses sub-meter scale perturbations, producing a very uniform field in the shielded region. With the inner shield alone, the external field would have to vary every 0.25 m with 100 mG amplitude to produce the residual variations inside the shield that we measured (see Fig. 8.3). With the full three-layer shield, the amplitude would have to be five orders of magnitude larger. As such variations were not measured in the ambient field (Fig. 8.1), the source of the short-wavelength residual field is more likely originating inside the shield or from the shield material itself.

## 8.5 Experimental implementations of shield joining methods

To complement the finite element analysis, we experimentally tested several methods for joining two mumetal segments to create a uniform field in the shielded region. We placed two segments of the inner layer of the full shield on an independent support structure. The shuttle and its magnetometer traveled along the axis of the shields within a PVC pipe of the same diameter as the vacuum tube of the full system. Data were taken at 0.15” intervals along the central 30” (0.8 m) length of the two-segment shield.

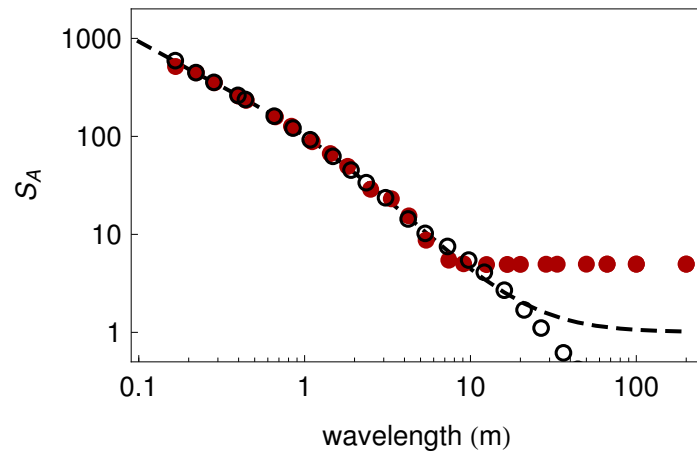


Figure 8.9: Dependence of the axial shielding ratio  $S_A$  on the wavelength of the field applied to a finite shield. The modeled shield has the same radius (3.68") and length (334.7", or 8.5 m) as the inner layer of the constructed shield. The filled red (open black) circles describe the shield's response to an applied field with a node (antinode) centered on the shield. The dashed black curve represents the simulations for the infinitely-long shield of the same radius (see Fig. 8.8). The system becomes nonlinear at wavelengths greater than the shield's length, and the method for calculating  $S_A$  begins to fail.

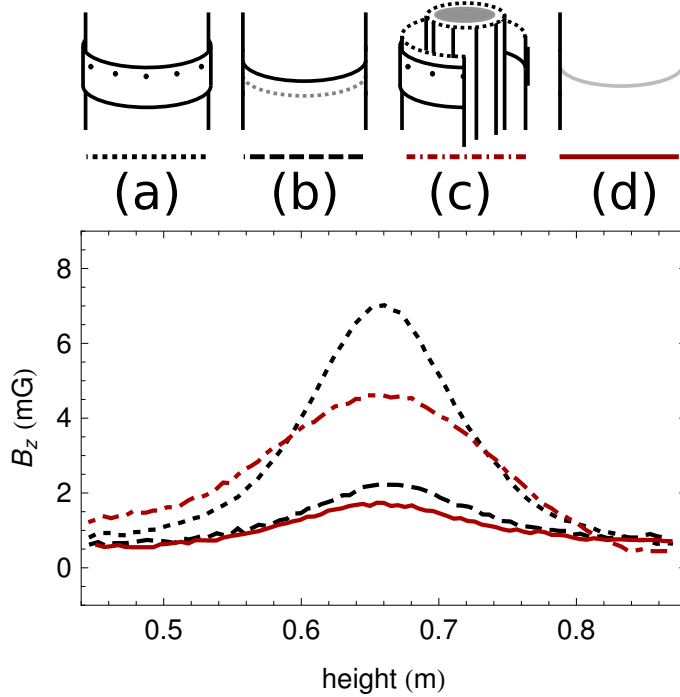


Figure 8.10: Residual axial magnetic field for multiple methods of joining the inner layers of a two-segment subset of the full shield. Labels a-d correspond to the subsections of Sec. 8.5 in the text. Arbitrary height and magnetic field offsets have been chosen for the best comparison of peak height. (a) Fasteners tightened with 30 in-lbs of torque. (b) A thermal interference fit. (c) Two long strips of Metglas wound helically around the center magnetometer support, topped by two layers of axial Metglas shielding. (d) The welded shield.

The joining methods included a) applying a well-defined torque to the fasteners joining the two layers, b) creating a thermal interference fit, c) wrapping a fourth shield with long strips of high permeability material (Metglas 2705M) inside the inner mumetal layer, and d) welding and re-annealing the segments. These measurements are summarized in Fig. 8.10. The two most promising methods (b and d) were further tested and degaussed in an environment designed to mimic the full, three-layer shield, as will be discussed below. Welding, reannealing and then degaussing the shields ultimately provided the best shielding and the best field uniformity.

### 8.5.1 Fastener torque

The joining band fasteners are placed every 2.3" around the circumference of the inner layer. Holes in the joining band of one segment align with 8-32 PEM nuts welded to the bottom of the next. Tightening these screws visibly reduced the radial gap size between the joining band and the next segment, but gaps of up to 0.06" remained. Applying 30 in-lbs of torque to the fasteners connecting the segments did reduce the peak height by a factor of 4 compared to the no torque case, but due to the remaining gaps the gains had already begun to taper by 30 in-lbs.

### 8.5.2 Thermal interference fit

To circumvent the limit of the fasteners in creating a tight mechanical fit, we removed the joining bands of the inner layers of two segments and machined them to create a thermal interference fit. The ID of the top of one segment and the OD of the bottom of a second were machined to be 0.001" oversized on the diameter, such that only by heating the bottom segment by more than 100°C could the two slide together. On cooling, the segments are permanently and tightly joined. The segments overlapped by 1".

The interference fit reduced the residual peak height by another factor of 4 from the high-torque case. The peak remaining could be a result of reduced permeability from both the machining process required to make a thermal interference fit and the stress in the mumetal material at the interference. [163]

### 8.5.3 Metglas wraps

We investigated the possibility of creating a more uniform innermost layer by wrapping long, 2"-wide strips of high-permeability Metglas in helical or axial layers, as described in Ref. [174]. Each helical layer was wrapped with 1" overlap; each axial layer had 1/4" overlap between strips. We wrapped two helical layers of opposite helicity around the magnetometer shuttle support inside the inner segmented mumetal shield (OD = 6.5"). On top we added two layers of axially-aligned strips. The Metglas layers were wrapped tightly with cellophane to maximize contact between the layers. To disentangle the

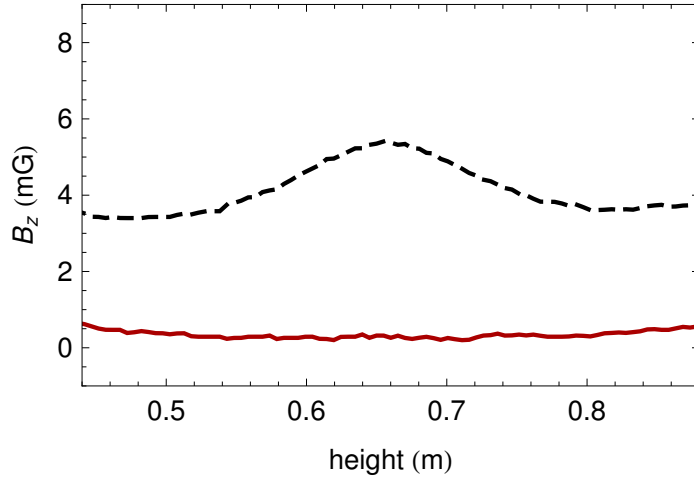


Figure 8.11: Magnetic field on the axis of a two-segment, three-layer shield with all joints welded, before and after degaussing with 3.5 G applied axial field. The trace has been cropped to isolate the region near the joint. The dashed black curve is the field before degaussing. The solid red curve is the field after degaussing. The offset between the curves is a result of the degaussing procedure.

effect of the Metglas from the effect of fastener torque, the fasteners on the inner mumetal shield were not tightened during this test. The Metglas outperformed the highly-torqued fasteners in suppressing the axial field, but the uniformity of the radial field was significantly degraded. The peak-to-peak variation in the radial field rose from less than 1 mG without the Metglas to 10 mG.

#### 8.5.4 Welding

To test a welded joint, we removed the joining band from the inner layer and welded the two inner segments together using a full penetration butt-weld. The same was done to two segments of the two outer layers. The 48" tall layers were then annealed following a standard procedure.

Before degaussing, the welded inner layer showed similar initial performance to the interference fit method, surpassing the performance of both the Metglas and the high-torque methods. We then applied a standard degaussing procedure. [172] While degaussing did not change the uniformity of the interference fit, the uniformity of the

welded shield was dramatically improved to the extent that a residual peak could no longer be detected. Critically, degaussing improved the field uniformity even when performed in the presence of a large applied field.

An evaluation of the field uniformity along the axis of the two-segment shield in a large field is important for our application because it mimics the environment of the full 14-segment shield. As outlined in Sec. 8.4.2 and the supplemental material (Sec. 8.7) the magnetic flux in the shield material at the midpoint of a long shield is much larger than that of a short shield of the same diameter. In the full shield, the inner layer, which has a length-to-diameter ratio of 45, will carry  $\sim 10$  times more flux than is present in this two segment test which has a ratio of 6.5. To replicate this high-field environment, we wrapped a solenoid around the outermost (welded) layer. This solenoid allowed us to apply up to 3.5 G to the three-layer shield – nearly 10 times more than the local Earth field – thus simulating the behavior of the joint in the full shield. Despite the high applied field, the welded shield still produced a very uniform field once degaussed (Fig. 8.11).

Even though the measured field appears uniform, the dynamic shielding ratio is in fact lower near the welded joint (Fig. 8.12). To measure the dynamic shielding ratio, we slowly changed the field applied by the solenoid by a small amount ( $< 50$  mG over 3 s at each magnetometer position) and measured the response in the shielded region. Since the solenoid was wrapped directly on the outermost shield layer, we could not measure the solenoid’s applied field independently. Nevertheless, by comparing the measured response to the field of the finite solenoid on axis calculated analytically, we extracted the dynamic axial shielding ratio shown in Fig. 8.12. For comparison, we also plot the dynamic shielding ratio for the interference fit segments. Not only is the welded shield’s uniformity better, but its dynamic shielding ratio is better as well.

Just as in the full shield case (Sec. 8.3.3) the uniformity of the field measured for the degaussed shield (Fig. 8.11) exceeds what would be expected from a simple division of the applied field by the axial shielding ratio (Fig. 8.12). Given the 3.5 G field applied and the variation in  $\Sigma_A$  shown in Fig. 8.11, we could expect a peak of  $\sim 4$  mG in the magnetic field profile inside the shielded region. The lack of such a peak again emphasizes both the benefit of degaussing for best field uniformity and

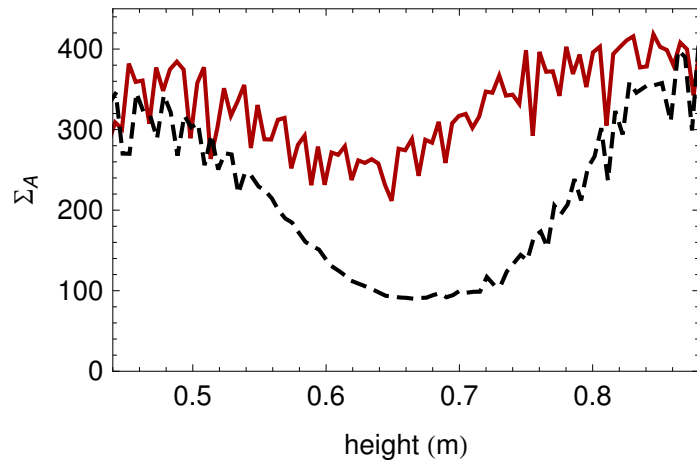


Figure 8.12: Dynamic axial shielding ratio of two-segment, three-layer shields. The traces have been cropped to isolate the region near the joint. In solid red is the axial shielding ratio for three layers of welded shielding. In dashed black, the inner welded layer has been replaced by the inner layer joined by a thermal interference fit. Both measurements were taken at a high (3.5 G) applied field and after a degaussing sequence. While the field is measured to be flat for the welded shield, the dynamic shielding ratio is lower near the joint.

the risk of sensitivity to time-dependent changes in the external field. Immediately after degaussing the field is uniform, but this uniformity will degrade if the ambient field changes.

Finally, we note that  $\Sigma_A$  for the two-segment shield is nearly two orders of magnitude larger than that of the full shield (Fig. 8.4). The values of  $\Sigma_A$  in Fig. 8.4 and Fig. 8.12 cannot be directly compared because of the different aspect ratios of the shields involved. Although the large field applied to the two-segment shield amplifies the effect of defects in the shield material, the shield's linear response is independent of the field magnitude up to field-dependent changes in the material permeability. This linear response is probed by small changes to the field during the measurement of  $\Sigma_A$ . Consequently,  $\Sigma_A$  is governed by the shield's aspect ratio, much like the theoretical and simulated shielding ratios (see Sec. 8.7). Indeed, performing the same measurement of  $\Sigma_A$  for the two-segment welded shields but varying the field about 150 mG rather than 3.5 G produces a profile similar to that shown in Fig. 8.12. Both with or without an initial degaussing procedure, the overall differences in magnitude fall within noise variations.

Simulations of this three-layer, two-segment shield produce a comparable axial shielding ratio of 370 when the permeability of the material is  $6 \times 10^4$ . While this permeability is more than twice the value that the full shield dynamic axial shielding ratio would suggest, this discrepancy may be due to differences in the annealing processes performed on the two-segment shield and on the full shield. [163]

## 8.6 Discussion

Instrumental to the success of the shield design was the finite element analysis we used to understand the performance of the segmented shield and its possible alternatives. Finite element simulations allowed us not only to model the detailed design of the shield, but also to explore the shield's homogenization of a non-uniform applied field. This flexibility makes finite element analysis a crucial step in effective magnetic shield design.

These simulations indicate that the homogenization of the degaussed shield is potentially better than our measurements would indicate: the amplitude and wavelength of the ambient field required to produce the amplitude and wavelength of the residual field far exceed what is observed. The residual field is then believed to be due to materials at or inside the innermost layer.

If the shield material itself had regions of higher or lower permeability, it could produce variations in the magnetic field on the cylinder axis. The likeliest location for permeability inhomogeneities of the shield would be the welded joints, but the residual features of the degaussed shield are not correlated with these locations. Moreover, we did not see such variations when performing tests with the two segments mounted on an independent support, even at the high fields that replicate the 14-segment environment.

In addition, the strongest transverse field ripple stops abruptly nearly 4 meters up the shield (see Fig. 8.3). As all shield segments were annealed simultaneously, it would be unusual for half the shield segments to develop inhomogeneities.

Despite extensive efforts to install only non-magnetic materials within the inner layer of the magnetic shield, it is nevertheless possible that these materials have some small magnetization. In particular, the heat tape used to bake the vacuum chamber, while nominally non-magnetic, is wrapped in two sections. The bottom section stops approximately halfway up the tube, and one contaminated heat tape could contribute to this residual field.

Beyond the details of this particular shield, it is certain that large length-to-diameter ratio shields create challenges in their design and construction. These shields channel more magnetic field than short shields, increasing the impact of inhomogeneities in the shield's permeability. No method we explored was able to create a more uniform permeability than welding the segments together, re-annealing them, and degaussing them. While this process does demand a large furnace, it enables a level of performance that far exceeds that of a segmented shield, creating a low-field, low-gradient magnetic environment suitable for precision measurements.

## Acknowledgements

The authors gratefully acknowledge the valuable conversations with B. Plaster, S. Koch, M. Adolf and J. Rudolph. TK acknowledges support from the Fannie and John Hertz Foundation. TK, SD and AS acknowledge support from the NSF GRFP. AS acknowledges support from an Anne T. and Robert M. Bass Stanford Graduate Fellowship and a DoD NDSEG Fellowship.

## 8.7 Supplemental material: analytical models for magnetic shield design

The design of multi-layer cylindrical magnetic shields typically begins with analytical equations for the transverse shielding ratio ( $S_T$ ) presented over a century ago. [164] This transverse shielding ratio is the fraction of the external magnetic field perpendicular to the cylinder's axis that can be measured at the center of the shield. The comparable fraction for field along the axis of the shield is the axial shielding ratio ( $S_A$ ). The mathematical models describing magnetic shielding are presented in several reviews [161, 167–169] and are summarized in Ref. [162]. We will briefly highlight the formulas for the transverse shielding ratio ( $S_T$ ) of a magnetic shield, then elaborate on the axial shielding ratio ( $S_A$ ) for large length-to-diameter ratio ( $\gamma = L/D$ ) shields in particular.

### 8.7.1 Transverse shielding ratio

The transverse shielding ratio  $S_T$  of a single cylindrical shield of high permeability ( $\mu \gg 1$ ) and infinite length, is given by [169]

$$S_T = \frac{\mu t}{D} \tag{8.2}$$

where the shield has thickness  $t$  and outer diameter  $D$ . The shield is assumed to be thin ( $t \ll D$ ).

It is also well known that multiple thin layered shields can outperform a single thick shield by a wide margin. The shielding factor of  $n$  thin layers nested together is

approximated by [167]

$$\begin{aligned} S_{tot} = 1 &+ \sum_{i=1}^n S_i + \sum_{i=1}^{n-1} \sum_{j>i}^n S_i S_j \left[ 1 - \left( \frac{X_i}{X_j} \right)^k \right] \\ &+ \dots + S_n \prod_{i=1}^{n-1} S_i \left[ 1 - \left( \frac{X_i}{X_{i+1}} \right)^k \right] \end{aligned} \quad (8.3)$$

For the multi-layer transverse shielding ratio of cylindrical shields,  $k = 2$ , the quantity  $X_i$  is the diameter of the  $i^{\text{th}}$  layer ( $D_i$ ), and the  $S_i$  are the transverse shielding ratios (Eq. (8.2)) calculated independently based on that layer's permeability, thickness, and diameter ( $S_i = \mu_i t_i / D_i$ ). The shields are indexed with  $i$  from the innermost shield outwards.

Often, the transverse shielding ratios are large enough that the last term dominates, but as  $D_i \rightarrow D_{i+1}$  this term vanishes and the first two dominate.

### 8.7.2 Axial shielding ratio

The axial shielding ratio of a finite-length single-layer cylindrical shield is typically given as a function of its transverse shielding ratio: [161]

$$S_A = 4NS_T + 1 \quad (8.4)$$

The (fluxmetric) demagnetizing factor  $N$  is a geometrical correction that folds in the length-to-diameter ratio,  $\gamma$ . If the length equals the diameter,  $N = 1$ . As  $\gamma$  increases,  $N \rightarrow 0$  and  $S_A \rightarrow 1$ , as is expected for an infinitely long cylinder. For long, finite cylinders ( $\gamma \gg 1$ ), the demagnetizing factor is given by [166]

$$N = \frac{1}{\gamma^2} \left[ \ln(2\gamma) - \frac{3}{2} \right] \quad (8.5)$$

We find that this formula matches finite element simulations of simple shields for  $\gamma > 10$  to better than 10%. In comparison, the demagnetization factor for an ellipsoid, [165] a common alternative, matches simulations only to within 30% over the same range

of  $\gamma$ .

From this factor and an assumption about the magnetic permeability of the material, we can design a single-layer shield with specified axial shielding capabilities. To approximate the axial shielding ratio of several layers nested together we can again use the recursive formula, Eq. (8.3), but now with  $k = 1$ ,  $X_i$  as the length of the  $i^{\text{th}}$  layer, and the  $S_i$  as the axial shielding ratio for each layer individually. [167] When comparing these calculations to simulations for the shields in the text (Sec. IIIA), however, we find that the calculations match the simulations best when the layers are closely-spaced. That is, they match best when  $D_i - D_j \ll D_i$ .

Endcaps or lids on the ends of the shields can modify axial shielding performance by a factor of  $(1 + \frac{1}{2\gamma})^{-1}$ , but due to our large values of  $\gamma$  this correction is small. [161, 165]

Finally, we note that the concentration of magnetic field within the shield material is proportional to  $\frac{1}{4N}$ , with the consequence that longer shields of the same diameter will divert more field through their material. [161] Not only does this bring the material closer to saturation, potentially decreasing its effectiveness as a shield, but it also has consequences for joints between shields.

# Chapter 9

## Current work – Large momentum transfer atom optics

The high acceleration sensitivity of the atom interferometer thus far, as anticipated in Eq. 3.21 and measured in Ch. 5, has relied on the extremely long drift time permitted in the 10 meter tower. With the extension of the interferometer time, the area enclosed by the interferometer arms increases, as does the size of the primary phase term,  $k_{\text{eff}}gT^2$ .

An alternative method of improving the interferometer sensitivity is to increase the area enclosed by making  $k_{\text{eff}}$  larger, or stated equivalently, by making the momentum separation between the two arms larger. This is the goal of large momentum transfer (LMT) interferometry.

### 9.1 Preliminary large momentum transfer interferometry results

In LMT interferometry, the two interferometer arms are separated not by two photon recoils ( $2\hbar k = \hbar k_{\text{eff}}$ ), but by many photon recoils ( $n\hbar k = n\hbar k_{\text{eff}}/2$ ). The extra momentum recoils can be imparted in several ways, including 1) a single multi-photon pulse that directly couples two states separated by several  $\hbar k_{\text{eff}}$  [81, 144, 175, 176],

2) an interferometer pulse followed by a series of mirror pulses that accelerate the two arms apart [81, 144, 175, 177], or 3) an interferometer pulse followed by a lattice (Bloch) acceleration of one or both interferometer arms [144, 176, 178]. As long as any acceleration duration is short compared to the total drift time, the interferometer sensitivity for all three options will scale approximately with the momentum separation  $n\hbar k$ .

It is important to note that all the sources of systematic error, like those of Tab. 3.1, also scale with  $k_{\text{eff}}$  and therefore  $n$ . These systematic errors will limit the fractional precision of the apparatus to the same level both with and without LMT. The speed at which the system will integrate to that precision, however, is dramatically faster with LMT.

The sensitivity of the long-time,  $2\hbar k$  interferometer discussed above is already impressive. At  $6.7 \times 10^{-12} g$  per 20 s cycle, it exceeds the previous record by two orders of magnitude [118]. Nevertheless, it would require a third of a year to integrate to below  $10^{-14} g$ . This integration time could be shortened by improving the cycle time, but such an improvement would scale only linearly.

With LMT interferometry, the required integration time falls quadratically with the momentum separation. A  $100\hbar k$  interferometer, for example, has a potential 50-fold increase in sensitivity below  $6.7 \times 10^{-12} g$ , and would integrate to below  $10^{-14} g$  in a little more than an hour. Achieving such a precision so rapidly makes it easier to perform the methodical exploration and mitigation of systematic error necessary for precision measurement.

Beyond its application to precision measurement, LMT interferometry also proves to be an excellent test for proposed modifications to quantum mechanics [65, 66]. These modifications explore the boundary between quantum and classical mechanics. One class of theories, for example, sets limits on the distance by which a massive quantum mechanical state can be extended before it is collapsed through spontaneous localization.<sup>1</sup> With 1 s drift time between the primary interferometer pulses, a high-contrast  $100\hbar k$  LMT interferometer would exclude such proposed modifications up to

---

<sup>1</sup>Another consequence of this spontaneous localization is a heating rate that limits the coldest effective temperatures achievable, as discussed in Ch. 7.

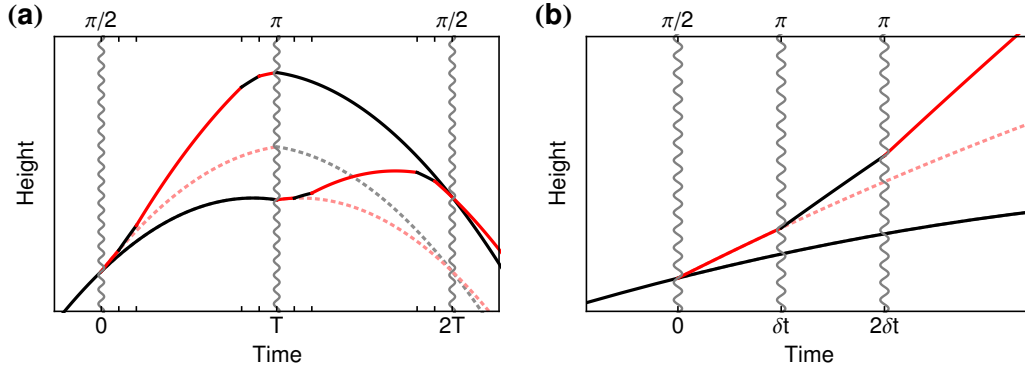


Figure 9.1: Comparison of  $2\hbar k$  (dotted) and  $6\hbar k$  (solid) Raman interferometers. Red versus black trajectories represent the two internal energy levels of the atom coupled by the Raman interferometer beams. (a) The three-pulse sequences, showing the increased area resulting from the increased momentum splitting of the LMT interferometer. For clarity, light pulses (grey) are shown only for the primary interferometer pulses. (b) A detail view of the first beamsplitter. In the LMT beamsplitter, the upper arm is accelerated away from the lower arm by a series of sequential mirror ( $\pi$ ) pulses.

the meter scale.

Building on previous work that demonstrated  $102\hbar k$  interferometry with short ( $\sim 10$  ms) interrogation times [81], we have implemented a sequential-Raman sequence that falls into the second of the three categories above (Fig. 9.1). The LMT beam splitter has two components: a standard two-photon Raman pulse that puts the atom wavepacket into a superposition of two states and a series of two-photon mirror pulses applied to one of the arms, accelerating it away. The construction of the LMT mirror and final beamsplitter pulses are similar.

With a total interferometer time of  $2T = 2.3$  s, we demonstrate up to  $12\hbar k$  LMT interferometry, which corresponds to a peak separation of 8.1 cm. For this large momentum separation, the contrast of the interferometer is small but noticeable, particularly through principal component analysis (described in Ch. 5). At  $2\hbar k$  momentum separation, the contrast is greater than 93%.

The atomic source used for these measurements has been previously described (Ch. 4 and 7 in particular). Briefly,  $^{87}\text{Rb}$  atoms are trapped and cooled by a 3D MOT followed by microwave evaporation in a TOP trap and a magnetic lens. The

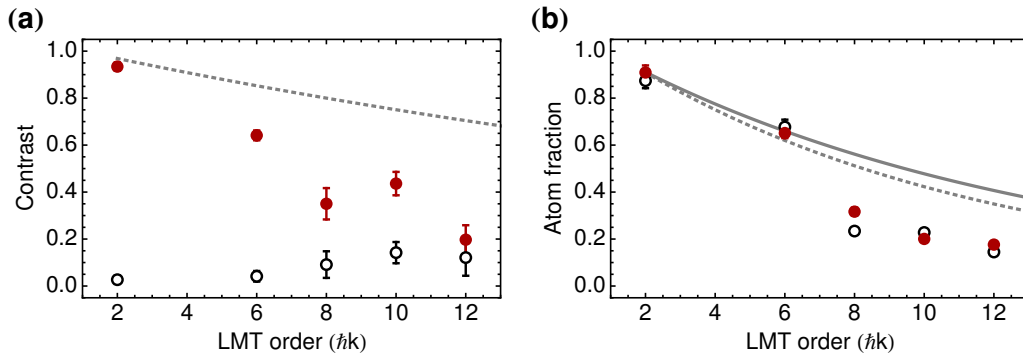


Figure 9.2: LMT interferometry at 3 GHz detuning. Filled red points represent interferometry; open black points represent the control experiments where interference is inhibited by delaying the third pulse by  $600 \mu\text{s}$  ( $1800 \mu\text{s}$  for  $2\hbar k$ ). Error bars indicate the  $1\sigma$  error in the measurement. (a) Decay of interferometer contrast with LMT order. The dashed grey curve is the expected loss of contrast due to atoms scattered during the third LMT pulse. (b) Fraction of atoms remaining compared to the theoretically expected trend from spontaneous emission. The dashed grey curve is the expected value if all spontaneous emission events of the first and second (but not third) LMT pulses result in effective atom loss. The  $2\hbar k$  interferometry data point is fixed at the value predicted by the dashed grey curve, and all other data points are normalized consistently. The solid grey curve is a fit to the measured decay rate of an independent spontaneous emission test, also fixed to have the same value as the dashed grey curve at  $2\hbar k$ .

resulting cloud contains  $10^5$  atoms at a few nanokelvin. After transferring these atoms with microwaves to a magnetically insensitive state, they are accelerated vertically with an optical lattice to 13 m/s. Once they have entered the magnetically shielded interferometer region, we apply the interferometer pulse sequence. Following the final beamsplitter pulse, we allow the atoms to fall into the detection region where we count the fraction of atoms in the two interferometer output ports with fluorescence imaging along two perpendicular axes.

The interferometer beams are generated by the high-power doubled 1560 nm system described in detail in Sec. 4.2.6. For the data in Fig. 9.2, the carrier of the phase-modulated Raman beams is tuned to be approximately midway between the  $|F = 1\rangle$  and  $|F = 2\rangle$  transitions of the  $^{87}\text{Rb}$   $D_2$  line. One beam path of the Raman pair is modulated at 6.8 GHz, such that a first-order sideband and the carrier of the other path satisfy the conditions for Raman resonance. The other beam path is modulated at 5 GHz, where the sidebands are used only for AC Stark shift compensation.

A consequence of choosing to use a sideband and a carrier as a Raman pair is that the interferometer detuning is limited to 3.4 GHz. This detuning is small enough to result in a spontaneous emission rate that is non-negligible over the many pulses of an LMT interferometer. The incoherent scattering of a photon during spontaneous emission causes the atom's wavefunction to collapse, and imparts a momentum kick in a random direction. For the first beamsplitter and the mirror pulse, the long drift time before imaging allows these kicked atoms to expand sufficiently far from the remaining ensemble to be measured simply as a loss of atoms. But the third interferometer pulse occurs only 260 ms before imaging. In that time, the scattered atoms can drift only 1.5 mm, or approximately the size of the typical cloud. As a consequence, they form an incoherent background for the interfering atoms, and are detected as a loss in contrast.

Figure 9.2(b) shows that much, though not all, of the decay in total atom number during interferometry can be attributed to loss due to spontaneous emission. This loss was measured independently by performing the interferometry sequence with the interferometer lasers detuned by 1 MHz from two-photon resonance, suppressing population transfer. Atom loss during interferometry in excess of this independent

measurement could indicate imperfect transfer efficiency of the Raman pulses.

The detuned-laser atom number decay rate is consistent with the predicted loss due to spontaneous emission from the first two LMT pulses, calculated (as described further below) from the applied frequency spectrum. The effect of the third pulse is not included in the atom loss calculation because of the insufficient drift time for the atoms to disperse. Instead, the effect of the third-pulse scattered atoms is calculated to lead to a  $\sim 30\%$  contrast loss for a  $12\hbar k$  interferometer, as shown in Fig. 9.2(a). Reducing this contrast loss demands larger beam detunings to suppress the rate of spontaneous emission, also discussed in detail below.

Additional contrast loss may be attributed to imperfect population transfer for the final LMT beamsplitter, despite efforts to optimize the detuning and pulse duration. Imperfect transfer, like spontaneous emission, produces a background population of non-interfering atoms. Another consideration is the uncertainty in the measured contrast as the atom number falls, indicated by the increasing size of the  $1\sigma$  error bars of Fig. 9.2(a). Finally, any perturbations in the wavefront of the interferometer beams or imperfections in Coriolis compensation can lead to phase inhomogeneities that would accumulate through the LMT procedure, again leading to a loss in contrast.

Nevertheless, the significance of spontaneous emission both for overall atom number and for interferometer contrast merits further investigation, and is the subject of the remainder of this chapter. The rate of spontaneous emission, however, depends on the exact frequency spectrum incident on the atoms, which in turn is fixed by the requirements for compensation of AC Stark shifts. We begin, therefore, with a more detailed discussion of the AC Stark shift compensation scheme before delving into the spontaneous emission calculation.

## 9.2 AC Stark compensation

In the implementation under discussion, frequency spurs for AC Stark compensation are created through phase modulation. An important advantage of this scheme is that the resulting interferometer beam induces no AC Stark shifts on the atom transitions, leading to a suppression of phase and detuning inhomogeneities. Unlike

compensation schemes that rely on balancing the intensities of the two interferometer beams, appropriate phase modulation results in beams that are self-compensating, alleviating concerns associated with relative intensity noise and beam overlap.

Phase modulation with a pure sine wave generates a symmetric spectrum of spurs separated by the modulation frequency  $\nu_{\text{mod}}$ . The intensity of the  $n$ -th order spur is determined by the square of the Bessel function of the first kind,  $J_n(\beta)^2$ , where the modulation depth  $\beta$  is related to the amplitude of the applied sine wave.

If the detuning of the carrier of the beam is approximately midway between  $|F = 1\rangle$  and  $|F = 2\rangle$  and the modulation frequency  $\nu_{\text{mod}}$  is large enough to place the first-order sidebands outside of the atomic transitions, then a modulation depth  $\beta$  exists that cancels not only the relative AC Stark shift between transitions, but also the absolute AC Stark shift of each transition. The evolution of the atoms' phase is therefore the same as if the beam were not present at all.

Compensation of the relative AC Stark shift is important for defining a uniform Raman resonance frequency over the entire beam intensity profile and is therefore critical for achieving atom optics with high transfer efficiency. Compensation of the absolute AC Stark shift eliminates phase inhomogeneities from height-dependent variations in the laser intensity, which can arise from the rapid diffraction of intensity perturbations with small spatial scale.<sup>2</sup> This effect is of concern primarily for the interferometer mirror pulse, where the two arms are separated by an appreciable amount. Over this separation, a small ripple may reasonably diffract as it propagates from the location of one arm to the other.

For example, if the absolute AC Stark shift changes by 1 kHz across the spatial width of the ensemble in one arm, this leads to a 0.1 rad phase shift inhomogeneity after a single pulse of 100  $\mu\text{s}$  duration (assuming, for simplicity, uniform absolute Stark shift across the cloud in the other arm). In LMT interferometry, the phase shift inhomogeneity accumulates with each applied pulse, of which there can be many, producing a rapid loss in contrast as the imparted momentum separation grows. In

---

<sup>2</sup>A tilt of the beam relative to the direction of the momentum separation can also result in an intensity difference between the two arms of the interferometer. For a beam large relative to the atom cloud size, the height-dependent intensity difference will be uniform across the cloud and will result in an overall interferometer phase offset but not a loss of contrast.

addition, the large separations between the arms of an LMT interferometer means that a small ripple can diffract to a greater extent, further amplifying the phase inhomogeneity acquired during each pulse.

In an extreme case, small-scale intensity perturbations can lead to surprisingly strong microlensing, which scales inversely with the square of the ripple size (see Ch. 7). If diffraction of the perturbation causes the degree of microlensing to differ between the two arms, contrast loss can result both through the lack of overlap of the atomic wavepacket at the final beamsplitter and through the coupling of the velocity inhomogeneities to other inertial effects (like rotations).

For a symmetric phase modulation spectrum, the carrier detuning necessary to null the absolute AC Stark shift in addition to the relative AC Stark shift is  $\Delta_0 = 2\pi 3.181 \text{ GHz}$  blue of the  $|F = 2\rangle \rightarrow |F' = 3\rangle$  cooling transition. The detuning is notably not  $6.834/2 \text{ GHz} = 3.417 \text{ GHz}$  because of the different transitions available to each ground state. In particular, the strongest line from the  $|F = 2\rangle$  manifold ( $|F = 2\rangle \rightarrow |F' = 3\rangle$ ) is 266 MHz higher in frequency than the strongest transition from the  $|F = 1\rangle$  manifold ( $|F = 1\rangle \rightarrow |F' = 2\rangle$ ). It is therefore not unexpected that the desired detuning would be less than the simple halving of the microwave transition frequency.

We can describe the demand that relative AC Stark shift cancellation places on the modulation depth in a simple way if we assume a low Rabi frequency ( $\Omega \ll \Delta$ ) and a large detuning of any phase modulation sideband from either ground state ( $\Delta$  much larger than any hyperfine splitting). The AC Stark shift can then be found in the far-detuned limit (Eq. 4.3), and the modulation depth that nulls the AC Stark shift for a particular state satisfies the relation

$$0 = \sum_{n \in \mathbb{Z}} \frac{J_n(\beta)^2}{\Delta_0 + n\nu_{\text{mod}}} . \quad (9.1)$$

Note that although  $\Delta_0$  is defined relative to  $|F = 2\rangle$ , its value is such that the detuning from  $|F = 1\rangle$  is the same magnitude, but opposite in sign. Because of this choice, the net AC Stark shift will be simultaneously nulled for both states. Figure 9.3 shows the intensity ratio of the carrier to the first sideband necessary for compensation as a

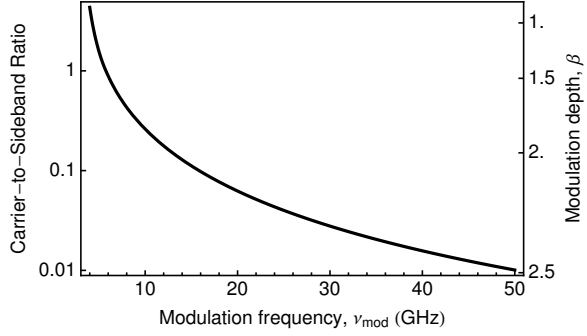


Figure 9.3: Modulation depth for AC Stark shift compensation. The carrier is detuned 3.181 GHz from the  $|F = 2\rangle \rightarrow |F' = 3\rangle$  cooling transition. As the modulation frequency grows, the carrier intensity falls relative to the first-order sideband.

function of the phase modulation frequency.

With this phase modulation method for single-beam AC Stark shift compensation, there are two beam combinations that can lead to Raman transitions. The first, used for Fig. 9.2, takes the carrier of one beam and a sideband of the other to form the Raman pair. As a result, the modulation frequency for one of the two beams will be near 6.8 GHz, and the interferometer detuning is fixed to be  $\sim 3$  GHz. The second pairs the red (or blue) sidebands of both beams. In this latter case, the Raman detuning can be made arbitrarily large, as long as the frequency difference between the two sidebands of interest is 6.8 GHz. In both cases, to avoid degeneracy between the red and blue sidebands, the carriers of the two beams should be offset by much less than the overall detuning from the atomic transitions but more than the largest possible Doppler shift. In this implementation, the carriers are offset by 160 MHz by a pair of AOMs [see Fig. 4.14(a)].

### 9.3 Spontaneous emission

Once the frequency spectrum is known, we can calculate the beam’s spontaneous emission rate. In particular, we are interested in determining the fraction of atoms that will be participating in interferometry after accounting for all the incoherent scattering that occurs during the interferometer pulses.

The scattering rate for a single transition is given by

$$R_{\text{sc}} = \frac{\Gamma}{2} \frac{I/I_{\text{sat}}}{1 + 4(\Delta/\Gamma)^2 + (I/I_{\text{sat}})^2}. \quad (9.2)$$

Here,  $\Gamma$  is the natural linewidth of the transition,  $I$  is the beam intensity,  $I_{\text{sat}}$  is the saturation intensity of the transition, and  $\Delta$  is the detuning from the transition. For atoms in the  $m_F = 0$  sublevel of either  $|F = 1\rangle$  or  $|F = 2\rangle$ ,  $I_{\text{sat}} = 2.50 \text{ mW/cm}^2$ .

At large detunings ( $\Delta \gg \Gamma$ , and  $\Delta/\Gamma \gg I/I_{\text{sat}}$ ) the spontaneous emission rate scales as  $\Delta^{-2}$ . But since the Rabi frequency decreases with detuning as  $\Omega \sim \Delta^{-1}$ , at a constant laser power each interferometer pulse must be longer in duration to maintain the same pulse area. Consequently, the number of spontaneous emission events per  $\pi$  pulse will scale as  $R_{\text{sc}}/\Omega \sim \Delta^{-1}$ . The detuning cannot be increased without limit, however, because the longer pulses will begin to cut into the atom number through velocity selection [79, 179]. Therefore, given a maximum available laser power there is a compromise to be made between large detunings, which best suppress spontaneous emission, and small detunings, which avoid velocity selection.<sup>3</sup>

Figures 9.4 and 9.5 illustrate this conflict within the context of the single-beam AC Stark compensation scheme described here. A desired loss rate at a desired LMT order specifies a minimum modulation frequency. Given that frequency, the desired pulse duration specifies the beam intensity, or vice versa. Results are shown both for infinite doubling bandwidth of the PPLN doubling crystals (see Appendix B), as well as for the measured 50 GHz bandwidth (HWHM of the sinc doubling envelope). While an envelope of this scale has minimal impact on the spontaneous emission rate (Fig. 9.4), it does affect the  $\pi$  pulse durations at modulation frequencies near and larger than the bandwidth (Fig. 9.5).

To find the number of spontaneous emission events and the pulse time, we first calculate the modulation depth needed to cancel AC Stark shifts for each modulation

---

<sup>3</sup>While the velocity acceptance can be improved through adiabatic rapid passage or composite pulses, both techniques increase the number of spontaneous emission events due to the increased pulse duration. Incorporating either requires care when considering the compromise between low spontaneous emission and short pulse time. For this work, we consider atom optics composed of only single optical pulses.

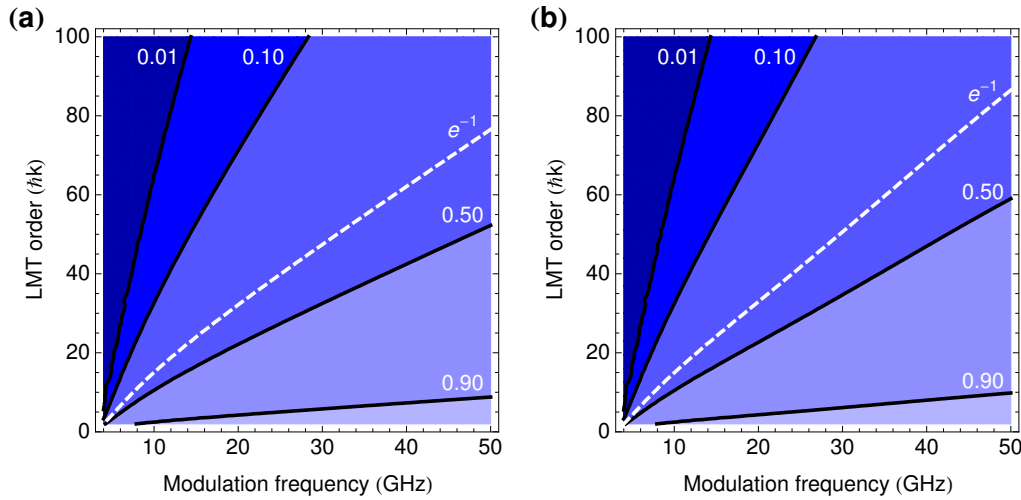


Figure 9.4: Fraction of the atom ensemble participating in the interferometer as a function of the phase modulation frequency and the large momentum transfer order for (a) a phase modulated pair of interferometer beams and (b) a phase modulated pair where the finite bandwidth of the 1560-to-780 doubling efficiency is taken into account. The number next to each contour indicates the fraction of the ensemble that remains coherent at the end of the interferometer sequence (the fraction that has not scattered a photon). The modulation frequency is that of the closer-detuned of the two Raman beams; the other beam is modulated at a frequency 6.8 GHz larger. The doubling efficiency bandwidth is taken to be the measured value, 50 GHz.

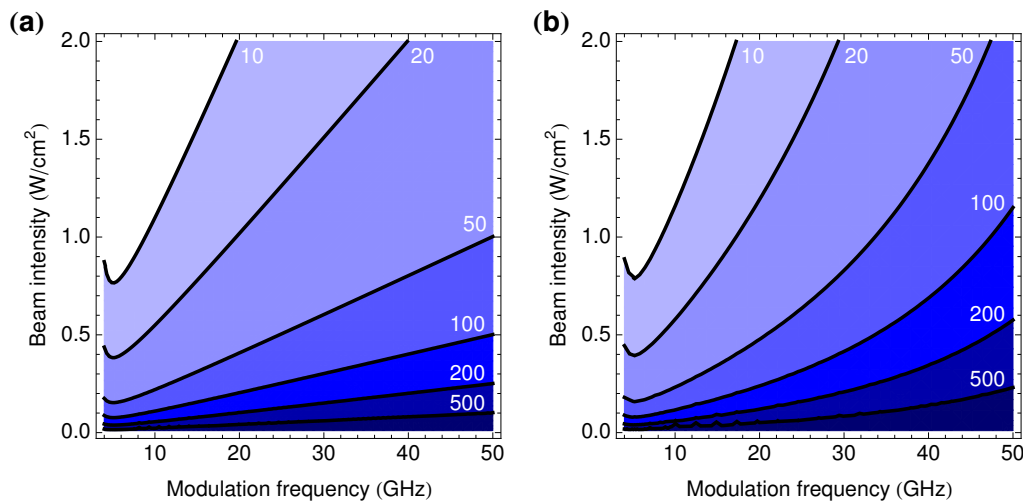


Figure 9.5: Duration of a  $\pi$  pulse as a function of the phase modulation frequency and the beam intensity for (a) a phase modulated pair of interferometer beams and (b) a phase modulated pair where the finite bandwidth of the 1560-to-780 doubling efficiency is taken into account. The number next to each contour indicates the duration of a  $\pi$  pulse in microseconds. The modulation frequency is that of the closer-detuned of the two Raman beams; the other beam is modulated at a frequency 6.8 GHz larger. The doubling efficiency bandwidth is taken to be the measured value, 50 GHz.

frequency. For two beams with modulation frequencies separated by 6.8 GHz, we then calculate the duration of a  $\pi$  pulse,  $\tau_\pi = \pi/\Omega \sim I^{-1}$ , and the number of scattering events per  $\pi$  pulse,  $N_\pi = R_{\text{sc}}\tau_\pi$ . Note that because  $R_{\text{sc}} \sim I$  in the far-detuned limit of the scattering rate,  $N_\pi$  is independent of the beam intensity. Also note that while  $\tau_\pi$  is largely monotonic with detuning, its trend reverses direction at small detunings because of the rapidly increasing fraction of power that must be diverted to the carrier in order to maintain AC Stark cancellation.

The spontaneous emission rates and pulse durations found through these calculations agree well, but not perfectly, with experimental data. The comparison of the calculated and measured spontaneous emission rates at 3 GHz detuning shown in Fig. 9.2(b) (solid and dashed curves) demonstrates one example of good agreement. Measurements at 30.7 GHz modulation, however, suggest that the predictions in Fig. 9.4 overestimate the spontaneous emission rate by almost a factor of 2, and those in Fig. 9.5 underestimate the pulse duration by a factor of 2/3. Nevertheless, the calculations serve as useful guides for exploring the available parameter space.

It is clear from Fig. 9.4 that a detuning of more than 10 GHz is necessary for  $100\hbar k$  LMT interferometry, unless the atom number is so high as to support large losses while still retaining enough atoms for low atom shot noise. With large detuning comes an increasing demand for either higher laser intensity to maintain a reasonable ( $\lesssim 100\mu\text{s}$ )  $\pi$  time given typical cloud temperatures, or vertically colder atom clouds to improve the transfer efficiency of the long, velocity-selective pulses. This type of analysis was instrumental in the decision to modify the high-power doubled 1560 nm laser system to accommodate modulation frequencies of up to 40 GHz.

Future work may also be devoted to improving our current delta-kick cooling techniques (Ch. 7). Further cooling in the transverse dimensions would allow higher Rabi frequencies through the use of smaller interferometer beams, permitted by the smaller cloud size at the end of the interferometer. Alternatively, further cooling in the vertical dimension would benefit the transfer efficiency of long, velocity selective pulses. Any one or more of these techniques may well enable  $100\hbar k$ -scale momentum splittings and record-breaking atom interferometer sensitivity.

# Chapter 10

## Future work – Dual species evaporation for atom interferometry

For the test of the equivalence principle, we will run simultaneous, overlapped interferometers on a dual-species cloud of ultracold  $^{85}\text{Rb}$  and  $^{87}\text{Rb}$ . It is of great importance that the ensembles of the two species be closely matched kinematically while being cold enough ( $\lesssim 10\text{ nK}$ ) for efficient interferometry. Transverse and vertical velocity or position errors exacerbate the differential effects of rotations, gravity gradients, and magnetic fields, and so the combined cooling and launching procedure must be optimized to produce the best kinematic overlap. In this chapter, I outline methods for achieving ultracold dual-species clouds of  $^{85}\text{Rb}$  and  $^{87}\text{Rb}$ , with an eye towards preparing well-matched ensembles prior to launching.

One of the important steps in creating ultracold clouds is evaporative cooling, which relies on a high collision rate to rethermalize the atom distribution after ejection of the hottest atoms. While the  $^{85}\text{Rb}$  and  $^{87}\text{Rb}$  single-species collision rates are comparable below  $100\text{ }\mu\text{K}$ , between  $\sim 150$  and  $600\text{ }\mu\text{K}$  the collisional cross-section of  $^{85}\text{Rb}$  with itself is one to two orders of magnitude smaller than the  $^{87}\text{Rb}$  collisional cross-section [61]. Since the initial temperature of the cloud is typically in this regime (see Fig. 4.11), evaporative cooling with this species alone is inefficient. Instead,

ultracold clouds of  $^{85}\text{Rb}$  can be created using  $^{87}\text{Rb}$  as a refrigerant: the  $^{87}\text{Rb}$  can be efficiently cooled through evaporative techniques, and the interspecies collisional cross-section and scattering lengths (comparable to those of  $^{87}\text{Rb}$  alone) are sufficient to cool  $^{85}\text{Rb}$ . Such dual-species sympathetic cooling with these isotopes has been previously demonstrated [62, 63].

There are two primary pairs of states of interest for dual-species evaporation:  $|F = 3, m_F = 3\rangle_{85} - |F = 2, m_F = 2\rangle_{87}$ , or  $|F = 2, m_F = -2\rangle_{85} - |F = 1, m_F = -1\rangle_{87}$ . These pairs have the two lowest interspecies inelastic collision rates at  $10^{-15} \text{ cm}^3/\text{s}$  and  $10^{-18} \text{ cm}^3/\text{s}$  respectively, where  $10^{-13} \text{ cm}^3/\text{s}$  is considered to be the maximum acceptable [61]. For reference,  $|F = 1, m_F = -1\rangle_{87}$  has an intraspecies inelastic scattering rate of  $10^{-18} \text{ cm}^3/\text{s}$ . The benefits of each dual species pair will be discussed further below.

Prior to evaporation, we must first collect and cool a dual-species cloud in a 3D MOT to  $\sim 10 - 100 \mu\text{K}$ . While most of the infrastructure for  $^{85}\text{Rb}$  was already extant [86], we added the RF necessary for dynamic control over the detuning of the cooling frequency (Sec. 10.1). In addition, because the energy from both species is removed through  $^{87}\text{Rb}$ , resulting in high loss rates, we have implemented optical pumping that increases the number of atoms available for evaporation by a factor of 3 or 5, depending on the  $^{87}\text{Rb}$  hyperfine state used (Sec. 10.2).

## 10.1 Dual species cMOT

The detuning of the locked laser light is chosen such that when phase-modulated at a particular frequency (2.527 GHz), the first order sideband provides repump light for  $^{85}\text{Rb}$  ( $|F = 2\rangle \rightarrow |F' = 3\rangle$ ), while the second-order provides repump light for  $^{87}\text{Rb}$  ( $|F = 1\rangle \rightarrow |F' = 2\rangle$ ). An independent fiber modulator for control of the  $^{85}\text{Rb}$  cooling and depump light has long been in place [86], but only recently have we implemented a scheme for dynamic control of the frequency of the light.

The dynamic control of the frequency comes from a DDS channel of the timing system, which is quadrupled, then amplified and filtered as necessary (Fig. 10.1). Since the master laser is locked 480 MHz blue of the  $^{85}\text{Rb}$   $|F = 3\rangle \rightarrow |F' = 2\rangle$ ,  $|F = 3\rangle \rightarrow$

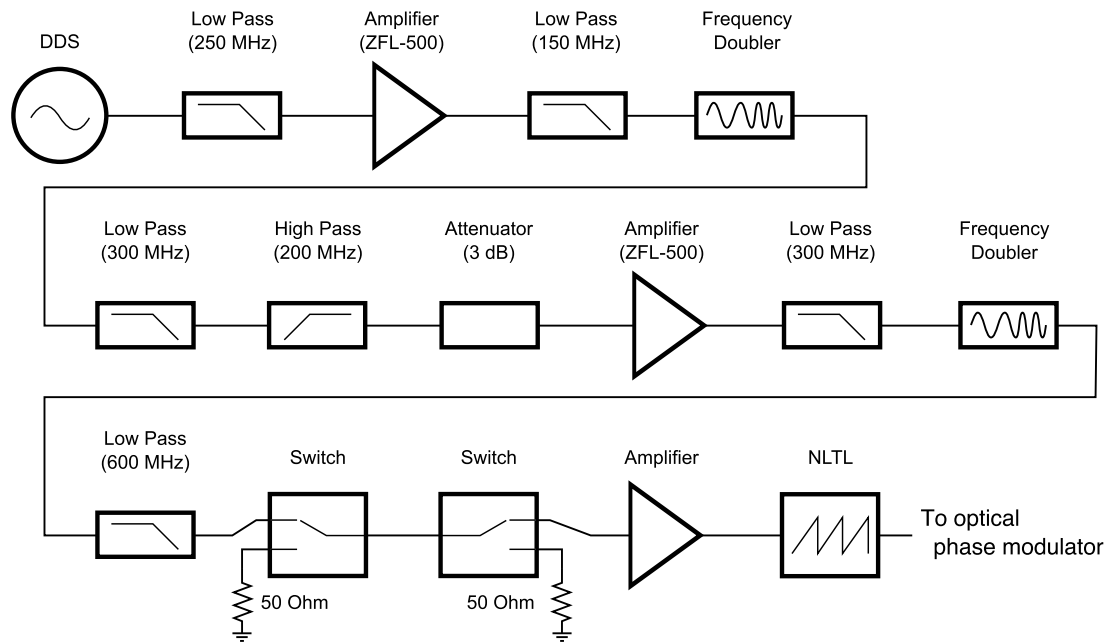


Figure 10.1: Microwave electronics for  $^{85}\text{Rb}$  cooling and depump frequencies, generated by a quadrupled DDS frequency. Two switches (the first in place for a future addition of a different frequency to this chain), can turn on and off the RF modulation power. After the final amplification stage, the microwaves are sent through a nonlinear transmission line (NLTL; Picosecond Pulse Labs 7112-110) that produces a sawtooth waveform. When applied to the optical phase modulator, the sawtooth waveform produces a single dominant optical frequency, shifted by the fundamental modulation frequency.

$|F' = 4\rangle$  crossover resonance, a DDS frequency of 97 MHz (quadrupled to 388 MHz) results in light resonant with the  $|F = 3\rangle \rightarrow |F' = 4\rangle$  cooling transition. A DDS frequency of 127 MHz (quadrupled to 508 MHz) results in light resonant with the  $|F = 3\rangle \rightarrow |F' = 3\rangle$  depump transition, used to pump atoms into the  $|F = 2\rangle$  ground state.

With the same laser powers and an analogous cMOT sequence as for  $^{87}\text{Rb}$  (described above in Sec. 4.1.1), we have been able to create single-species cMOTs with  $4 \times 10^9$  atoms of either  $^{87}\text{Rb}$  or  $^{85}\text{Rb}$ . When loading a dual-species cMOT for evaporation, we bias the laser powers and detunings to favor the  $^{87}\text{Rb}$  atoms, which experience more loss through the sympathetic cooling process. Previous work has shown efficient sympathetic cooling [63] and creation of ultracold dual-species clouds [62] with an order of magnitude more  $^{87}\text{Rb}$  atoms than  $^{85}\text{Rb}$  atoms. Both these works, however, use radiofrequency evaporation, which is not perfectly isotope-selective and can result in active evaporation – and therefore loss – of  $^{85}\text{Rb}$  when the two species have comparable atom numbers. Conversely, the microwave evaporation used in this work is perfectly isotope selective (see Sec. 10.3), and we may be able to further suppress the initial number of  $^{85}\text{Rb}$  atoms relative to  $^{87}\text{Rb}$ , leading to more efficient sympathetic cooling.

## 10.2 Optical pumping

In three out of the four states of interest (the exception being  $|F = 1, m_F = -1\rangle_{87}$ ), there are multiple Zeeman sublevels that can be magnetically trapped. If the Zeeman sublevels are populated uniformly, then by transferring into the magnetic trap, only 1/5 of the atoms will be in the anticipated  $|m_F = 2\rangle$  state for the  $|F = 2\rangle$  atoms, or 1/7 in the  $|m_F = 3\rangle$  state for the  $|F = 3\rangle$  atoms. Beyond the reduction of atoms in the desired state, atoms trapped in other sublevels can have negative consequences for evaporation. These sublevels have potentially worse intrastate, interstate, and interspecies inelastic collision rates, increasing the overall atom loss. And in general, different sublevels become resonant with the evaporation knife at different distances from the trap center, resulting in a slow evaporation as one sublevel sympathetically cools the others.

With circularly-polarized light and a magnetic bias field along the propagation direction of the beam, the atoms can be efficiently pumped into one of the extreme Zeeman sublevels, e.g.  $m_F = \pm 2$  for  $F = 2$ . Following Ref. [180], we have implemented a scheme where pulses of circularly-polarized light (from the probe beam used for absorption imaging) are timed to coincide with a certain phase of the rotating bias field used for TOP evaporation. The phase of the rotating bias field is deterministically reset each experimental cycle. By changing the delay of the application time of the optical pumping pulses, we can change the direction of the field during the light pulse. Only when the field is optimally parallel or antiparallel to the propagation direction of the light (depending on the sign of the circular polarization) will the atoms be efficiently transferred into the trappable state. When applying multiple optical pulses, each of duration much less than the TOP rotation period, the optimal pulse spacing should be the period of the bias field rotation.

For dense clouds with high optical density, only an outer half-shell of atoms will be transferred due to the low penetration depth of the light. While operating with increased optical detuning can improve the penetration depth, rescattering of photons within the cloud limits the fraction of atoms transferred into the desired state.

We explored optical pumping into the  $|F = 2, m_F = 2\rangle$  state of  $^{87}\text{Rb}$ . After optimizing the field strength (3.5 G), pulse duration (100  $\mu\text{s}$ ), detuning (12 MHz), and pulse number (3), we find  $> 85\%$  of the atoms pumped into the state of interest (Fig. 10.2). We measure the number of atoms in this state by a fit of the magnetic trap shape to an absorption image taken after transferring the atoms into the quadrupole trap. Given the field strength just prior to imaging, the shape of the cloud is consistent with atoms in the  $m_F = 2$  Zeeman sublevel, and inconsistent with those in the  $m_F = 1$  sublevel, further evidence for efficient pumping. A sinusoidal fit to the atom number reports a frequency consistent with the expected 2.6 kHz of the bias field rotation.

### 10.3 Evaporation considerations

For radiofrequency evaporation, where a megahertz-scale frequency couples Zeeman levels of the same hyperfine state, an important consideration is the relative size

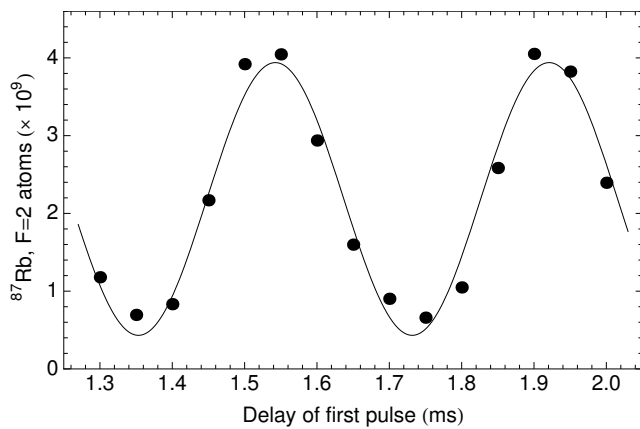


Figure 10.2: Impact of optical pumping on the number of  $|F = 2, m_F = 2\rangle$   $^{87}\text{Rb}$  atoms transferred into the quadrupole trap. The curve is a sinusoidal fit to the data, reporting a period of  $378 \pm 6 \mu\text{s}$  that is consistent with the expected period of the bias field rotation,  $385 \mu\text{s}$ . Three pulses were applied, each  $100 \mu\text{s}$  in duration and separated by approximately the same period (for this particular sequence, the pulse separation was  $395 \mu\text{s}$ , based on a sinusoidal fit to an earlier data set). The delay is defined to be the time between the turn-on of the bias coils and the center of the first pulse. The overall  $1.2 \text{ ms}$  delay (approximately three full cycles of the rotating bias coils) allows the field in the bias coils to build to the peak value,  $3.5 \text{ G}$ .

of the surface of evaporation for the two species, which determines the species that will predominately lose atoms through the evaporation process. For the evaporation implemented in this work, the gigahertz-scale microwaves couple a trapped state in one hyperfine level to an untrapped state in another hyperfine level. Since the hyperfine splitting is different for  $^{85}\text{Rb}$  and  $^{87}\text{Rb}$  by several gigahertz (3.0 and 6.8 GHz respectively), the microwave knife is species selective. As noted above, the higher intraspecies scattering cross-section for  $^{87}\text{Rb}$  makes it the logical choice for the actively-evaporated species.<sup>1</sup>

Evaporation with a microwave knife does carry an added complication when working with the  $|F = 2, m_F = 2\rangle_{87}$  state in particular. The knife transfers atoms from the trapped  $|F = 2, m_F = 2\rangle_{87}$  state to the untrapped  $|F = 1, m_F = 1\rangle_{87}$  state. As the untrapped atoms are pushed away from the trap center, they come into resonance again with the microwave knife and can be transferred to the trapped  $|F = 2, m_F = 1\rangle$  state [90]. If the field magnitude at the trap minimum does not change over the course of evaporation (i.e., the quadrupole gradient and the rotating bias field magnitude of the TOP trap remain constant), the atoms in this undesired state can be cleared by choosing the carrier frequency of the single-sideband mixer (the local oscillator of Fig. 4.5) to be resonant with the transition coupling the minimum of the  $|F = 2, m_F = 1\rangle$  trap to the untrapped  $|F = 1, m_F = 0\rangle$  state, as demonstrated in Ref. [90]. Alternatively, the frequency of the microwave knife could be periodically hopped to that same resonance as needed.

Because there is a single trapped state in the  $F = 1$  manifold, this is not a concern for evaporation in the  $|F = 1, m_F = -1\rangle_{87}$  state.

For sympathetic cooling to be effective, the thermal clouds of the two species must exhibit good overlap in the trap. In general, the two species have different masses and different responses to magnetic fields. For large differences in mass and magnetic dipole moment, small clouds can be displaced by more than their width, suppressing sympathetic cooling. A benefit of the  $|F = 3, m_F = 3\rangle_{85}$  and  $|F = 2, m_F = 2\rangle_{87}$  combination is the fact that the two have the same magnetic dipole

---

<sup>1</sup>A comparatively small cloud of  $^{87}\text{Rb}$  could nominally be used to mediate interactions between atoms in a cloud of  $^{85}\text{Rb}$  atoms, but the overall thermalization rate would be slower.

moments and therefore feel the same force from magnetic fields; the only contribution to a displacement is the small 2% mass difference.

Nevertheless, even with the  $|F = 2, m_F = -2\rangle_{85}$  and  $|F = 1, m_F = -1\rangle_{87}$  combination (where the strength of the magnetic force on the  $^{85}\text{Rb}$  atoms is larger by 1/3) the displacement at the field gradients used for evaporation is negligible relative to the cloud radius. For example, at the end of the TOP evaporation described in Sec. 4.1.2, the  $^{87}\text{Rb}$  cloud radius is  $7\ \mu\text{m}$ , the bias field is 300 mG, and the quadrupole gradient is 109 G/cm. Assuming the radii of the two ensembles at the end of a dual-species evaporation are comparable, the  $0.3\ \mu\text{m}$  separation between this  $^{87}\text{Rb}$  ensemble and a hypothetical  $^{85}\text{Rb}$  ensemble is more than an order of magnitude less than the cloud radius. While acceptable at the high gradients of evaporation, the differential magnetic force will become a more significant effect at the low gradients and large bias fields of the magnetic lens, discussed below.

Finally, a third consideration is the difference in collision rates, both elastic and inelastic, of the two state combinations. As noted above, the inelastic collision rates for the  $|F = 2, m_F = -2\rangle_{85}$  and  $|F = 1, m_F = -1\rangle_{87}$  combination is three orders of magnitude lower than the  $|F = 3, m_F = 3\rangle_{85}$  and  $|F = 2, m_F = 2\rangle_{87}$  combination. The latter, however, confines the atoms more tightly for the same quadrupole gradient, increasing the elastic collision rate for the  $^{87}\text{Rb}$  atoms by a factor of  $2^{4/3} = 2.5$ . The higher collision rate can lead to a potentially non-linear increase in evaporation speed, especially in the early stages of evaporation when the collision rate is low and the quadrupole gradient is at its maximum. Thus, which state pair yields the largest ultracold clouds after evaporation may depend in part on competing atom loss mechanisms, such as the vacuum pressure and the resulting atom lifetime in the trap.

## 10.4 Magnetic lensing

For a dual species cloud, a lensing stage is important not only for the reduction in temperature it offers, but also because of the reduction in chemical potential. Dense clouds of  $^{85}\text{Rb}$  and  $^{87}\text{Rb}$  are not typically miscible due to the comparatively low intraspecies repulsion ( $^{85}\text{Rb}$  is in fact attractive) relative to the large interspecies

repulsion [181]. This inhibits the formation of a well-overlapped cloud. Although further research will be required, expanding from a small source into a regime that is not dominated by interactions, as occurs in delta-kick cooling, may limit the effect of immiscibility to the size scale of the initial small source.<sup>2</sup>

The difference between the two state combinations is very apparent in a magnetic lens cooling stage. In this type of lens, the difference in the response to magnetic fields strongly affects the trajectories of the atoms in the trap, and therefore the collimation time at which each isotope is at its coldest. With a single isotope, the magnetic gradient and bias field of the TOP trap is chosen to synchronize the vertical and radial expansion of the cloud after a certain duration in the trap. With two isotopes, there are six parameters of interest that must be synchronized: the vertical and radial expansions for *both* ensembles, as well as their relative vertical position and vertical velocity errors.<sup>3</sup> At the very least, a simultaneous launch demands that the relative velocities must be  $\ll 2\hbar k/m = 12 \text{ mm/s}$ , the spacing between adjacent lattice momentum states. In the best case, we would be able to suppress the relative position and velocity for excellent overlap of the ensembles, reducing the impact of overlap-dependent systematic errors (e.g. terms 2, 4, 6, 10, and 11 of Tab. 3.1).

The  $|F = 3, m_F = 3\rangle_{85}$  and  $|F = 2, m_F = 2\rangle_{87}$  combination is the simpler pair to characterize, since the magnetic force on both species is the same. Due to the different gravitational sag of the two species, the collimation times and relative kinematics slowly diverge as the clouds oscillate in the trap. The best procedure is the one that minimizes the time of free oscillation in the trap, thus minimizing the divergence. Using an effective 3D (2D cylindrically symmetric) Monte Carlo simulation, detailed in Ch. 7, we can solve for the trajectories in the TOP trap of a collection of 1000 particles drawn from a particular initial position and velocity distribution. This allows us to evaluate a variety of single- and dual-species magnetic lensing protocols.

From simulation, shown in Fig. 10.3, if a  $1 \mu\text{K}$  dual-species cloud is released from

---

<sup>2</sup>Alternatively, the two species can be made miscible by manipulating the relative scattering lengths through the available intra- and interspecies Feshbach resonances [181].

<sup>3</sup>By symmetry of the TOP potential, the radial positions and velocities at the end of the magnetic lens will be very similar. Micromotion, resulting from the atoms imperfectly averaging over the bias field rotation, can lead to differential radial kinematics and is worthy of independent study.

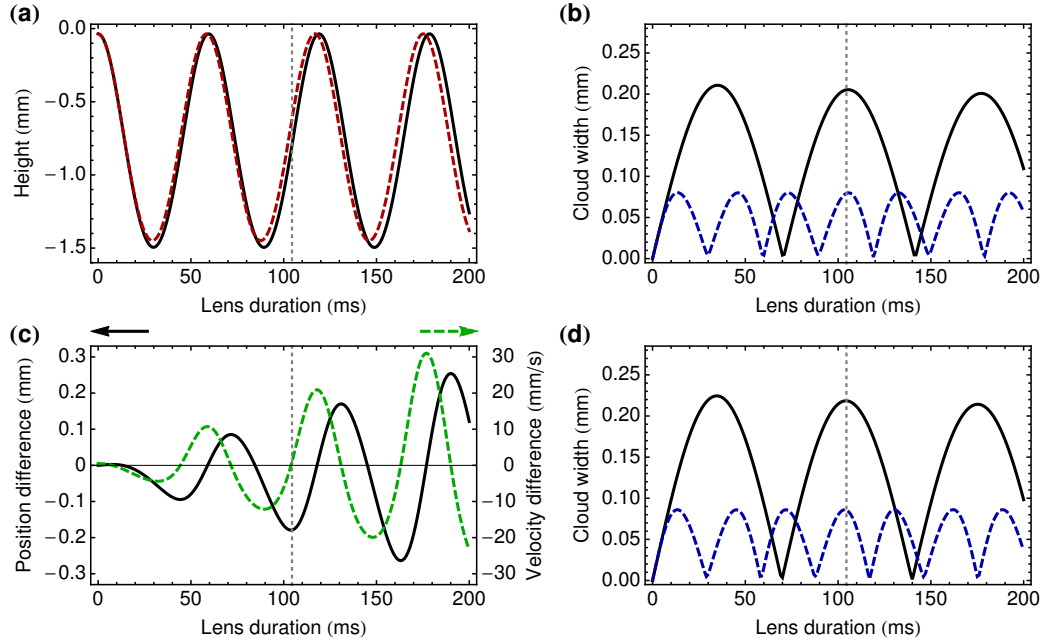


Figure 10.3: Comparison of  $|F = 3, m_F = 3\rangle_{85}$  and  $|F = 2, m_F = 2\rangle_{87}$  magnetic lensing in a TOP trap, formed by a radial quadrupole gradient of 20.0 G/cm and a rotating bias field of 6.9 G. (a) The vertical center-of-mass motion of  $^{87}\text{Rb}$  (solid black) and  $^{85}\text{Rb}$  (dashed red) diverge slowly due to the slightly different gravitational force on the two species. The height is referenced from the location of the quadrupole field zero. (c) The relative offset in the vertical center-of-mass position (solid black) and velocity (dashed green). Breathing modes in the radial (solid black) and vertical (dashed blue) dimensions are shown in (b) for  $^{87}\text{Rb}$  and (d) for  $^{85}\text{Rb}$ . The vertical dotted grey line marks 104.5 ms, where there is a coincidence of large cloud widths (low temperatures) and small relative velocity error. See Tab. 10.1 for cloud parameters at this time.

a point source into a TOP trap with a radial quadrupole gradient of 20.0 G/cm and a rotating bias field of 6.9 G, there is a coincidence around 104.5 ms where the two species are near full expansion in all three dimensions.<sup>4</sup> At the same time, the relative vertical velocity error is small enough for a simultaneous launch (1.1 mm/s).

Three factors that affect the minimum temperature achievable are 1) anharmonicities of the TOP trap, 2) imperfect synchronicity of the expansion of the two dimensions and two species, and 3) the initial cloud size. Figure 10.3, which assumes a cloud of zero initial size, addresses the first two: anharmonicity and asynchronicity lead to residual temperatures for both species that are low, but non-zero (< 2 nK radially and  $\sim 10$  nK vertically). For initial sizes of up to  $\sim 50 \mu\text{m}$  in both dimensions, simulations indicate that the cloud size at full expansion in the TOP trap is largely independent of the initial cloud size. As the  $1 \mu\text{K}$  cloud in Fig. 10.3 grows to  $80 \mu\text{m}$  vertically, typical initial cloud sizes of 10 to  $30 \mu\text{m}$  would lead to final temperatures between 20 and 150 nK.

The disadvantage of this simple procedure is the relative vertical position error. At  $180 \mu\text{m}$ , it is twice the typical cloud size at the end of the magnetic lens and four orders of magnitude away from the level desired for the WEP test. While increasing the magnetic trap strength reduces the relative position and velocity errors by diminishing the impact of the differential gravitational sag, it also results in undesirable higher final temperatures by reducing the expansion of the cloud.

One possibility to improve the kinematic overlap is the use of a lattice to confine the atoms in the vertical dimension. We have shown a lattice to be an effective alternative for synchronizing the vertical and radial expansions (see Sec. 7.1.6). The general procedure involves trapping the atoms in the lattice at the very beginning of the magnetic lens, when the atoms are still small.<sup>5</sup> The atoms then freely expand radially, but are confined vertically. After a certain time, the lattice is turned off and

---

<sup>4</sup>A similar coincidence occurs with a radial quadrupole gradient of 10.3 G/cm, but the weaker, more anharmonic trap results in much worse relative vertical position and velocity errors and worse residual temperatures while increasing the final size by less than 2 (see Tab. 10.1).

<sup>5</sup>Large clouds that extend over several lattice sites in the vertical gravitational or magnetic field gradient will display spatial population fringes. These arise because different wells of the vertical lattice evolve phase at different rates due to the environmental potential, leading to a phase gradient across the cloud. Small clouds suppress this effect.

the atoms can freely expand in both dimensions. Since the oscillations in the magnetic lens for the vertical dimension are faster than for the radial dimension, the expansion of the vertical dimension will catch up to the expansion in the radial dimension. For the appropriate lattice turn-off time, both dimensions reach their fullest extent and coldest temperatures in just a quarter-cycle of the vertical oscillation after release from the lattice.

Because the atoms are free in the critical vertical dimension for only a quarter cycle, the relative vertical position error has had less time to accumulate (Fig. 10.4). For the same  $1\ \mu\text{K}$  source and magnetic fields as in the latticeless case, the radial and vertical expansions coincide after only 36 ms, 22.5 ms of which are spent vertically confined by the lattice. The resulting relative vertical position error is only a few microns, two orders of magnitude better than without the lattice, while the relative vertical velocity error is comparable at 1.1 mm/s.

Compared to the latticeless procedure above, the residual temperature due to anharmonicity and asynchronicity is even lower (< 1 nK in both dimensions for both species). For clouds of finite initial size, the coldest temperatures are of similar magnitude since the final expansions are of similar size (20 - 150 nK for initial sizes 10 - 30  $\mu\text{m}$ ). Further improvements to the temperature reduction are possible by reducing the quadrupole gradient or increasing the bias field and changing the duration spent in the vertical lattice, but these come at the cost of degraded cloud overlap.<sup>6</sup> Yet the ability to decouple the vertical and radial components of the oscillation in the magnetic trap through the vertical lattice adds a very useful degree of freedom to this constrained problem.

The  $|F = 2, m_F = -2\rangle_{85}$  and  $|F = 1, m_F = -1\rangle_{87}$  combination is more complex because the strong difference in the magnetic force on the two states leads to highly divergent trajectories in the trap. Preliminary investigation suggests that it may be possible to achieve low temperatures, but with poor center-of-mass kinematic overlap.

---

<sup>6</sup>For example, reducing the quadrupole gradient to 14 G/cm gives residual temperatures below 1 nK in both dimensions and for both species (see Tab. 10.1). The final sizes are 320  $\mu\text{m}$  radially and 120  $\mu\text{m}$  vertically, for final temperatures of < 10 nK and < 60 nK respectively for initial sizes of < 30  $\mu\text{m}$ . But at the same time, the center-of-mass displacement has doubled to 12  $\mu\text{m}$ . The vertical velocity difference has also grown slightly, to 1.7 mm. The choice of quadrupole gradient will therefore depend on the dynamic range of the subsequent procedures used to fine-tune the kinematic overlap.

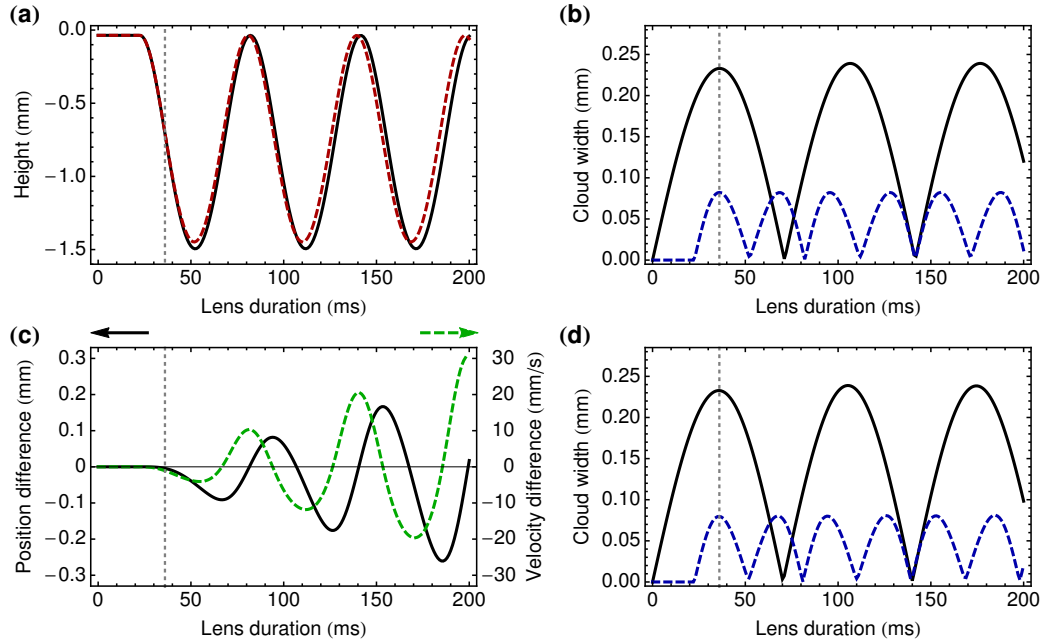


Figure 10.4: Comparison of lattice-aided  $|F = 3, m_F = 3\rangle_{85}$  and  $|F = 2, m_F = 2\rangle_{87}$  magnetic lensing in a TOP trap, formed by a radial quadrupole gradient of  $20.0 \text{ G/cm}$  and a rotating bias field of  $6.9 \text{ G}$ . The lattice turns off after  $22.5 \text{ ms}$ , at which point the atoms begin their vertical center-of-mass oscillation. (a) The vertical center-of-mass motion of  $^{87}\text{Rb}$  (solid black) and  $^{85}\text{Rb}$  (dashed red) diverge slowly due to the slightly different gravitational force on the two species. The height is referenced from the location of the quadrupole field zero. (c) The relative offset in the vertical center-of-mass position (solid black) and velocity (dashed green). Breathing modes in the radial (solid black) and vertical (dashed blue) dimensions are shown in (b) for  $^{87}\text{Rb}$  and (d) for  $^{85}\text{Rb}$ . The vertical dotted grey line marks  $36 \text{ ms}$ , where there is a coincidence of large cloud widths (low temperatures) and small relative position and velocity error. See Tab. 10.1 for cloud parameters at this time.

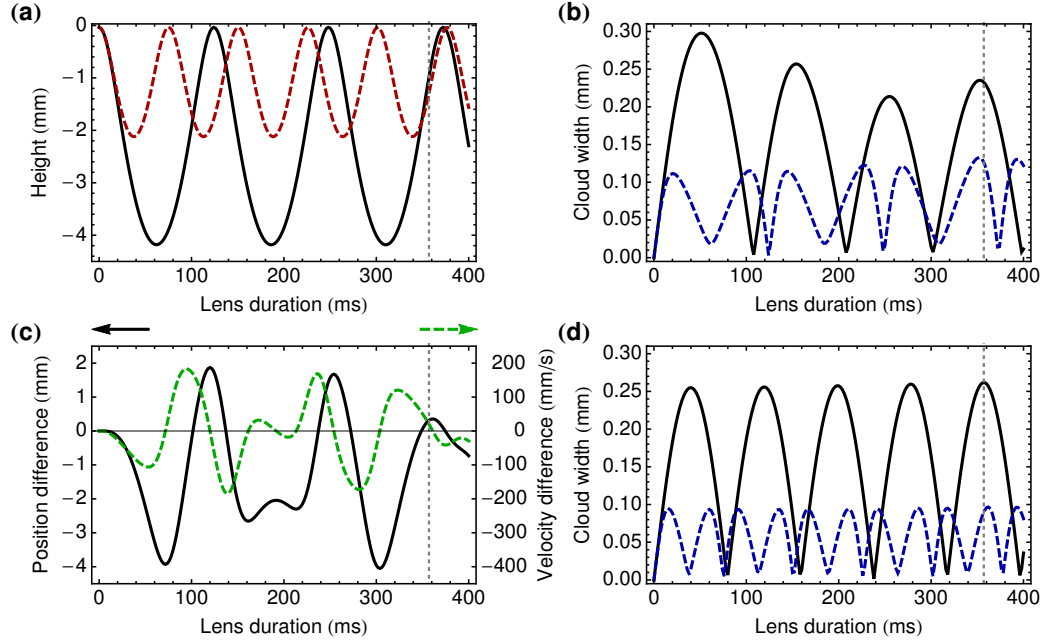


Figure 10.5: Comparison of  $|F = 2, m_F = -2\rangle_{85}$  and  $|F = 1, m_F = -1\rangle_{87}$  magnetic lensing in a TOP trap, formed by a radial quadrupole gradient of 21.9 G/cm and a rotating bias field of 6.9 G. Note the different scale of the time axis relative to the other figures. (a) The vertical center-of-mass motion of  ${}^{87}\text{Rb}$  (solid black) and  ${}^{85}\text{Rb}$  (dashed red) diverge rapidly due to the very different magnetic forces on the two species. The height is referenced from the location of the quadrupole field zero. (c) The relative offset in the vertical center-of-mass position (solid black) and velocity (dashed green). Breathing modes in the radial (solid black) and vertical (dashed blue) dimensions are shown in (b) for  ${}^{87}\text{Rb}$  and (d) for  ${}^{85}\text{Rb}$ . The vertical dotted grey line marks 357 ms, where there is a coincidence of large cloud widths (low temperatures). See Tab. 10.1 for cloud parameters at this time.

Without a lattice (Fig. 10.5), synchronization of the breathing modes occurs only after many oscillations. While the temperature radially can be quite low ( $< 20 \text{ nK}$  for initial cloud sizes of  $< 30 \mu\text{m}$ ), they are limited vertically by asynchronicity to  $\sim 80 \text{ nK}$ . Meanwhile, the center-of-mass position and velocity displacements are significant:  $300 \mu\text{m}$  and  $20 \text{ mm/s}$ . Unlike the  $|F = 3, m_F = 3\rangle_{85}$  and  $|F = 2, m_F = 2\rangle_{87}$  combination, this vertical velocity well-exceeds the velocity acceptance of the lattice launch, making an independent means of coarsely controlling the kinematic overlap a crucial addition to the procedure.

The temperature results improve with a lattice to delay the vertical expansion (Fig. 10.6), although kinematic displacements are still large. The residual temperature due to anharmonicity and asynchronicity is  $< 20 \text{ nK}$  for both dimensions and both species. With finite initial sizes of  $\sim 30 \mu\text{m}$ , the temperatures grow to  $20 \text{ nK}$  radially and  $110 \text{ nK}$  vertically. The center-of-mass displacements are marginally better than in the latticeless case, at  $100 \mu\text{m}$  in position and  $19 \text{ mm/s}$  in velocity. Nevertheless, this velocity difference also exceeds the velocity acceptance of the lattice launch.

For both possible state combinations, independent methods to adjust the relative center-of-mass kinematics would greatly relax the demands on the magnetic lens, which could then be used solely to achieve the desired temperatures. Such independent methods could include the timing of the post-lens transfer to the magnetically insensitive state or the particular combination of lattice detunings for the lattice launch, which also has a mass-dependent response.

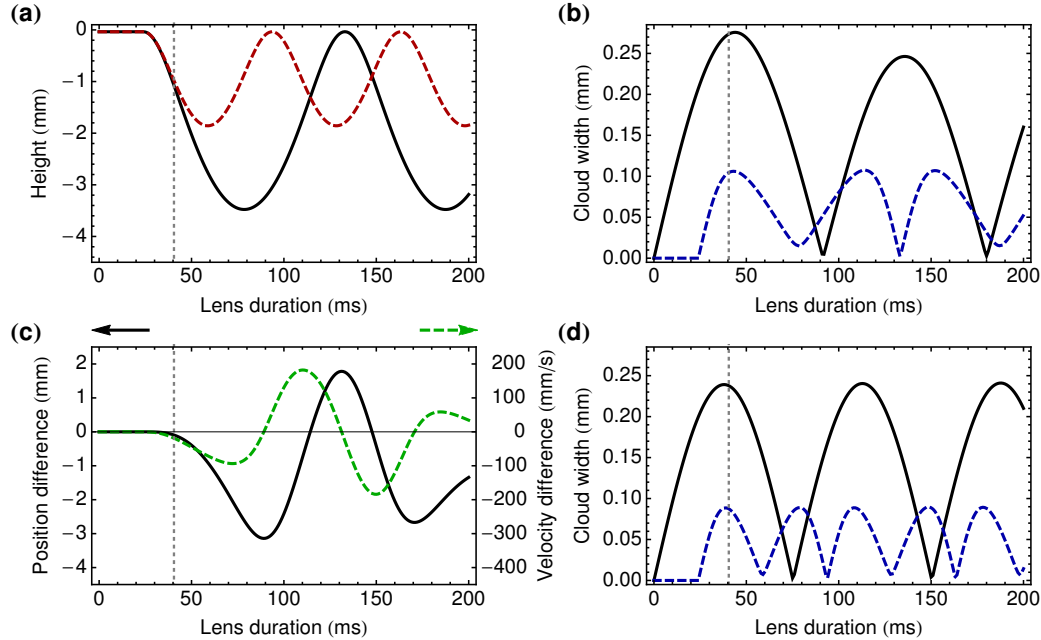


Figure 10.6: Comparison of lattice-aided  $|F = 2, m_F = -2\rangle_{85}$  and  $|F = 1, m_F = -1\rangle_{87}$  magnetic lensing in a TOP trap, formed by a radial quadrupole gradient of  $23.0 \text{ G/cm}$  and a rotating bias field of  $6.9 \text{ G}$ . The lattice turns off after  $24 \text{ ms}$ , at which point the atoms begin their vertical center-of-mass oscillation. (a) The vertical center-of-mass motion of  $^{87}\text{Rb}$  (solid black) and  $^{85}\text{Rb}$  (dashed red) diverge rapidly due to the very different magnetic forces on the two species. The height is referenced from the location of the quadrupole field zero. (c) The relative offset in the vertical center-of-mass position (solid black) and velocity (dashed green). Breathing modes in the radial (solid black) and vertical (dashed blue) dimensions are shown in (b) for  $^{87}\text{Rb}$  and (d) for  $^{85}\text{Rb}$ . The vertical dotted grey line marks  $40.5 \text{ ms}$ , where there is a coincidence of large cloud widths (low temperatures). See Tab. 10.1 for cloud parameters at this time.

Fig.	$A$ (G/cm)	$B_0$ (G)	$\Delta t_{\text{lens}}$ (ms)	$\Delta t_{\text{hold}}$ (ms)	$\Delta z$ ( $\mu\text{m}$ )	$\Delta v_z$ (mm/s)	$\sigma_\rho$ ( $\mu\text{m}$ )	$\sigma_z$ ( $\mu\text{m}$ )	$T_\rho$ (nK)	$T_z$ (nK)
<b>10.3</b>	20.0	6.9	104.5	–	179	-1.1	218	205	79	0.15
–	10.3	6.9	238.5	–	-2114	5.3	366	357	166	4.6
<b>10.4</b>	20.0	6.9	36	22.5	4.3	1.1	233	233	80	0.17
–	14.0	6.9	50.5	30	10	1.7	319	327	121	0.071
<b>10.5</b>	21.9	6.9	357	–	-314	-20	262	233	90	127
<b>10.6</b>	23.0	6.9	40.5	24	94	19	238	274	87	105
									13	16
									18	17

Table 10.1: Summary of dual species magnetic lens Monte Carlo simulations. If there is a figure associated with a particular simulation, it is indicated in the first column. Each row is labeled according to the simulation input parameters: quadrupole gradient ( $A$ ), rotating bias field magnitude ( $B_0$ ), and duration of oscillation in the lens ( $\Delta t_{\text{lens}}$ ). The duration of the hold in the lattice is noted where relevant ( $\Delta t_{\text{hold}}$ ). All simulations assume sources with zero initial size. Results from the simulation are calculated from 1000 particle trajectories at the noted lens duration. Results include the center-of-mass vertical position displacement ( $\Delta z$ ), the center-of-mass vertical velocity difference ( $\Delta v_z$ ), the radial ( $\sigma_\rho$ ) and vertical ( $\sigma_z$ ) position widths, and the radial ( $T_\rho$ ) and vertical ( $T_z$ ) temperatures.

# Chapter 11

## Conclusion

The progress towards a precision test of the weak equivalence principle described in this work is significant. The apparatus is working at its anticipated  $2\hbar k$  sensitivity and we are making excellent headway on further improvements through large momentum transfer atom optics. To mitigate potential systematic errors, we have not only taken care with the design of the system, as in the case of the magnetic shielding, but we have also begun to analyze and characterize suppression strategies, notably for those errors arising from the Coriolis effect. The rotation sensitivity is already sufficient to suppress the Coriolis phase shift to be consistent with a test at  $10^{-13} g$ ,<sup>1</sup> matching the current best limits on violations of the WEP. Future work can further improve the sensitivity to the  $10^{-15}$  level through more integration, large momentum transfer interferometry, better dual-species kinematic overlap, or other novel methods.

This work also describes a possible next stage of the experiment, the creation of a dual-species cold cloud. After achieving this near-term goal, several other tasks await before testing the WEP: simultaneous dual-species launches, optimization of the dual-species kinematic overlap, simultaneous interferometry, and dual species detection. From a practical standpoint, the complexity of the system and the importance of the ability to integrate multiple experimental cycles will likely demand a significant amount of automation and stabilization of the apparatus as a whole. And from a scientific standpoint, there is much to be explored and learned about sources of

---

<sup>1</sup> Assumes  $1 \mu\text{m}/\text{s}$  relative velocity error between species.

systematic error.

But as of yet there is no aspect of the proposed test that has been found experimentally to be insurmountable. And in the coming years, I expect to hear not only about the WEP test, but also about the pursuit of other scientific goals accessible to this apparatus, ranging from multi-meter coherent separation of atomic wavepackets, to testing aspects of a gravitational wave detector, to direct measurements of general relativistic effects.

## Appendix A

# Historical equivalence principle experiments

Date	Precision	Experiment type	Primary author(s)	Reference
1610	$2 \times 10^{-3}$	Pendulum	Galileo	[182]
1680	$1 \times 10^{-3}$	Pendulum	Newton	[182]
1832	$2 \times 10^{-5}$	Pendulum	Bessel	[182]
1890	$5 \times 10^{-8}$	Torsion Balance	Eötvös	[183]
1910	$5 \times 10^{-6}$	Pendulum	Southerns	[182]
1918	$3 \times 10^{-8}$	Torsion Balance	Zeeman	[182]
1922	$4 \times 10^{-9}$	Torsion Balance	Eötvös et al.	[184]
1923	$3 \times 10^{-6}$	Pendulum	Potter	[182]
1935	$2 \times 10^{-9}$	Torsion Balance	Renner	[182]
1964	$1 \times 10^{-11}$	Torsion Balance	Roll et al.	[182]
1972	$1 \times 10^{-12}$	Torsion Balance	Braginskii and Panov	[185]

Table A.1 – *Continued on next page*

Table A.1: Historical equivalence principle experiments. A complementary plot can be found in Ch. 2 (Fig. 2.1). AI: Atom Interferometry.

Table A.1 – *Continued from previous page*

Date	Precision	Experiment type	Primary author(s)	Reference
1976	$7 \times 10^{-12}$	Lunar Laser Ranging	Shapiro et al.	[28]
1976	$3 \times 10^{-4}$	Free Fall	Koester	[182]
1979	$4 \times 10^{-11}$	Floating on Water	Keiser and Faller	[182]
1982	$1 \times 10^{-4}$	Magnetic Suspension	Worden	[182]
1987	$5 \times 10^{-10}$	Drop Tower	Niebauer et al.	[182]
1989	$1 \times 10^{-11}$	Torsion Balance	Heckel et al.	[182]
1994	$2 \times 10^{-12}$	Torsion Balance	Su et al.	[186]
2001	$7 \times 10^{-9}$	AI/Free Fall	Peters et al.	[35]
2004	$1.4 \times 10^{-13}$	Lunar Laser Ranging	Williams et al.	[19]
2004	$1.2 \times 10^{-7}$	Atom Interferometry	Fray et al.	[51]
2008	$1.8 \times 10^{-13}$	Torsion Balance	Schlamminger et al.	[12]
2012	$1.3 \times 10^{-13}$	Lunar Laser Ranging	Williams et al.	[29]
2013	$3.2 \times 10^{-7}$	Atom Interferometry	Bonnin et al.	[52]
2014	$1.6 \times 10^{-7}$	Atom Interferometry	Tarallo et al.	[54]
2014	$5.4 \times 10^{-7}$	Atom Interferometry	Schlippert et al.	[53]

Table A.1: Historical equivalence principle experiments. A complementary plot can be found in Ch. 2 (Fig. 2.1). AI: Atom Interferometry.

## Appendix B

# Frequency doubling in nonlinear media

Second-harmonic generation in a medium arises from a nonlinearity in the dielectric coefficient,  $\chi$ , which converts two pump photons into a single photon at twice the frequency with a well-defined phase and polarization [187, 188]. The amplitude of the doubled field  $E_2$  is given by [188]

$$\frac{dE_2}{dz} \propto E_1^2 \chi e^{-i\Delta kz} \quad (\text{B.1})$$

where  $\Delta k = k_2 - 2k_1$  characterizes the evolution of the phase relationship between the two fields in the medium. The wavevectors of the two wavelengths,  $k_1 = \omega n(\omega)/c$  for the pump and  $k_2 = 2\omega n(2\omega)/c$  for the doubled light, depend on the index of refraction  $n(\omega)$ . As a consequence, dispersion in the medium can significantly affect the phase relationship. Integration of Eq. B.1 (assuming no depletion of the pump field and a constant nonlinear coefficient) yields

$$E_2 \propto 2E_1^2 \chi e^{-i\Delta kz/2} z \operatorname{sinc}(\Delta kz/2) . \quad (\text{B.2})$$

As the beam intensity is the square of the electric field,  $I_i = |E_i|^2$ , the intensity of the doubled light is proportional to the square of the pump intensity. In a non-dispersive

medium  $\Delta k = 0$ , and  $I_2$  grows quadratically with the length of the crystal. In the more-typical dispersive medium where  $\Delta k \neq 0$ , the growth is modulated by the  $\text{sinc}^2$  envelope. This describes a periodic process where two pump photons combined later in the crystal contribute a doubled photon that is out of phase with respect to earlier doubled photons, resulting in destructive interference and a reduction of the power in the doubled beam. It can also be understood as a reversal of the doubling, where a single doubled photon is converted back into a pair of pump photons. While the reverse process is useful for creating entangled photon pairs (e.g. [189]), it inhibits the production of a high-power doubled beam.

A popular solution to this periodic destructive interference is quasi-phase matching [188, 190, 191]. In quasi-phase matching, the sign of the crystal's dielectric coefficient is reversed just as the phase between the pump and doubled light begins to degrade the doubling efficiency. This reversal is performed by periodic inversion of the crystal's orientation (periodic poling). The length  $\Lambda/2$  of each domain of uniform  $\chi$  is chosen such that

$$\Delta k = 2m\pi/\Lambda, \quad \text{for } m \in 1, 3, 5, 9, \dots \quad (\text{B.3})$$

for a particular pump frequency. From Eq. B.2 we see that reversing the sign of  $\chi$  gives a  $\pi$  phase shift to the doubled photons. These now add constructively with the photons from the previous domain, allowing the intensity of the doubled beam to grow. With quasi-phase matching, the beam intensity grows with the square of the crystal length, albeit more slowly than if  $\Delta k = 0$  [by a factor of  $(2/m\pi)^2$ ] [188].

It is interesting to note that doubling an array of independent beams with various frequencies is very different from doubling a phase-modulated beam. A pair of independent beams simultaneously pumping the crystal will result in doubled light at twice the frequency of each beam, as well as a strong intermodulation contribution at the frequency halfway between the other two. This arises because the square of the pump field in Eq. B.2 is non-trivial when the pump is multi-frequency. Suppose the pump beam contains two frequencies,  $\omega_A$  and  $\omega_B$ , with electric field amplitudes  $\mathcal{E}_{1,A}$

and  $\mathcal{E}_{1,B}$ . The square of the pump electric field is

$$E_1^2 = (\mathcal{E}_{1,A}e^{-i\omega_A t} + \mathcal{E}_{1,B}e^{-i\omega_B t})^2 \quad (\text{B.4})$$

$$= \mathcal{E}_{1,A}^2 e^{-i2\omega_A t} + \mathcal{E}_{1,B}^2 e^{-i2\omega_B t} + 2\mathcal{E}_{1,A}\mathcal{E}_{1,B}e^{-i(\omega_A+\omega_B)t}, \quad (\text{B.5})$$

where the final term represents the intermodulation contribution. A phase-modulated beam does not have such interference terms:

$$E_1^2 = (\mathcal{E}_1 e^{-i\omega t} e^{-i\phi(t)})^2 = \mathcal{E}_1^2 e^{-i2\omega t} e^{-i2\phi(t)}. \quad (\text{B.6})$$

In fact, it is the modulation depth of the phase-modulated beam that doubles through the doubling process, not the sideband frequency spacing.

The span of wavelengths that experience efficient doubling for a given poling spacing  $\Lambda$  is determined by the length of the crystal. The doubled intensity is modulated by the envelope  $\text{sinc}^2(\Delta k' L/2)$ , where  $\Delta k' = k_2 - 2k_1 - 2m\pi/\Lambda$ . From the envelope we can derive the FWHM intensity bandwidth [188],

$$\delta\lambda = \frac{0.4429\lambda}{L} \left| \frac{n_2 - n_1}{\lambda} + \frac{\partial n_1}{\partial \lambda} - \frac{1}{2} \frac{\partial n_2}{\partial \lambda} \right|^{-1} \quad (\text{B.7})$$

where  $\lambda$  is the pump wavelength in vacuum,  $n_1$  and  $n_2$  are the indices of refraction in the nonlinear medium for the pump and doubled beams respectively. Typically, the slope of the index of refraction is small and can be ignored in a single-pass configuration.

The bandwidth is of particular interest in our application, where the pump beam is phase modulated to produce frequency-shifted sidebands. How efficiently the crystal doubles the sidebands can significantly change the interferometer parameters, as shown by Fig. 9.4 and 9.5. To determine the bandwidth of our crystal, we use the temperature-dependent Sellmeier equation [191, 192]:

$$n(\lambda, T)^2 = a_1 + b_1 f(T) + \frac{a_2 + b_2 f(T)}{\lambda^2 - [a_3 + b_3 f(T)]^2} + \frac{a_4 + b_4 f(T)}{\lambda^2 - a_5^2} - a_6 \lambda^2 \quad (\text{B.8})$$

Parameter	Value
$a_1$	5.756
$a_2$	0.0983
$a_3$	0.2020
$a_4$	189.32
$a_5$	12.52
$a_6$	$1.32 \times 10^{-2}$
$b_1$	$2.860 \times 10^{-6}$
$b_2$	$4.700 \times 10^{-8}$
$b_3$	$6.113 \times 10^{-8}$
$b_4$	$1.516 \times 10^{-4}$

Table B.1: Sellmeier coefficients for the extra-ordinary index of refraction of 5% doped MgO:PPLN crystal [192]. With these parameters, the wavelength entered into the Sellmeier equation should be provided in microns.

where

$$f(T) = (T - 24.5^\circ\text{C}) (T + 570.82) . \quad (\text{B.9})$$

Temperature  $T$  is in Celsius.<sup>1</sup> The coefficients for 5% doped MgO:PPLN are given in Tab. B.1.

Our crystal is 40 mm in length, with a poling period that efficiently doubles 1560 nm at  $T = 153^\circ\text{C}$ . The FWHM bandwidth according to Eq. B.7 is  $\delta\lambda = 0.663$  nm ( $\pm 40$  GHz). As a consequence, 40 GHz sidebands will double half as efficiently as the carrier. A crystal twice as short would approximately double the efficiency of the sidebands relative to the carrier, but the overall doubling efficiency would drop by a factor of 4. The current crystal length is therefore near-optimal for single-pass operation.

The doubling efficiency of a single frequency can be greatly improved by allowing the pump beam to pass through the nonlinear medium multiple times, with care to ensure phase matching with each pass. Multi-pass operation has been implemented with a set of crystals in series [193, 194] and by placing the crystal in a cavity resonant with the pump beam [195–197]. The latter is particularly convenient as it saves the

---

<sup>1</sup>The function  $f$  parameterizes the temperature dependence, nominally in units of Kelvin squared. It includes, however, an offset that sends  $f$  to zero at the reference temperature  $24.5^\circ\text{C}$ , hence the hybrid use of units in the definition of  $f$ .

space and expense of multiple crystals.

In a two-mirror cavity, if one of the two mirrors is reflective at both the pump and doubled wavelengths while the other reflects only the pump wavelength, then all the doubled power emits from the latter mirror. Because of the intracavity build-up of the pump power, the doubling efficiency increases. Naively, the efficiency scales with the square of the cavity finesse, but the efficiency cannot exceed 100%. Instead, at efficiencies  $\gtrsim 10\%$ , pump depletion becomes significant [190].

Working with a cavity at efficiencies approaching 100% has the added benefit of greatly increasing the doubling bandwidth for resonant pump frequencies. As the doubling efficiency of a beam near the center of the single-pass doubling bandwidth saturates, the doubling efficiencies of frequencies on the side of the single-pass bandwidth grow in comparison. In the limit of perfect pump depletion (perfect efficiency), the doubling bandwidth is infinitely large.

A multi-frequency pump beam requires a little more care to implement in a mutli-pass configuration, largely because of the finite linewidth of the cavity. A phase-modulated beam is therefore particularly convenient due to the regular spacing of the sidebands: the cavity free spectral range can be chosen to match the desired sideband spacing. For example, a cavity of length of 6.430 cm that includes a MgO:PPLN crystal 20 mm long at 153°C would transmit sidebands every 1.71 GHz. This cavity length is particularly interesting for Raman transitions in  $^{87}\text{Rb}$  because sidebands could be spaced by 6.834 GHz. As we currently do not deplete our 30 W pump beams, even a very low finesse cavity could produce much higher power interferometer beams.

## Appendix C

# Preliminary absolute gravity and gravity gradient measurements

We have performed a series of absolute gravity measurements [35] at several interferometer launch heights to make a preliminary measurement of gravity gradients, the source of the dominant systematic error for an equivalence principle test [71]. The data show no gravity gradients at a precision of  $10^{-6} g/m$  over meter length scales (Fig. C.1).

These absolute gravimeter interferometers are of short duration, no more than  $T = 30 \text{ ms}$ , such that gravity is probed locally. Interferometry occurs at the apex of the atom's trajectory, minimizing the spatial extent of the interferometer to 5 cm or less. In an ideal experiment, an accelerometer with  $T = 30 \text{ ms}$  could measure gravity to  $(\sqrt{N}k_{\text{eff}}T^2)^{-1} \approx 10^{-7} g$  in a single experimental cycle for  $N = 10^5$  atoms. For such a short interferometer, phase noise from vibrations of the retroreflection mirror are suppressed relative to the longer  $T = 1.15 \text{ s}$  interferometry discussed elsewhere in this work (see Fig. 5.4 in particular), enabling absolute gravimetry.

Nevertheless, phase noise at the tenths of radians level limits the sensitivity. This phase noise is likely due to a combination of several effects including 1) vibrations in the retroreflection mirror, which result in increased phase noise for longer, more sensitive interferometers, and 2) relative phase noise between the counterpropagating interferometer beams, which result in large phase noise even for short interferometers

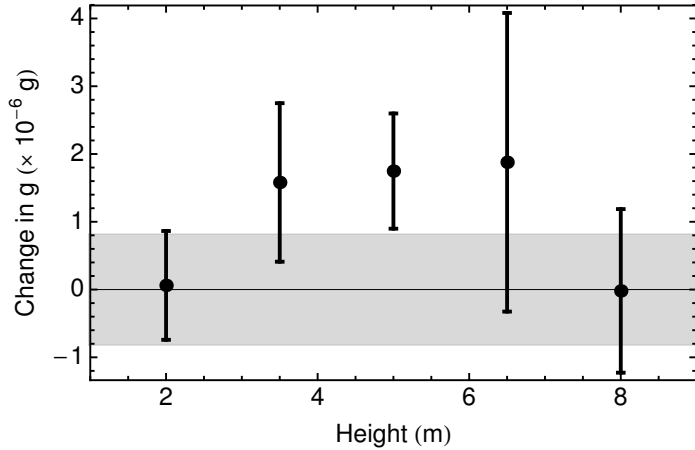


Figure C.1: Preliminary gravity measurements at five heights above the center of the detection chamber. Each point represents an absolute gravimeter measurement based on the relative phase shift of a  $T = 30$  ms interferometer at the apex of the atom trajectory. The absolute scale is referenced to the gravimeter measurement at 8.5 m,  $9.800342 \text{ m/s}^2$ , where the grey bands indicate the error in that measured value.

provided that the noise frequency is sufficiently high. The measurements display both significant phase noise at short time scales and an increase in that phase noise with increasing interferometer time. For an equivalence principle test, it should be noted, these two effects would be largely common to the two species.

With interferometers at  $T = 30$ , 15, and 7 ms at a height of 8.5 m above the detection region, we measure gravity to be  $9800.342 \pm 0.008 \text{ mm/s}^2$ . The stated error is calculated purely from the chi-squared analysis of the fit to the data, and does not account for any potential systematic effects. But with more stable phase noise and a careful study of height-dependent systematic effects, this technique may aid in the understanding of the local gravity gradients of the apparatus.

# Appendix D

## Recipe – La Bête Noire

La Bête Noire: the black beast [198]. Approximately the density of a neutron star, one of these flourless chocolate cakes (Fig. D.1) serves more than you might expect.

### D.1 Ingredients

#### Cake

- 1 cup water
- 3/4 cup sugar
- 9 tablespoons (1 stick plus 1 tablespoon) unsalted butter, diced
- 18 ounces bittersweet (not unsweetened) or semisweet chocolate, chopped
- 6 large eggs

#### Ganache

- 1 cup heavy whipping cream
- 8 ounces bittersweet (not unsweetened) or semisweet chocolate, chopped

Accompany with lightly sweetened whipped cream.



Figure D.1: La Bête Noire cross-section, showing the typical relative thickness of the ganache layer to the cake. The optimal size of the whipped cream dollop is independent of the size of the section of cake, but depends solely on the preference of the consumer. The downwards curve of the upper surface of the cake section from the outside (right) to the inside (left) is a consequence of removing the section from the whole cake round: the downwards pressure of the knife and the poor structural integrity of the thinner region near the apex combine to form this sloping feature. It does not, however, affect the resulting taste.

*SMD note: I often add a secret ingredient to the cake, the ganache, or to both – 1 teaspoon cinnamon, or 1 teaspoon cardamom, or 3 tablespoons Grand Marnier. My favorite, however, is to replace the 1 cup of water with 1/4 cup espresso and 3/4 cup hot water.*

## D.2 Preparation

### For cake

Preheat oven to 350F. Butter 10-inch-diameter springform pan. Line bottom of pan with parchment round; butter parchment. Wrap 3 layers of heavy-duty foil around outside of pan, bringing foil to top of rim [Fig. D.2(a)]. Combine 1 cup water and sugar in small saucepan. Bring to boil over medium heat, stirring until sugar dissolves. Simmer 5 minutes. Remove from heat.

Melt butter in large saucepan over low heat. Add chocolate and whisk until smooth. Whisk sugar syrup into chocolate; cool slightly. Add eggs to chocolate mixture and whisk until well blended. Pour batter into prepared pan. Place cake pan in large roasting pan. Add enough hot water to roasting pan to come halfway up sides of cake pan [Fig. D.2(b)].

Bake cake until center no longer moves when pan is gently shaken, about 50 minutes. Remove from water bath; transfer to rack. Cool completely in pan [Fig. D.2(c)].

### For ganache

Bring whipping cream to simmer in small saucepan over medium heat. Remove from heat. Add chocolate and whisk until smooth. Pour over top of cake still in pan. Gently shake pan to distribute ganache evenly over top of cake [Fig. D.2(d)]. Refrigerate cake in pan until ganache is set, about 2 hours. DO AHEAD: Can be made 2 days ahead. Cover and keep refrigerated.

Run knife around pan sides to loosen cake; release sides [Fig. D.2(e)]. Cut cake into wedges and serve with whipped cream.

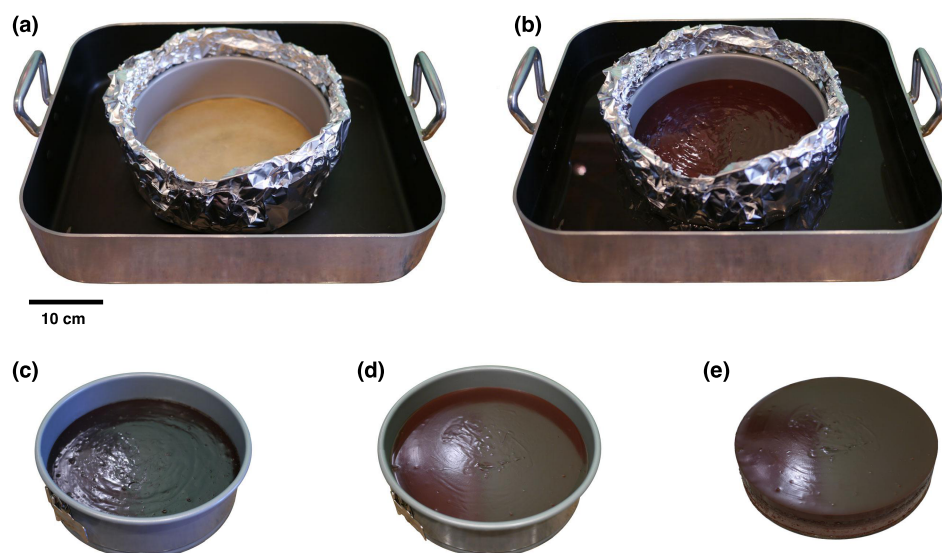


Figure D.2: La Bête Noire baking sequence. (a) Parchment paper lines the bottom of the triply foil-wrapped springform pan, which is placed in a large baking dish. (b) After the batter is poured into the pan, hot water (best identified by the specular reflection in the lower left of the dish) is poured into the dish. (c) The cake after baking. Note the darkening of the cake color. (d) The ganache layer provides a lighter final color and a smoother top. (e) The final cake round, after removal from the springform pan.

# Appendix E

## Recipe – Lemon Curd Cheesecake

As with most of my favorites, this recipe comes from [epicurious.com \[199\]](#). With this cheesecake (Fig. E.1), I'm often tempted to make extra lemon curd, but I realize that I would be liable to go too far. It can be shown that

$$\lim_{\frac{\text{lemon}}{\text{cream cheese}} \rightarrow \infty} \text{Lemon curd cheesecake} = \text{Lemon tart} \quad (\text{E.1})$$

which, while tasty, is another thing entirely.

### E.1 Ingredients

Special equipment: a 9 to 9 1/2-inch (24-cm) springform pan. *SMD note: I used a 10-inch pan with no issues.* Accompaniment: blueberries

#### For lemon curd

- 1 teaspoon finely grated fresh lemon zest
- 1/2 cup fresh lemon juice
- 1/2 cup sugar
- 3 large eggs

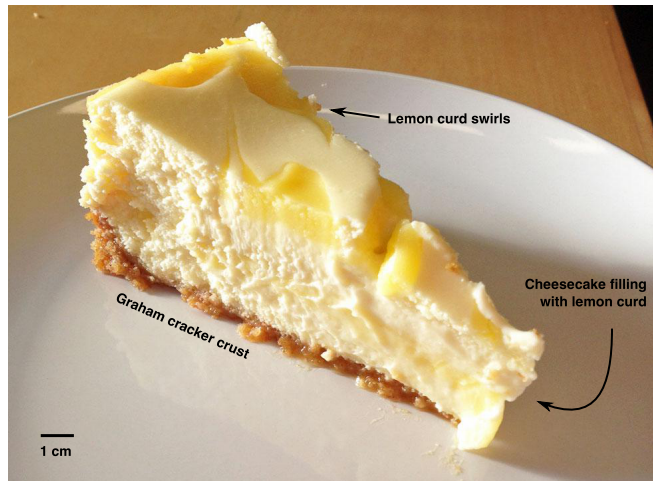


Figure E.1: Lemon curd cheesecake cross-section, with the crust, filling, and decorative lemon curd swirls indicated. Note that the texture of the cake changes as a function of the distance from the center of the cake. Further away from the center (left in the figure) the cake is drier with a crumblier texture. Closer to the center (toward the right), the texture is smoother. This is a result of the different temperature profiles experienced by the different regions of the cake while baking. The center of the cake is partially shielded by the thermal mass of the outer cake region, which bears the full brunt of the oven's heat.

- 1/2 stick (1/4 cup) unsalted butter, cut into small pieces

**For crust**

- 1 1/3 cups finely ground graham cracker crumbs (5 oz)
- 1/3 cup sugar
- 1/8 teaspoon salt
- 5 tablespoons unsalted butter, melted

**For filling**

- 3 (8-oz) packages cream cheese, softened
- 1 cup sugar
- 3 large eggs
- 3/4 cup sour cream
- 1 teaspoon vanilla

## E.2 Preparation

**Make lemon curd**

Whisk together zest, juice, sugar, and eggs in a 2-quart heavy saucepan. Add butter and cook over moderately low heat, whisking frequently, until curd is thick enough to hold marks of whisk and first bubbles appear on surface, about 6 minutes.

Force lemon curd through a fine-mesh sieve into a wide shallow dish, scraping bottom of sieve, then cover surface with wax paper. Cool completely, stirring occasionally, about 30 minutes.

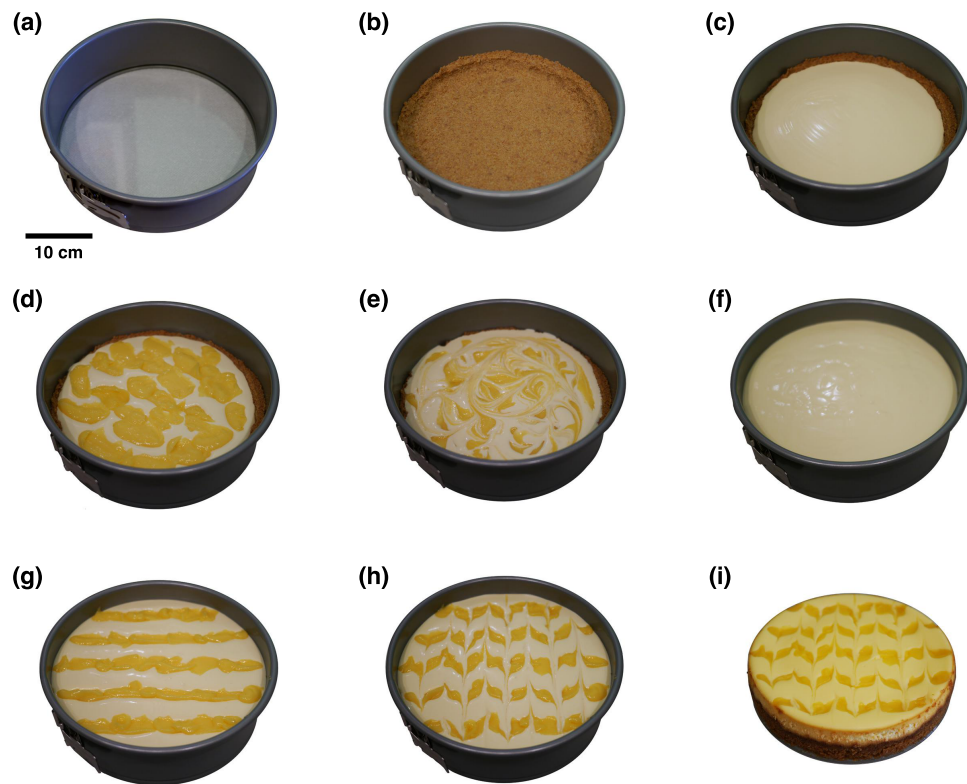


Figure E.2: Lemon curd cheesecake baking sequence. (a) The empty springform pan. This particular pan has a glass bottom. (b) Graham cracker crust, after baking. (c) The first layer of cream cheese filling. (d) Dollops of lemon curd. (e) After swirling the lemon curd into the cream cheese filling. (f) The second layer of cream cheese filling. (g) Stripes of lemon curd filling. (h) After drawing a knife perpendicularly through the stripes of lemon curd. (i) The final cake, baked and removed from the springform pan.

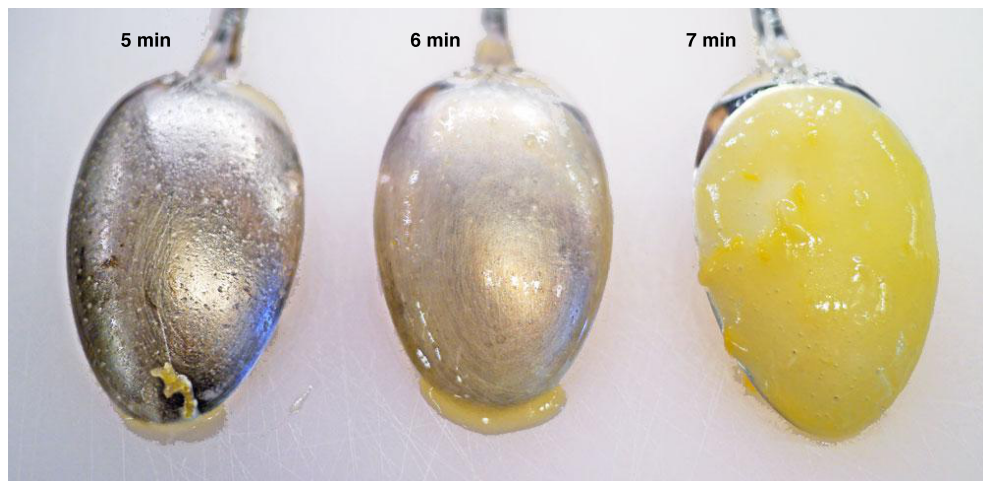


Figure E.3: Lemon curd consistency versus cooking time. From left to right are identical spoons dipped into the lemon curd after cooking for different durations, as noted above each spoon. The precise timing will depend on the particular heat setting of the burner, but this sequence shows that the lemon curd undergoes an abrupt transition within the span of a minute. A thick layer coating the back of the spoon is ideal. The lemon curd cooked for 7 minutes to reach such a consistency in this test.



Figure E.4: Marbling procedure. (a) Use a small spoon or the side of a knife to place dollops of lemon curd in lines on the cheesecake surface. (b) Drag a clean knife perpendicularly through the lemon curd, without touching the crust underneath. (c) For this pattern, pull the knife in opposite directions for adjacent lines. As an alternative to straight lines, drop the lemon curd in concentric circles and drag the knife radially to and from the center of the cake.

### Make and bake crust

Put oven rack in middle position and preheat oven to 350°F. Invert bottom of springform pan (to make it easier to slide cake off bottom), then lock on side. Stir together crust ingredients in a bowl, then press onto bottom and 1 inch up side of springform pan. Place springform pan in a shallow baking pan and bake 10 minutes, then cool crust completely in springform pan on a rack [E.2(b)].

### Make filling and bake cheesecake

Reduce oven temperature to 300°F.

Beat together cream cheese and sugar in a bowl with an electric mixer at medium speed until smooth, 1 to 2 minutes. Reduce speed to low and add eggs 1 at a time, beating until incorporated. Beat in sour cream and vanilla until combined.

Pour two thirds of cream cheese filling into crust, then spoon half of lemon curd over filling and swirl curd into filling with a small knife [E.2(c-e)]. (Avoid touching crust with knife to prevent crumbs getting into filling.) Repeat with remaining filling and curd [E.2(f-h)].

*SMD note: I like to marble the top. See Fig. E.4.*

Bake cheesecake until set 1 1/2 inches from edge but center trembles when pan is gently shaken, about 45 minutes. (Center of cake will appear very loose but will continue to set as it cools.) Transfer springform pan to a rack and immediately run a knife around top edge of cake to loosen. Cool completely, about 2 hours, then chill, uncovered, at least 4 hours. Remove side of springform pan before serving [E.2(i)].

### Cooks' Notes

- Lemon curd can be made 1 week ahead and chilled, covered.
- Crust (without filling) can be made 1 day ahead and kept, covered, at room temperature.
- Cheesecake can be chilled, loosely covered, up to 2 days. Cheesecake must be completely chilled before covering to prevent condensation on its surface.

# Bibliography

- [1] Susannah M. Dickerson, Jason M. Hogan, Alex Sugarbaker, David M. S. Johnson, and Mark A. Kasevich. Multiaxis Inertial Sensing with Long-Time Point Source Atom Interferometry. *Physical Review Letters*, 111(8):083001, August 2013.
- [2] Alex Sugarbaker, Susannah M. Dickerson, Jason M. Hogan, David M. S. Johnson, and Mark A. Kasevich. Enhanced Atom Interferometer Readout through the Application of Phase Shear. *Physical Review Letters*, 111(11):113002, September 2013.
- [3] Tim Kovachy, Jason M. Hogan, Alex Sugarbaker, Susannah M. Dickerson, Christine A. Donnelly, Chris Overstreet, and Mark A. Kasevich. Matter wave lensing to picokelvin temperatures. (arXiv:1407.6995v1), 2014.
- [4] Susannah Dickerson, Jason M. Hogan, David M. S. Johnson, Tim Kovachy, Alex Sugarbaker, Sheng-wei Chiow, and Mark A. Kasevich. A high-performance magnetic shield with large length-to-diameter ratio. *Review of Scientific Instruments*, 83(6):065108, June 2012.
- [5] Aristotle. On the heavens. In Jonathan Barnes, editor, *Aristotle: The Complete Works. Electronic edition.*, pages 447–511. Princeton University Press, Princeton, 1984.
- [6] Stillman Drake. *History of Free Fall: Aristotle to Galileo*. Wall & Thompson, Toronto, 1989.

- [7] John Philoponus, Simplicius, David J. Furley, and Christian Wildberg. *Philoponus: Corollaries On Place and Void. With, Simplicius: Against Philoponus On the Eternity of the World.* Duckworth, London, 1991.
- [8] Prabhakar Gondhalekar. *The Grip of Gravity.* Cambridge University Press, Cambridge, 2001.
- [9] Galileo Galilei and Stillman Drake. *Two new sciences: including centers of gravity and force of percussion.* Wall & Thompson, Toronto, 2nd edition, 1989.
- [10] Roberto Vergara Caffarelli. *Galileo Galilei and motion: a reconstruction of 50 years of experiments and discoveries.* Società Italiana di Fisica, Bologna, 2009.
- [11] C. W. F. Everitt, T. Damour, K. Nordtvedt, and R. Reinhard. Historical perspective on testing the Equivalence Principle. *Advances in Space Research*, 32(7):1297–1300, 2003.
- [12] S. Schlamminger, K.-Y. Choi, T. Wagner, J. Gundlach, and E. Adelberger. Test of the Equivalence Principle Using a Rotating Torsion Balance. *Physical Review Letters*, 100(4):041101, January 2008.
- [13] E. G. Adelberger, J. H. Gundlach, B. R. Heckel, S. Hoedl, and S. Schlamminger. Torsion balance experiments: A low-energy frontier of particle physics. *Progress in Particle and Nuclear Physics*, 62(1):102–134, January 2009.
- [14] T. A. Wagner, S. Schlamminger, J. H. Gundlach, and E. G. Adelberger. Torsion-balance tests of the weak equivalence principle. *Classical and Quantum Gravity*, 29(18):184002, September 2012.
- [15] Clifford M. Will. The Confrontation between General Relativity and Experiment. *Living Reviews in Relativity*, 9, 2006.
- [16] L. I. Schiff. On Experimental Tests of the General Theory of Relativity. *American Journal of Physics*, 28(4):340, 1960.

- [17] Alan Lightman and David Lee. Restricted Proof that the Weak Equivalence Principle Implies the Einstein Equivalence Principle. *Physical Review D*, 8(2):364–376, July 1973.
- [18] Kip Thorne, David Lee, and Alan Lightman. Foundations for a Theory of Gravitation Theories. *Physical Review D*, 7(12):3563–3578, June 1973.
- [19] James Williams, Slava Turyshev, and Dale Boggs. Progress in Lunar Laser Ranging Tests of Relativistic Gravity. *Physical Review Letters*, 93(26):261101, December 2004.
- [20] S. M. Ransom, et al. A millisecond pulsar in a stellar triple system. *Nature*, pages 0–5, January 2014.
- [21] S. Baeß ler, B. R. Heckel, E. G. Adelberger, J. Gundlach, U. Schmidt, and H. Swanson. Improved Test of the Equivalence Principle for Gravitational Self-Energy. *Physical Review Letters*, 83(18):3585–3588, November 1999.
- [22] E. G. Adelberger. New tests of Einstein’s equivalence principle and Newton’s inverse-square law. *Classical and Quantum Gravity*, 18(13):2397–2405, July 2001.
- [23] A. E. Charman, et al. Description and first application of a new technique to measure the gravitational mass of antihydrogen. *Nature Communications*, 4:1785, January 2013.
- [24] P. Perez and Y. Sacquin. The GBAR experiment: gravitational behaviour of antihydrogen at rest. *Classical and Quantum Gravity*, 29(18):184008, September 2012.
- [25] A. Kellerbauer, et al. The AEGIS experiment at CERN. *Hyperfine Interactions*, 209(1-3):43–49, March 2012.
- [26] Daniele S. M. Alves, Martin Jankowiak, and Prashant Saraswat. Experimental constraints on the free fall acceleration of antimatter. (arXiv:0907.4110), 2009.

- [27] Michael A. Hohensee, Holger Müller, and R. B. Wiringa. Equivalence Principle and Bound Kinetic Energy. *Physical Review Letters*, 111(15):151102, October 2013.
- [28] Irwin Shapiro, Charles Counselman, and Robert King. Verification of the Principle of Equivalence for Massive Bodies. *Physical Review Letters*, 36(11):555–558, March 1976.
- [29] James G. Williams, Slava G. Turyshev, and Dale H. Boggs. Lunar laser ranging tests of the equivalence principle. *Classical and Quantum Gravity*, 29(18):184004, September 2012.
- [30] B. Dubetsky and M. Kasevich. Atom interferometer as a selective sensor of rotation or gravity. *Physical Review A*, 74(2):023615, August 2006.
- [31] J. B. Fixler, G. T. Foster, J. M. McGuirk, and M. A. Kasevich. Atom interferometer measurement of the newtonian constant of gravity. *Science*, 315(5808):74–7, January 2007.
- [32] G. Lamporesi, A. Bertoldi, L. Cacciapuoti, M. Prevedelli, and G. Tino. Determination of the Newtonian Gravitational Constant Using Atom Interferometry. *Physical Review Letters*, 100(5):050801, February 2008.
- [33] Andreas Wicht, Joel M. Hensley, Edina Sarajlic, and Steven Chu. A Preliminary Measurement of the Fine Structure Constant Based on Atom Interferometry. *Physica Scripta*, T102(1):82, 2002.
- [34] Rym Bouchendira, Pierre Cladé, Saida Guellati-Khélifa, François Nez, and François Biraben. State of the art in the determination of the fine structure constant: test of Quantum Electrodynamics and determination of  $h/\mu_0$ . *Annalen der Physik*, 525(7):484–492, July 2013.
- [35] A. Peters, K. Y. Chung, and S. Chu. High-precision gravity measurements using atom interferometry. *Metrologia*, 38(1):25–61, February 2001.

- [36] J. M. McGuirk, G. T. Foster, J. B. Fixler, M. J. Snadden, and M. A. Kasevich. Sensitive absolute-gravity gradiometry using atom interferometry. *Physical Review A*, 65(3):033608, February 2002.
- [37] T. L. Gustavson, P. Bouyer, and M. A. Kasevich. Precision Rotation Measurements with an Atom Interferometer Gyroscope. *Physical Review Letters*, 78(11):2046–2049, March 1997.
- [38] J. K. Stockton, K. Takase, and M. A. Kasevich. Absolute Geodetic Rotation Measurement Using Atom Interferometry. *Physical Review Letters*, 107(13):133001, September 2011.
- [39] Savas Dimopoulos, Peter Graham, Jason Hogan, Mark Kasevich, and Surjeet Rajendran. Atomic gravitational wave interferometric sensor. *Physical Review D*, 78(12):122002, December 2008.
- [40] Peter W. Graham, Jason M. Hogan, Mark A. Kasevich, and Surjeet Rajendran. New Method for Gravitational Wave Detection with Atomic Sensors. *Physical Review Letters*, 110(17):171102, April 2013.
- [41] Savas Dimopoulos, Peter Graham, Jason Hogan, and Mark Kasevich. Testing General Relativity with Atom Interferometry. *Physical Review Letters*, 98(11), March 2007.
- [42] Savas Dimopoulos, Peter Graham, Jason Hogan, and Mark Kasevich. General relativistic effects in atom interferometry. *Physical Review D*, 78(4):042003, August 2008.
- [43] Paul Hamilton, Andrey Zhmoginov, Francis Robicheaux, Joel Fajans, Jonathan S. Wurtele, and Holger Müller. Antimatter Interferometry for Gravity Measurements. *Physical Review Letters*, 112(12):121102, March 2014.
- [44] B. Canuel, et al. Six-Axis Inertial Sensor Using Cold-Atom Interferometry. *Physical Review Letters*, 97(1):010402, July 2006.

- [45] H. Müntinga, et al. Interferometry with Bose-Einstein Condensates in Microgravity. *Physical Review Letters*, 110(9):093602, February 2013.
- [46] R. Geiger, et al. Detecting inertial effects with airborne matter-wave interferometry. *Nature Communications*, 2:474, January 2011.
- [47] Robert D. Reasenberg, Biju R. Patla, James D. Phillips, and Rajesh Thapa. Design and characteristics of a WEP test in a sounding-rocket payload. *Classical and Quantum Gravity*, 29(18):184013, September 2012.
- [48] MAIUS, <http://www.iqo.uni-hannover.de/551.html>.
- [49] Jason M. Hogan, et al. An atomic gravitational wave interferometric sensor in low earth orbit (AGIS-LEO). *General Relativity and Gravitation*, 43(7):1953–2009, May 2011.
- [50] G. M. Tino, et al. Precision Gravity Tests with Atom Interferometry in Space. *Nuclear Physics B - Proceedings Supplements*, 243-244:203–217, October 2013.
- [51] Sebastian Fray, Cristina Diez, Theodor Hänsch, and Martin Weitz. Atomic Interferometer with Amplitude Gratings of Light and Its Applications to Atom Based Tests of the Equivalence Principle. *Physical Review Letters*, 93(24):240404, December 2004.
- [52] A. Bonnin, N. Zahzam, Y. Bidel, and A. Bresson. Simultaneous dual-species matter-wave accelerometer. *Physical Review A*, 88(4):043615, October 2013.
- [53] Dennis Schlippert, Jonas Hartwig, Henning Albers, L. L. Richardson, Christian Schubert, Albert Roura, W. P. Schleich, Wolfgang Ertmer, and E. M. Rasel. Quantum Test of the Universality of Free Fall. *Physical Review Letters*, 112(20):203002, May 2014.
- [54] M. G. Tarallo, T. Mazzoni, N. Poli, D. V. Sutyrin, X. Zhang, and G. M. Tino. Test of Einstein Equivalence Principle for 0-Spin and Half-Integer-Spin Atoms: Search for Spin-Gravity Coupling Effects. *Physical Review Letters*, 113(2):023005, July 2014.

- [55] Paul Hamilton, Tom Barter, Geena Kim, Biswaroop Mukherjee, and Holger Müller. Progress towards a test of the universality of free fall using a  ${}^6\text{Li}$ - ${}^7\text{Li}$  atom interferometer. In *Bulletin of the American Physical Society*, page T5.00004, Anaheim, California, 2012.
- [56] R. A. Nyman, et al. I.C.E.: a transportable atomic inertial sensor for test in microgravity. *Applied Physics B*, 84(4):673–681, August 2006.
- [57] G. Varoquaux, R. A. Nyman, R. Geiger, P. Cheinet, A. Landragin, and P. Bouyer. How to estimate the differential acceleration in a two-species atom interferometer to test the equivalence principle. *New Journal of Physics*, 11(11):113010, November 2009.
- [58] Sven Herrmann, Hansjörg Dittus, and Claus Lämmerzahl. Testing the equivalence principle with atomic interferometry. *Classical and Quantum Gravity*, 29(18):184003, September 2012.
- [59] Michael A. Hohensee, Steven Chu, Achim Peters, and Holger Müller. Equivalence Principle and Gravitational Redshift. *Physical Review Letters*, 106(15):151102, April 2011.
- [60] M. H. Anderson, J. R. Ensher, M. R. Matthews, C. E. Wieman, and E. A. Cornell. Observation of bose-einstein condensation in a dilute atomic vapor. *Science*, 269(5221):198–201, July 1995.
- [61] James P. Burke Jr., John L. Bohn, B. D. Esry, and Chris H. Greene. Prospects for Mixed-Isotope Bose-Einstein Condensates in Rubidium. *Physical Review Letters*, 80(10):2097–2100, March 1998.
- [62] Immanuel Bloch, Markus Greiner, Olaf Mandel, Theodor Hänsch, and Tilman Esslinger. Sympathetic cooling of  ${}^{85}\text{Rb}$  and  ${}^{87}\text{Rb}$ . *Physical Review A*, 64(2):85–88, July 2001.
- [63] P. A. Altin, N. P. Robins, D. Döring, J. E. Debs, R. Poldy, C. Figl, and J. D. Close.  ${}^{85}\text{Rb}$  tunable-interaction Bose-Einstein condensate machine. *Review of Scientific Instruments*, 81(6):063103, June 2010.

- [64] Asimina Arvanitaki, Savas Dimopoulos, Andrew A. Geraci, Jason Hogan, and Mark Kasevich. How to Test Atom and Neutron Neutrality with Atom Interferometry. *Physical Review Letters*, 100(12):120407, March 2008.
- [65] Angelo Bassi, Kinjalk Lochan, Seema Satin, Tejinder P. Singh, and Hendrik Ulbricht. Models of wave-function collapse, underlying theories, and experimental tests. *Reviews of Modern Physics*, 85(2):471–527, April 2013.
- [66] Stefan Nimmrichter and Klaus Hornberger. Macroscopicity of Mechanical Quantum Superposition States. *Physical Review Letters*, 110(16):160403, April 2013.
- [67] Thomas Juffmann, Adriana Milic, Michael Müllneritsch, Peter Asenbaum, Alexander Tsukernik, Jens Tüxen, Marcel Mayor, Ori Cheshnovsky, and Markus Arndt. Real-time single-molecule imaging of quantum interference. *Nature Nanotechnology*, 7(5):297–300, May 2012.
- [68] J. M. Weisberg, D. J. Nice, and J. H. Taylor. Timing measurements of the relativistic binary pulsar PSR B1913+16. *The Astrophysical Journal*, 722(2):1030–1034, October 2010.
- [69] P. A. R. Ade, et al. BICEP2 I: Detection Of B-mode Polarization at Degree Angular Scales. (arXiv:1403.3985v2), March 2014.
- [70] The Matter wave laser Interferometry Gravitation Antenna (MIGA), <https://sites.google.com/site/migaproject/>.
- [71] Jason M. Hogan, David M. S. Johnson, and Mark A. Kasevich. Light-pulse atom interferometry. In E. Arimondo, W. Ertmer, and W. P. Schleich, editors, *Proceedings of the International School of Physics "Enrico Fermi" on Atom Optics and Space Physics*, pages 411–447, Amsterdam, June 2009. IOS Press.
- [72] Babak N. Saif, Jason Hogan, and Mark A. Kasevich. Atom Interferometry for Detection of Gravitational Waves: NIAC Phase 1 Final Report. Technical report, 2013.

- [73] Paul R. Berman, editor. *Atom Interferometry*. Academic Press, San Diego, 1997.
- [74] Pippa Storey and Claude Cohen-Tannoudji. The Feynman path integral approach to atomic interferometry. A tutorial. *Journal de Physique II*, 4(11):1999–2027, November 1994.
- [75] Christian J. Bordé. Quantum Theory of Atom-Wave Beam Splitters and Application to Multidimensional Atomic Gravito-Inertial Sensors. *General Relativity and Gravitation*, 36(3):475–502, March 2004.
- [76] Ch. J. Bordé. 5D optics for atomic clocks and gravito-inertial sensors. *The European Physical Journal Special Topics*, 163(1):315–332, November 2008.
- [77] K. Bongs, R. Launay, and M. A. Kasevich. High-order inertial phase shifts for time-domain atom interferometers. *Applied Physics B*, 84(4):599–602, August 2006.
- [78] Harold J. Metcalf and Peter van der Straten. *Laser cooling and trapping*. Springer-Verlag, New York, 1999.
- [79] Kathryn Moler, David Weiss, Mark Kasevich, and Steven Chu. Theoretical analysis of velocity-selective Raman transitions. *Physical Review A*, 45(1):342–348, January 1992.
- [80] M. Kozuma, L. Deng, E. Hagley, J. Wen, R. Lutwak, K. Helmerson, S. Rolston, and W. Phillips. Coherent Splitting of Bose-Einstein Condensed Atoms with Optically Induced Bragg Diffraction. *Physical Review Letters*, 82(5):871–875, February 1999.
- [81] Sheng-wey Chiow, Tim Kovachy, Hui-Chun Chien, and Mark A. Kasevich. 102k Large Area Atom Interferometers. *Physical Review Letters*, 107(13):130403, September 2011.
- [82] Daniel Adam Steck. Rubidium 87 D Line Data, 2010.

- [83] Daniel Adam Steck. Rubidium 85 D Line Data, 2010.
- [84] Albert Roura, Wolfgang Zeller, and W. P. Schleich. Overcoming loss of contrast in atom interferometry due to gravity gradients. (arXiv:1401.7699), January 2014.
- [85] A. Bertoldi, et al. Atom interferometry gravity-gradiometer for the determination of the Newtonian gravitational constant G. *The European Physical Journal D*, 40(2):271–279, September 2006.
- [86] Jason Hogan. *Towards Precision Tests of General Relativity Using an Atom Interferometer*. PhD thesis, Stanford University, 2010.
- [87] David M. S. Johnson. *Long baseline atom interferometry*. PhD thesis, Stanford University, June 2011.
- [88] Alex Sugarbaker. *Atom Interferometry in a 10 M Fountain*. PhD thesis, Stanford University, 2014.
- [89] H. J. Lewandowski, D. M. Harber, D. L. Whitaker, and E. A. Cornell. Simplified system for creating a BoseEinstein condensate. *Journal of Low Temperature Physics*, 132(September):309–367, 2003.
- [90] M. Haas, V. Leung, D. Frese, D. Haubrich, S. John, C. Weber, A. Rauschenbeutel, and D. Meschede. Species-selective microwave cooling of a mixture of rubidium and caesium atoms. *New Journal of Physics*, 9(5):147–147, May 2007.
- [91] J. Söding, D. Guéry-Odelin, P. Desbiolles, F. Chevy, H. Inamori, and J. Dalibard. Three-body decay of a rubidium Bose Einstein condensate. *Applied Physics B*, 69:257–261, 1999.
- [92] T. H. Bergeman, Patrick McNicholl, Jan Kycia, Harold Metcalf, and N. L. Balazs. Quantized motion of atoms in a quadrupole magnetostatic trap. *Journal of the Optical Society of America B*, 6(11):2249, November 1989.

- [93] Wolfgang Petrich, Michael Anderson, Jason Ensher, and Eric Cornell. Stable, Tightly Confining Magnetic Trap for Evaporative Cooling of Neutral Atoms. *Physical Review Letters*, 74(17):3352–3355, April 1995.
- [94] Franco Dalfovo, Stefano Giorgini, and L. P. Pitaevskii. Theory of Bose-Einstein condensation in trapped gases. *Reviews of Modern Physics*, 71(3):463–512, 1999.
- [95] H. M. J. M. Boesten, C. C. Tsai, J. R. Gardner, D. J. Heinzen, and B. J. Verhaar. Observation of a shape resonance in the collision of two cold  $^{87}\text{Rb}$  atoms. *Physical Review A*, 55(1):636–640, January 1997.
- [96] N. Newbury, C. Myatt, and C. Wieman. s-wave elastic collisions between cold ground-state  $^{87}\text{Rb}$  atoms. *Physical Review A*, 51(4):R2680–R2683, April 1995.
- [97] Michael Loy. Observation of Population Inversion by Optical Adiabatic Rapid Passage. *Physical Review Letters*, 32(15):814–817, April 1974.
- [98] Nikolay V. Vitanov, Thomas Halfmann, Bruce W Shore, and Klaas Bergmann. Laser-induced population transfer by adiabatic passage techniques. *Annual Review of Physical Chemistry*, 52:763–809, January 2001.
- [99] Boyan T. Torosov, Stéphane Guérin, and Nikolay V. Vitanov. High-Fidelity Adiabatic Passage by Composite Sequences of Chirped Pulses. *Physical Review Letters*, 106(23):233001, June 2011.
- [100] Tim Kovachy, Sheng-wei Chiow, and Mark A. Kasevich. Adiabatic-rapid-passage multiphoton Bragg atom optics. *Physical Review A*, 86(1):011606, July 2012.
- [101] Malcolm H. Levitt. Composite pulses. *Progress in Nuclear Magnetic Resonance Spectroscopy*, 18(2):61–122, January 1986.
- [102] David L. Butts, Krish Kotru, Joseph M. Kinast, Antonije M. Radojevic, Brian P. Timmons, and Richard E. Stoner. Efficient broadband Raman pulses for large-area atom interferometry. *Journal of the Optical Society of America B*, 30(4):922, March 2013.

- [103] Geert Vrijsen. *Collective quantum behavior of atomic ensembles in high-finesse optical cavities*. PhD thesis, Stanford University, December 2011.
- [104] P. D. Lett, W. D. Phillips, S. L. Rolston, C. E. Tanner, R. N. Watts, and C. I. Westbrook. Optical molasses. *Journal of the Optical Society of America B*, 6(11):2084, November 1989.
- [105] Marco Pisani and Milena Astrua. Angle amplification for nanoradian measurements. *Applied Optics*, 45(8):1725–9, March 2006.
- [106] J. M. Hogan, J. Hammer, S.-W. Chiow, S. Dickerson, D. M. S. Johnson, T. Kovachy, A. Sugarbaker, and M. A. Kasevich. Precision angle sensor using an optical lever inside a Sagnac interferometer. *Optics Letters*, 36(9):1698–1700, April 2011.
- [107] Rym Bouchendira, Pierre Cladé, Saïda Guellati-Khélifa, François Nez, and François Biraben. New Determination of the Fine Structure Constant and Test of the Quantum Electrodynamics. *Physical Review Letters*, 106(8):080801, February 2011.
- [108] Mark Kasevich and Steven Chu. Atomic interferometry using stimulated Raman transitions. *Physical Review Letters*, 67(2):181–184, July 1991.
- [109] K. B. Davis, M. O. Mewes, M. R. Andrews, N. J. van Druten, D. S. Durfee, D. M. Kurn, and W. Ketterle. Bose-Einstein Condensation in a Gas of Sodium Atoms. *Physical Review Letters*, 75(22):3969–3973, November 1995.
- [110] R. Dubessy, K. Merloti, L. Longchambon, P.-E. Pottie, T. Liennard, A. Perrin, V. Lorent, and H. Perrin. Rubidium-87 Bose-Einstein condensate in an optically plugged quadrupole trap. *Physical Review A*, 85(1):1–12, January 2012.
- [111] Hubert Ammann and Nelson Christensen. Delta Kick Cooling: A New Method for Cooling Atoms. *Physical Review Letters*, 78(11):2088–2091, 1997.
- [112] C. Monroe, W. Swann, H. Robinson, and C. Wieman. Very cold trapped atoms in a vapor cell. *Physical Review Letters*, 65(13):1571–1574, September 1990.

- [113] J. Hecker Denschlag, J. E. Simsarian, H. Häffner, C. McKenzie, A. Browaeys, D. Cho, K. Helmerson, S. L. Rolston, and W. D. Phillips. A Bose-Einstein condensate in an optical lattice. *Journal of Physics B: Atomic, Molecular and Optical Physics*, 35(14):3095–3110, July 2002.
- [114] Shau-Yu Lan, Pei-Chen Kuan, Brian Estey, Philipp Haslinger, and Holger Müller. Influence of the Coriolis Force in Atom Interferometry. *Physical Review Letters*, 108(9):090402, February 2012.
- [115] Stephen R. Segal, Quentin Diot, Eric A. Cornell, Alex A. Zozulya, and Dana Z. Anderson. Revealing buried information: Statistical processing techniques for ultracold-gas image analysis. *Physical Review A*, 81(5):053601, May 2010.
- [116] G. T. Foster, J. B. Fixler, J. M. McGuirk, and M. A. Kasevich. Method of phase extraction between coupled atom interferometers using ellipse-specific fitting. *Optics Letters*, 27(11):951–953, 2002.
- [117] Occasional trials (< 5%) that display no interference appear at the center of the ellipses and are rejected. These trials are clearly distinct from those on the ellipses, and result from experimental glitches (e.g., a loss of laser lock).
- [118] Holger Müller, Sheng-wei Chiow, Sven Herrmann, Steven Chu, and Keng-Yeow Chung. Atom-Interferometry Tests of the Isotropy of Post-Newtonian Gravity. *Physical Review Letters*, 100(3):031101, January 2008.
- [119] Jürgen Audretsch and Karl-Peter Marzlin. Ramsey fringes in atomic interferometry: Measurability of the influence of space-time curvature. *Physical Review A*, 50(3):2080–2095, September 1994.
- [120] M. Kasevich and S. Chu. Measurement of the gravitational acceleration of an atom with a light-pulse atom interferometer. *Applied Physics B Photophysics and Laser Chemistry*, 54(5):321–332, May 1992.
- [121] M. V. R. K. Murty. The Use of a Single Plane Parallel Plate as a Lateral Shearing Interferometer with a Visible Gas Laser Source. *Applied Optics*, 3(4):531, April 1964.

- [122] T. Schumm, S. Hofferberth, L. M. Andersson, S. Wildermuth, S. Groth, I. Bar-Joseph, J. Schmiedmayer, and P. Krüger. Matter-wave interferometry in a double well on an atom chip. *Nature Physics*, 1(1):57–62, September 2005.
- [123] Florian Baumgärtner, R. J. Sewell, S. Eriksson, I. Llorente-Garcia, Jos Dingjan, J. P. Cotter, and E. A. Hinds. Measuring Energy Differences by BEC Interferometry on a Chip. *Physical Review Letters*, 105(24):243003, December 2010.
- [124] S. Cahn, A. Kumarakrishnan, U. Shim, T. Sleator, P. Berman, and B. Dubetsky. Time-Domain de Broglie Wave Interferometry. *Physical Review Letters*, 79(5):784–787, August 1997.
- [125] S. Gupta, K. Dieckmann, Z. Hadzibabic, and D. Pritchard. Contrast Interferometry using Bose-Einstein Condensates to Measure  $h/m$  and  $\alpha$ . *Physical Review Letters*, 89(14):1–4, September 2002.
- [126] S. Beattie, B. Barrett, M. Weel, I. Chan, C. Mok, S. Cahn, and A. Kumarakrishnan. Influence of spontaneous emission on a single-state atom interferometer. *Physical Review A*, 77(1):013610, January 2008.
- [127] Sajun Wu, Alexey Tonyushkin, and Mara Prentiss. Observation of Saturation of Fidelity Decay with an Atom Interferometer. *Physical Review Letters*, 103(3):034101, July 2009.
- [128] B. Barrett, A. Carew, S. Beattie, and A. Kumarakrishnan. Measuring the atomic recoil frequency using a modified grating-echo atom interferometer. *Physical Review A*, 87(3):033626, March 2013.
- [129] We determine this correction factor with an independent measurement of the fringe spatial frequency versus imaging time. For horizontal fringes, the observed spatial frequency decreases by 5% for 5 ms imaging.
- [130] The point source limit is relevant here only as an imaging artifact, resulting from  $t_d > t_3$ . It is not necessary for beam-tilt PSR.

- [131] Alexander D. Cronin and David E. Pritchard. Optics and interferometry with atoms and molecules. *Reviews of Modern Physics*, 81(3):1051–1129, July 2009.
- [132] G. Wilpers, T. Binnewies, C. Degenhardt, U. Sterr, J. Helmcke, and F. Riehle. Optical Clock with Ultracold Neutral Atoms. *Physical Review Letters*, 89(23):230801, November 2002.
- [133] Olaf Mandel, Markus Greiner, Artur Widera, Tim Rom, Theodor W. Hänsch, and Immanuel Bloch. Controlled collisions for multi-particle entanglement of optically trapped atoms. *Nature*, 425(6961):937–40, October 2003.
- [134] Waseem S. Bakr, Jonathon I. Gillen, Amy Peng, Simon Fölling, and Markus Greiner. A quantum gas microscope for detecting single atoms in a Hubbard-regime optical lattice. *Nature*, 462(7269):74–7, November 2009.
- [135] A. E. Leanhardt. Cooling Bose-Einstein Condensates Below 500 Picokelvin. *Science*, 301(5639):1513–1515, September 2003.
- [136] S. Chu, J. E. Bjorkholm, A. Ashkin, J. P. Gordon, and L. W. Hollberg. Proposal for optically cooling atoms to temperatures of the order of 10-6 K. *Optics Letters*, 11(2):73, February 1986.
- [137] E. Maréchal, S. Guibal, J.-L. Bossennec, R. Barbé, J.-C. Keller, and O. Gorceix. Longitudinal focusing of an atomic cloud using pulsed magnetic forces. *Physical Review A*, 59(6):4636–4640, June 1999.
- [138] M. Morinaga, I. Bouchoule, J.-C. Karam, and C. Salomon. Manipulation of Motional Quantum States of Neutral Atoms. *Physical Review Letters*, 83(20):4037–4040, November 1999.
- [139] S. Myrskog, J. Fox, H. Moon, J. Kim, and A. Steinberg. Modified  $\delta$ -kick cooling using magnetic field gradients. *Physical Review A*, 61(5):1–6, April 2000.
- [140] Pierre Meystre. *Atom Optics*. Springer-Verlag, New York, 2001.

- [141] Eric Cornell, Chris Monroe, and Carl Wieman. Multiply loaded, ac magnetic trap for neutral atoms. *Physical Review Letters*, 67(18):2439–2442, October 1991.
- [142] David A. Smith, Aidan S. Arnold, Matthew J. Pritchard, and Ifan G. Hughes. Experimental single-impulse magnetic focusing of launched cold atoms. *Journal of Physics B: Atomic, Molecular and Optical Physics*, 41(12):125302, June 2008.
- [143] Juris Kalnins, Jason Amini, and Harvey Gould. Focusing a fountain of neutral cesium atoms with an electrostatic lens triplet. *Physical Review A*, 72(4):043406, October 2005.
- [144] G. D. McDonald, C. C. N. Kuhn, S. Bennetts, J. E. Debs, K. S. Hardman, M. Johnsson, J. D. Close, and N. P. Robins.  $80\hbar k$  momentum separation with Bloch oscillations in an optically guided atom interferometer. *Physical Review A*, 88(5):053620, November 2013.
- [145] An initially correlated ensemble corresponds to a virtual source with an effective initial size smaller than  $\Delta x_o$ .
- [146] W. J. Engelen, M. A. van der Heijden, D. J. Bakker, E. J. D. Vredenbregt, and O. J. Luiten. High-coherence electron bunches produced by femtosecond photoionization. *Nature Communications*, 4:1693, January 2013.
- [147] See Supplemental Material in arXiv ancillary files.
- [148] E. Giese, W. Zeller, S. Kleinert, M. Meister, V. Tamma, A. Roura, and W. P. Schleich. The interface of gravity and quantum mechanics illuminated by Wigner phase space. 2014.
- [149] The lattice’s depth is 40 times the recoil energy and its  $1/e^2$  radial waist is 1.5 mm.
- [150] Vladimir Minogin, James Richmond, and Geoffrey Opat. Time-orbiting-potential quadrupole magnetic trap for cold atoms. *Physical Review A*, 58(4):3138–3145, October 1998.

- [151] E. Hodby, G. Hechenblaikner, O. M. Maragò, J. Arlt, S. Hopkins, and C. J. Foot. Bose-Einstein condensation in a stiff TOP trap with adjustable geometry. *Journal of Physics B: Atomic, Molecular and Optical Physics*, 33(19):4087–4094, October 2000.
- [152] S. Hirosato, K. Yamazaki, Yu. Haraguchi, K. Muramatsu, A. Haga, K. Kamata, K. Kobayashi, A. Matsuura, and H. Sasaki. Design and Construction Method of an Open-Type Magnetically Shielded Room for MRI Composed of Magnetic Square Cylinders. *IEEE Transactions on Magnetics*, 45(10):4636–4639, 2009.
- [153] D. Cohen. Large-volume conventional magnetic shields. *Revue de Physique Appliquée*, 5(1):53–58, 1970.
- [154] V. Kelhä, J. Pukki, R. Peltonen, A. Penttilä, R. Ilmoniemi, and J. Heino. Design, construction, and performance of a large-volume magnetic shield. *IEEE Transactions on Magnetics*, 18(1):260–270, January 1982.
- [155] Y. H. Lee, K. K. Yu, J. M. Kim, H. Kwon, K. Kim, and Y. K. Park. 64-channel second-order axial gradiometer system based on DROS for magnetocardiogram in a thin shielded room. *Physica C: Superconductivity*, 468:1942–1945, 2008.
- [156] Helmut Soltner, et al. Design, construction, and performance of a magnetically shielded room for a neutron spin echo spectrometer. *Nuclear Instruments and Methods in Physics Research Section A: Accelerators, Spectrometers, Detectors and Associated Equipment*, in press, 2011.
- [157] T. Bitter, et al. A large volume magnetic shielding system for the ILL neutron-antineutron oscillation experiment. *Nuclear Instruments and Methods in Physics Research Section A: Accelerators, Spectrometers, Detectors and Associated Equipment*, 309(3):521–529, November 1991.
- [158] W. F. Randall. Nickel-iron alloys of high permeability, with special reference to mumetal. *Journal of the Institution of Electrical Engineers*, 80(486):647–658, 1937.

- [159] S. Sgobba. Physics and measurements of magnetic materials. In *CERN-2010-004, Proceedings of the CERN Accelerator School: Specialised Course on Magnets*, pages 39–63 (arXiv:1103.1069), Bruges, Belgium, 2009.
- [160] E. A. Burt and C. R. Ekstrom. Optimal three-layer cylindrical magnetic shield sets for scientific applications. *Review of Scientific Instruments*, 73(7):2699, 2002.
- [161] A. Mager. Magnetic shields. *IEEE Transactions on Magnetics*, 6(1):67–75, March 1970.
- [162] E. A. Donley, E. Hodby, L. Hollberg, and J. Kitching. Demonstration of high-performance compact magnetic shields for chip-scale atomic devices. *Review of Scientific Instruments*, 78(8):083102, August 2007.
- [163] Richard M. Bozorth. *Ferromagnetism*. Van Nostrand, New York, 1951.
- [164] A. P. Wills. On the Magnetic Shielding Effect of Trilamellar Spherical and Cylindrical Shells. *Physical Review (Series I)*, 9(4):193–213, October 1899.
- [165] A. Mager. Magnetic Shielding Efficiencies of Cylindrical Shells with Axis Parallel to the Field. *Journal of Applied Physics*, 39(3):1914, 1968.
- [166] D. Chen, E. Pardo, and A. Sanchez. Fluxmetric and magnetometric demagnetizing factors for cylinders. *Journal of Magnetism and Magnetic Materials*, 306(1):135–146, November 2006.
- [167] T. J. Sumner, J. M. Pendlebury, and K. F. Smith. Conventional magnetic shielding. *Journal of Physics D: Applied Physics*, 20(9):1095–1101, September 1987.
- [168] Alan K. Thomas. Magnetic Shielded Enclosure Design in the DC and VLF Region. *IEEE Transactions on Electromagnetic Compatibility*, EMC-10(1):142–152, March 1968.

- [169] W. G. Wadey. Magnetic Shielding with Multiple Cylindrical Shells. *Review of Scientific Instruments*, 27(11):910, 1956.
- [170] Matthew L. Terraciano, Mark Bashkansky, and Fredrik K. Fatemi. A single-shot imaging magnetometer using cold atoms. *Optics Express*, 16(17):13062–9, August 2008.
- [171] Florian Thiel. Demagnetization of Layered Ferromagnetic Structures for Magnetically Shielding: Frequency Considerations. *IEEE Transactions on Magnetics*, 14(12):392–5314, December 2009.
- [172] Degaussing was performed by a set of wires wrapped longitudinally around the layers. We applied a 60 Hz or 1 Hz (60 Hz only for the two-segment shield of Sec.8.5) alternating current to generate a saturating peak field of  $\sim 1 \text{ A/cm}$  within the shield material. We linearly ramped up to the voltage required, held, and linearly ramped back down. Each stage lasted for 900 cycles of the current. The shield performance did not depend on the number of layers degaussed at once nor the frequency at which the shields were degaussed.
- [173] COMSOL Multiphysics. We used the standard magnetostatics module with a 2D axially-symmetric geometry.
- [174] S. Malkowski, R. Adhikari, B. Hona, C. Mattie, D. Woods, H. Yan, and B. Plaster. Technique for high axial shielding factor performance of large-scale, thin, open-ended, cylindrical Metglas magnetic shields. *Review of Scientific Instruments*, 82(7):075104, 2011.
- [175] T. Lévèque, A. Gauguet, F. Michaud, F. Pereira Dos Santos, and A. Landragin. Enhancing the Area of a Raman Atom Interferometer Using a Versatile Double-Diffraction Technique. *Physical Review Letters*, 103(8):080405, August 2009.
- [176] Holger Müller, Sheng-wei Chiow, Sven Herrmann, and Steven Chu. Atom Interferometers with Scalable Enclosed Area. *Physical Review Letters*, 102(24):240403, June 2009.

- [177] J. M. McGuirk, M. J. Snadden, and M. A. Kasevich. Large Area Light-Pulse Atom Interferometry. *Physical Review Letters*, 85(21):4498–4501, November 2000.
- [178] Pierre Cladé, Saïda Guellati-Khélifa, François Nez, and François Biraben. Large Momentum Beam Splitter Using Bloch Oscillations. *Physical Review Letters*, 102(24):240402, June 2009.
- [179] Mark Kasevich, David Weiss, Erling Riis, Kathryn Moler, Steven Kasapi, and Steven Chu. Atomic velocity selection using stimulated Raman transitions. *Physical Review Letters*, 66(18):2297–2300, May 1991.
- [180] Brian Philip Anderson. *Bose-Einstein Condensation and Macroscopic Interference With Atomic Tunnel Arrays*. PhD thesis, Stanford, 2000.
- [181] S. Papp, J. Pino, and C. Wieman. Tunable Miscibility in a Dual-Species Bose-Einstein Condensate. *Physical Review Letters*, 101(4):040402, July 2008.
- [182] Ignazio Ciufolini and John Archibald Wheeler. *Gravitation and Inertia*. Princeton University Press, Princeton, 1995.
- [183] R. v. Eötvös. Über die Anziehung der Erde auf verschiedene Substanzen. *Mathematische und Naturwissenschaftliche Berichte aus Ungarn*, 8:65, 1890.
- [184] Roland v. Eötvös, Desiderius Pekár, and Eugen Fekete. Beiträge zum Gesetze der Proportionalität von Trägheit und Gravität. *Annalen der Physik*, 373(9):11–66, 1922.
- [185] V. B. Braginskii and V. I. Panov. Verification of the Equivalence of Inertial and Gravitational Mass. *Soviet Journal of Experimental and Theoretical Physics*, 34(3):463–466, 1972.
- [186] Y. Su, B. Heckel, E. Adelberger, J. Gundlach, M. Harris, G. Smith, and H. Swanson. New tests of the universality of free fall. *Physical Review D*, 50(6):3614–3636, September 1994.

- [187] P. Franken, A. Hill, C. Peters, and G. Weinreich. Generation of Optical Harmonics. *Physical Review Letters*, 7(4):118–119, August 1961.
- [188] M. M. Fejer, G. A. Magel, D. H. Jundt, and R. L. Byer. Quasi-phase-matched second harmonic generation: tuning and tolerances. *IEEE Journal of Quantum Electronics*, 28(11):2631–2654, 1992.
- [189] Paul G. Kwiat, Edo Waks, Andrew G. White, Ian Appelbaum, and Philippe H. Eberhard. Ultrabright source of polarization-entangled photons. *Physical Review A*, 60(2):R773–R776, August 1999.
- [190] K. C. Rustagi, S. C. Mehendale, and S. Meenakshi. Optical frequency conversion in quasi-phase-matched stacks of nonlinear crystals. *IEEE Journal of Quantum Electronics*, 18(6):1029–1041, June 1982.
- [191] D. H. Jundt. Temperature-dependent Sellmeier equation for the index of refraction,  $n(e)$ , in congruent lithium niobate. *Optics Letters*, 22(20):1553–5, October 1997.
- [192] O. Gayer, Z. Sacks, E. Galun, and A. Arie. Temperature and wavelength dependent refractive index equations for MgO-doped congruent and stoichiometric LiNbO<sub>3</sub>. *Applied Physics B*, 91(2):343–348, April 2008.
- [193] G. K. Samanta, S. C. Kumar, Kavita Devi, and M. Ebrahim-Zadeh. Multicrystal, continuous-wave, single-pass second-harmonic generation with 56% efficiency. *Optics Letters*, 35(20):3513–3515, 2010.
- [194] Sheng-wei Chiow, Tim Kovachy, Jason M. Hogan, and Mark A. Kasevich. Generation of 43 W of quasi-continuous 780 nm laser light via high-efficiency, single-pass frequency doubling in periodically poled lithium niobate crystals. *Optics Letters*, 37(18):3861–3, September 2012.
- [195] R. Smith. Theory of intracavity optical second-harmonic generation. *IEEE Journal of Quantum Electronics*, 6(4):215–223, April 1970.

- [196] Tobias Meier, Benno Willke, and Karsten Danzmann. Continuous-wave single-frequency 532 nm laser source emitting 130 W into the fundamental transversal mode. *Optics Letters*, 35(22):3742–4, November 2010.
- [197] Stefan Ast, Ramon Moghadas Nia, Axel Schönbeck, Nico Lastzka, Jessica Steinlechner, Tobias Eberle, Moritz Mehmet, Sebastian Steinlechner, and Roman Schnabel. High-efficiency frequency doubling of continuous-wave laser light. *Optics Letters*, 36(17):3467–9, September 2011.
- [198] Jason Aronen. La Bête Noire, 2006. URL: [www.epicurious.com/recipes/food/views/la-bete-noire-235831](http://www.epicurious.com/recipes/food/views/la-bete-noire-235831).
- [199] Maggie Ruggiero. Lemon Curd Cheesecake, 2006. URL: [www.epicurious.com/recipes/food/views/lemon-curd-marbled-cheesecake-1222199](http://www.epicurious.com/recipes/food/views/lemon-curd-marbled-cheesecake-1222199).